

CR 137657  
AVAILABLE TO THE  
PUBLIC

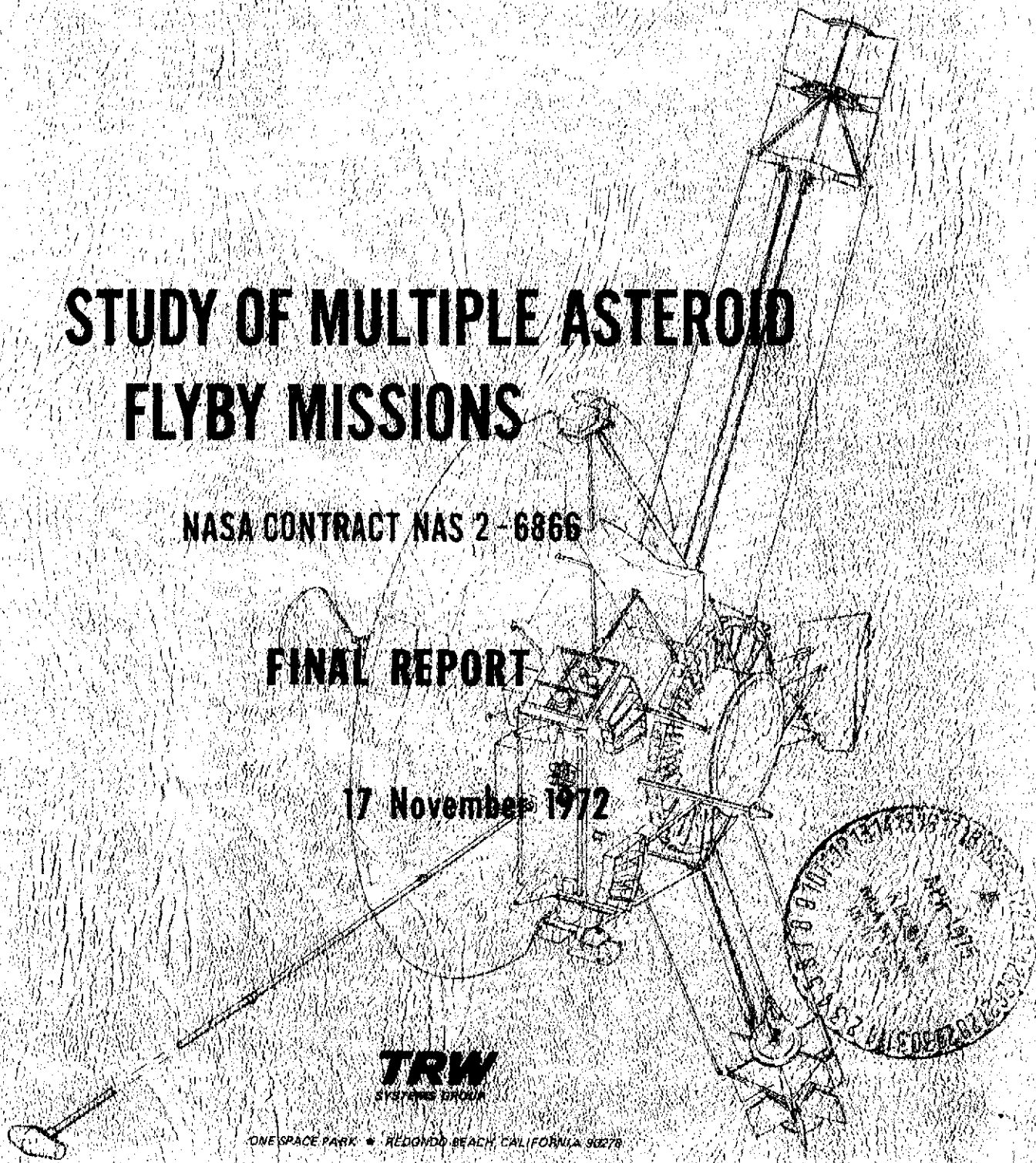
22442-6003-RU-00

# STUDY OF MULTIPLE ASTEROID FLYBY MISSIONS

NASA CONTRACT NAS 2-6866

FINAL REPORT

17 November 1972



**TRW**  
SYSTEMS GROUP

ONE SPACE PARK • REDONDO BEACH, CALIFORNIA 92078

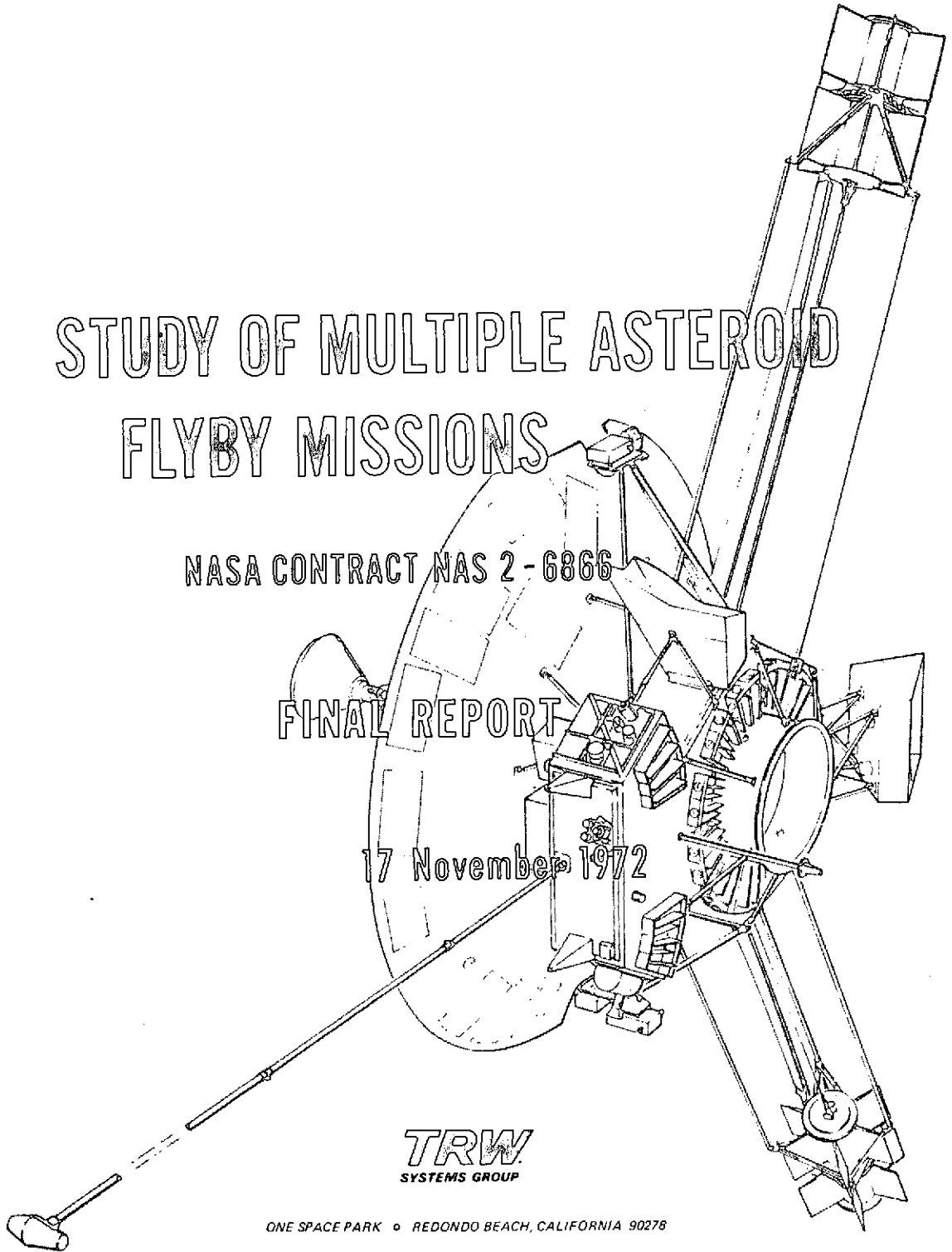
(NASA-CR-137657) - STUDY OF MULTIPLE ASTEROID  
FLYBY MISSIONS Final Report (TRW Systems  
Group) - 238 p HC \$7.50 - N75-20418  
CSCL 22A  
Unclas  
G3/12 18206

# STUDY OF MULTIPLE ASTEROID FLYBY MISSIONS

NASA CONTRACT NAS 2-6866

FINAL REPORT

17 November 1972



**TRW**  
SYSTEMS GROUP

### Acknowledgements

This study was conducted under NASA Contract for the Ames Research Center and was directed by Mr. B. Padrick. Langley Research Center co-sponsored this effort, and Mr. David R. Brooks monitored progress in detail. His original concepts of multiple asteroid and asteroid/comet flyby missions are reflected in this report. The TRW Study Manager, Mr. H. F. Meissinger, wishes to acknowledge the many useful suggestions contributed by Messrs. Padrick and Brooks in the course of this study. The direction and suggestions received from Drs. H. A. Lassen and W. J. Dixon of TRW Systems during technical progress reviews contributed significantly to the work reported herein.

## ABSTRACT

This report discusses the feasibility, scientific objectives, mission profile characteristics, and implementation of an asteroid belt exploration mission by a spacecraft guided to intercept three or more asteroids at close range. With the abundance of possible targets in the asteroid belt a large number of such mission opportunities exist the year round. A few opportunities have also been identified where a comet can be included among the targets. Since physical characteristics of these small solar system bodies are still almost entirely unknown, the large amount of new data that could thus be gathered in a single flight makes this mission concept highly attractive and cost-effective.

A principal consideration in planning a multi-asteroid mission is to cut cost by adapting an available and flight-proven spacecraft design such as Pioneer F and G, augmenting its propulsion and guidance capabilities and revising the scientific payload complement in accordance with required mission characteristics. The purpose of this study has been to determine how much spacecraft modification would actually be necessary in order to meet the objectives and requirements of the mission. A ground rule of the study was to hold design changes to a minimum and to utilize available technology as much as possible. However, with mission dates not projected before the end of this decade, a reasonable technology growth in payload instrument design and some subsystem components is anticipated that can be incorporated in the spacecraft adaptation.

A modified Pioneer spacecraft capable of performing a mission to Ceres and two smaller asteroids in mid-1978, or other mission options with similar velocity requirements, would have a gross weight of 970 pounds, including 340 pounds of hydrazine for retargeting and terminal guidance maneuvers, and would provide a science payload capacity of 75 pounds. As in Pioneer F and G, the launch vehicle is Atlas/Centaur, TE364-4. The RTG power sources of Pioneer F/G can be retained. The communications and data handling subsystems are modified to provide the increased telemetry bit rate (32.8 kpbs) required by an updated imaging system and other asteroid observation instruments.

## CONTENTS

	Page
1. EXECUTIVE SUMMARY	1-1
1.1 Background: Scientific Interest in Asteroid Exploration	1-1
1.2 Multiple Asteroid Flyby Missions	1-2
1.3 Study Objectives and Guidelines	1-4
1.4 Key Design Factors for the Pioneer Multi-Asteroid Spacecraft	1-5
1.5 Pioneer Design Modifications for Multi-Asteroid Missions	1-6
1.6 Mission Capability Constraints	1-11
1.7 Applicability of Asteroid Spacecraft to Combined Comet/Asteroid Missions	1-13
1.8 Summary of Results	1-14
1.9 Cost Economy	1-16
1.10 Present Versus New Technology	1-17
1.11 Recommended Study Areas	1-18
2. SCIENTIFIC MISSION OBJECTIVES AND PAYLOAD	2-1
2.1 Scope	2-1
2.2 Scientific Mission Objectives	2-1
2.2.1 Rationale for Asteroid Flyby Missions	2-1
2.2.2 Target Asteroid Selection Criteria	2-3
2.3 Payload Instrument Selection	2-5
2.4 Constraints Imposed by Science Objectives on Spacecraft Design Features and Observation Modes	2-7
2.4.1 Influence on Spacecraft Design	2-7
2.4.2 Influence on Selection of Encounter Conditions and Observation Modes	2-8
2.5 Imaging	2-10
2.5.1 Desired Image System Observation Capabilities	2-10
2.5.2 Imaging by a Line-Scan Image System	2-11
2.5.3 Performance Criteria for Line Scan Image System	2-13
2.5.4 Description of the Solid State Photodetector Array	2-13
2.5.5 Sensor System Characteristics	2-17

## CONTENTS (CONTINUED)

	Page
2.6 Asteroid Mass Determination	2-19
2.6.1 Doppler Measurements	2-19
2.6.2 Measurement by Gravity Gradiometer	2-21
2.6.3 Comparison of Doppler and Gravity Gradiometer Measurements	2-23
2.7 Compatibility of Spin-Stabilized Spacecraft Configuration with Scientific Objectives	2-26
2.8 A Photosensor for Meteoroid/Asteroid Detection	2-27
3. PERFORMANCE CHARACTERISTICS	3-1
3.1 Launch Vehicle Performance	3-1
3.2 Velocity Requirements of Candidate Missions	3-2
3.3 Weight Constraints and Tradeoffs	3-6
3.4 Typical Mission Velocity Requirements Versus Spacecraft Capabilities	3-9
3.5 Composite Launch Window for 1978 Sample Mission	3-12
3.6 Launch Phase Characteristics	3-13
3.6.1 Declination of Launch Asymptote	3-13
3.6.2 Direct Ascent Mode	3-15
3.6.3 Orbital Launch Mode	3-15
3.7 Summary of Spacecraft Maneuvers	3-18
4. MISSION PROFILE CHARACTERISTICS	4-1
4.1 Principal Characteristics of Multi-Asteroid Flyby Missions	4-1
4.1.1 Flyby Sequence	4-1
4.1.2 Trajectory Characteristics Affecting Encounter Conditions	4-4
4.2 Trajectory of 1978 Sample Mission	4-5
4.3 Asteroid Acquisition Problem	4-7
4.4 Encounter Conditions of Three Asteroids in Sample Mission	4-13
4.5 Scientific Instrument Pointing Program During Flyby	4-15
4.5.1 Time Variation of Viewing Conditions	4-15
4.5.2 Line-Scan Imaging Geometry	4-16
4.5.3 Image System Pointing and Updating	4-19
4.6 Summary of Mission Event Sequence	4-26

## CONTENTS (CONTINUED)

	Page
4.7 Combined Asteroid/Comet Flyby Missions	4-28
4.7.1 Trajectories	4-28
4.7.2 Typical Comet Encounter Geometry	4-30
5. TERMINAL NAVIGATION AND GUIDANCE	5-1
5.1 Terminal Navigation Concept	5-1
5.2 Asteroid Acquisition Range and Limits of Intercept Locations	5-6
5.3 Terminal Acquisition and Maneuver Requirements	5-8
5.4 Asteroid Position Uncertainty	5-12
5.5 Illustrative Terminal Guidance Examples	5-13
5.6 Terminal Navigation Sensor Design Characteristics and Error Sources	5-17
5.6.1 Design Characteristics	5-17
5.6.2 Error Sources	5-20
5.6.3 Operational Requirements	5-22
6. SPACECRAFT DESIGN	6-1
6.1 Constraints and Selection Criteria	6-1
6.2 Scope of the Design Study	6-3
6.3 Spacecraft Configuration	6-4
6.3.1 Configuration Layout	6-4
6.3.2 Design Modifications	6-7
6.3.3 Configuration Detail	6-13
6.3.4 Accommodation of Science Payload Instruments	6-14
6.3.5 Functional Block Diagram	6-16
6.4 Mass Properties	6-19
6.4.1 Weight Summary	6-19
6.4.2 Estimated Mass Properties	6-22
6.5 Dynamics	6-24
6.5.1 Attitude Stability and Pointing	6-24
6.5.2 Third Stage Injection Errors	6-26
6.5.3 Nutation Damping	6-26
6.5.4 $\Delta V$ Maneuvers	6-26
6.5.5 Optical Sensor Pointing	6-28
6.6 Power Requirements	6-29

## CONTENTS (CONTINUED)

	Page
SUBSYSTEMS	7-1
7.1 Propulsion Subsystem	7-1
7.1.1 General Approach	7-1
7.1.2 Propulsion Requirements and Constraints	7-2
7.1.3 Alternative Approaches and Tradeoffs	7-4
7.1.4 Propulsion Subsystem Description	7-13
7.2 Attitude Control Subsystem	7-16
7.2.1 Summary	7-16
7.2.2 Recommended Design	7-17
7.2.3 Wobble and Precession Effects	7-21
7.3 Data Handling Subsystem	7-22
7.3.1 Data Handling Design Concept	7-22
7.3.2 Solid State Imaging	7-27
7.3.3 Cruise and Encounter Modes	7-30
7.3.4 Required Modifications	7-31
7.4 Communications	7-32
7.4.1 Communication Subsystem Requirements	7-34
7.4.2 Recommended Communication Subsystem Design	7-37
7.5 Power and Electrical Distribution	7-45
7.5.1 Summary	7-45
7.5.2 Electrical Power Requirements	7-47
7.5.3 Power Availability During the Mission	7-48
7.6 Thermal Subsystem	7-50
7.6.1 Summary	7-51
7.6.2 Recommended Approach	7-51
7.6.3 Comparison with Pioneer F and G Thermal Conditions	7-52
APPENDIX A MICROMETEOROID PHOTO-SENSOR	A-1
APPENDIX B ESTIMATED NUMBER OF ACCESSIBLE ASTEROIDS FOR A MISSION WITH ARBITRARY LAUNCH DATE	B-1
APPENDIX C MICROMETEOROID EXPOSURE DURING ASTEROID ENCOUNTER	C-1
APPENDIX D MULTIPLE DSIF STATION COVERAGE (210- FOOT ANTENNAS)	D-1

## ILLUSTRATIONS

		Page
1-1	Multiple Asteroid Flyby Mission	1-3
1-2	Key Design Factors for Pioneer Multi-Asteroid Spacecraft	1-7
1-3	Pioneer Modifications for MAF Missions	1-8
1-4	Matrix of Modifications	1-10
1-5	Mission Capability Limits	1-12
2-1	Relative Orientation of Flyby Trajectory	2-8
2-2	Flyby Trajectory Options for a Given Approach Vector $V_{\infty}$	2-10
2-3	Desired Image System Observation Capabilities	2-12
2-4	Performance Criteria for Line-Scan Image System	2-14
2-5	Solid State Photodetector Array	2-15
2-6	LSA Phototransistor Circuit and Operating Cycle	2-16
2-7	Closest Approach Distance Required for $\pm 1$ Percent Gravity Measurement by Doppler Tracking Method (from Anderson, Ref. 2-11)	2-19
2-8	Influence of Mass Determination Error on Density Error	2-21
2-9	Attitudes Required for One Percent Gravity Measurement by Doppler and Gravity Gradient Techniques (From Ref. 2-12)	2-24
2-10	Comparison of Doppler and Gradiometer Techniques for 10 Percent Measurements Accuracy	2-25
2-11	Comparison of Doppler and Gradiometer Techniques in Terms of Mass Measurement Accuracy	2-25
2-12	Meteoroid Photosensor System	2-28
3-1	Launch Vehicle Performance	3-2
3-2	Mission Energy Requirements for Three-Asteroid Encounter Missions (Group B in Table 3-1)	3-5
3-3	Spacecraft Weight Characteristics Vs Mission Energy	3-6
3-4	Exchange Ratios Between Payload, Propellant and Gross Weight	3-8

## ILLUSTRATIONS (CONTINUED)

		Page
3-5	Typical Mission Velocity Requirements	3-10
3-6	Variation of Velocity Requirements with Launch Date	3-10
3-7	Effect of Launch Data Variation for 1978 Sample Mission	3-11
3-8	Composite Launch Window Duration for 1978 Sample Mission	3-12
3-9	Seasonal Effect of Launch Asymptote Declinations	3-14
3-10	Launch Azimuths for Direct Ascent	3-16
3-11	Launch Azimuth Boundaries for Orbital Ascent	3-16
4-1	Asteroid Flyby Compared to Jupiter Flyby	4-2
4-2	Relative Velocity Diagram	4-4
4-3	Sample Multi-Asteroid Trajectory	4-6
4-4	Asteroid Viewing Conditions in Encounters Before and After Perihelion	4-8
4-5	Comparison of Several Phase Functions	4-10
4-6	Phase Angle Variation Vs Solar Distance and Aphelion Distance	4-11
4-7	Variation of Acquisition Distance with Asteroid Position and Brightness	4-12
4-8	Encounter Conditions of Three Asteroids in Sample Mission	4-14
4-9	Time Variation of Encounter Viewing Conditions	4-15
4-10	Imaging Geometry Near Encounter	4-17
4-11	Pointing Error Geometry (In Two Dimensions)	4-19
4-12	Error Angles due to $\Delta X$ and $\Delta Y$	4-20
4-13	Contributions of $\Delta X$ and $\Delta Y$ to Pointing Angle Error $\Delta\phi$	4-20
4-14	Image System Pointing Program and Updating Functional Diagram	4-21
4-15	Imaging System Pointing Errors Due to Crossrange Offset $\Delta Y$	4-22

## ILLUSTRATIONS (CONTINUED)

		Page
4-16	Camera Pointing Vs Asteroid Image Motion Near Encounter (Zero-Order Pointing Correction)	4-24
4-17	Image Loss with Corrected and Uncorrected Pointing Angles (Geometry as in Example 1)	4-25
4-18	Main Event Sequence Near Encounter (Closest Approach Distance 100 km; Time Scale for $V_{rel} = 6$ km/sec)	4-29
4-19	Combined Asteroid/Comet Flyby Missions	4-31
4-20	Typical Comet Encounter Geometry	4-32
5-1	Terminal Navigation Sensor and Operational Concept	5-2
5-2	Navigation and Guidance Functional Block Diagram	5-4
5-3	Typical Asteroid Detection Ranges	5-7
5-4	Terminal Acquisition and Guidance Maneuver Diagram	5-9
5-5	Criteria for Selecting Terminal Sensor Sensitivity and Accuracy	5-11
5-6	Maneuver Requirements Vs Sensor Detection Threshold and Acquisition Range	5-11
5-7	Navigation by Simple Two-Point Triangulation	5-14
5-8	Upper Limit of Navigation Error and Maneuver $\Delta V$	5-15
5-9	Star Mapper Principle of Operation	5-18
6-1	Spacecraft Configuration	6-5
6-2	Pioneer Modifications for Asteroid Mission	6-8
6-3	Equipment Bay Layout	6-9
6-4	Pioneer F and G Equipment Compartment	6-11
6-5	Functional Block Diagram	6-17

## TABLES

		Page
1-1	Preliminary Payload Instrument List	1-11
2-1	Preliminary Payload Instrument List	2-6
2-2	Characteristics of Three Representative Line-Scan Image Systems	2-18
3-1	Multiple Encounter Sequences on a Flyby of Ceres	3-3
3-2	Multiple Encounter Sequences on Randomly Chosen Launch Dates in Mid-1977	3-4
3-3	Spacecraft Maneuver Summary (m/sec)	3-18
4-1	Typical Sequence of Main Events Leading to Asteroid Encounter	4-27
5-1	$1\sigma$ Ephemeris Uncertainties of Ten Selected Asteroids	5-13
5-2	Examples of Terminal Maneuver Requirements and Accuracy	5-16
5-3	Terminal Maneuver Allocations in Sample Mission	5-16
5-4	Sensor Characteristics	5-19
5-5	Star Mapper Error Sources ( $1\sigma$ )	5-21
6-1	Electric Power Requirements (Watts) (Steady Loads)	6-20
6-2	Moments of Inertia for Pioneer F and G and Jupiter Orbiter (slug-ft <sup>2</sup> )	6-23
6-3	Jupiter Orbiter - Mass Properties Estimate	6-23
6-4	Mass Properties Requirements	6-24
6-5	Maximum Pointing Errors (Degrees)	6-28
6-6	Estimated Power Requirements by Mission Phase	6-30

## 1. EXECUTIVE SUMMARY

### 1.1 BACKGROUND: SCIENTIFIC INTEREST IN ASTEROID EXPLORATION

In recent years the general scientific interest in the small bodies of the solar system, i. e. , asteroids and comets, has increased to the point where early unmanned exploration missions to these targets are now being seriously discussed and studied by astrophysicists, space mission planners, and spacecraft designers. The rationale for such missions may be summarized as follows:

- The body of existing knowledge on the physics and origin of asteroids and comets is limited and would be greatly enhanced by in-situ observation.
- Observability from earth is hampered by the small size, faint visual magnitude, and generally large observation distance of most of these objects.
- Many researchers believe that increased knowledge of the evolutionary history and present physical state of the small bodies would be an important contribution to understanding the evolution of the solar system as a whole.
- Of particular interest will be any new evidence regarding processes of fragmentation and accretion of asteroids; this can only be obtained by close observation of their physical features and surface characteristics.
- The enormously large number of such objects in all size classes facilitates the selection of convenient targets for flyby missions that could be launched almost any time. Furthermore, the energy requirements for such missions are generally quite modest.

Several important conferences have been held recently which specifically considered the physics of asteroid and comets (References 1-1, 1-2, and 1-3), and included discussions of potential mission plans and objectives. The Proceedings of the International Conference on Physical Studies of Minor Planets (Tucson, Arizona 1971) (Reference 1-1) is a particularly useful document containing a collection of nearly 70

up-to-date papers on asteroid research, including contributions of leading scientists in this field. Articles in this volume will be referenced throughout this report.

A 1971-72 NASA Advisory Panel on Comet and Asteroid Exploration, under the Chairmanship of Dr. E. Stuhlinger, has issued a report on the strategy of exploration of asteroids and comets (NASA TM X-64677, Reference 1-4). Mission classes considered in this report range from simple ballistic flyby missions to multiple flybys, rendezvous, docking, and surface sample return to earth. Scientific mission objectives and payload complements to be carried on such missions are also discussed in this report.

A mission class that has been recommended by the Advisory Panel for early implementation is the multiple flyby mission, involving either several asteroids or a comet and several asteroids. The advantages of such missions, i. e., their potentially high-scientific yield and high cost-effectiveness are obvious, but this is offset by a somewhat greater complexity of implementation. A study of these aspects and a determination of feasibility and technology requirements is therefore of timely interest.

TRW Systems' Study of Multiple Asteroid Flyby Missions based on an adaptation of the Pioneer F and G spacecraft which is reported here, reflects in part the recommendations of the NASA Small Bodies Panel, and provides data that will be useful in assessing feasibility and defining mission planning requirements.

## 1.2 MULTIPLE ASTEROID FLYBY MISSIONS

The large population of observed asteroids (nearly 2000 of them numbered and catalogued and about 2000 more identified by the Palomar-Leyden survey) offers many opportunities for multiple asteroid flyby missions that require only modest retargeting maneuvers between encounters. Brooks, et al of NASA Langley Research Center (Reference 1-5) have compiled a large list of such mission opportunities in the late 70's and early 80's with total retargeting maneuver requirements of less than 1000 m/sec. Their study recommended the use of the Pioneer spacecraft, modified to provide the required additional propulsion capability and on-board target detection for terminal navigation and guidance, as a low-cost

approach to multi-asteroid missions. The feasibility of this approach and the required modifications of the Pioneer F and G design are the subject of this study.

Figure 1-1 illustrates the concept of a multiple asteroid flyby mission. The solid line is a reference ballistic trajectory through the asteroid belt selected such that the spacecraft encounters at least one asteroid (Target 1), but passes close to several others. Retargeting maneuvers are performed after passage of each target to minimize  $\Delta V$  expenditures. The resulting trajectory (dashed line) is in effect a "broken-field run" composed of conic arcs.

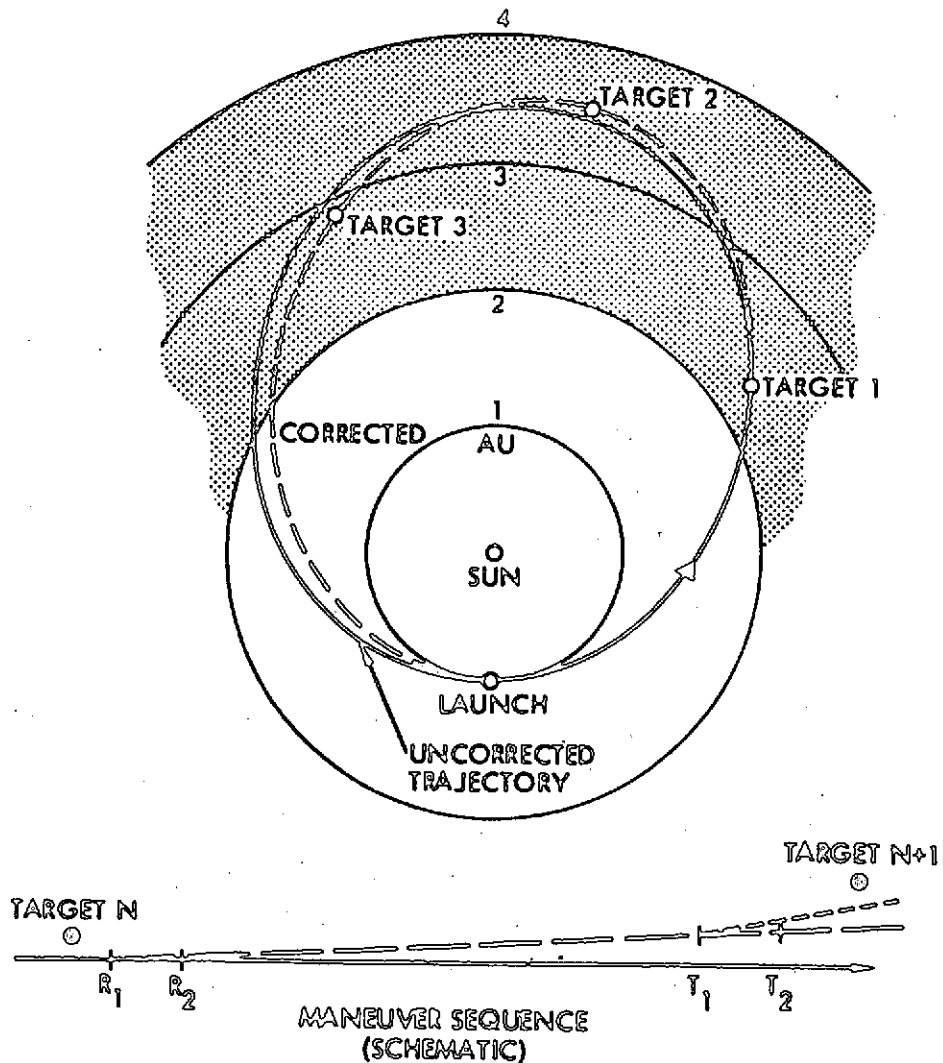


Figure 1-1. Multiple Asteroid Flyby Mission

A schematic illustration of the required maneuver sequence is shown at the bottom of Figure 1-1. After passing the Nth target a re-targeting maneuver  $R_1$  is performed, followed by a trim maneuver  $R_2$  if required, to deflect the solid (reference) trajectory as close to the target  $N + 1$  as possible, using the best available prediction of the position of that target at encounter. Terminal guidance corrections,  $T_1$  and  $T_2$  will be performed as required as soon as onboard target detection permits updating of position data.

The use of iterated terminal maneuvers reduces the propellant expenditure and increases terminal guidance accuracy. A very close approach, typically of the order of 100 km, is required for small asteroids primarily to be able to observe gravitational effects, e. g., by small doppler velocity changes, and thus to determine the asteroid's mass. This requires that the spacecraft be equipped with an optical target sensor for accurate terminal navigation measurements since earth-based terminal navigation is unsatisfactory, with asteroid ephemeris uncertainties as large as several thousand km.

Similar mission profiles can also be flown which include comet and asteroid encounters, using the same techniques of re-targeting and terminal guidance. Such missions have been investigated by Brooks (Reference 1-6), Bourke and Bender (Reference 1-7) and in a recent TRW study (Reference 1-8), and will be discussed below in Section 1.7.

### 1.3 STUDY OBJECTIVES AND GUIDELINES

The preceding sections have outlined the principal requirements of a multi-asteroid mission. In this study only the basic feasibility questions, spacecraft performance requirements and design characteristics were to be investigated, using the existing Pioneer F and G spacecraft as a baseline. The study objectives may thus be summarized as follows:

- Perform mission analysis of multi-asteroid flyby and define spacecraft design and operating requirements
- Define scientific objectives of the mission and determine preliminary science payload complements that meet these objectives

- Define a preliminary mission profile, including details of the asteroid encounter phase
- Determine feasibility of achieving multi-asteroid missions with a Pioneer F and G type spacecraft and identify the required modification from the present Pioneer F and G configuration
- Define the terminal navigation and guidance method compatible with Pioneer and evaluate its accuracy
- Show Pioneer applicability to combined asteroid/comet flyby missions
- Identify areas for additional study and development pertaining to multi-asteroid mission implementation.

The principal criteria to be used in defining the required design modifications of the existing Pioneer F and G configuration must be simplicity and cost economy as expressed by the following guidelines, which were established at the outset of the study.

- Hold modifications of Pioneer F and G configuration to a minimum
- Emphasize mission implementation simplicity and cost savings
- Stay within the launch performance envelope of Atlas/Centaur/TE-364-4
- Use current state-of-technology (e. g. , for terminal navigation and guidance)
- Achieve at least triple asteroid flyby
- Provide flexibility of launch dates for a variety of target options starting in the late 1970's.

#### 1.4 KEY DESIGN FACTORS FOR THE PIONEER MULTI-ASTEROID SPACECRAFT

Adaptation of the Pioneer spacecraft to the requirements of a multi-asteroid flyby mission involves primarily:

- A larger maneuver capability commensurate with the required retargeting and terminal guidance maneuvers
- An accurate terminal navigation system

- A change in the science payload complement keyed to asteroid observation objectives.

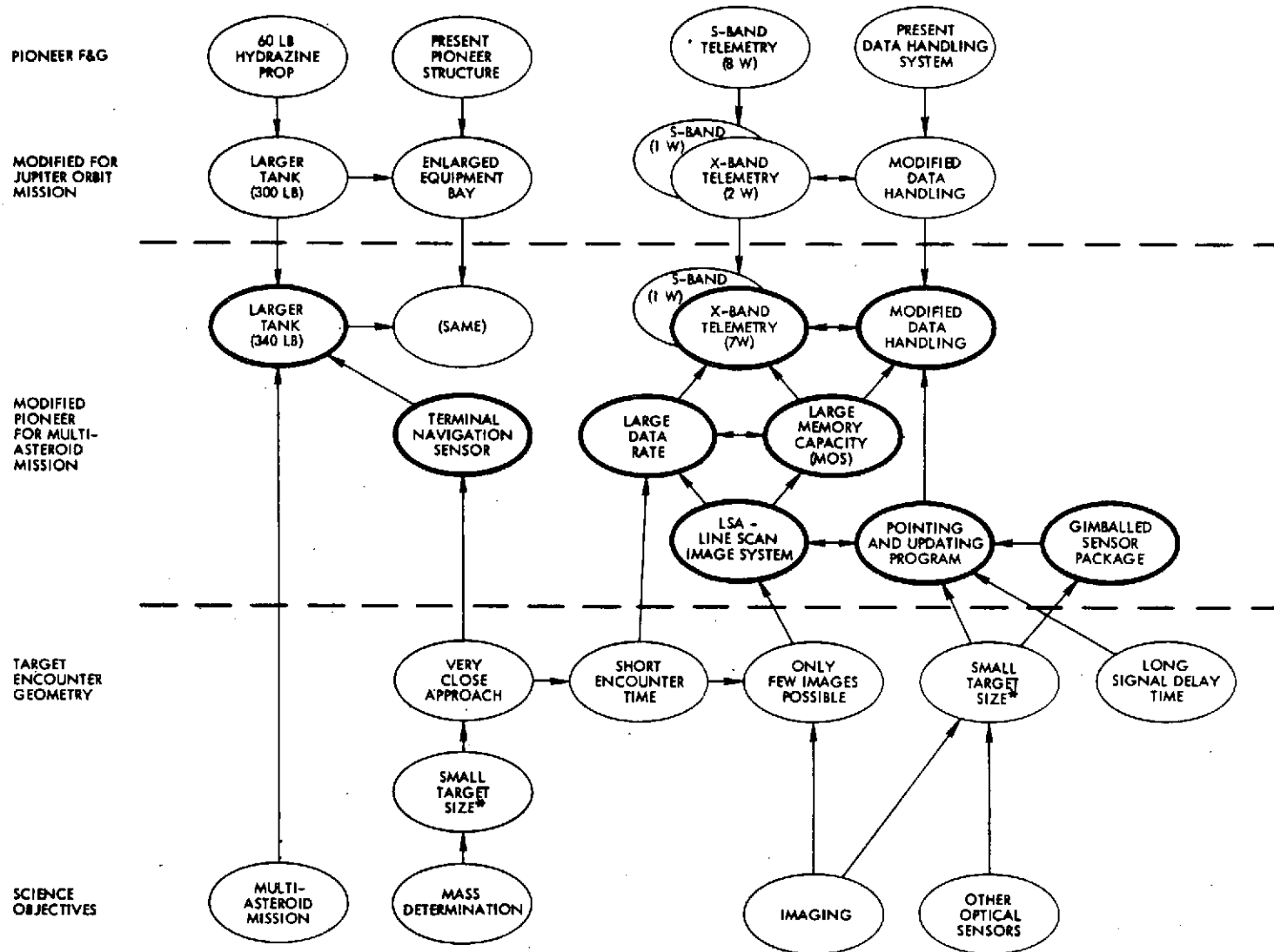
A recent study by TRW Systems has defined a conceptual design which adapts the Pioneer F and G spacecraft to a Jupiter Orbiter mission (Reference 1-9). This study concluded that the current hydrazine propulsion system, which provides a  $\Delta V$  capability of 200 m/sec, can be enlarged to provide 800-900 m/sec without major structural redesign of the spacecraft, by increasing the size of the hydrazine tank from its present diameter of 16.5 inches to 25 inches. This change necessitates relocation of some other components, but the basic spacecraft configuration remains intact. If 600 m/sec of this propulsion capability is allocated to retargeting maneuvers, and the balance to terminal maneuvers, midcourse maneuvers, and attitude control, the spacecraft would be able to perform at least one-half of the large number of asteroid mission options that are listed in Brooks' paper (Reference 1-5), i. e., a total of 48 missions in the time period from 1978 to 1981.

The modified Pioneer design for the Jupiter Orbiter is a logical step in the direction of the design adaptations to be made for the asteroid mission. An outline of other steps required in this evolution from the baseline Pioneer F and G is illustrated by the flow chart shown in Figure 1-2. Factors that dictate the selection of design features in the modified Pioneer are the scientific objectives and the target encounter geometry.

Adaptation of the Pioneer spacecraft to the asteroid mission requirements follows a logical flow of design choices, as indicated by a network of arrows. Design features of the asteroid spacecraft that differ from the Pioneer F and G baseline and the Jupiter Orbiter design are indicated in heavy outline. The imaging requirements and the constraint of a very short encounter time lead to design modifications particularly in data handling and storage, telemetry and optical sensor pointing control.

#### 1.5 PIONEER DESIGN MODIFICATIONS FOR MULTI-ASTEROID MISSIONS

Figure 1-3 indicates exterior modifications that are necessary to adapt the Pioneer F and G spacecraft to the requirements of multi-asteroid flyby missions. Modifications to various subsystems (not shown here) include:



ORIGINAL PAGE IS  
OF POOR QUALITY

\*THIS FACTOR SHOWN TWICE FOR CONVENIENCE.

Figure 1-2. Key Design Factors for Pioneer Multi-Asteroid Spacecraft

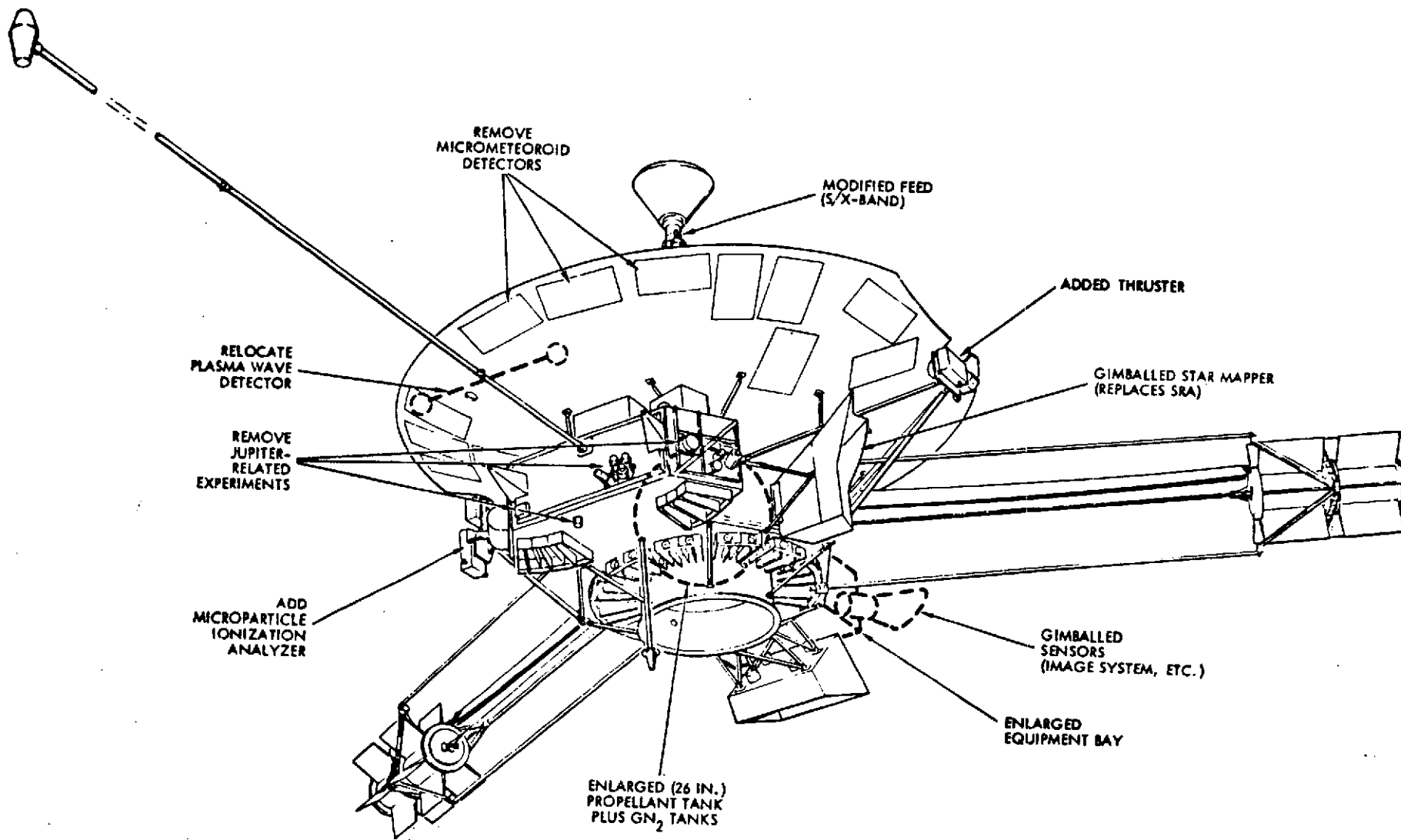


Figure 1-3. Pioneer Modifications for MAF Missions

- A dual X-/S-band communication subsystem that provides up to 32.8 kbps of data rate capability to accommodate the improved line-scan image system.
- Addition of a 600 kbit solid-state data storage unit replacing the 50 kbit core memory of the present Pioneer.
- Adaptation of the data handling and command distribution subsystems as required by the change in the communication subsystem and DSU.

The principal design modifications of Pioneer F and G are summarized in Figure 1-4 allowing a comparison of the multi-asteroid spacecraft with the original Pioneer F and G and the Jupiter Orbiter configurations. Items marked by light shading are those already modified in the Jupiter Orbiter. Items marked by dark shading require new or additional modification in the asteroid spacecraft.

The most significant set of new changes involves the adoption of a gimballed line-scan camera, high-data rate telemetry, changes in the DTU and CDU and addition of a large capacity MOS data storage unit. The enlarged maneuver capacity of the Jupiter Orbiter is used in the asteroid spacecraft practically without change, except for a much smaller 5-lbf main thruster in the asteroid spacecraft.

The science payload instruments required for asteroid flyby differ appreciably from the Jupiter flyby instruments as indicated by the legend in Figure 1-3. All but four of the Pioneer F and G science payload instruments have been eliminated and only those that are useful in direct asteroid observation or for measurements of ambient phenomena have been retained.

Table 1-1 lists the payload instruments tentatively selected for the multi-asteroid mission. The total weight (57.4 pounds) and power requirement (30.3 watts) is compatible with spacecraft capabilities. Experiments with highest priority are those directly related to the physics (structure, composition, shape, texture, thermal properties, magnetism mass, etc.) of the asteroid and its immediate environment. All others have a lower priority. The magnetometer and plasma wave detector determine the interaction of the asteroid with the solar wind and

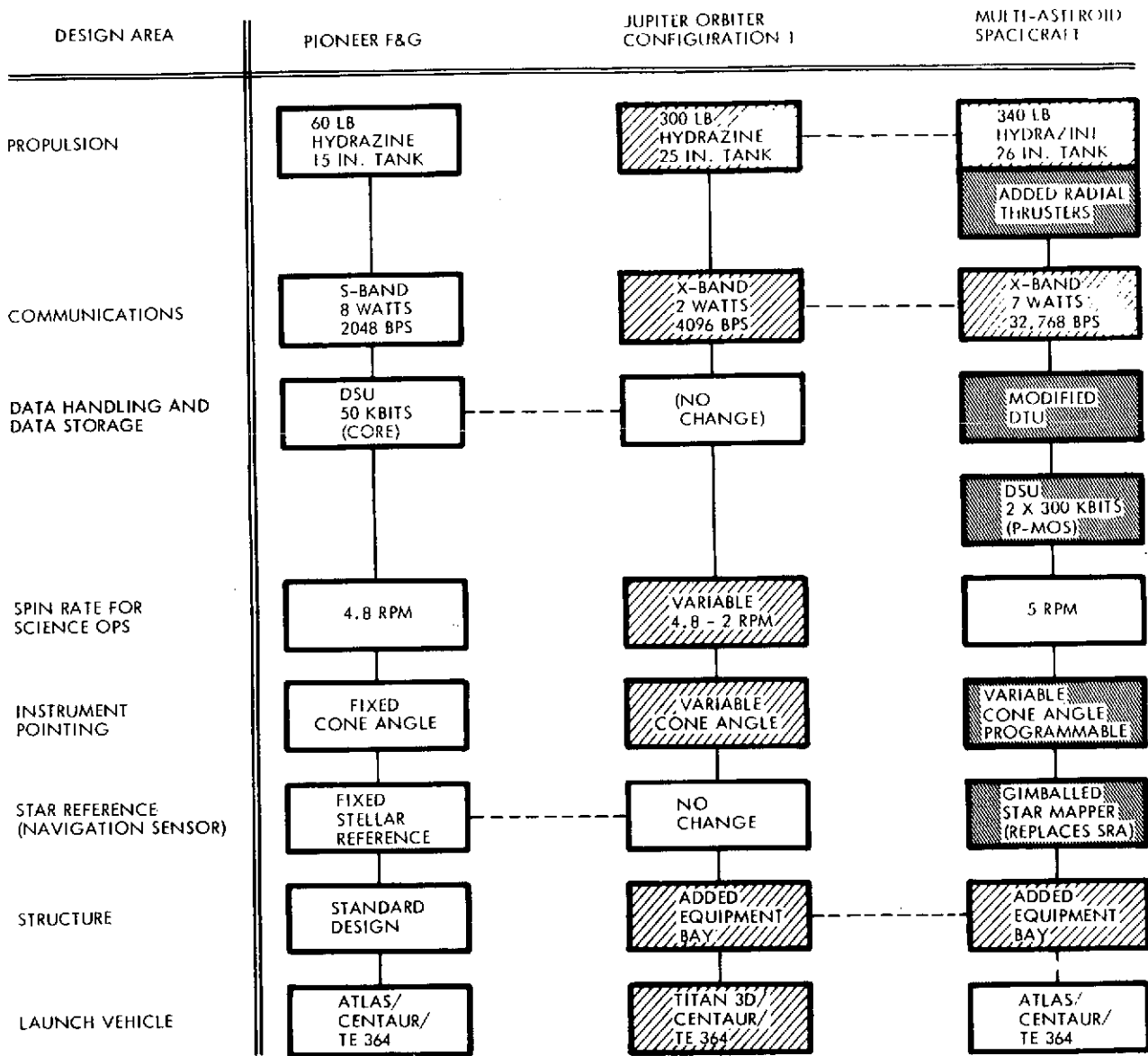


Figure 1-4. Matrix of Modifications

the interplanetary magnetic field if any. But even the lack of such interaction or of a measurable asteroid magnetic field, if ascertained by the mission, would be an important contribution to understanding asteroid physics.

The meteoroid sensors are justifiable as payload elements because during the cruise they perform measurements as to origin and composition of dust particles to provide clues as to fragmentation and accretion processes at work in the asteroid belt, while near encounter they may detect an influence of the asteroid on the particle flux environment. The asteroid/meteoroid detector (Sisyphus) may also be useful in detecting asteroids that pass at some distance.

Table 1-1. Preliminary Payload Instrument List

INSTRUMENT	PHENOMENA TO BE OBSERVED
LINE SCAN IMAGE SYSTEM	SURFACE FEATURES SHAPE OF ASTEROID
IR RADIOMETER*	TEMPERATURE PROFILES THERMAL CONDUCTIVITY
PHOTO-POLARIMETER*	SURFACE COMPOSITION AND TEXTURE ASTEROID PHOTOMETRIC CHARACTERISTICS
ASTEROID/METEOROID DETECTOR	METEOROID DISTRIBUTION
COSMIC DUST ANALYZER	COMPOSITION OF DUST PARTICLES
MAGNETOMETER*	MAGNETIC DISTURBANCE CAUSED BY ASTEROID MAGNETIC FIELD, IF ANY
PLASMA WAVE DETECTOR	SOLAR WIND INTERACTION WITH ASTEROID
GRAVITY GRADIOMETER	ASTEROID GRAVITY (BACKUP TO DOPPLER GRAVITY MEASUREMENT)

\*CARRIED BY PIONEER F AND G.

since the spacecraft requires nearly 130 watts of power with all science instruments operating simultaneously. However, some of the less essential instruments may be turned off if necessary for encounters occurring after two years.

The selected X-band transmitter power (7 watts) permits telemetry at the desired bit rate of 32.8 kbps to communication distances of 3.5 AU, as indicated by the wave-shaped boundary in the upper portion of the plot. Operating at the lower bit rate of 16.4 kbps beyond this boundary, would mean that only two out of three image frames (230 kbits each) can be transmitted rather than every image obtainable during an asteroid encounter. Communication blackout zones that may occur after about one and two years from launch are of little importance and can generally be avoided.

## 1.6 MISSION CAPABILITY CONSTRAINTS

Principal constraints on mission capability of the modified Pioneer are illustrated in Figure 1-5. This graph shows solar distance versus time for a set of asteroid belt orbits with aphelia up to 4 AU. The injection capability of the Atlas/Centaur/TE-364-4 (980 pounds total spacecraft weight at  $V_{\infty} = 7.7$  km/sec) would allow a maximum aphelion distance of 3.8 AU in a trajectory confined to the ecliptic plane. Actually the aphelion could be significantly lower for trajectories with a major out-of-plane component.

The SNAP-19 RTG power sources adopted from Pioneer F and G give only marginal power for mission times exceeding two years

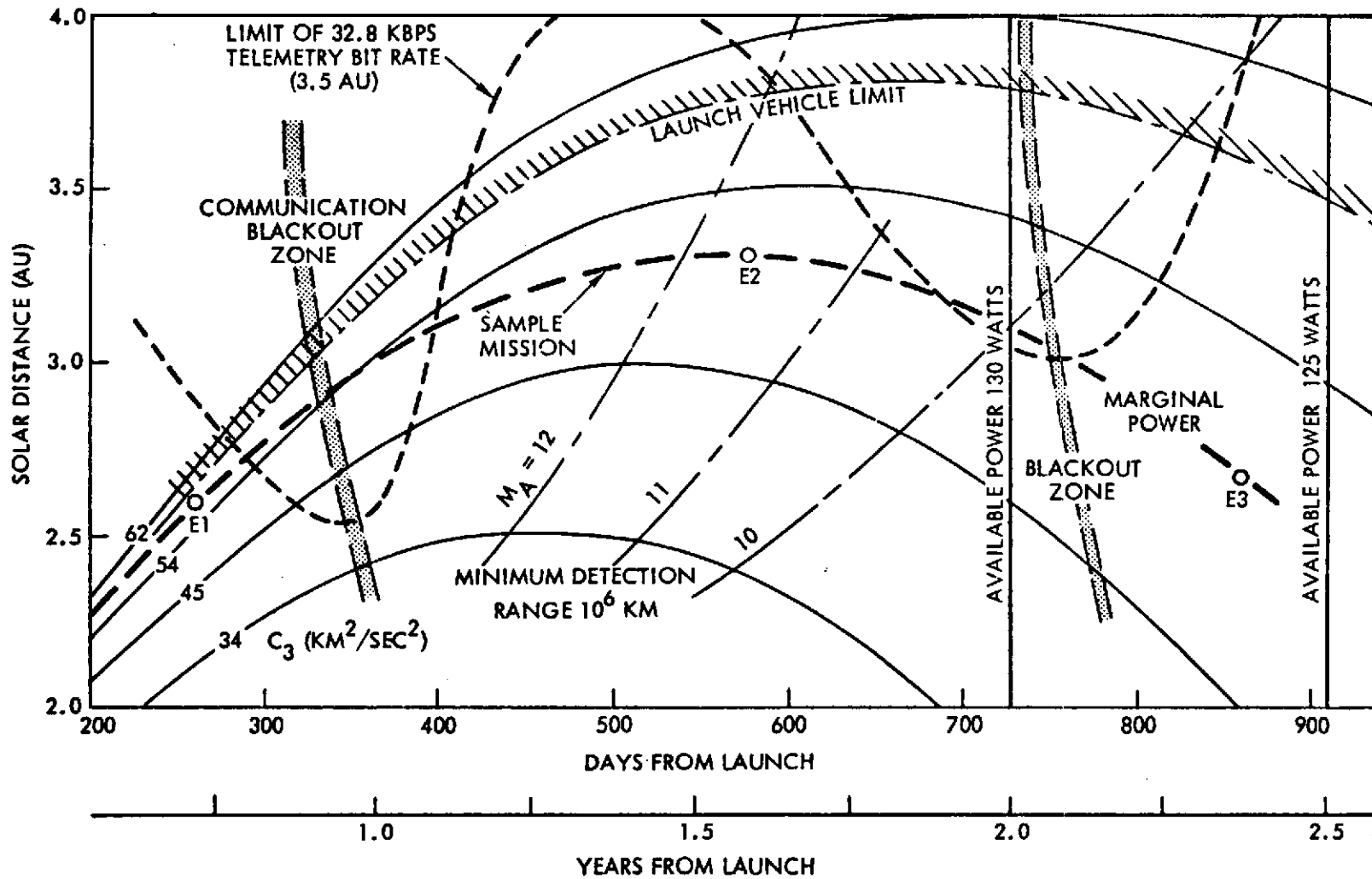


Figure 1-5. Mission Capability Limits

A more significant constraint is imposed by the asteroid detection range that is required for effective navigation. For asteroids fainter than magnitude 12 the selected sensor with a detection threshold of 5th magnitude makes the acquisition range, and hence, the time remaining for terminal maneuvers, critically short. In the selected 1978 sample mission that will be discussed in subsequent sections of this report shown by a dashed trajectory in Figure 1-5, the third encounter, at 860 days from launch, is with the large asteroid Ceres (4th magnitude). This eliminates the acquisition problem in spite of the poor lighting conditions that characterize encounters in this region of the spacecraft trajectory.

As a summary of mission capability versus capability limits, this mission map shows that the spacecraft can perform satisfactorily within a wide range of mission options, but would encounter functional constraints if a nominal range of conditions is exceeded (e. g. , communication range, mission duration, target acquisition capabilities, etc. ). As the limits of nominal performance are reached under these conditions, the capabilities decline gradually rather than abruptly.

Each of the constraints illustrated in the mission map could be alleviated by increasing the performance characteristics of some subsystems, viz, RTG power, transmitter power, sensitivity threshold of the navigation sensor, propellant capacity, etc. Actually to conform with the stated objectives of design simplicity and cost economy it is preferable to accept limited performance under some conditions than to design or modify the system to the point where its performance exceeds nominal mission requirements.

#### 1.7 APPLICABILITY OF ASTEROID SPACECRAFT TO COMBINED COMET/ASTEROID MISSIONS

Several comets accessible in the late 70's have been considered as possible targets in missions which also include asteroid flybys (References 1-6, 1-7 and 1-8). Thus, a mission to comet Whipple launched in early 1977 would encounter Asteroid 939 (Isbergar) or several others. A mission to comet Forbes, launched in late 1977 would encounter Asteroid 49 (Pales) a large asteroid with a diameter of about 100 km, and a third target e. g. , asteroids 303, 327, and 609. These missions

can be performed within the 900 m/sec maneuver capability of the Pioneer asteroid spacecraft.

The scientific return expected from a combined comet/asteroid flyby mission is of course much greater than if only one type of target is encountered. Commonality of the spacecraft features required to achieve asteroid or comet flyby make combined missions feasible and highly cost-effective.

The following characteristics are noteworthy:

- The reference trajectory is targeted to the comet; only a modest  $\Delta V$  (typically  $\leq 600$  m/sec) is required for retargeting maneuvers to two asteroids.
- The comet should be selected as the last target if possible, to permit observation close to perihelion which is scientifically more rewarding, and to reduce the risk factor.
- Comets are more readily detectable than asteroids after aphelion passage.
- Some comet flybys are nearly in a radial direction along the tail: this permits extended comet observation in spite of the high relative velocity ( $>10$  km/sec).
- Observation modes are otherwise comparable to asteroid encounters.
- The science payload must include instruments not carried in missions to asteroids only (e. g., spectrometry of gas and ion constituents), hence extra payload weight allowance is required.

## 1.8 SUMMARY OF RESULTS

Results obtained in this study are briefly summarized as follows:

- 1) Mission Concept and Implementation
  - a) Multi-asteroid missions are feasible for a modified Pioneer F and G spacecraft with augmented propulsion capability and equipped with a terminal navigation sensor.
  - b) A total  $\Delta V$  capability of 900 m/sec (of which 600 m/sec is allocated to retargeting maneuvers) is sufficient for a wide range of multiple asteroid

mission options, and even some comet/asteroid missions.

- c) A star mapper with a sensitivity of 5th magnitude and 0.1 mrad accuracy meets onboard terminal navigation requirements.
- d) Terminal guidance corrections starting one to two days before encounter require 50 m/sec on the average in each case.
- e) Desired closest approach distance is 100 to 300 km, depending on asteroid size.
- f) Asteroid a priori position errors as large as 10,000 km can be corrected with a terminal accuracy of 20-50 km if target brightness is sufficient for an early acquisition ( $10^6$  km).
- g) Unless encountered in the first half of the mission, faint asteroids ( $M \geq 12$ ) cannot be detected in time for terminal maneuvers.

## 2. Spacecraft Adaptation and Science Instruments

- a) Required minimum configuration change of Pioneer F and G: greater propellant load, addition of thrusters and gimbaled terminal navigation sensor.
- b) The equipment bay is enlarged to accommodate equipment displaced by the enlarged propellant tank.
- c) The electronic system redesign involves the telemetry system, data handling, data storage, and command distribution.
- d) The Jupiter Orbiter design concept (Configuration 1) is directly applicable to this mission. With a  $\Delta V$  capacity increased to 950 m/sec a wide range of multi-asteroid mission opportunities are available.
- e) With  $V_{\infty}$  requirements of about 7 to 7.5 km/sec Atlas/Centaur is adequate for all candidate missions.
- f) No spacecraft reorientation is required except during retargeting maneuvers after each asteroid encounter.
- g) The SNAP-19 RTG (four units) of Pioneer F and G provide adequate power for most mission options.
- h) The science payload complement of Pioneer F and G must be changed for effective asteroid observation, but four of the existing Pioneer F and G instruments can probably be retained.

- i) A line-scan image system with 195 picture cell solid-state detectors is proposed which provides a surface resolution of better than 100 m at 100 km approach distance.
- j) Gimballing of the optical sensor package is essential. A reprogrammable pointing sequence is used that can be automatically updated during flyby, using image system data for pointing error detection.

## 1.9 COST ECONOMY

The multi-asteroid mission concept is inherently cost-effective since the scientific yield of the mission increases with the number of targets encountered. Different asteroids are expected to have different physical characteristics that can be explored in a single flight. A combined asteroid/comet flyby mission would be even more cost-effective in this respect.

To make this mission economically attractive we emphasized simplicity of implementation and limited the modifications of the basic Pioneer F and G spacecraft, in accordance with the study guidelines. Constraints on mission options and spacecraft capabilities permit major cost reductions without compromising feasibility or scientific value of the mission. These points can be summarized as follows:

- The cost-effectiveness of multi-target missions is high, especially if both asteroid and comet flybys can be achieved in a single mission.
- Reasonable limits on spacecraft performance can greatly reduce cost and complexity without redundancy scientific value of the mission (e. g. , propellant weight, power, and telemetry rate limits).
- Launch vehicle and onboard propulsion ( $\Delta V$ ) economy is achieved through restriction of mission options.
- Modifications of the baseline Pioneer F and G design are held to a minimum.
- The selected design is compatible with other advanced Pioneer missions, e. g. , Jupiter Orbiter.
- Only modest onboard navigation sensor accuracy and sensitivity is required.
- No onboard computation is required.

A quantitative cost-versus-capability tradeoff, not possible within the framework of this study, should still be performed.

#### 1.10 PRESENT VERSUS NEW TECHNOLOGY

The study has shown that multi-asteroid missions are feasible with the present technology as embodied by Pioneer F and G, but improved capabilities are required in some subsystems as listed below. Most of the technology required for this improvement is available today, the limiting factor being primarily the cost of redesign, test, etc. Also listed are areas of new technology development and/or adaptation of novel techniques required to implement the mission.

##### 1. Present Pioneer Technology

- Basic Pioneer spacecraft (configuration, electrical design, etc.)
- Basic mission profile and duration
- Ground system interfaces
- 50 percent of present Pioneer F and G payload instruments are retained.

##### 2. Upgraded Pioneer Capabilities (Technology Available)

- Increased propellant load
- Onboard terminal navigation sensor
- X-/S-band communications (maximum bit rate 32.8 kbps)
- Solid-state photodetector for line-scan imaging system.

##### 3. New Technology Development or Adaptation

- Practical implementation of terminal navigation concept (spacecraft and ground system)
- New scientific payload instruments (especially for comet flyby)
- Autonomous payload pointing during critical flyby phase.

## 1.11 RECOMMENDED STUDY AREAS

Additional study is warranted in several areas that could not be covered in sufficient depth within the framework of this study phase.

These subjects are:

1. Payload Complement
  - Instrument selection and definition
  - Interfaces
  - Adequacy of spacecraft resources (power, data rate, and weight capacity).
2. Line-Scan Image System
  - Technology adaptation
3. Navigation Sensor
  - Technology adaptation
4. Precision Sensor Pointing During Flyby
  - Image tracking (additional study)
  - Selected aim points on asteroid surface
5. Combined Comet/Asteroid Missions
  - Commonality with multi-asteroid spacecraft
6. Next Phase of Multi-Asteroid Spacecraft Design

Among the study areas listed above, three tasks have higher priority than others (not necessarily in the order listed) and are recommended for inclusion in a follow-on study.

- Determine compatibility of the multi-asteroid spacecraft configuration with comet/asteroid mission requirements (Item 5).
- Define common design improvements required for other advanced Pioneer missions as well as for the multi-asteroid (and comet) mission (Items 2, 3 and 4).
- Define payload instruments (Item 1): this is required to determine adequacy of the conceptual spacecraft design.

The next spacecraft design phase (Item 6) must await better definition of overall plans for asteroid/comet exploration and can be postponed at least until concurrent studies of other advanced Pioneer applications are completed.

## REFERENCES

- 1-1 "Physical Studies of Minor Planets," NASA SP-267, T. Gehrels, Ed., Washington, D. C. 1971.
- 1-2 "Proceedings of the NASA Comet Conference," University of Arizona, Tucson, Arizona, April 8-9, 1970 (in preparation).
- 1-3 Proceedings of the Cometary Science Working Group, Yerkes Observatory, Ed. D. L. Roberts, December 1971.
- 1-4 "Comets and Asteroids: A Strategy for Exploration," NASA TM X-64677, Report of the Comet and Asteroid Mission Study Panel, May 1972.
- 1-5 David R. Brooks, Joseph W. Drewry, and William F. Hampshire II, "Multiple Asteroid Flyby Opportunities in the 1970's and 1980's," presented at the AIAA 10th Aerospace Sciences Meeting, San Diego, California, January 17-19, 1972. AIAA Paper No. 72-52.
- 1-6 David R. Brooks, "Mission Strategy for Combined Comet-Asteroid Flybys," presented at the AIAA/AAS Astrodynamics Conference, Palo Alto, California, September 11-12, 1972, AIAA Paper No. 72-939.
- 1-7 D. F. Bender and Roger D. Bourke, "Multi-Asteroid Comet Missions Using Solar Electric Propulsion," presented at AIAA 9th Electric Propulsion Conference, Bethesda, Md., April 17-19, 1972, AIAA Paper No. 72-429.
- 1-8 "Study of a Comet Rendezvous Mission," Volume 1, Technical Report, prepared for Jet Propulsion Laboratory under Contract No. 953247, TRW Systems Group, 20513-6006-R0-00, 12 May 1972.
- 1-9 "Study of Follow-On Pioneer Missions to Jupiter," Volume 2, Technical, Pioneer Jupiter Orbiter Mission, 20406-6004-R0-00, TRW Systems Group, Redondo Beach, California, August 13, 1971.
- 1-10 "Pioneer F/G Spacecraft Operational Characteristics Study," 71-7531, 9-14, TRW Systems Group, Redondo Beach, California, 23 April 1971.

## 2. SCIENTIFIC MISSION OBJECTIVES AND PAYLOAD

### 2.1 SCOPE

In keeping with study guidelines, this investigation of scientific mission objectives and payload composition was aimed primarily at defining mission profile, observation mode, and spacecraft design requirements that are dictated by these objectives.

The tasks included:

- Determination of principal scientific objectives and their relative priorities
- Selection of a representative science payload complement
- Determination of mission profile requirements and constraints, dictated by scientific objectives and science instrument operation
- Definition of spacecraft design requirements and operational modes that must be implemented to meet the mission objectives and accommodate the (postulated) payload instruments.

A description of the scientific instruments and measurement techniques was omitted except for the imaging system which has a dominant effect on spacecraft design and operation. Some important tradeoffs in asteroid mass determination were also investigated.

### 2.2 SCIENTIFIC MISSION OBJECTIVES

#### 2.2.1 Rationale for Asteroid Flyby Missions

Scientific objectives of asteroid observation by flyby and rendezvous missions are discussed in several articles contained in the Proceedings of the IAU Symposium on Minor Planet Studies (Reference 1-1). Many other papers on asteroid physics and objectives of asteroid research in general that are included in the Proceedings provide relevant background material for this study.

Some of the papers in Reference 1-1, notably articles by Alfvén and Arrhenius (References 2-1, 2-2), Stuhlinger (Reference 2-3) Bratenahl (Reference 2-4), Gehrels (Reference 2-5), and Marsden (Reference 2-6) discuss the merits of relatively simple asteroid flyby missions and make strong arguments for an early implementation of missions of this class.

The strategy of asteroid and comet exploration developed by the 1971 NASA Advisory Group on Small Bodies Missions (Reference 1-4) envisions the role of early asteroid flybys as precursors to more elaborate future missions that would include rendezvous, landing or "docking," and even the return of sample material to earth. In such a sequence, the initial physical data gathered via flyby will be indispensable to the formulation of an effective program of future missions, and the evolution of spacecraft design and scientific instrumentation.

Summarizing from the contents of the referenced articles, the scientific objectives of asteroid flyby include the following:

1. Observations by optical sensors
  - Asteroid shape and size
  - Rotational characteristics
  - Surface features
  - Surface composition and texture
  - Cratering, fractures, and other evidence of past collisions
  - Photometric characteristics
  - Thermal characteristics such as temperature profiles and thermal conductivity.
2. Determination of asteroid mass and density
  - Gravity (or gravity gradients) and mass
  - Density, inferred from mass and dimensions.
3. Physical observation of asteroid environment
  - Magnetic field (if any)
  - Interaction with solar wind
  - Micrometeoroid flux in immediate vicinity.
4. Phenomena related to general mission objective
  - Spatial density of asteroidal and cometary meteoroids, and of asteroids that can be detected in the distance
  - Composition of meteoroids
  - Magnetic field and plasma phenomena in different regions of the asteroid belt.

Optical observation, in particular acquisition of high-surface resolution images, and mass and density determination are regarded as priority objectives. From interpretation of surface features (such as size and distribution of craters, percent of surface coverage by craters, evidence of major collisions, existence of fracture zones) the age and evolutionary history of the asteroid can be deduced. This has been demonstrated impressively in the case of high resolution pictures taken by Mariner 9 of the Martian satellites Phobos and Deimos (References 2-7 and 2-8) at distances of 5500 km or greater. These satellites are believed to be very similar to asteroids in size, shape, and surface features.

Interest in asteroid mass and density is related in general to questions regarding the origin of the asteroids and their relation to comets and meteoroids. Of particular interest would be evidence that mass density decreases systematically with solar distance.

A recent theory on the condensation of material from the solar nebula postulates that the density of the evolving planets and planetoids is correlated with equilibrium temperatures in the solar system (Reference 2-9). Evidence needed to confirm this theory may be found by detecting a systematic variation of asteroidal density with solar distance. This suggests that target asteroids be selected from the inner and outer region of the belt, and that asteroids in near-circular orbits promise to supply more relevant data than those in eccentric orbit that may have been perturbed from the initial circular orbit.\*

This objective underscores the importance of accuracy in the determination of mass and size, and hence mean density, of the asteroids encountered (see Section 2.6).

### 2.2.2 Target Asteroid Selection Criteria

One of the principal advantages of a multiple asteroid flyby mission is the large variety of choices open to the mission planner in selecting preferred target asteroids. Scientific interest in large and small asteroids is equally strong. Asteroids of different size classes should be selected

---

\*Personal communication from Dr. J. E. Lewis of MIT.

as targets since data obtainable by observation of large and small asteroids can be expected to complement each other in contributing to the general knowledge of asteroid physics.

Of particular interest is an apparent anomaly in the statistical distribution of asteroids of the larger versus the smaller size classes inferred from photometric observations (Reference 2-9). The characteristic bend in the distribution curve occurring in the range of asteroid magnitude 10 to 12 could be the result of the continual collision and fragmentation process in the asteroid belt. The population density of the smaller asteroids would thus tend to deviate increasingly from an original, more nearly Gaussian distribution of the whole population.

Although the small sample of asteroids to be observed in one or several multiple asteroid missions cannot provide enough statistical evidence regarding this hypothesis, the search for characteristic differences correlated with asteroid size is considered an important mission objective that should influence the target selection.

Practical considerations favor the larger targets: their orbital characteristics are generally better known, thus the a priori guidance errors are smaller; terminal guidance correction is facilitated by the greater ease of obtaining early navigational fixes; and for a given flyby distance more physical data can be acquired, the mass determination is more accurate, and magnetic/solar wind interactions are more likely to be observable.\* These factors must be traded off against the equally high scientific interest in the small but harder to reach asteroids.

As the most logical approach to target size selection we propose that a large, a medium, and a small asteroid be included among the targets of a three-asteroid flyby mission, or at least one large and two small asteroids. A mission to more than three asteroids would be desirable but is rarely feasible under the constraints of limited maneuver capability.

---

\* Reference 2-13.

### 2.3 PAYLOAD INSTRUMENT SELECTION

In accordance with the priorities of scientific observations outlined in Section 2.2, a complement of eight payload instruments was selected, see Table 2-1. This selection is tentative and will undoubtedly be revised in subsequent studies as specific mission plans become more firmly established. However, the listed set of instruments can be used as representative example for purposes of defining mission profile options, spacecraft design features and observation modes that are essential for making effective use of this payload.

The table lists the instruments; the principal phenomena to be observed by each; some of the constraints which they impose on mission design and spacecraft functions; and estimated weight and power requirements. The total weight (57.4 pounds) and power (30.3 W) are compatible with a Pioneer type spacecraft, although the power requirement (Pioneer F/G: 24 W) is on the high side, see Sections 6, 7.

Not all of the instruments listed have equally high priority. The imaging system, IR radiometer, photo-polarimeter,\* gravity gradiometer, and magnetometer measure physical characteristics of the asteroid itself and rank higher on the priority list than the asteroid/meteoroid detector ("Sisyphus"),\*\* the cosmic dust analyzer and the plasma wave detector which observe the near or distant environment.

A strong argument can be made for including the latter three instruments in the proposed list. The two micrometeoroid sensors are justifiable because by measuring distribution, origin and composition of dust particles encountered along the trajectory, they provide data on the fragmentation and accretion processes continuously at work in the asteroid belt. Close to encounter these sensors may detect the asteroid's influence on the particle flux environment, particularly if the asteroid is one of the larger ones. By counting larger meteoroids or asteroids passing within detectable range, the asteroid/meteoroid detector provides additional data on spatial density distribution. Observation of the background particle flux is a relevant objective of the mission, although not directly associated with the asteroid flyby.

---

\* Reference 2-14. \*\* Reference 2-15.

Table 2-1. Preliminary Payload Instrument List

INSTRUMENT	PHENOMENA TO BE OBSERVED	CONSTRAINTS ON MISSION/SPACECRAFT	WEIGHT (LBS)	POWER (W)
LINE SCAN IMAGE SYSTEM	SURFACE FEATURES SHAPE OF ASTEROID	MUST BE GIMBAL-MOUNTED. REPROGRAMMABLE POINTING SEQUENCE.	(e) 12.0	(e) 8.0
IR RADIOMETER *	TEMPERATURE PROFILES THERMAL CONDUCTIVITY		4.3	1.7
PHOTO-POLARIMETER *	SURFACE COMPOSITION AND TEXTURE ASTEROID PHOTOMETRIC CHARACTERISTICS	IMAGE SYSTEM REQUIRES HIGHER MEMORY CAPACITY AND HIGHER TELEMETRY BIT RATES THAN PIONEER F AND G ESTABLISHES PREFERRED B-VECTOR ORIENTATION	9.1	4.1
ASTEROID/METEOROID DETECTOR	METEOROID DISTRIBUTION	NONE	7.3	2.8
COSMIC DUST ANALYZER	COMPOSITION OF DUST PARTICLES	NONE	(e) 6.0	(e) 2.6
MAGNETOMETER *	MAGNETIC DISTURBANCE CAUSED BY ASTEROID MAGNETIC FIELD, IF ANY	MAINTAIN HIGH MAGNETIC CLEANLINESS REQUIRES CLOSE APPROACH	5.2	4.1
PLASMA WAVE DETECTOR	SOLAR WIND INTERACTION WITH ASTEROID		REQUIRES CLOSE APPROACH	3.5
GRAVITY GRADIOMETER	ASTEROID GRAVITY (BACKUP TO DOPPLER GRAVITY MEASUREMENT)	REQUIRES CLOSE APPROACH ESTABLISHES PREFERRED B-VECTOR ORIENTATION SPACECRAFT ORIENTATION CON- STRAINS MEASUREMENT	(e) 10.0	(e) 5.0
TOTAL			57.4	30.3

\* CARRIED BY PIONEER F AND G.  
(e) ESTIMATED VALUES

The plasma wave detector used in combination with the magnetometer determines interactions of the asteroid with the solar wind and the interplanetary magnetic field, if any. Even the absence of such interactions or a magnetic field strong enough to be registered by the sensors would constitute information that contributes to an understanding of the physics of asteroids.

Mass determination will be performed by gravity gradient measurements onboard the spacecraft and by Doppler velocity measurements by the DSN stations. The two approaches complement each other as their accuracy is differently affected by asteroid size and encounter geometry.

## 2.4 CONSTRAINTS IMPOSED BY SCIENCE OBJECTIVES ON SPACECRAFT DESIGN FEATURES AND OBSERVATION MODES

### 2.4.1 Influence on Spacecraft Design

Asteroid imaging is one of the highest-priority objectives of the mission. The spacecraft design must provide the necessary equipment for pointing the image system at the target under rapidly changing aspect angles. The pointing mechanism must be designed for effective image taking unaffected by the continuous rotation of the spacecraft. This mechanism can be shared by the other two optical sensors (IR radiometer and photopolarimeter) that must be pointed in the same direction.

Effective asteroid viewing is compatible with a spinning spacecraft if the sensors are gimbal-mounted and oriented at the proper cone angle such that the sensor field of view encompasses the asteroid for some time interval during each rotational sweep. In principle this limits the number of close-up images obtainable during the short flyby. However, in practice the amount of image data that can be acquired and telemetered to earth proves to be more severely limited by available telemetry rates than by the intermittency of exposure.

As will be discussed below a high resolution line scan image system with 200 x 200 picture cells per frame, at 6 bits per picture cell, generates 240 kbits per frame and requires a telemetry bit rate of 20 kbps with one exposure occurring during every 12 second revolution period. To accommodate this data flow a high-capacity buffer storage must be provided replacing the 50 kbit core memory used in Pioneer F and G,

and the data handling and telemetry subsystems must be modified. The primary concern in this study with capabilities of the image system and with the design requirements it imposes on the spacecraft is explained by these factors. The data requirements of all other sensors combined are negligible by comparison.

#### 2. 4. 2 Influence on Selection of Encounter Conditions and Observation Modes

Asteroid encounter conditions that are best suited for effective scientific observations can be achieved by controlling the position of the closest-approach point relative to the asteroid, i. e., the closest approach distance as well as the angle of the  $\vec{B}$  vector in the impact plane  $R, T$  (see Figure 2-1). In a major planet flyby mission this is accomplished by appropriate targeting of the trajectory at launch and by midcourse correction. In an asteroid flyby mission the trajectory uncertainties relative to the asteroid are much greater, and control of the closest approach point can be exercised by terminal guidance maneuvers only after the trajectory errors are determined with sufficient accuracy by onboard measurement, one to several days before the encounter. Thus, the addition of an onboard terminal navigation sensor to Pioneer is a requirement imposed by scientific mission objectives.

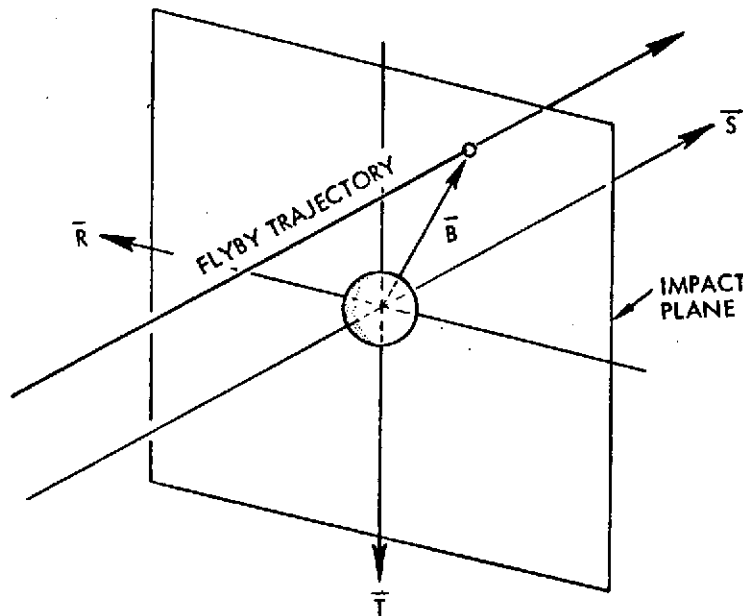


Figure 2-1. Relative Orientation of Flyby Trajectory

A close approach to the asteroid is dictated primarily by the scientific objective of accurate mass determination. For small asteroids this requires closest approach distances of 100 km or less as will be discussed in Section 2.6. Miss uncertainties can be as large as 500 km due to the asteroid's ephemeris uncertainty. Even for the largest asteroid Ceres with a well established ephemeris the uncertainty is several hundred km. Obviously, a terminal guidance maneuver that reduces the miss by several thousand km can also be used to position the  $\bar{B}$ -vector at an orientation that is favorable for visual and infrared observations, practically without additional propellant cost.

Concern with the relative latitude position of the closest approach point arises primarily with larger asteroids because of the different phenomena observably by overflight of different latitudes. Figure 2-2 shows different flyby trajectories in terms of their surface tracks for a given approach vector ( $\bar{V}_{\infty}$ ). The trajectories cover different latitude zones of the asteroid, providing a variety of observation options that can be summarized as follows:

<u>Case</u>	<u>Observation Option</u>
1	Low illumination on close approach. Small thermal gradients.
2	Higher illumination and thermal gradients. Good contrasts. Preferred observation geometry.
3	Flyby nearly in ecliptic. Highest illumination, poor contrasts, not suitable for spin-scan imaging near subearth point.
4	Similar to 2, but poorer observation of terminator region due to distance. Best view of equatorial region.

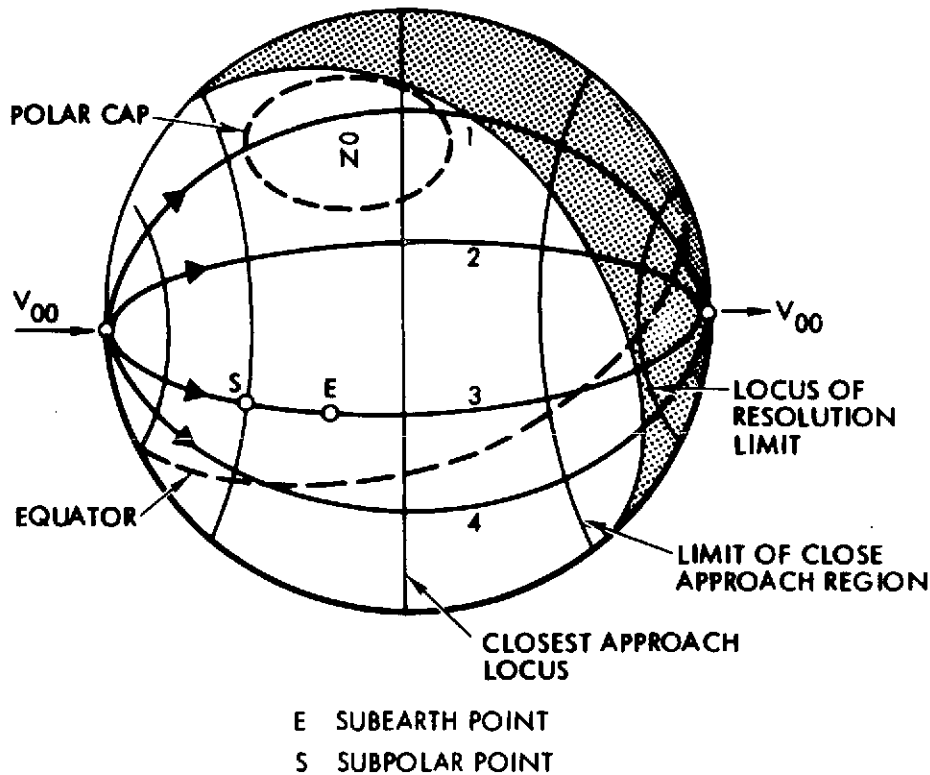


Figure 2-2. Flyby Trajectory Options for a Given Approach Vector  $V_{\infty}$

Of the options shown, Case 2 is most favorable from a visual and infrared observation standpoint. It also provides a good compromise between relative geometry requirements of mass measurements by the gravity gradient technique versus the earth based Doppler technique. For best gravity gradient measurements with an earth-oriented spinning spacecraft, the overflight Option 1 would be preferred. For best Doppler measurement Option 3 would be preferable which maximizes the gravity-induced Doppler velocity change measurable at earth. Option 1 would be least favorable for detection of small gravity perturbations and thus would require a much closer approach to the asteroid than Option 4.

## 2.5 IMAGING

### 2.5.1 Desired Image System Observation Capabilities

A closest approach of the order of 100 km which is dictated by the mass determination objective permits relaxation of image system resolution requirements. At a range of 100 km an image system with 1 mrad resolution would achieve about the same surface resolution as the

0.02 mrad camera of Mariner 9 in the observation of the Martian satellite Phobos at 5550 km range. The resolution that is obtainable by 195 sense cells on a 6-degree FOV camera is 0.5 mrad. This number of cells is compatible with the telemetry data rate of 32.8 Kbps and a data storage capacity of 230 Kbps which can be met with a reasonably small modification of the Pioneer subsystems.

Figure 2-3 shows the surface resolution obtainable as a function of distance in relation to typical surface features, their assumed dimension and desired resolution ranges. The parametric lines can be used to find the subtended angle of asteroidal dimensions at a given range and to show at what range an asteroid will fill a specified field of view. For example the smallest asteroids considered for this mission class roughly fill a 6-degree FOV at 100 km range.

#### 2.5.2 Imaging by a Line-Scan Image System

The proposed imaging system<sup>\*</sup> consists of a linear array of a large number of solid-state photo detectors which are swept in push-broom fashion across the visual scene being observed. The line elements describe concentric circles around the spin axis, the radii of these circles being determined by the cone angle at which the optical axis of the instrument is pointed. The sweep rate varies with the sine of the cone angle.

For cone angles near 0 and 180 degrees, the imaging process deteriorates. Viewing conditions where the visual scene is at or near a point on the extended spacecraft spin axis must therefore be avoided.

The preference for a line scan image system in this application is based on the following considerations:

- A point scan image system such as the imaging photo polarimeter used on Pioneer F and G for taking pictures of Jupiter is unsatisfactory for purposes of asteroid imaging since the extremely short encounter and the rapid change of viewing conditions precludes the use of a mosaic technique.
- Conventional image forming (vidicon) TV systems are not compatible with the 5 rpm Pioneer spin rate without further state-of-technology advances.

---

\*Reference 2-17

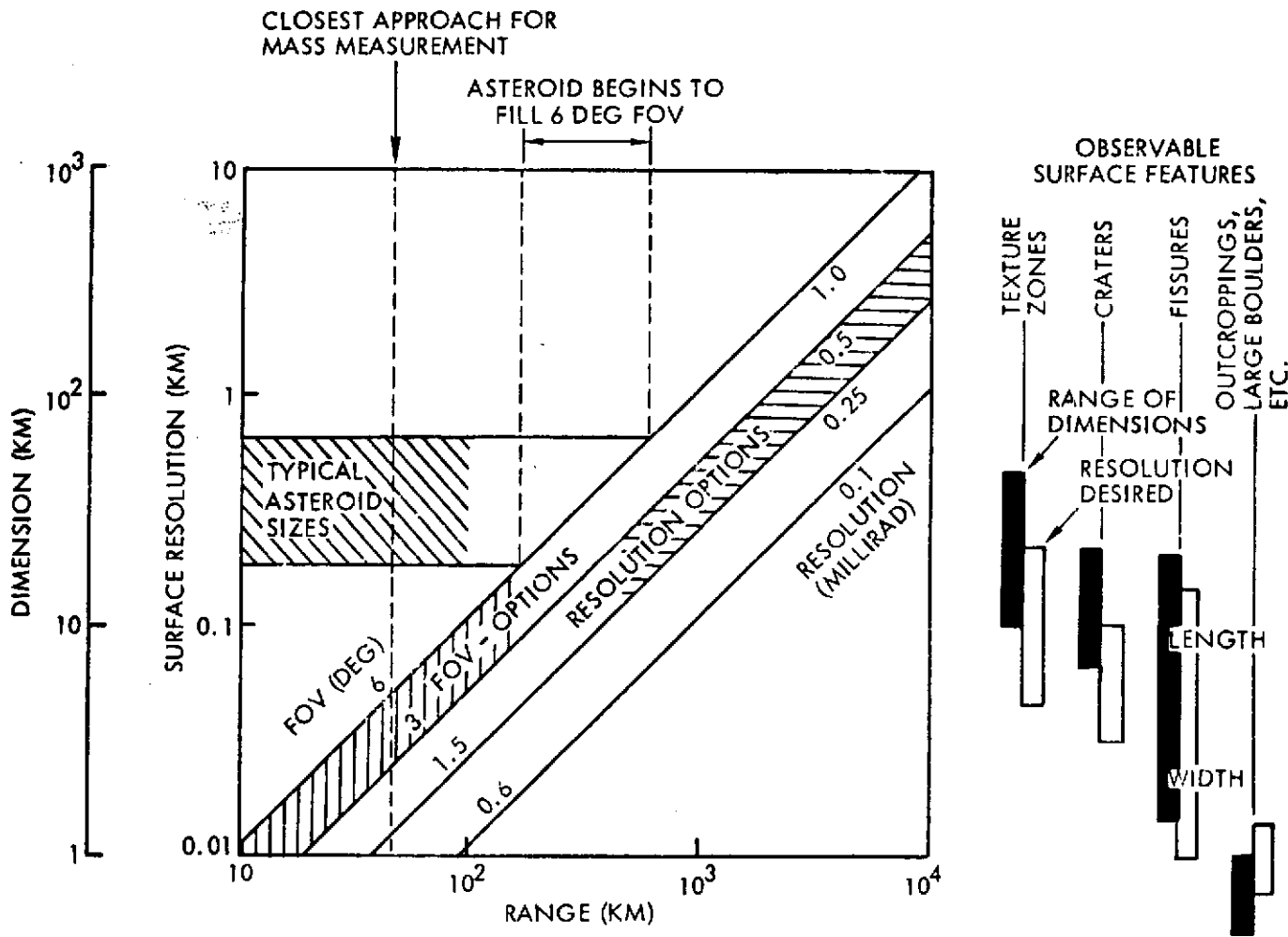


Figure 2-3. Desired Image System Observation Capabilities

ORIGINAL PAGE IS  
OF POOR QUALITY

- The solid-state line scan photodetector, developed originally for near-earth applications, is compatible with the spinning Pioneer spacecraft, offers high geometric accuracy, long life, compact design and has a low power requirement.

Design features of the line scan system will be discussed in Sections 2.5.4 and 2.5.5.

### 2.5.3 Performance Criteria for Line Scan Image System

The image system is limited in resolution in the direction normal to the sensor array, i. e., the spin scan direction, by the required minimum exposure time of each detector cell. The present state of technology requires at least 0.5 msec, which for a 5 rpm spin rate translates into about 0.3 milliradians of image smear. Resolution along the sensor array is determined by the field of view (FOV) and the number of cells without taking other characteristics of the optical system into account.

Figure 2-4 presents performance criteria of the line scan image system in terms of resolution along the sensor array versus the direction normal to the sensor array. The nominal design point indicated in the graph corresponds to a 6-degree FOV and 195 sensor cells. It was selected on the basis of spacecraft system tradeoffs and permits an exposure time of 1 msec, rather than 0.5 msec, for equal resolution of 0.5 mrad in the two scan directions.

### 2.5.4 Description of the Solid State Photodetector Array

The large scale array (LSA) shown in Figure 2-5 consists of 195 phototransistors, fabricated by triple-diffusion in silicon on a single chip. The array consists of two rows of phototransistors containing 97 and 98 elements, respectively. This configuration provides sufficient spacing between adjacent elements along the array to prevent crosstalk due to penetration of the incident radiation into the base material. The size of the photosensitive area of each phototransistor is  $0.7 \times 10^{-3}$  by  $0.9 \times 10^{-3}$  inches, and the pitch spacing determines the limiting spatial resolution of the array.

In addition to the 195 phototransistor element, the LSA chip contains an equal number of individual amplifiers, a shift register and

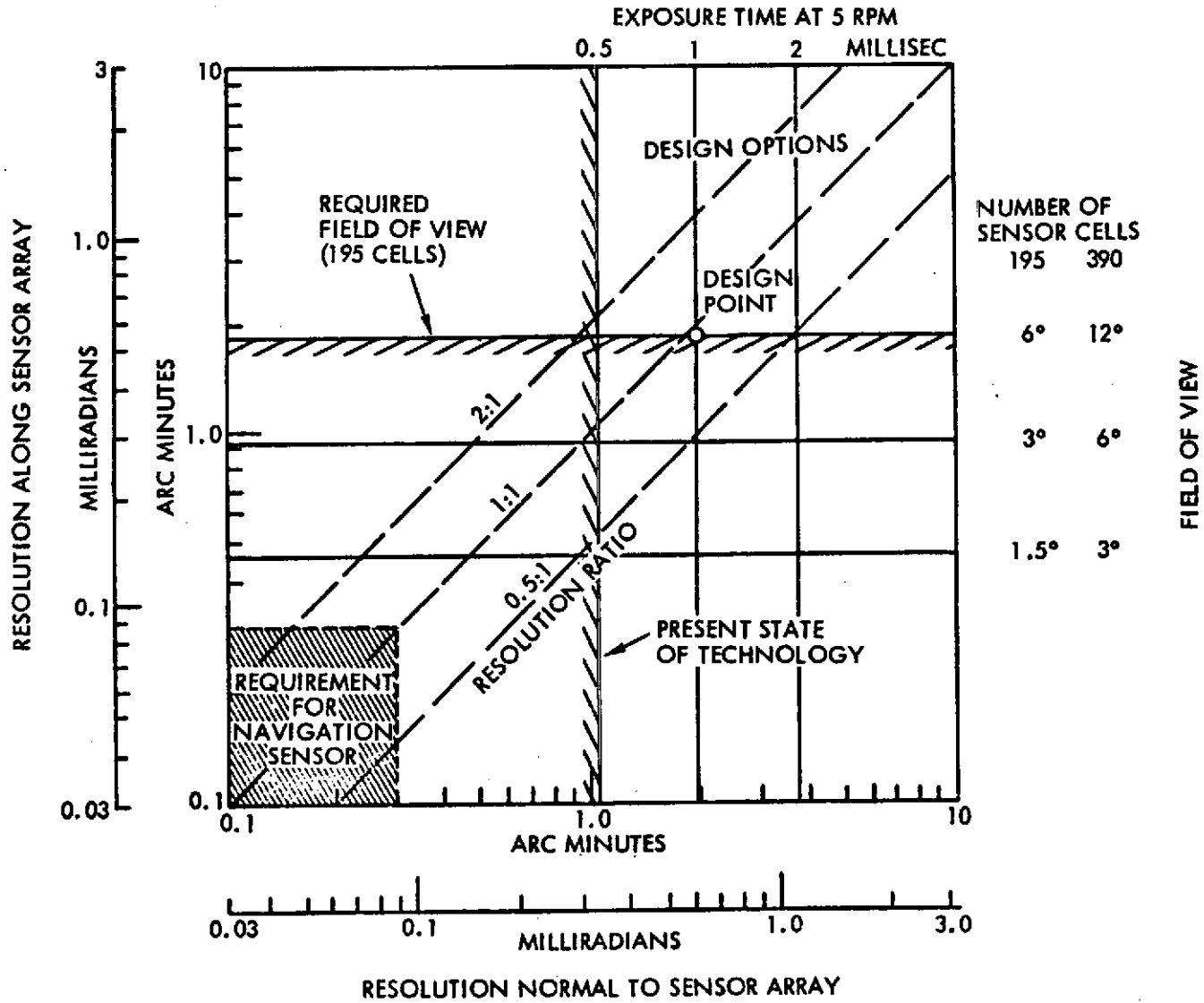


Figure 2-4. Performance Criteria for Line-Scan Image System

ORIGINAL PAGE IS  
OF POOR QUALITY

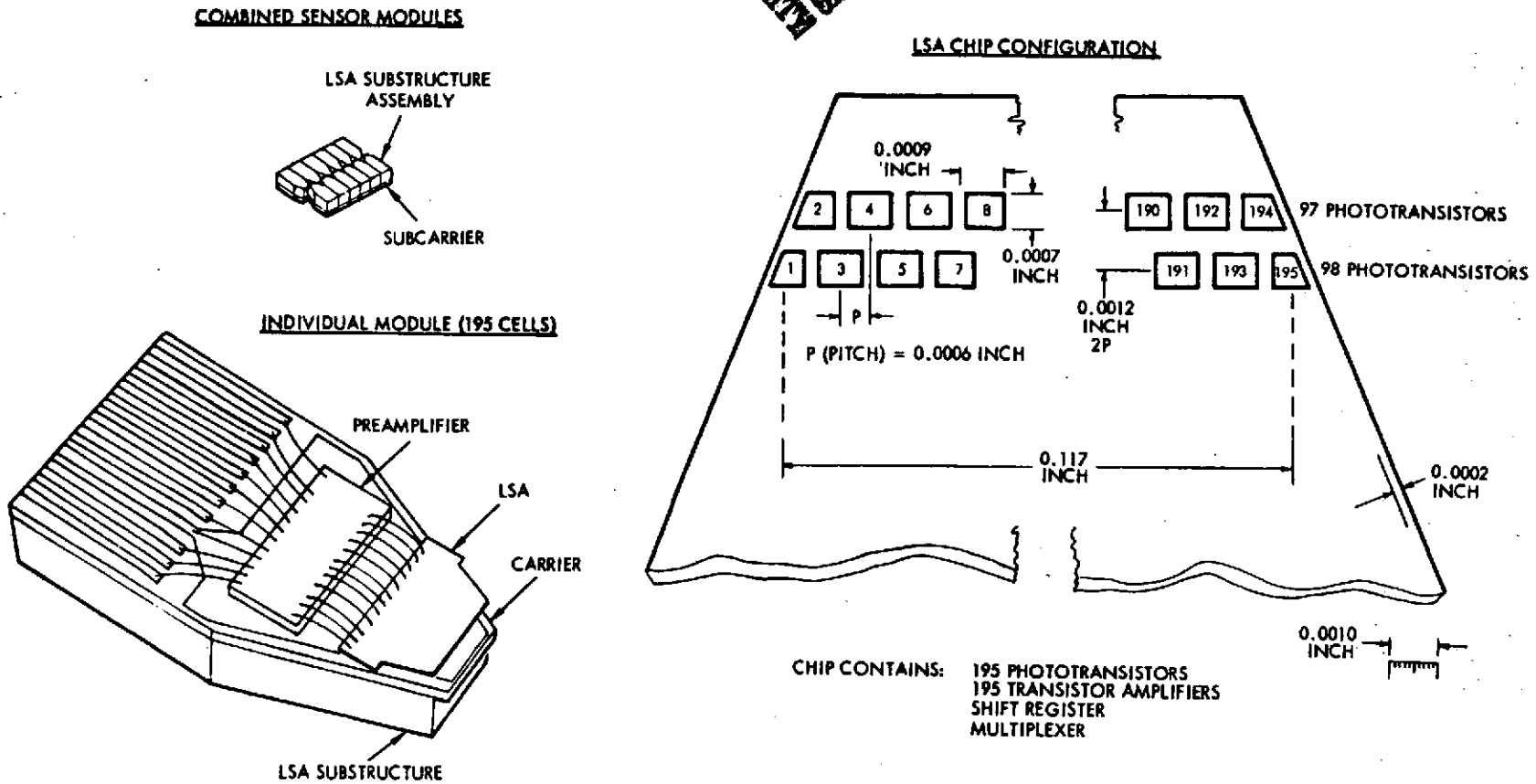
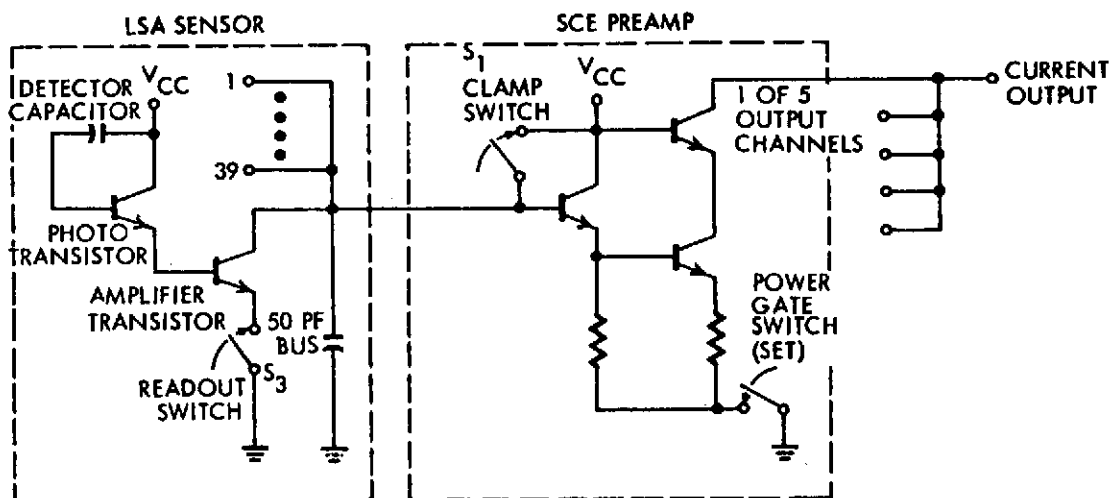


Figure 2-5. Solid State Photodetector Array

multiplexer. The multiplexer is used to commutate the outputs of the 195 preamplifiers onto five signal leads, each containing the serial output of 39 preamplifiers. These five signal leads are hard-wired to a second chip, containing five signal conditioning electronics (SCE) amplifiers, which further amplify the five serial signals prior to digital processing of the signals. Interfaces of this sensor with the data handling subsystem will be discussed in Section 7.

The equivalent circuit of the LSA, illustrated in Figure 2-6, consists of a phototransistor and preamplifier transistor. After bias is applied to the base-collector capacitance of the phototransistor through terminal  $V_{CC}$ , the base-collector capacitance is charged to a specified value. Light incident on this junction generates hole-electron pairs which discharge the initial bias applied to the junction, proportionally to the amount of energy absorbed during the exposure. The voltage change of the base-collector capacitance is amplified by the preamplifier.

#### EQUIVALENT CIRCUIT



#### OPERATING CYCLE

##### TIMING SEQUENCE OF LSA CHIP-DETECTOR

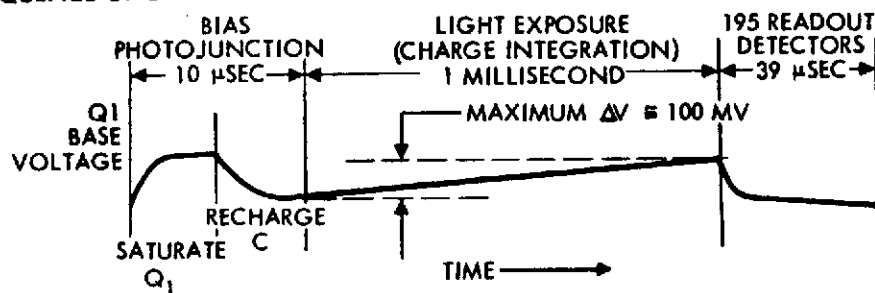


Figure 2-6. LSA Phototransistor Circuit and Operating Cycle

The 195 signals from the phototransistors are commutated in five groups of 39. Readout is accomplished by closing of the readout switches (S3), in sequence. This switching is actually accomplished by individual transistors under control of a shift register. The readout, or sampling, of the output of each preamplifier is accomplished in 2  $\mu$ sec thus 78  $\mu$ sec are required for serial sampling of each group of 39. After this sampling, the photojunctions of the phototransistors are again biased, and the cycle is repeated.

The SCE preamplifier consists of two stages of gain, with five parallel groups being contained on a single chip to amplify the five multiplexed signals. The clamp switch, S1, is used to reset the signal to a reference level between each of the 39 serial samples from the LSA sensor. The power gate switch is used only to apply power to the SCE preamplifier to initiate operation.

#### 2.5.5 Sensor System Characteristics

The optical design and system characteristics for three sensor configurations were analyzed and are summarized in Table 2-2. These configurations differ in size (lens diameter and focal length) and field-of-view width. The results of system analysis discussed in Section 4 required the selection of a 6 x 6 degree field of view to avoid loss of image coverage due to inaccurate camera pointing. With a fixed number of photodetector cells this has the effect of changing the resolution along the sensor array from 0.268 mrad to 0.536 mrad which is considered acceptable for purposes of this mission.

Table 2-2. Characteristics of Three Representative Line-Scan Image Systems

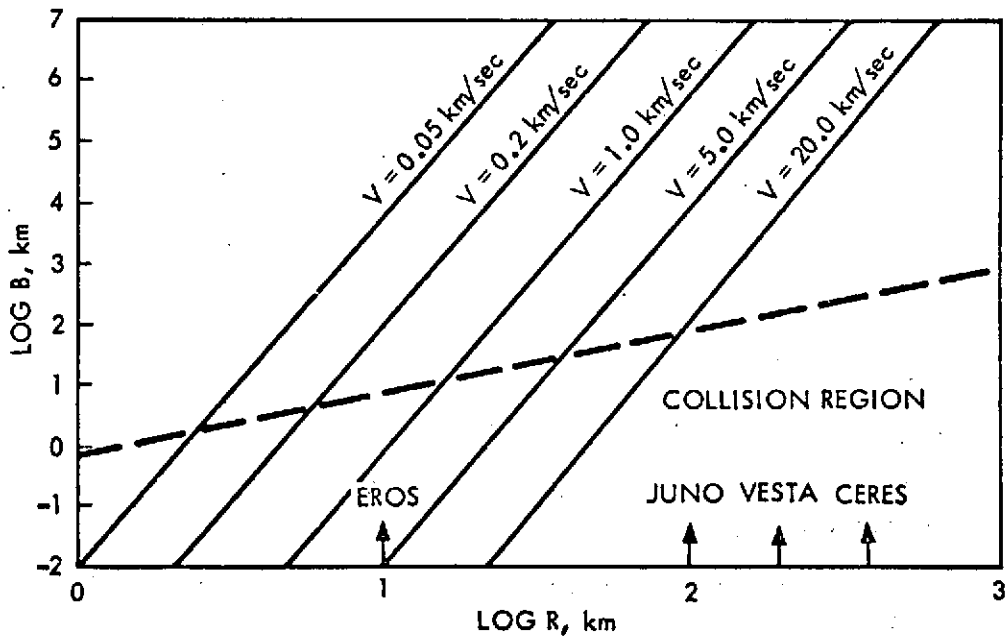
	1	2	3
<u>OPTICS</u>			
Focal length (in.)	2.25	7.2	3.6
f-number	1.2	1.2	1.2
Aperture diameter (in.)	1.875	6.0	3.0
Configuration	Reflective with refractive correctors		
<u>SOLID STATE DETECTOR</u>			
Number of elements	← 195 →		
Detector size (mil)	0.7 x 0.9	2.24 x 2.88	1.88 x 2.88
Detector spacing (mil)	0.6	1.92	3.84
Configuration	← Staggered Array →		
Wavelengths (μm)	← 0.4 to 0.8 →		
Exposure time (msec)	1.0	1.0	1.0
<u>SENSOR SCANNING</u>			
Field of view (square frame) (deg)	3 x 3	3 x 3	6 x 6
Resolution along array (mrad)	0.267	0.267	0.536
Resolution along scan (mrad)	0.525	0.525	0.525
<u>DATA RATE</u>			
Maximum acquisition rate (bps)	2.28 x 10 <sup>6</sup>	2.28 x 10 <sup>6</sup>	1.14 x 10 <sup>6</sup>
	per 0.1 sec	per 0.1 sec	per 0.2 sec
Bits per picture cell	6	6	6
Average data rate (bps)	19 x 10 <sup>3</sup>	19 x 10 <sup>3</sup>	19 x 10 <sup>3</sup>
<u>SENSOR PERFORMANCE</u>			
Imaging:			
Minimum S/N	4.5	14.4	18.7
At mrad per line pair	0.535	0.535	1.07
Navigation*:			
Minimum S/N	7	7	7
Against object of visual magnitude	3.65	5	4.5

\*Use of sensor as terminal navigation instrument would provide unsatisfactory resolution (required 0.1 to 0.2 mrad) and marginal sensitivity.

## 2.6 ASTEROID MASS DETERMINATION

### 2.6.1 Doppler Measurements

To detect the small trajectory perturbation due to asteroid gravity requires Doppler tracking of highest accuracy. A recent paper by Anderson (Reference 2-11) discusses the capabilities and limitations of the Doppler gravity measurement technique. The highest Doppler accuracy that is achievable at present under favorable tracking conditions is about 0.5 mm/sec. Assuming this Doppler sensitivity threshold, the closest approach distance  $B$  that is required for a gravity measurement of  $\pm 1$  percent accuracy is shown in Figure 2-7 as function of asteroid radius  $R$  with relative velocity  $V$  as parameter (from Reference 2-11). The diagram shows a theoretical lower limit of closest approach distances (dashed line) corresponding to flyby trajectories that would graze the asteroid's surface. Thus with relative velocities of 5 to 10 km/sec which are typical for asteroid encounters the spacecraft cannot approach close enough for a 1 percent accurate gravity measurement unless the asteroid is larger than 30 to 60 km in radius.



ASSUMED DENSITY	3.33 G/CM <sup>3</sup>
DOPPLER ACCURACY	0.5 MM/SEC

Figure 2-7. Closest Approach Distance Required for  $\pm 1$  Percent Gravity Measurement by Doppler Tracking Method (from Anderson, Ref. 2-11)

Actually a more realistic accuracy requirement for gravity measurements would be of the order of 10 rather than 1 percent. This permits an increase of the required closest approach distance B by a factor of 100. Thus, for an asteroid of 30 km radius and a relative velocity of 5 km/sec, the closest approach distance can be increased to 300 km.

The accuracy requirement of mass determination which has such a critical affect on the required closest approach distance and hence on terminal navigation requirements should be considered in the light of the desired end result, namely the mean density of the asteroid. The density is obtained from the mass measurement and the estimated volume which is inferred from visual observation. The volume estimate is based on the asteroid's dimensions which are determined from the observation distance and the subtended angles of the asteroid image. This volume estimate therefore is subject to appreciable errors due to range and angle uncertainty. However, the predominant error source, especially for small asteroids, is the irregular shape, partly hidden in darkness and viewed only under limited aspect angles. Thus the error in volume estimates could easily exceed 20 percent.

Figure 2-8 shows the effect of the mass measurement error ( $\sigma_M$ ) on the mean density error ( $\sigma_D$ ) if significant errors are contributed by other sources, such as

Range estimate error	$\sigma_R$	= 3 percent
Angle determination error (best)	$\sigma_\alpha$	= 5 percent
Angle determination error (intermediate)	$\sigma_\beta$	= 10 percent
Angle determination error (worst)	$\sigma_\gamma$	= 10 to 30 percent

The worst-case angle determination error involving the hidden part of the asteroid can easily amount to 20 percent. The results lead to the conclusion that mass determination to an accuracy better than 10 to 20 percent is not warranted, and hence the closest approach distances required for small asteroids can be greatly relaxed.

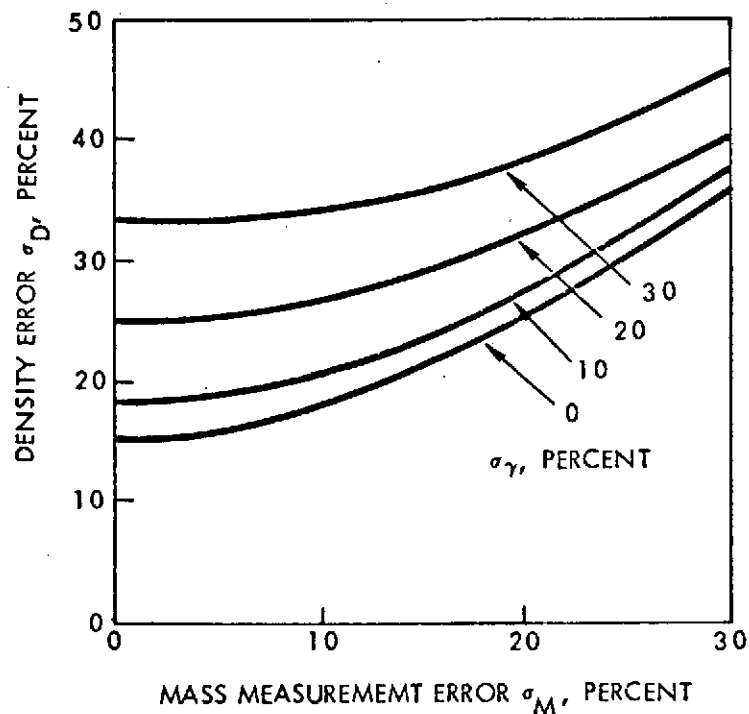


Figure 2-8. Influence of Mass Determination Error on Density Error

### 2.6.2 Measurement by Gravity Gradiometer

Various instruments have been proposed to measure the gravity gradient field of a planet or asteroid from a spacecraft. All of these work on the principle of measuring the differential tensions, compressions or torques induced in the sensor by the gravity gradient, that is, the effect of tidal forces. Several gravity gradiometers have been developed by the Hughes Research Laboratories and MIT. The application of such instruments to asteroid missions is discussed in a paper by R. L. Forward (Reference 2-12). References to the extensive literature on gradiometry are also given in that paper.

Compared to the Doppler technique, the gravity gradiometer can perform an accurate mass determination for asteroids of smaller size provided the approach distance is sufficiently small. The measurement sensitivity is limited by the design characteristics and can be refined if desired, while the Doppler technique is limited by the DSN Doppler tracking threshold sensitivity. One of the potential advantages of the

gradiometer is its ability, under optimal observation conditions, to detect and resolve non-uniform mass distributions, as discussed in Reference 2-12. However, the question of whether this is feasible during a fast flyby, even for a large asteroid, still requires further study.

The gradiometer described in Reference 2-12 consists of a pair of spinning dumbbells in a cruciform arrangement that sense the gravity gradient (and hence, the local gravity) as a periodic perturbation at a frequency equal to twice the spin rate. This induces small oscillation of the two dumbbell arms with respect to each other at an amplitude which depends on the mass-spring characteristics of the system. The sensor response is enhanced if the mass-spring system is tuned to resonance at twice the spin rate.

Two design options were considered for the Pioneer spacecraft application:

- a) A stationary configuration of the two sensor arms, designed to make use of the spacecraft's own spin motion as the mechanism for providing the periodic gravity gradient perturbations.
- b) The more conventional arrangement (Reference 2-12) where the gradiometer is a self-contained unit operating at a spin rate of several hundred rpm.

Because of the small spin rate of Pioneer, the stationary configuration would be exposed to only a few torque oscillation cycles during the short flyby interval. For a desired measurement sensitivity, the stationary design would therefore require much larger dimensions than the spinning configuration.

The spinning configuration is preferred for this mission because of its compact size, light weight and convenience of installation and test. Because of the short duration of its active use, bearing life will be no problem. However, the use of a drive motor increases the power requirement compared to the stationary configuration.

Sensitivities of the spinning gravity gradiometer configurations that have been developed by Hughes under NASA and USAF contracts range from 1 EU,\* for a 6-inch diameter unit requiring 10 seconds of integration time, to 0.01 EU for a 3-foot diameter unit requiring 35 seconds of integration time.

At the surface of the asteroid, the gravity gradient is typically 3000 EU (regardless of its radius). Since it varies inversely with the third power of distance the range of gravity gradients expected for approach distances of 5 to 10 times the asteroid radius is about 3 to 30 EU. Thus, an instrument sensitivity of 0.1 EU would be desirable but 1 EU is acceptable to conserve instrument size and weight.

### 2.6.3 Comparison of Doppler and Gravity Gradiometer Measurements

The two techniques are compared in Figure 2-9 in terms of the altitude required for mass determination at one percent accuracy. The figure shows that applicability of the Doppler technique depends more critically on asteroid size (radius R) since the required approach distance varies with the sixth power of R, while for the gravity gradiometer technique this distance only changes proportionally with R. This is illustrated by the crossover of the altitude-versus-radius characteristics of the two techniques.

If the measurement accuracy is relaxed to 10 percent (see previous discussion in Section 2.6.1) the required approach distances increase by a factor of 100 in the case of the Doppler technique, but only by 3.16 ( $= \sqrt{10}$ ) in the case of the gradiometer technique. As a result, the crossover point between the Doppler and gradiometer curves would be located at 150 km altitude and at  $R = 30$  km, as illustrated in Figure 2-10. (Figures 2-10 and 2-11 and the discussion of the results shown therein are from an unpublished report by R. L. Forward and are included here with his permission.) The second scale on the ordinate in this diagram gives the "interaction time"  $\tau = B/V$  defined as the time interval during which the spacecraft travels a distance equal to the offset B in close

---

\* EU = Eötvös unit =  $10^{-9}$  sec<sup>-2</sup> is used as the standard unit of the gravity gradient.

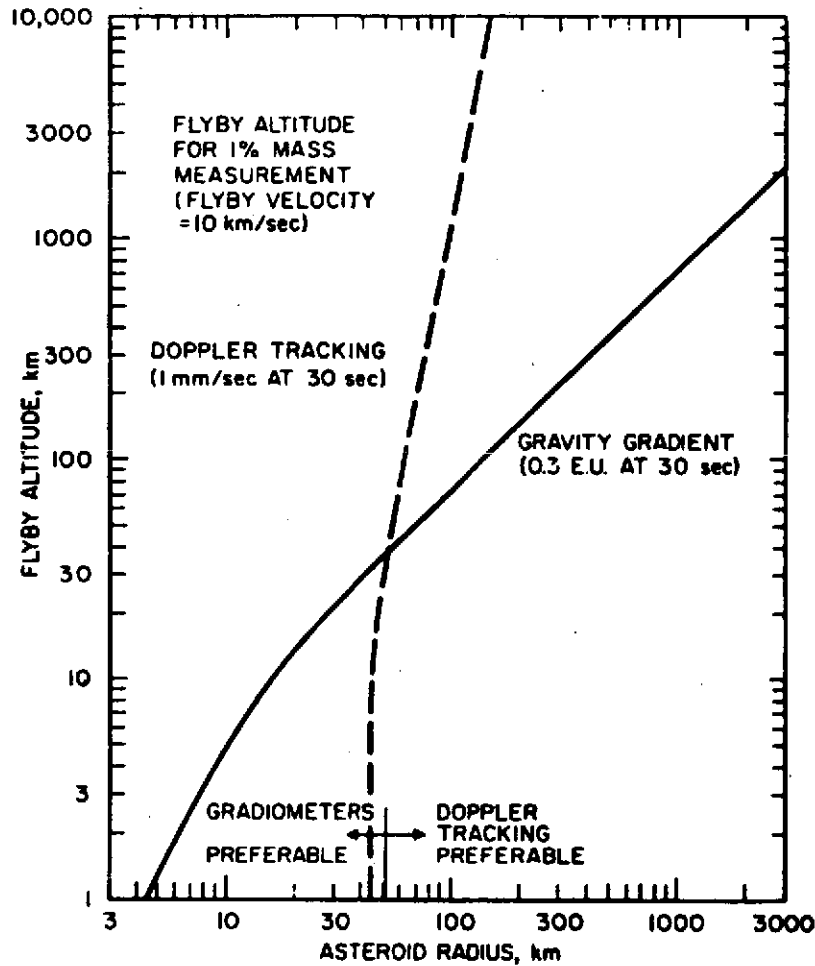


Figure 2-9. Attitudes Required for One Percent Gravity Measurement by Doppler and Gravity Gradient Techniques (From Reference 2-12)

vicinity of the asteroid, with range varying at most 12 percent. If the interaction time is short then it is possible to use coherent integration utilizing matched filters. For longer interaction times the measurement technique uses sampled data (incoherent integration). A corresponding change in integration techniques applies in the case of Doppler tracking.

Figure 2-11 compares Doppler and gradiometer measurements in terms of required flyby distance versus mass measurement accuracy with asteroid radius as parameter. As in Figures 2-9 and 2-10 it is evident from the results shown in Figure 2-11 that mass determination for small asteroids ( $R < 30$  km) is best performed by gradiometry. The crossover for  $R = 30$  km is at 8 percent, and for  $R = 20$  km at 23 percent measurement accuracy.

2-25

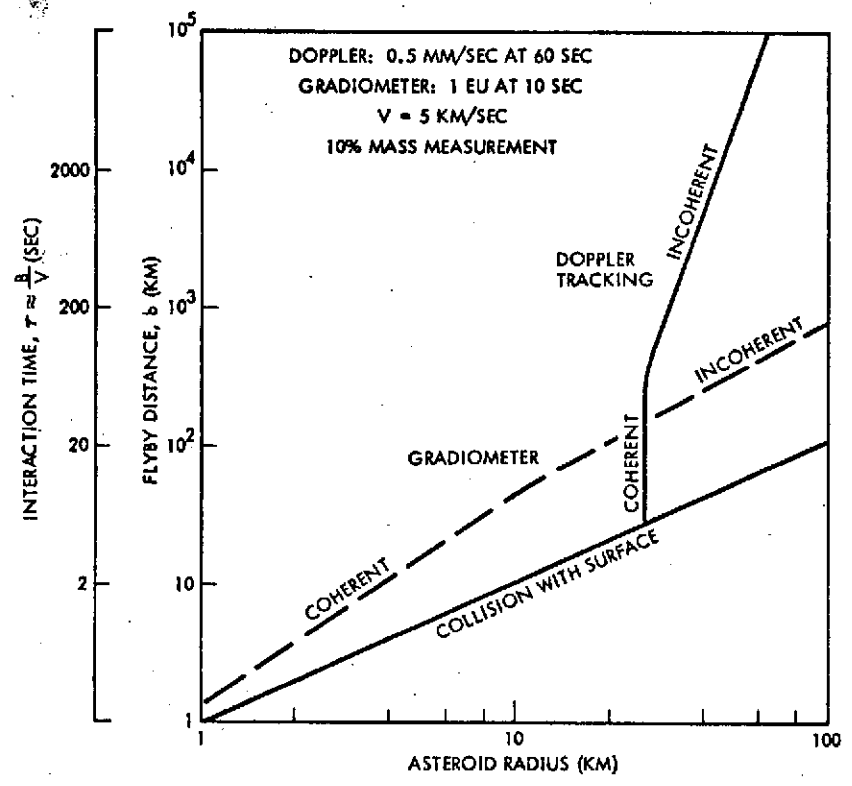


Figure 2-10. Comparison of Doppler and Gradiometer Techniques for 10 Percent Measurements Accuracy

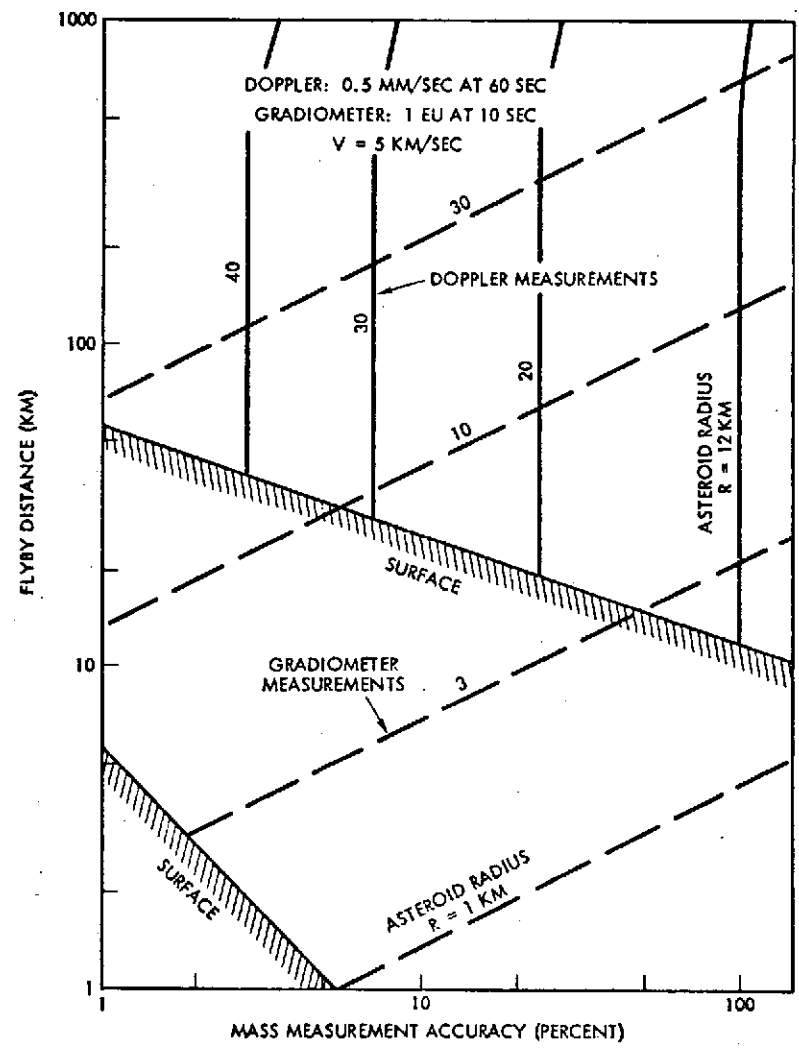


Figure 2-11. Comparison of Doppler and Gradiometer Techniques in Terms of Mass Measurement Accuracy

## 2.7 COMPATIBILITY OF SPIN-STABILIZED SPACECRAFT CONFIGURATION WITH SCIENTIFIC OBJECTIVES

Specific questions regarding the ability of the spin-stabilized Pioneer spacecraft to accomplish the scientific mission objectives and to meet all requirements of effective payload operation have been addressed in this study along with the ground questions of system performance and implementation.

The results presented in Sections 4, 6, and 7 establish the compatibility of the spinner with these objectives. The engineering approaches used to circumvent functional constraints inherent in target observation from a spinning spacecraft are discussed in detail, and the relevant trade-offs are analyzed in these sections. A brief summary of the main results is presented here.

- 1) Imaging and other optical sensor observations are performed by making effective use of the scan motion of the spinning spacecraft.
- 2) If the target subtends an angle equal to or greater than the field of view the scan motion is particularly valuable since the sensor does not require a scan articulation of its own.
- 3) A single-axis gimbal drive is used for cone angle pointing of all optical sensors. The rapid motion of the target line of sight is met by cone angle changes between exposures.
- 4) In the case of the image system the exposure is limited to a scan segment equivalent to a 6 x 6 deg.<sup>2</sup> square field of view because of data rate limitations. The other optical sensors, having a lower data acquisition rate, can take advantage of a more extended scan segment.
- 5) Some image smear due to the 1 m/sec exposure time required for the photodetector cells is unavoidable. However, the resulting resolution limit of 0.5 mrad is satisfactory in this application.
- 6) Non-optical sensors can take advantage of the spin axis motion for multi-directional exposure without requiring articulation.

The spin motion requirement of the gravity gradiometer could be met by a spinning spacecraft, but a higher spin rate than that of Pioneer would be

required due to the extremely short interaction time with the asteroid. Hence the need for independent spin action by the instrument.

- 7) Engineering subsystems are designed for the spinning vehicle and provide all the necessary support functions to the payload irrespective of the spin motion. Most design aspects of spin stabilization actually simplifies the interfaces between the payload and the engineering subsystems (except for Item 8).
- 8) The autonomous payload pointing correction is the only exception: the intermittent image system exposure complicates the image tracking process to some extent, but this can be handled by proper design of the data processing circuits.

The dominant factor that complicates target observation during the brief encounter is the rapid change of viewing conditions. This means that accomplishment of scientific objectives is not made problematic so much by the spin motion of the spacecraft as by the dynamics of range and angle variation inherent in the mission.

## 2.8 A PHOTSENSOR FOR METEOROID/ASTEROID DETECTION

To complement the payload instruments discussed earlier in this section an additional photosensor is proposed that is designed to detect meteoroids at longer range than the Sisyphus sensor of Pioneer F and G (Reference 2-15). The effective cross-section area that would be intercepted by passing particles increases with the square of the detection range. Thus, if the detection range can be increased by a factor of 10 from that of Sisyphus, the area, and hence the expected count of particles of a given mass would increase hundredfold.

The sensor, shown schematically in Figure 2-12, is described and evaluated in Appendix A. Derived from any earlier detection concept proposed by TRW Systems, the configuration proposed for this application has a reticle consisting of several alternately transparent and opaque concentric rings. A photomultiplier is used as a sensor. The instrument's optical axis is aligned with the spin axis. The field of view is assumed as 30 degrees, and the threshold sensitivity for particle detection is 6th magnitude.

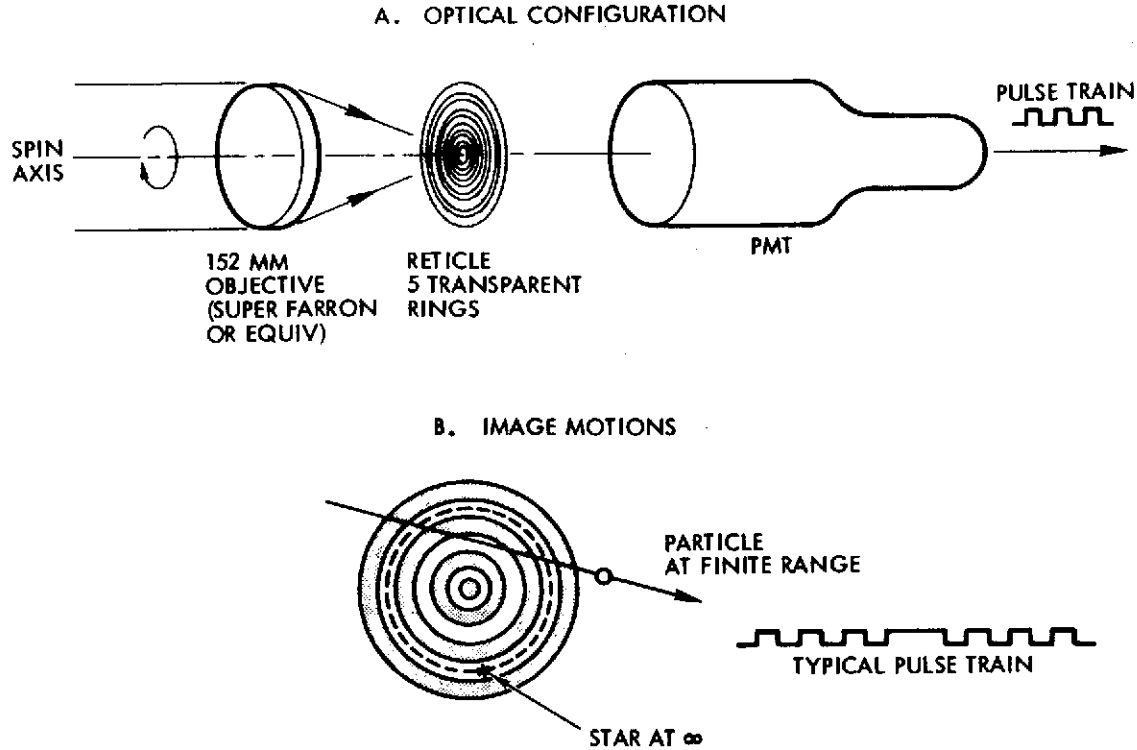


Figure 2-12. Meteoroid Photosensor System

If an illuminated particle of sufficient brightness crosses the field of view the photomultiplier will generate a pulse train with a frequency and waveform characteristic that depends on the particle's line-of-sight rate and its relative flight path geometry.

The pulse train can be interpreted to provide data on the relative encounter geometry except the range. However, the range can be estimated within upper and lower limits by assuming relative velocity brackets and determining the angular rate of the particle by processing the pulse train. If the range is estimated from these data the size of the asteroid can be deduced from the intensity of the signals detected. The following features of the instrument are relevant to this application:

- Stars that are in the field of view appear to move in concentric circles relative to the reticle pattern. Thus, ideally, their incident light is not modulated.
- Moving objects are detected as modulated light sources, since they cross the reticle rings. The pulse train contains the signature of the particle

indicating the relative orientation of its flight path, range rate, etc., in addition to the inferred range information.

- The stars seen by the photodetector will produce a nearly constant sky background current. The signal processing circuits are designed to discriminate against unmodulated light sources and to respond only to moving objects that cause pulses in a selected frequency range (i. e., objects within upper and lower range brackets).
- If, due to misalignment of the optical axis, some stars enter and exit the opaque rings of the reticle, and thus produce square waves at the spin rate of the spacecraft, this effect can be detected and nulled by minor angle adjustments in two orthogonal directions using a process analogous to an automatic conical scan axial alignment.
- Since during the cruise phase a large unused down-link data rate capacity is available, the waveforms generated by passing particles can be telemetered to earth for data processing and evaluation.

Compared to Sisyphus upward of  $10^{-6}$  grams which is designed to detect smaller particles and has a sensitivity threshold of magnitude 2.75, this instrument can operate at higher sensitivity ( $m = 6$ ) because of its effective star background discrimination feature. This is discussed in the analysis presented in Appendix A.

The following examples of asteroid detection capabilities illustrate the value of this sensor as a secondary payload instrument for this mission. The sensor can detect a 100 m diameter asteroid as a 6th magnitude object at  $30 \times 10^3$  km range. The effective cross-section for detecting asteroids of this size is therefore  $2.3 \times 10^8 \text{ km}^2$ . The spatial density of bodies of this size or larger is assumed to be in the range of  $10^{-16}$  to  $10^{-18}$  per  $\text{km}^3$  (see Reference 2-16). With a relative velocity of 10 km/sec this yields estimated event rates of 0.07 to 7 events per year. For a 10-m diameter asteroid this would increase 0.35 to 35 per year.

## REFERENCES

- 2-1. H. Alfvén and G. Arrhenius, "Arguments for a Mission to an Asteroid," NASA SP-267 Physical Studies of Minor Planets, Washington D. C., 1971.
- 2-2. G. Arrhenius and H. Alfvén, "Asteroidal Theories and Experiments," NASA SP-267 Physical Studies of Minor Planets, Washington, D. C., 1971.
- 2-3. Ernst Stuhlinger, "Exploration in the Solar System with Electric Spacecraft," NASA SP-267 Physical Studies of Minor Planets, Washington, D. C., 1971.
- 2-4. A. Bratenahl, "Potentials of Asteroid Space Missions," NASA SP-267 Physical Studies of Minor Planets, Washington, D. C., 1971.
- 2-5. T. Gehrels et al, Introduction, Physical Studies of Minor Planets, NASA SP-267, Washington, D. C., 1971.
- 2-6. B. G. Marsden, "Precision of Ephemerides for Space Missions," Physical Studies of the Minor Planets, Tucson, Arizona, March 8-10, 1971.
- 2-7. H. Masursky et al, "Mariner 9 Television Reconnaissance of Mars and Its Satellites: Preliminary Results," Science, Vol. 175, No. 4019, 21 January 1972, p.294.
- 2-8. J. B. Pollack et al, "Mariner 9 Television Observations of Phobos and Deimos," paper being prepared for publication, NASA Ames Research Center, Moffet Field, California.
- 2-9. J. S. Lewis, "Low Temperature Condensation from the Solar Nebula," Massachusetts Institute of Technology, Cambridge, Massachusetts, August 25, 1971.
- 2-10. T. Gehrels, "Photometry of Asteroids," Ch. 6 in Surfaces and Interiors of Planets and Satellites, ed., A. Dollfus, Academic Press, New York, 1970.
- 2-11. John D. Anderson, "Feasibility of Determining the Mass of an Asteroid from a Spacecraft Flyby," Physical Studies of the Minor Planets, Tucson, Arizona, March 8-10, 1971.
- 2-12. R. L. Forward, "Asteroid Mass Distribution Measurement with Gravity Gradiometers," Physical Studies of the Minor Planets, Tucson, Arizona, March 8-10, 1971.
- 2-13. E. W. Greenstadt, "Possible Magnetic Interaction of Asteroids with the Solar Wind," NASA SP-267 Physical Studies of Minor Planets, Washington, D. C., 1971.

## REFERENCES (Continued)

- 2-14. C. E. KenKnight, "Observations in the Asteroid Belt with the Imaging Photopolarimeter of Pioneers F and G," NASA SP-267 Physical Studies of Minor Planets, Washington, D.C., 1971.
- 2-15. R. K. Soberman, S. L. Neste, and A. F. Petty, "Asteroid Detection from Pioneers F and G?", NASA SP-267, Physical Studies of Minor Planets, Washington, D.C., 1971.
- 2-16. D. J. Kessler, "Estimate of Particle Densities and Collision Danger for Spacecraft Moving Through the Asteroid Belt," NASA SP-267 Physical Studies of Minor Planets, Washington, D.C. 1971.
- 2-17. N. P. Laverty, "The Application of Linear Arrays of Silicon Phototransistors to Multispectral Imaging of Earth Resources, TRW Systems Group, Redondo Beach, California, November 1972.

### 3. PERFORMANCE CHARACTERISTICS

#### 3.1 LAUNCH VEHICLE PERFORMANCE

The injection capability of Atlas/Centaur/TE-364-4, the booster being used for the Pioneer F and G Jupiter flyby missions, is adequate for most of the multi-asteroid flyby missions under consideration. The injected weight of the modified spacecraft including about 340 pounds of hydrazine propellant is in the 1000-pound class. Since the asteroid missions have aphelion distances generally well below 4 AU and only moderate orbit inclination relative to the ecliptic, the required injection energy  $C_3$  does not exceed  $60 \text{ km}^2/\text{sec}^2$  in most cases.

Figure 3-1 shows the injection performance of the Atlas SLV-3D/Centaur D-1A/TE-364-4 in the velocity range of interest (solid line). The dashed line projects the performance improvement obtainable if the TE-364-11 is substituted for the present TE-364-4 upper stage, based on data supplied by Thiokol. This upgraded stage which is equal in size to TE-364-4 gives about three percent greater impulse due to a slightly higher  $I_{sp}$  value and higher propellant density, and thus increases the injected payload weight by about 40 pounds in the velocity range shown. This stage has been developed and test-fired by Thiokol under the Delta program but has not yet been authorized for flight qualification tests.

The projected performance improvement is not essential to MAF mission achievement but would provide a useful additional margin. Actually the amount of onboard propellant that can be carried by a moderately revised Pioneer spacecraft configuration is an equally important constraint on mission selection as launch vehicle performance. This point will be further discussed below under weight tradeoffs.

By restricting the booster size to the Atlas/Centaur family rather than considering a larger booster of the Titan/Centaur family we reduce the cost of the mission without an appreciable sacrifice in mission options in keeping with the study guidelines. In addition, we avoid possible procurement and scheduling problems that may result from priority allocation of Titan boosters to other missions in the late 1970's.

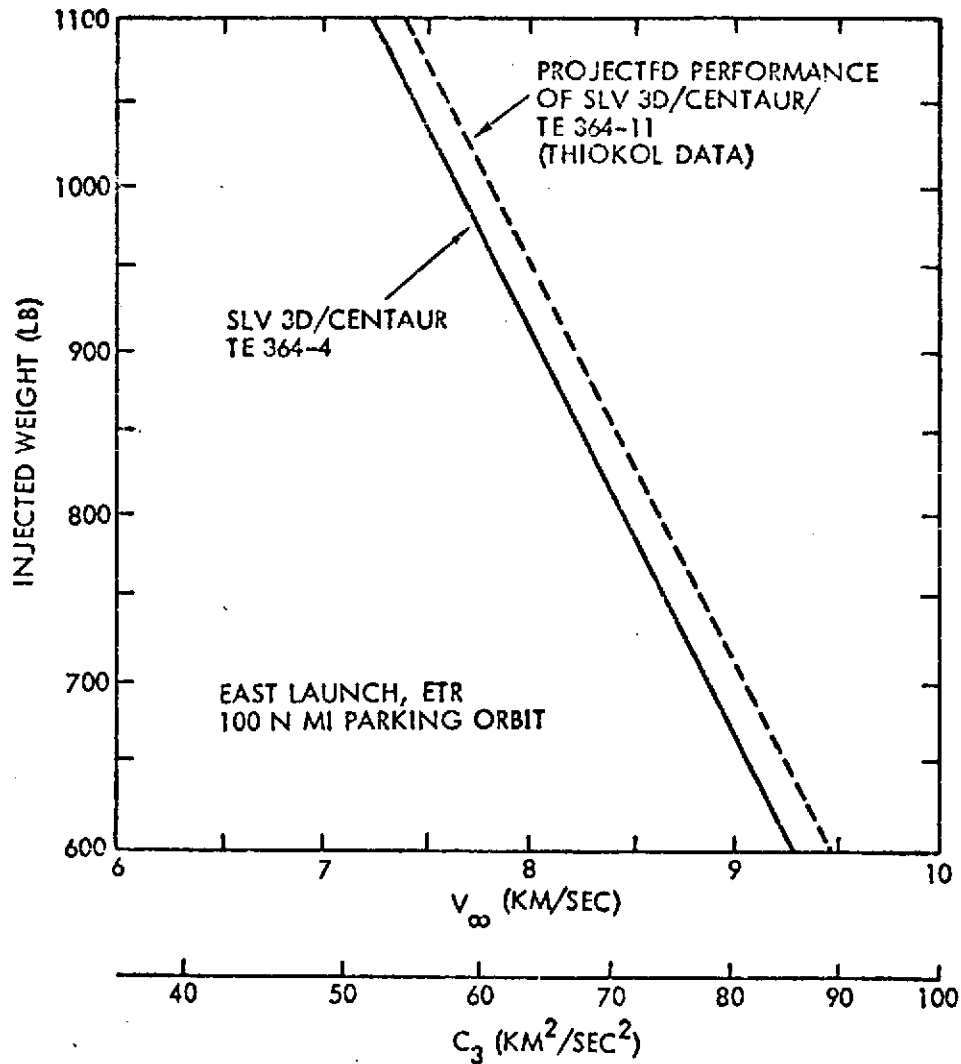


Figure 3-1. Launch Vehicle Performance

### 3.2 VELOCITY REQUIREMENTS OF CANDIDATE MISSIONS

In studies performed by Brooks et al (Reference 3-1 and 3-2) a large number of multi-asteroid mission candidates were identified that only require modest retargeting maneuvers such that the spacecraft deviates but slightly from a suitably selected Kepler orbit through the asteroid belt. Table 3-1 excerpted from Reference 3-2 lists mission-candidates with launch dates from mid-1978 to late 1980, all involving a flyby of Ceres. Table 3-2 lists encounter sequences on randomly chosen launch dates in mid-1977, also from Reference 3-2. The encounter sequences are given in terms of asteroid numbers (Ceres is No. 1). For each case the Julian launch date is stated and two alternate

Table 3-1. Multiple Encounter Sequences on a Flyby of Ceres\*

ENCOUNTER SEQUENCE	JULIAN DATE OF LAUNCH (244XXXX)	MINIMUM $\Delta V$		MINIMUM $V_{\infty}$			LAST ASTEROID IN SEQUENCE		
		SPACECRAFT $\Delta V$ (KM/SEC)	$V_{\infty}$ (KM/SEC)	JULIAN DATE OF LAUNCH (244XXXX)	SPACECRAFT $\Delta V$ (KM/SEC)	$V_{\infty}$ (KM/SEC)	$V_{rel}$ (KM/SEC)	$\theta$	DIAMETER (KM)
A. LAUNCH IN MID-1978									
1719-1031-1**	3645	0.568	8.00	3630	1.000	7.49	8.2	4.0	770
549-1031-1	3650	0.852	8.23	3640	0.959	7.59			
960-1014-1	3625	0.564	7.40	3630	0.588	7.35			
270-420-1	3655	0.728	7.74	3640	0.819	7.41			
1430-420-1	3660	0.648	8.09	3640	0.813	7.03			
1184-420-1	3655	0.574	7.78	3640	0.801	7.32			
960-828-1	3650	0.972	7.98	3645	1.021	7.65			
1719-828-1	3645	0.525	8.02	3630	0.805	7.54			
B. LAUNCH IN MID-1979									
422-1-993	4050	0.938	6.44	4035	1.033	5.97	5.4	13.3	8
422-1-1153	4050	0.638	6.35	4035	0.774	5.88	6.7	13.3	8
1473-1-1153	4060	0.116	7.01	4040	0.233	6.14	6.7	13.3	8
1473-1-443	4025	0.566	6.60	4040	0.676	6.23	10.1	11.5	19
C. LAUNCH IN LATE 1980									
67-1-367	4545	0.7326	7.51	4565	0.841	6.63	10.1	12.0	15
67-1-641	4570	0.6346	6.58	4565	0.650	6.54	8.2	13.7	7
67-1-544	4585	0.357	7.53	4565	0.369	6.60	12.3	11.2	21
67-1-1216	4550	0.2154	7.16	4565	0.302	6.64	15.3	13.3	8
68-1-1257	4565	0.7198	7.19	4565	0.720	7.19	10.0	12.8	10
68-1-1293	4560	0.655	7.40	4565	0.862	7.13	9.4	15.1	4
352-1-1224	4565	0.197	6.94	4560	0.342	6.93	5.5	12.8	10
136-1-544	4575	0.444	7.03	4565	0.493	6.68	(VALUES SAME AS ABOVE FOR CORRESPONDING THIRD ASTEROID IN SEQUENCE)		
136-1-1216	4575	0.440	7.04	4565	0.527	6.69			
136-1-367	4580	0.275	7.42	4565	0.440	6.69			
352-1-1257	4560	0.563	6.95	4560	0.563	6.95			
352-1-1293	4560	0.448	6.95	4560	0.448	6.95			
391-1-367	4580	0.537	7.27	4565	0.680	6.83			
391-1-544	4580	0.283	7.28	4570	0.368	6.84			
391-1-1216	4580	0.613	7.28	4565	0.747	6.83			
615-1-367	4570	0.761	6.70	4560	0.783	6.52			
615-1-544	4565	0.564	6.52	4560	0.579	6.49			
615-1-1216	4570	0.353	6.69	4560	0.389	6.51			
708-1-1224	4555	0.622	6.54	4560	0.648	6.54			
708-1-1257	4540	0.730	7.23	4555	0.905	6.56			
708-1-1293	4545	0.747	6.90	4560	0.917	6.55			
953-1-367	4585	0.292	7.80	4565	0.486	6.69			
953-1-641	4565	0.955	6.61	4565	0.955	6.61			
953-1-544	4575	0.282	6.95	4565	0.342	6.66			
953-1-1216	4580	0.274	7.32	4565	0.457	6.68			
1060-1-1224	4565	0.373	7.13	4560	0.412	7.04			
1060-1-1257	4560	0.348	7.07	4560	0.348	7.07			
1060-1-1293	4560	0.281	7.07	4560	0.281	7.07			
1281-1-544	4585	0.700	7.63	4565	0.880	6.81			
1281-1-1216	4585	0.456	7.65	4565	0.731	6.83			
1340-1-1224	4545	0.684	6.99	4555	0.860	6.55			
1340-1-544	4560	0.727	6.60	4555	0.792	6.52			
1340-1-1216	4565	0.671	6.54	4555	0.738	6.52			
1430-1-1224	4570	0.266	7.22	4565	0.333	7.19			
1430-1-1257	4565	0.723	0.719	4565	0.723	7.19			
1430-1-1293	4565	0.546	7.19	4565	0.546	7.19			
1527-1-544	4560	0.676	6.55	4560	0.676	6.55			
1527-1-1216	4565	0.614	6.67	4560	0.622	6.56			

\* FROM BROOKS, REFERENCE 3-2.

\*\* ENCOUNTER SEQUENCES IDENTIFIED BY ASTEROID CATALOG NUMBER (REFERENCE 3-3).

ORIGINAL PAGE IS  
OF POOR QUALITY

Table 3-2. Multiple Encounter Sequences on Randomly Chosen Launch Dates in Mid-1977\*

ENCOUNTER SEQUENCE	MINIMUM $\Delta V$			MINIMUM $V_{\infty}$			LAST ASTEROID IN SEQUENCE		
	JULIAN DATE OF LAUNCH (244XXXX)	SPACECRAFT $\Delta V$ (KM/SEC)	$V_{\infty}$ (KM/SEC)	JULIAN DATE OF LAUNCH (244XXXX)	SPACECRAFT $\Delta V$ (KM/SEC)	$V_{\infty}$ (KM/SEC)	$V_{rel}$ (KM/SEC)	$\rho$	DIAMETER (KM)
736-621-223	3290	0.372	6.82	3295	0.400	6.77	6.7	11.0	23
736-621-1497	3290	0.546	6.98	3295	0.547	6.94	6.3	12.9	10
736-621-488	3290	0.680	6.93	3295	0.726	6.88	6.4	8.9	62
1156-621-223	3285	0.643	6.99	3300	0.799	6.65	6.7	11.0	23
540-621-1553	3280	0.547	7.38	3300	0.660	6.81	7.9	12.7	11
1156-116-1100	3310	0.571	6.93	3300	0.604	6.64	5.5	12.2	14
540-621-488	3275	0.673	7.77	3300	0.854	6.80			
1156-116-223	3305	0.450	6.63	3300	0.456	6.52			
1156-116-1497	3310	0.505	7.01	3300	0.565	6.73			
1156-116-488	3310	0.552	6.95	3300	0.623	6.66			
1156-116-1553	3310	0.512	6.97	3300	0.554	6.68			
540-116-1100	3310	0.978	6.89	3295	1.090	6.55			
540-116-223	3305	0.777	6.57	3295	0.841	6.42			
540-116-1553	3310	0.587	6.94	3300	0.613	6.59			

\* FROM BROOKS, REFERENCE 3-2.

options are compared: trajectories that minimize (1) the total  $\Delta V$  requirement for retargeting between encounters, or (2) the departure hyperbolic excess velocity  $V_{\infty}$ . The criterion used for inclusion of mission opportunities as candidates in these listings is that each encounter sequence must require no more than 1 km/sec of total retargeting  $\Delta V$  requirement (i. e., not counting the  $\Delta V$  required for initial midcourse corrections and terminal guidance maneuvers).<sup>\*</sup> Further discussion of the conditions underlying the selection of these mission candidates, and the computer approach used in obtaining the results, may be found in Reference 3-2.

As seen in these tables the launch dates between the minimum  $\Delta V$  and minimum  $V_{\infty}$  mission options are separated by 10 to 20 days on the average. A typical profile of  $\Delta V$  and  $V_{\infty}$  variation during the launch window is shown in Figure 3-2. These characteristics suggest that a tradeoff between  $\Delta V$  and  $V_{\infty}$  can be made to meet spacecraft capabilities and constraints, as will be discussed below.

In the mission opportunities (Group A) listed at the beginning of Table 3-1 the large asteroid Ceres is encountered last, i. e., on the return of the spacecraft from aphelion. In this position early acquisition of a target by the spacecraft for the purposes of acquiring terminal navigation fixes is inhibited by unfavorable lighting conditions, or phase

\* Appendix B discusses asteroid accessibility and  $\Delta V$  requirements in statistical terms

angles (see Section 4.3). Hence, it is desirable to select a bright asteroid as the third target in the mission. In the other mission opportunities listed (Groups B and C in Table 3-1, and all of Table 3-2) the asteroid encountered last is much fainter. Depending on how far beyond aphelion the third encounter would take place, conditions for terminal navigation and guidance can be quite unfavorable particularly if the relative velocity is large, as will be discussed in Sections 4 and 5. As a consequence, some mission opportunities that would be acceptable from the standpoint of velocity requirements must be rejected in the final selection of mission candidates because of feasibility problems of terminal navigation. To identify such conditions the magnitudes, estimated diameters and relative velocities of the last asteroids to be encountered in each mission sequence are also listed in Tables 3-1 and 3-2.

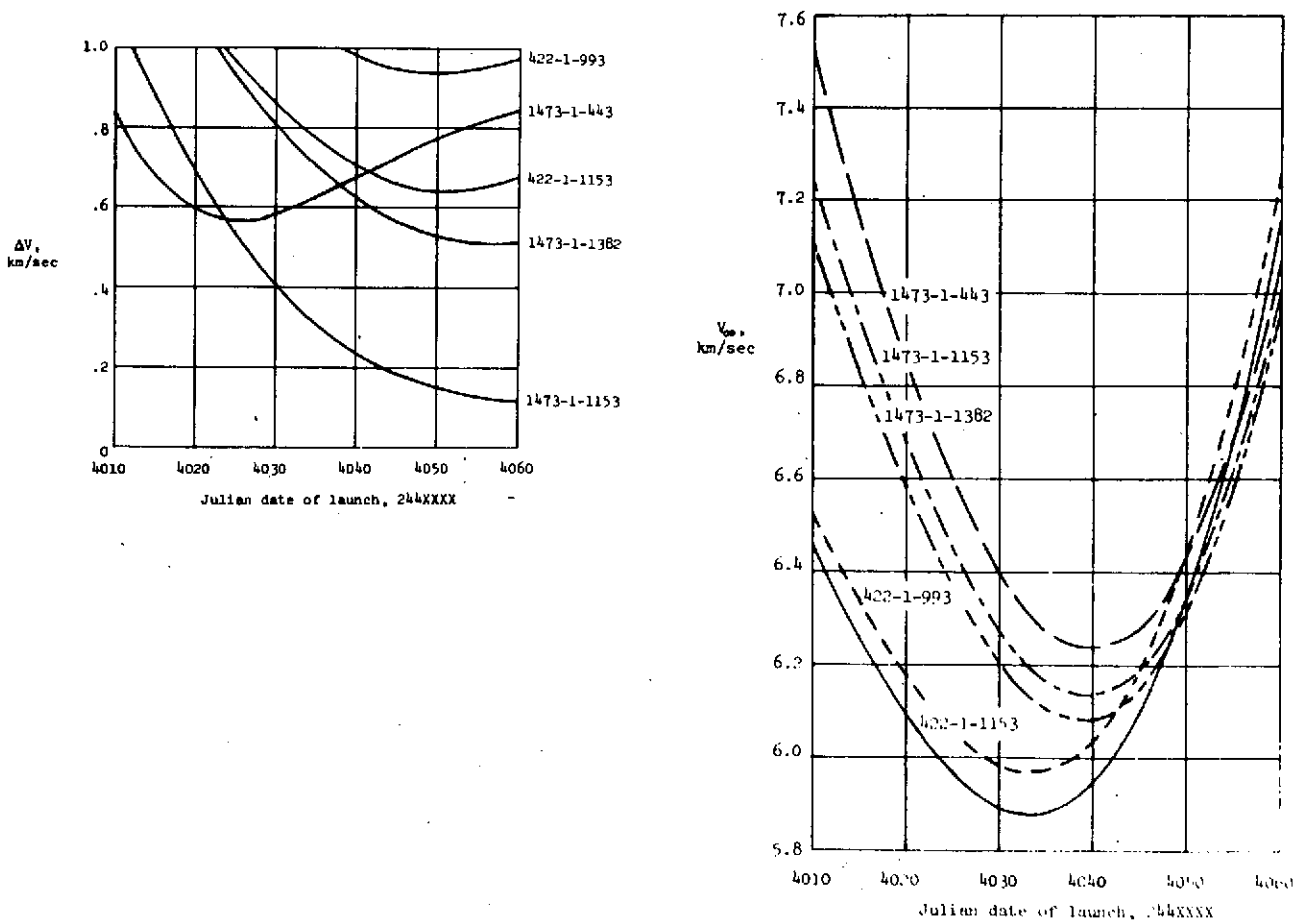


**Figure 3-2. Mission Energy Requirements for Three-Asteroid Encounter Missions (Group B in Table 3-1).**

### 3.3 WEIGHT CONSTRAINTS AND TRADEOFFS

The net (science) payload weight capacity of the spacecraft and the required propellant weight depend on

- Total maneuver requirements of the mission
- Gross weight and dry weight of the spacecraft
- Propulsion system parameters.

Results of a parametric performance analysis are presented in this section to show the interdependence of payload capability and other characteristics and to allow tradeoffs.

Figure 3-3 shows curves of constant net payload weight (dashed) and propellant weight (solid lines) in a diagram of injected gross weight,  $W_T$ , versus total maneuver capability  $\Delta V$ . A conservative average

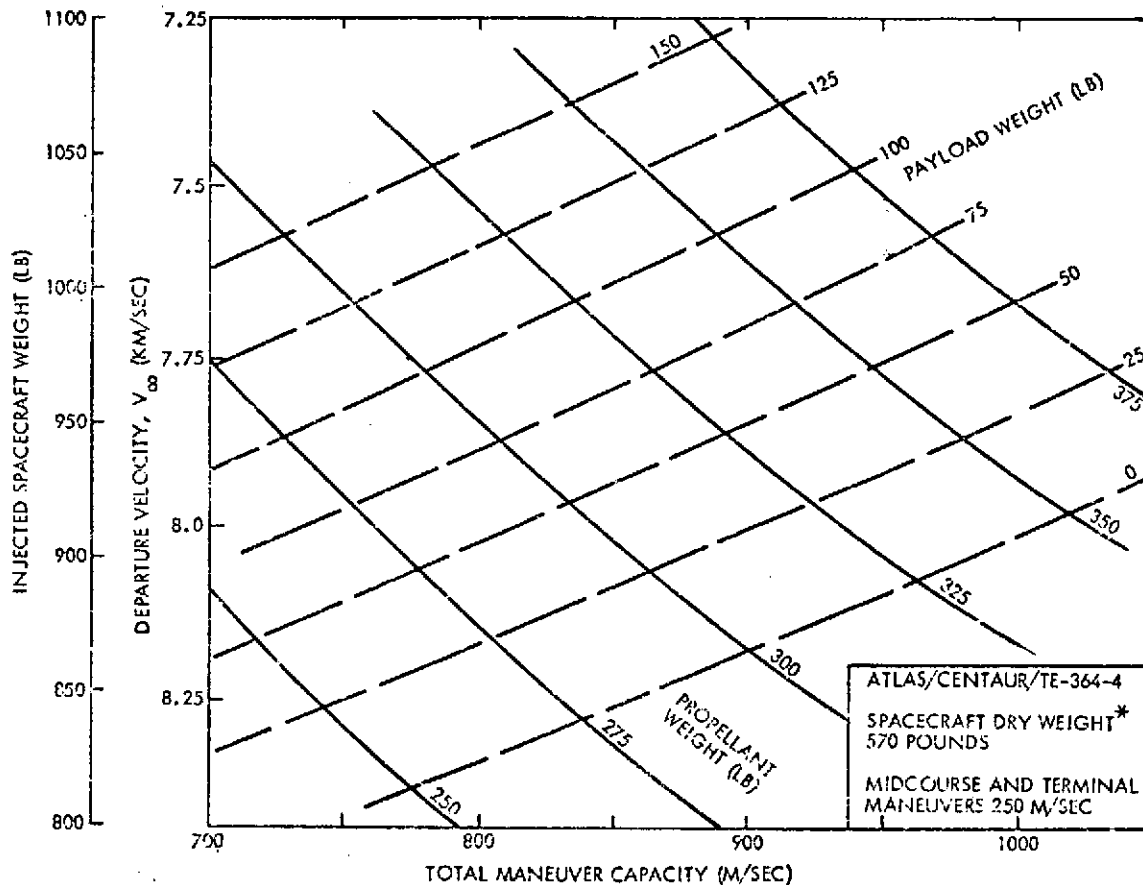


Figure 3-3. Spacecraft Weight Characteristics Vs Mission Energy

\* Dry weight excluding propellant.

specific impulse value,  $I_{sp} = 215$  seconds, for the monopropellant hydrazine propulsion system was used in this analysis and the spacecraft dry weight  $W_o$  (excluding science payload) was assumed as 570 pounds based on results of Section 6. The weight breakdown is as follows

$$W_T = W_o + W_{PL} + W_{PR}$$

Total	Dry weight	Net	Propellant
Injected	(minus	+ Payload	+ Weight
Weight	payload)	Weight	

The small variation of  $W_o$  with  $W_{PR}$ , reflecting tankage and feed system, was ignored for simplicity.

The curves in Figure 3-3 express the fact that propellant weight increases linearly with net payload for a given dry weight  $W_o$ , viz.

$$W_{PR} = (r - 1)(W_o + W_{PL}) \quad 3-1$$

where  $r = \exp(\Delta V / g I_{sp})$  is the mass ratio  $W_T / (W_T - W_{PR})$ .

The following expressions derived from Equation 3-1 are useful in making weight tradeoffs:

$$W_{PL} = \frac{1}{r - 1} W_{PR} - W_o \quad 3-2$$

$$W_{PL} = \frac{1}{r} W_T - W_o \quad 3-3$$

$$W_{PR} = \frac{r - 1}{r} W_T \quad 3-4$$

The exchange ratios  $\Delta W_{PL} / \Delta W_{PR}$ ,  $\Delta W_{PL} / \Delta W_T$  are  $\Delta W_{PR} / \Delta W_T$  that govern weight allocations if no limits are imposed on propellant weight capacity or gross weight can be directly taken from Equations 3-2 to 3-4. Figure 3-4 shows these parameters as functions of the mass ratio  $r$ . A second abscissa scale indicates the corresponding maneuver capability  $\Delta V$ . The mass ratio  $r$  for typical maneuver requirements varies from 1.5 to 1.6. These data show that an increase in total spacecraft weight can be used partially to increase the payload weight. Some portion of the increase must be allocated to an increase in propellant if the maneuver capacity is to remain unchanged. On the average, only

2/3 of the weight increment is available for payload use. For example, if the spacecraft weight is increased by 30 pounds, 10 pounds of this must be allocated as additional propellant and 20 pounds can be used as net payload increment. However, this applies only if there is enough space available for the extra propellant.

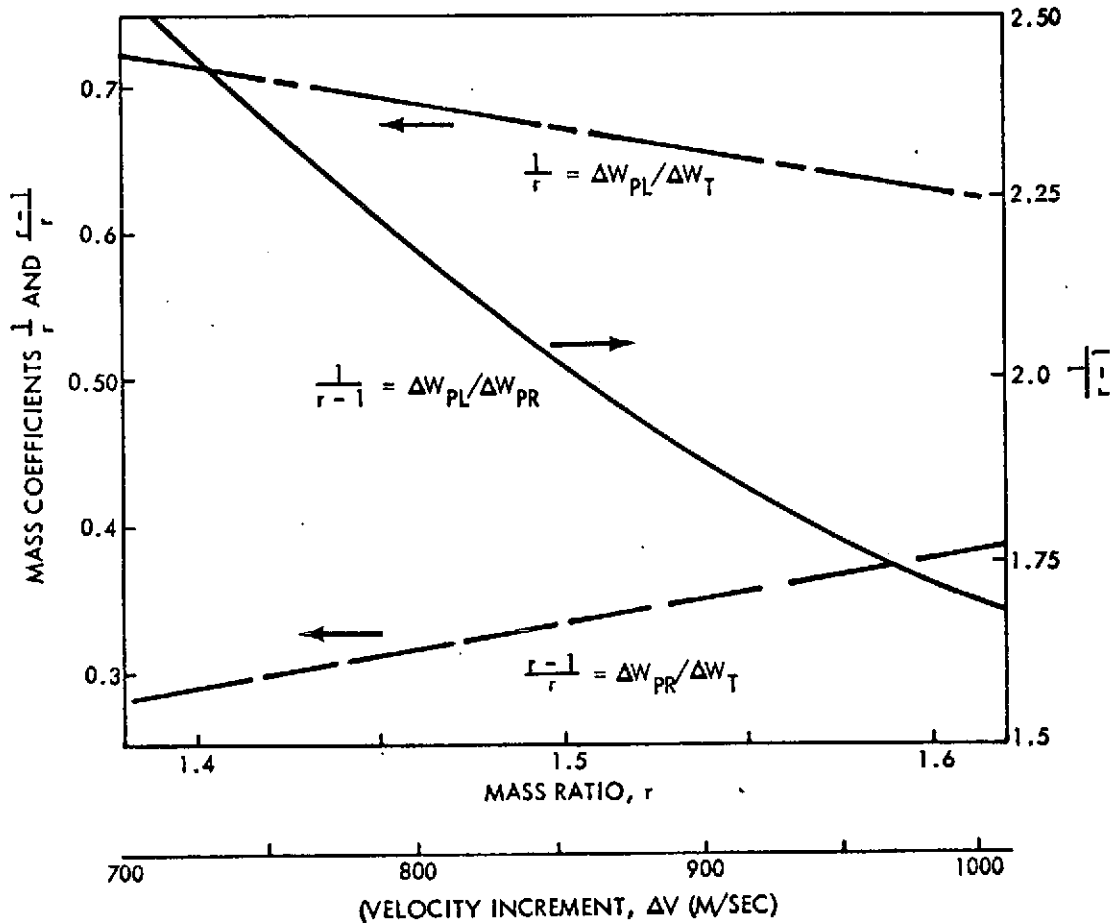


Figure 3-4. Exchange Ratios Between Payload, Propellant and Gross Weight

Weight and space limitations affect the tradeoff strongly. If an upper limit of total spacecraft weight is imposed the payload and propellant weight capabilities are traded on a 1:1 basis, such that a net payload increase of 25 pounds reduces maneuvering capability by 75 to 100 m/sec. On the other hand, if the propellant capacity is the limiting factor a 25-pound payload increase would reduce the maneuver capability by only 25 to 40 m/sec.

To summarize, we note that a limit on total spacecraft weight affects the payload versus maneuverability tradeoff more severely than a limit on propellant capacity; however, the former is launch vehicle dependent and can be more readily avoided than the latter which is imposed by the spacecraft configuration, at least in the asteroid missions being studied.

The curves in Figure 3-3 were obtained by relating weight characteristics to maneuvering capability  $\Delta V$  regardless of the launch vehicle used. For a given launch vehicle, in this case the Atlas/Centaur/TE-364-4, the total spacecraft weight can be related to the departure asymptotic velocity  $V_{\infty}$  as shown by the second scale along the ordinate. This makes the diagram useful for evaluating payload capabilities in terms of mission requirements  $V_{\infty}$  and  $\Delta V$  as will be discussed in the next section.

It should also be noted that the curves of this diagram remain valid if a change is made in the assumed empty weight  $W_0$ : any increment  $\Delta W_0$  from the reference value (570 pounds) would simply have to be subtracted from the indicated payload weight figures. The propellant weights shown in the diagram remain unchanged.

### 3.4 TYPICAL MISSION VELOCITY REQUIREMENTS VERSUS SPACECRAFT CAPABILITIES

Using the results from the preceding section we can now evaluate typical mission velocity requirements in terms of weight characteristics and constraints of the modified Pioneer spacecraft.

Figure 3-5 shows velocity requirements of a large set of triple-flyby trajectories in terms of  $\Delta V$ - $V_{\infty}$ -pairs. These pairs correspond to launch conditions that minimize either the required retargeting velocity ( $\Delta V$ ) or the departure velocity ( $V_{\infty}$ ) of each mission candidate in accordance with the data listed in Table 3-1. Most of the examples shown are for trajectories launched in late 1980. The 1978 mission to asteroids 1184, 420, and 1 which was selected for more detailed investigation is also depicted in the graph. Based on the payload and propellant curves of Figure 3-3 the operating region delineated by a shaded outline is constrained by the 330-pound propellant capacity of the modified Pioneer,

and the desired minimum science payload weight of 75 pounds. While a large portion of the total number of missions shown are eliminated by these constraints it is evident that a sufficient number of options still remain that can be performed by the Atlas/Centaur launched spacecraft.

The slanted line segments that connect associated  $\Delta V$ - $V_{\infty}$  pairs require interpretation. Each line segment actually characterizes tangents such that the points of tangency (the end points of the line segment) represent the minima of  $\Delta V$  or  $V_{\infty}$  as shown in Figure 3-6A. This parabola approximates the variation of  $\Delta V$  and  $V_{\infty}$  with launch date (Figure 3-6B). The method by which this parabola can be constructed from the given slant line is illustrated in the diagram.

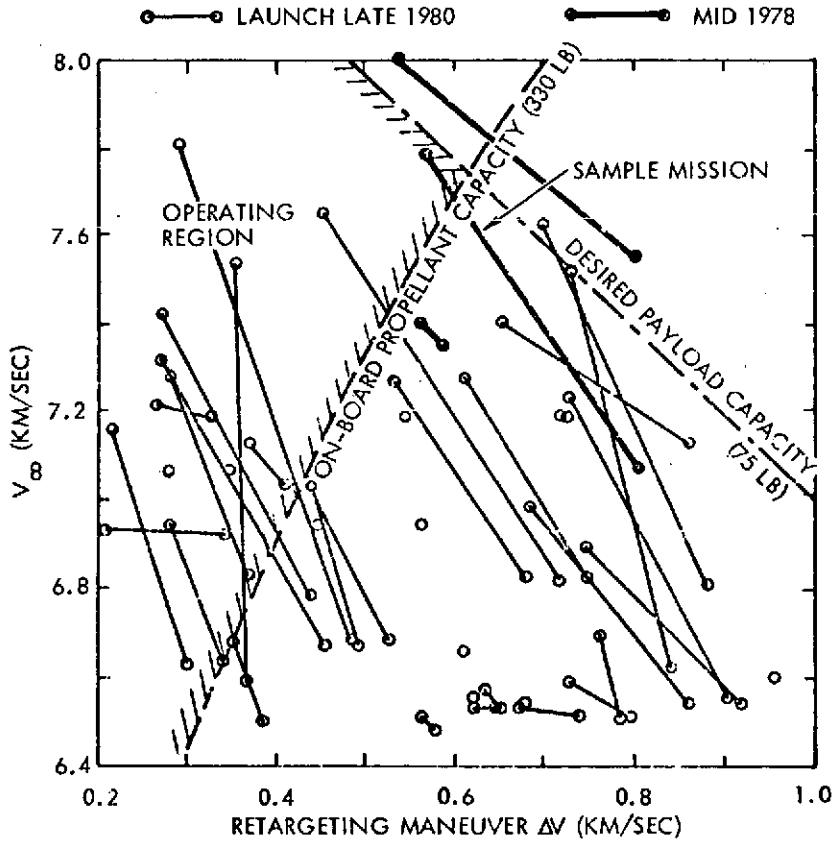


Figure 3-5. Typical Mission Velocity Requirements

given slant line is illustrated in the diagram.

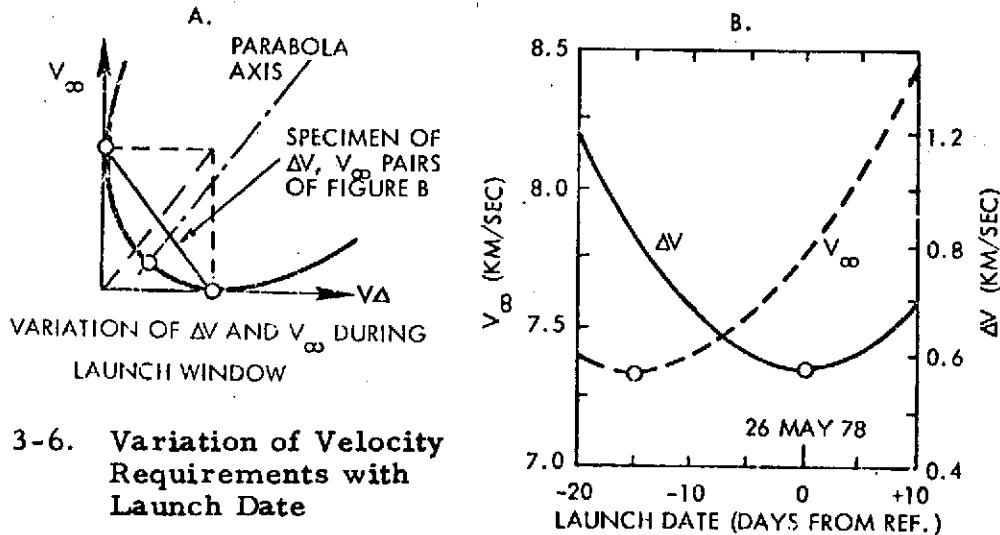


Figure 3-6. Variation of Velocity Requirements with Launch Date

Making use of this interpretation of mission velocity requirements and their dependence on launch date, detailed velocity and weight characteristics for three representative mission specimens, all with asteroid Ceres as the third target, were derived as shown in Figure 3-7. The encounter sequences are 1184-420-1, 960-1014-1, and 1719-828-1 (see Table 3-1, Group A). The three missions have similar launch dates and energy requirements. Launch dates are shown parametrically along the curves. Lines of fixed propellant and science payload weights delineate possible operating regions. For 340 pounds of propellant and 75 pounds of payload capacity only small segments of the three mission opportunities can be accommodated. Thus, a composite launch window of up to 30 days (with interruptions) is available made up of five to ten day intervals during which one of the missions can be launched. This condition is typical for many of the multi-asteroid mission groupings. The high sensitivity of velocity requirements to launch date variation is offset by the many mission alternative available.

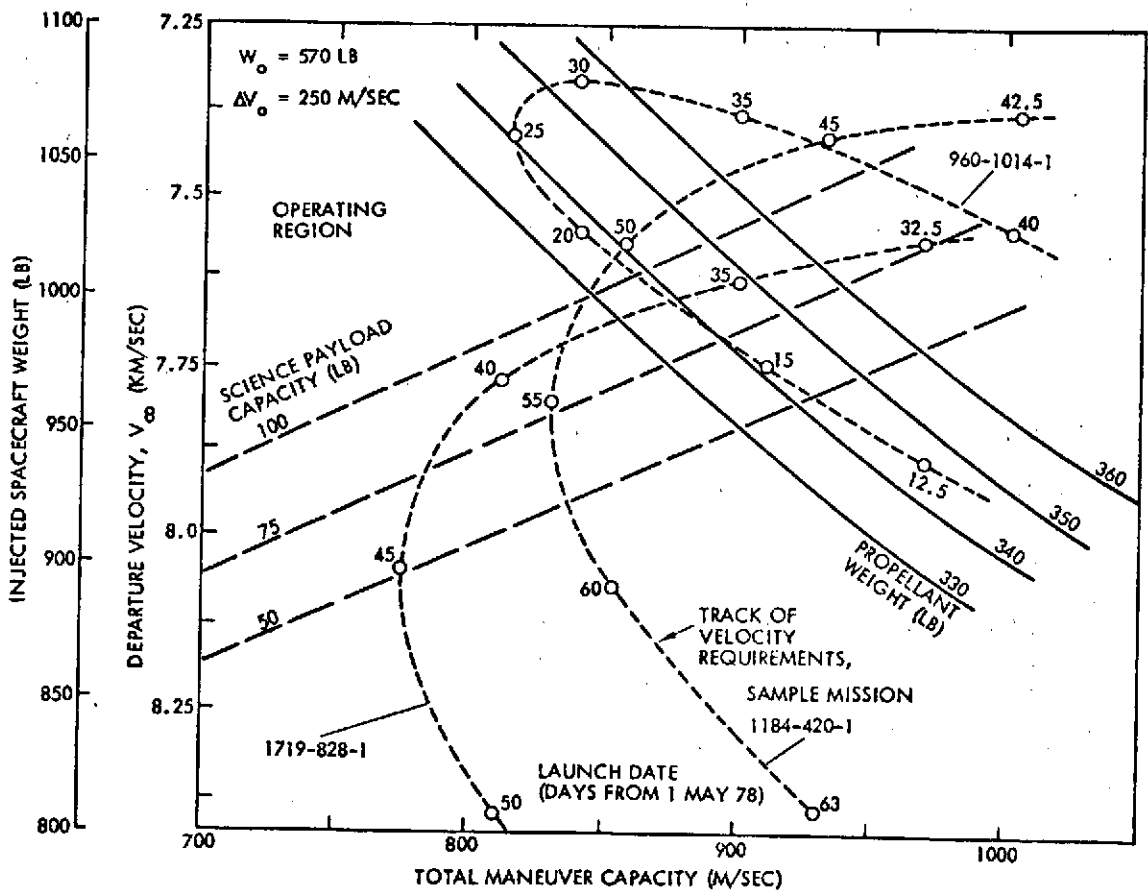


Figure 3-7. Effect of Launch Date Variation for 1978 Sample Mission

### 3.5 COMPOSITE LAUNCH WINDOW FOR 1978 SAMPLE MISSION

As explained in Figure 3-7 the launch window duration for each of the three missions considered is strongly influenced by the desired payload weight and the available propellant. The resulting "net" composite launch window duration (not counting the days of interruption) is shown in Figure 3-8. In order to obtain a total of 20 days at a desired payload weight of 75 pounds about 350 pounds of propellant is required. Since the Pioneer configuration limits the propellant to 330-340 pounds a shorter net launch window than 20 days must be accepted. In general, propellant must be off-loaded as time progresses to maintain the minimum desired payload capacity. Operationally this presents no difficulty on the launch stand. However, the extended total occupancy of the launch pad (more than 40 days) could become a matter of some concern if other missions are also scheduled for launch within this time period. Fortunately, the asteroid mission is sufficiently flexible to permit further changes of targets and launch dates if necessary.

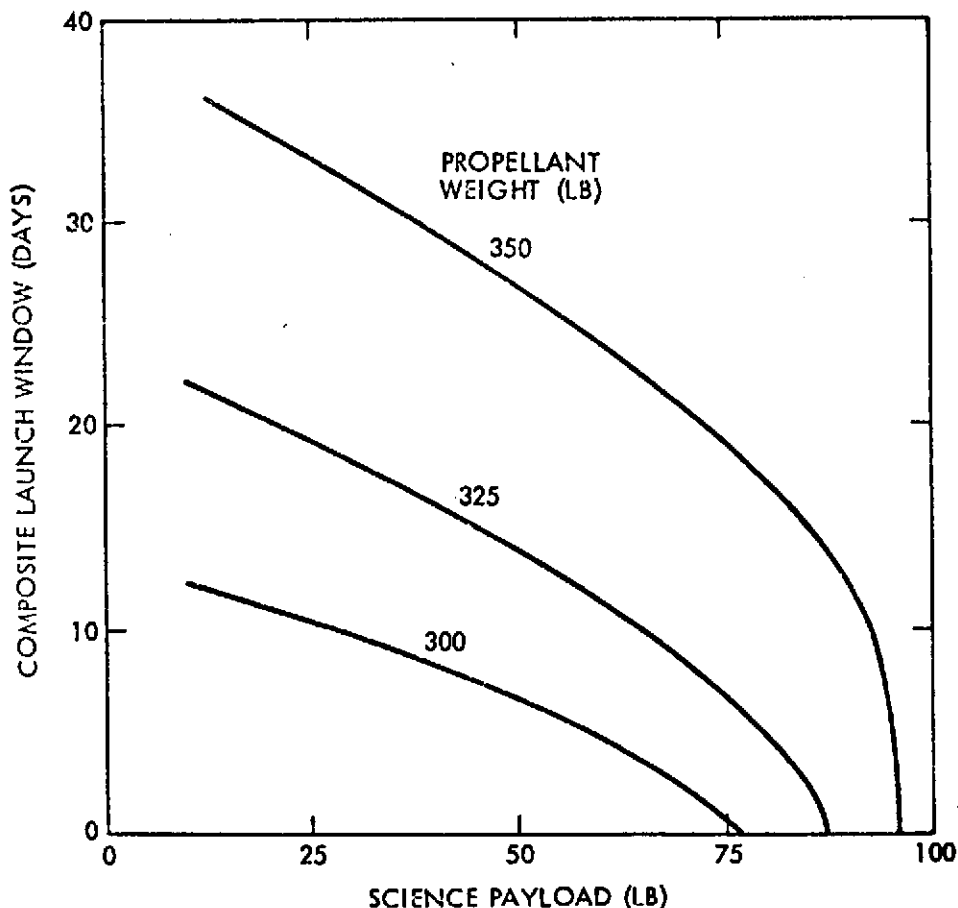


Figure 3-8. Composite Launch Window Duration for 1978 Sample Mission

### 3.6 LAUNCH PHASE CHARACTERISTICS

Analysis of the launch phase geometry is required to determine weight penalties that may accrue under unfavorable launch modes and launch azimuths for a typical range of asteroid mission departure conditions. Only a preliminary analysis was performed in the framework of this study.

#### 3.6.1 Declination of Launch Asymptote

Some of the candidate missions have trajectory inclinations of several degrees relative to the ecliptic since they intercept asteroids in inclined orbits at positions other than the respective ascending or descending nodes. The 1978 sample mission to Ceres via the asteroids 1184 and 420 may be considered typical. It has an orbit inclination of nearly 3 degrees which requires that the  $\bar{V}_{\infty}$  vector be inclined approximately 15 degrees in a northerly direction. For the launch date of this mission, i. e., mid-June 1977 (see Figure 3-7) the declination of the departure asymptote exceeds  $10^{\circ}\text{N}$ . This precludes launching the mission by direct ascent within reasonable launch azimuth limits as will be discussed below.

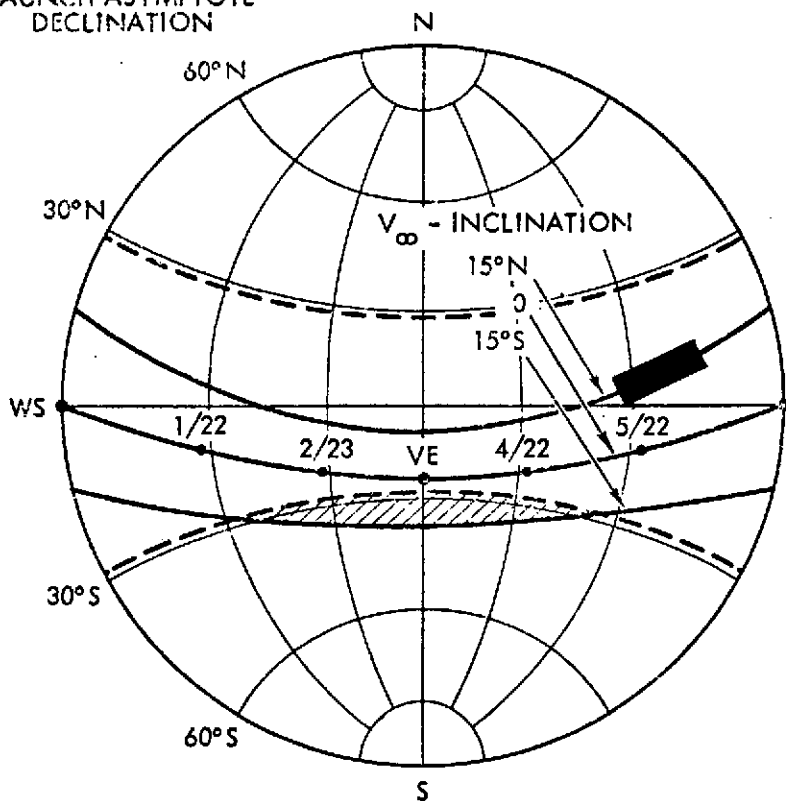
Figure 3-9A and B illustrate the effect of launch date on the declination angle for trajectories launched at  $\bar{V}_{\infty}$  inclinations between  $15^{\circ}\text{N}$  and  $15^{\circ}\text{S}$ . The launch window of the 1978 sample mission, mid-May to mid-June, is indicated in the left figure. The two diagrams show that northern declinations, unfavorable for direct ascent, can only be avoided if the launch date falls near the vernal equinox. However, even during this launch season some of the missions are subject to appreciable azimuth penalties if the direct ascent mode is used.

The shaded, lens-shaped areas in Figure 3-9A and B, having large southern declinations in spring (left graph) or large northern declinations in fall (right graph) delineate conditions where some weight penalties must be taken into consideration even for ascent via parking orbit. This must be analyzed individually for each mission.

ORIGINAL PAGE IS  
OF POOR QUALITY

3-14

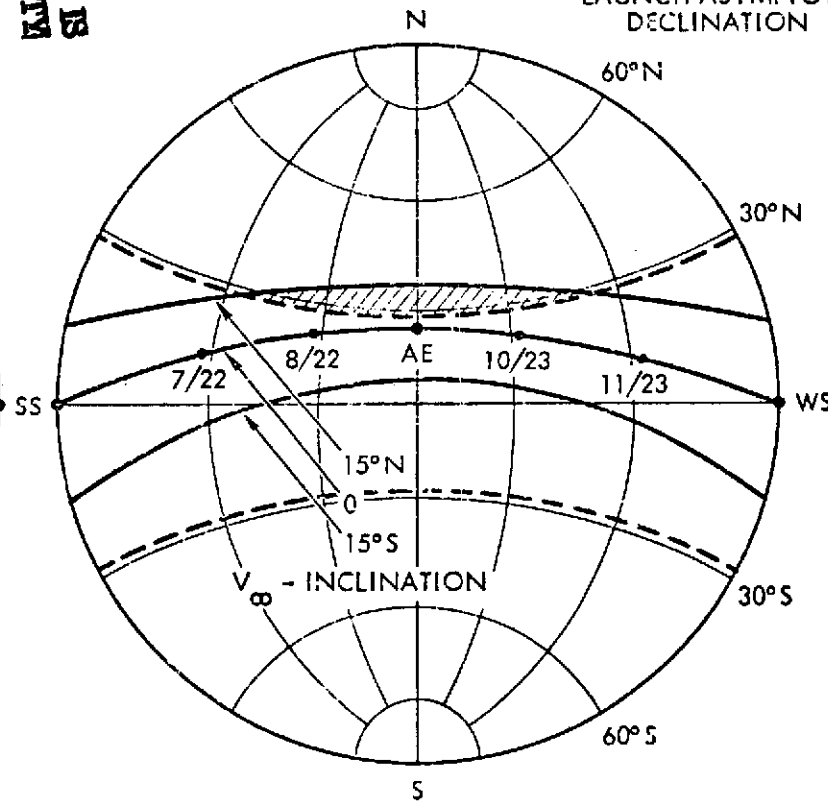
LAUNCH ASYMPTOTE  
DECLINATION



SPRING

A

LAUNCH ASYMPTOTE  
DECLINATION



FALL

B

(  Launch window for sample mission).

Figure 3-9. Seasonal Effect on Launch Asymptote Declinations

We conclude from this general survey that only a small percentage of mission candidates will be appreciably penalized due to launch phase restriction.

### 3.6.2 Direct Ascent Mode

Figure 3-10 illustrates the influence of launch seasons on azimuth for  $15^{\circ}\text{N}$ , zero, and  $15^{\circ}\text{S}$  inclinations of  $\bar{V}_{\infty}$  in the case of direct ascent from Cape Kennedy. As was noted in connection with Figure 3-9, the launch dates near vernal equinox (VE) are favorable for direct ascent under small inclinations of  $\bar{V}_{\infty}$ . With a  $\bar{V}_{\infty}$ -inclination of  $15^{\circ}\text{N}$  direct ascent is unfavorable at almost any time of the year. Even near VE the azimuth deviation to the north is about 20 degrees and exceeds the maximum northern azimuth limit (45 degrees) of ETR launches for departure dates that differ by more than 2.5 months from VE. Note that the 1978 sample mission would require a launch azimuth in this region. For southerly  $\bar{V}_{\infty}$  inclinations the variation of azimuth is not as severe but still ranges from 118 degrees at vernal equinox to 55 degrees at autumnal equinox (AE) in the case of  $\bar{V}_{\infty}$ -inclination of  $15^{\circ}\text{S}$ . The weight penalty is about 30 pounds if the launch azimuth deviates by 30 degrees, and 60 pounds if it deviates by 45 degrees from due east. These figures correspond to incremental velocities of 60 and 120 m/sec, respectively, at the representative  $V_{\infty}$ -value of 7.5 km/sec. We conclude that about one-half of the mission candidates, bracketed by  $\pm 15$  degrees of  $V_{\infty}$ -inclination, would be subject to an azimuth penalty in excess of 15 pounds if launched by direct ascent. In some of these cases, launch via parking orbit would be preferable.

### 3.6.3 Orbital Launch Mode

A corresponding analysis was performed for the case of orbital ascent. The results shown in Figure 3-11 illustrate the influence of launch dates on azimuth for  $\bar{V}_{\infty}$ -inclinations of 10, 15 and 20 degrees, North and South. The closed contour curves shown at VE are for the southern inclinations, those at AE for the northern inclination of  $\bar{V}_{\infty}$ .

---

\*Note: The results were obtained by graphical analysis with an accuracy of a few degrees, sufficient for purposes of this discussion.

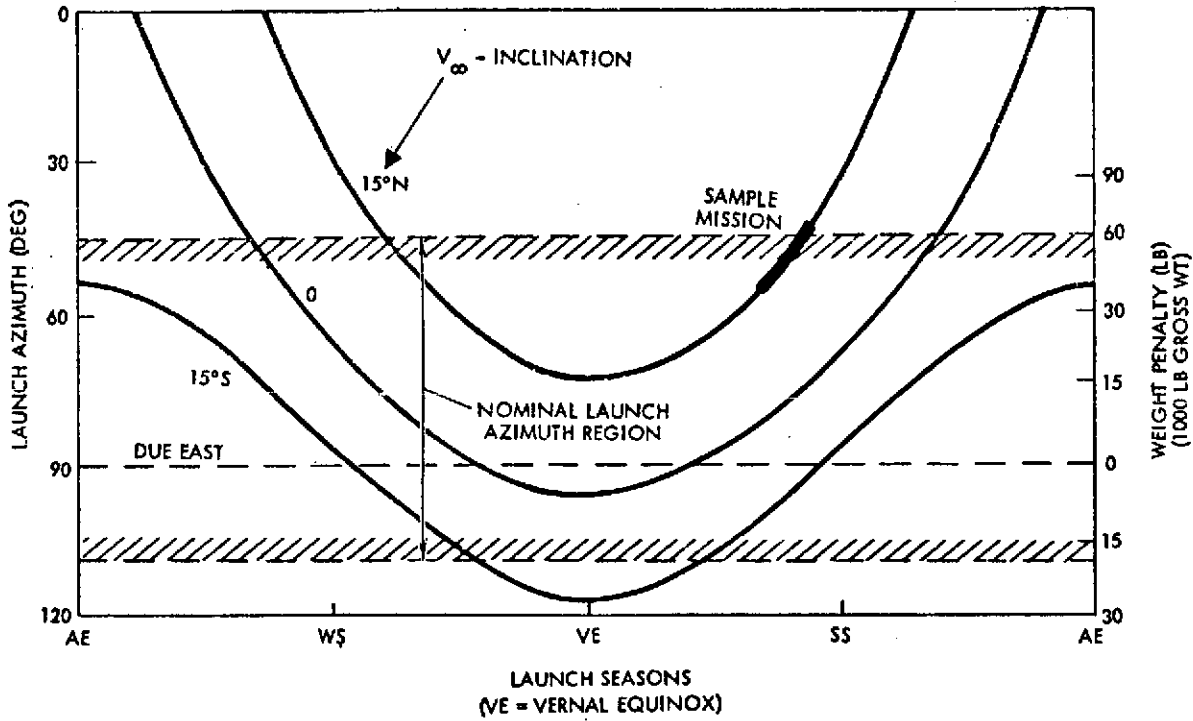


Figure 3-10. Launch Azimuths for Direct Ascent

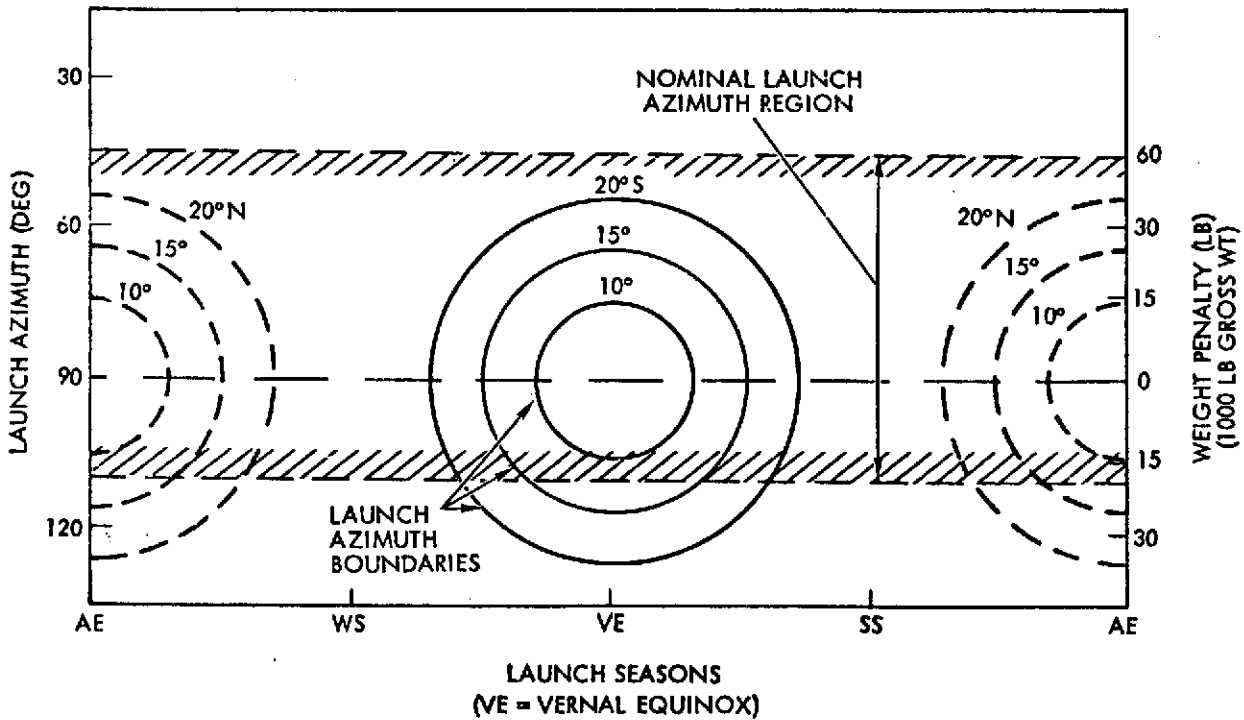


Figure 3-11. Launch Azimuth Boundaries for Orbital Ascent

Thus, the 1978 sample mission, for example, being launched in June incurs no azimuth penalty. Missions launched near VE with inclinations exceeding  $12^{\circ}\text{S}$  and those launched near AE with inclinations exceeding  $12^{\circ}\text{N}$  cannot make use of southern azimuth launch options because of the 110-degree azimuth limitation of Cape Kennedy. In all other cases two options are available. The boundaries shown define the minimum deviation from due east launch that must be used to reach the desired outgoing asymptote declination, i. e. , the points inside of each boundary curve are excluded.

Evaluation of launch options available within the range of acceptable azimuths shows that more than 90 percent of missions within the +15 degree inclination bracket can be launched by the orbital ascent mode, and about 60 percent with launch penalties of less than 15 pounds. Comparison of Figures 3-10 and 3-11 also reveals that a minimum of 15 pounds azimuth penalty (20-degree azimuth deviation from due east) accrues to some of the missions regardless of which of the two ascent modes is being used.

In comparing the direct and orbital ascent modes we must take into consideration a weight penalty inherently imposed by orbital ascent since the Centaur stage requires additional attitude control while coasting in the parking orbit. According to data received from General Dynamics, Convair Aerospace Division,\* the current best estimate of two-burn ascent penalties are <sup>46</sup>~~46~~ pounds for coast periods of less than 25 minutes, and <sup>85</sup>~~39~~ pounds for coast periods up to one hour. (This reflects weight penalties on Centaur vehicle of <sup>115</sup>~~105~~ and <sup>249</sup>~~255~~ pounds, respectively.)

Actually the question as to preferred launch mode requires further study since, in addition to weight penalties and azimuth limitations, the characteristics of the daily launch window must be taken into account. They are generally less restrictive in the case of the orbital launch mode.

---

\*Communication with R. Drowns, October 27, 1972.

### 3.7 SUMMARY OF SPACECRAFT MANEUVERS

In addition to the retargeting maneuver requirements listed in Tables 3-1 and 3-2, a number of other, generally much smaller maneuvers, i.e., midcourse corrections, trim maneuvers, and terminal guidance corrections, must be provided for in determining the total on-board propellant requirements. Table 3-3 gives the best estimates of  $\Delta V$  requirements in each category.

Table 3-3. Spacecraft Maneuver Summary (m/sec)

MAIN RETARGETING MANEUVERS (2)	600
MIDCOURSE CORRECTION AND TRIM MANEUVERS (AT LEAST ONE)	100
TERMINAL GUIDANCE CORRECTIONS (ITERATED MANEUVERS AT EACH ENCOUNTER)	<u>150</u>
SUBTOTAL	850
.....	
LOSSES DUE TO COMBINED THRUST, AXIAL AND RADIAL AVERAGE: 25% OF 150 M/SEC	38
LOSSES DUE TO PULSED THRUSTING COSINE LOSSES AND $I_{sp}$ LOSSES 20% OF 75 M/SEC	<u>15</u>
TOTAL	903

The estimated  $\Delta V$  value for the initial midcourse correction (100 m/sec) is less than the very conservative 200 m/sec allowed for the Pioneer F and G Jupiter missions but can be justified as follows. In the asteroid mission an aim point bias for planetary quarantine (imposed on Jupiter flyby) is not required. Control of

the exact arrival time at the target cannot be exercised because of the large ephemeris uncertainty of all but the largest asteroids. Without these requirements the Jupiter flyby mission would need less than 100 m/sec to cover probable guidance errors on a  $3\sigma$  basis.

A second factor permitting reduction of the midcourse  $\Delta V$  allowance is the smaller velocity increment that is delivered by the third stage (TE-364-4) in the case of an asteroid mission compared to a Jupiter mission, i.e., about 2900 m/sec versus 3900 m/sec, or a difference of 25 percent. The third-stage velocity increment is the largest single contributor to the total launch velocity error.

Finally with the flight time to the first asteroid being about two to three times shorter than to Jupiter the miss distance sensitivity is proportionally smaller. Thus, even without a quantitative analysis of injection errors and midcourse correction requirements we conclude that an allowance of 100 m/sec for this purpose is highly conservative.

Trim maneuvers are practically unnecessary for the initial mid-course correction as well as for the two major retargeting maneuvers of 200 to 400 m/sec each required during the mission since targeting accuracies better than the respective ephemeris errors would be wasteful and since terminal maneuvers are necessary in any case. Actual trim  $\Delta V$  requirements can be met by the margin included in the conservative 100 m/sec midcourse correction allowance.

The terminal maneuver allocation of 150 m/sec is based on results of the navigation and guidance analysis presented in Section 5, with 50 m/sec typically required for terminal corrections at each of the three encounters.

An interesting  $\Delta V$ -tradeoff exists between retargeting and terminal guidance maneuvers. If the retargeting capability is increased above the minimum of about 400 m/sec, it is evident from the mission requirements listed in Tables 3-1 and 3-2 that the number of possible target options increases rapidly. As a result, a greater choice of missions with favorable target sizes and encounter conditions becomes available and terminal navigation becomes simpler, with terminal  $\Delta V$  requirements being reduced accordingly. This offers the additional benefits of greater mission flexibility and higher probability of successful encounters.

At the bottom of Table 3-3 some  $\Delta V$  losses due to the use of pulsed radial thrusters are accounted for. A primary mission constraint is to avoid spacecraft reorientation and hence, loss of the communication link when the spacecraft is at large distances from earth. Only two reorientations (for retargeting maneuvers) are permissible. The introduction of radial thrusters not carried by Pioneer F and G permits maneuvers in all directions while the spin axis remains earth oriented. The losses include the following: extra  $\Delta V$  required for thrusting in arbitrary direction through vector addition of axial and radial thrust components; cosine loss due to pulsed thrusting over a finite thrust arc; and  $I_{sp}$  losses due to pulsed operation. Details of the combined axial/radial thrust operation and the resulting performance penalties will be discussed in Section 7.

## REFERENCES

- 3-1 David R. Brooks and William F. Hampshire, II: "Multiple Asteroid Flyby Missions," presented at 12th Colloquium of the International Astronomical Union, Tucson, Arizona, March 8-10, 1971. In Physical Studies of Minor Planets, T. Gehrels, ed., NASA SP-267, 1971.
- 3-2 David R. Brooks, Joseph W. Drewry, and William F. Hampshire II, "Multiple Asteroid Flyby Opportunities in the 1970's and 1980's," presented at the AIAA 10th Aerospace Sciences Meeting, San Diego, California, January 17-19, 1972. AIAA Paper No. 72-52.
- 3-3 Anon. : Ephemerides of the Minor Planets for 1971. Russian Academy of Sciences, Institute for Theoretical Astronomy, Leningrad, U. S. S. R. , 1970.

## 4. MISSION PROFILE CHARACTERISTICS

This section presents typical characteristics of multi-asteroid missions and defines the scenario of events prior to and during asteroid encounters. Of particular concern are sequences of spacecraft operations that are critically important for mission success such as timely acquisition of the asteroid for terminal navigation, and accurate pointing of payload instruments during the flyby. In addition to multiple asteroid missions, combined asteroid and comet flyby missions will be discussed to show the similarity of the two mission types.

### 4.1 PRINCIPAL CHARACTERISTICS OF MULTI-ASTEROID FLYBY MISSIONS

#### 4.1.1 Flyby Sequence

The mission profile of an asteroid flyby mission differs from that of a major planet mission for which the Pioneer spacecraft was originally designed primarily in terms of operating modes, observation requirements, and observation constraints during the target encounter. Figure 4-1 shows typical Jupiter and asteroid flyby trajectories for direct comparison of the main sequence of events. In both cases the same approach velocities (8.5 km/sec) are assumed. However, because of the great difference in target dimension and mass, and the closest approach distances chosen ( $\sim 2.2 \times 10^5$  km for Jupiter versus 100 km for the asteroid), the viewing conditions are very dissimilar. Principal differences are summarized as follows:

- The close approach required for asteroid observation imposes large line-of-sight rotation rates (maximally about 5 deg/sec).
- Only a few minutes are available for useful observation of the asteroid because of its small size. By contrast, the observation time of Jupiter extends over more than 100 hours.
- In the asteroid flyby the small target can escape observation during most of the encounter unless an accurate pointing program for the image system and other optical sensors is implemented. Conditions for Jupiter flyby observations are much less critical.

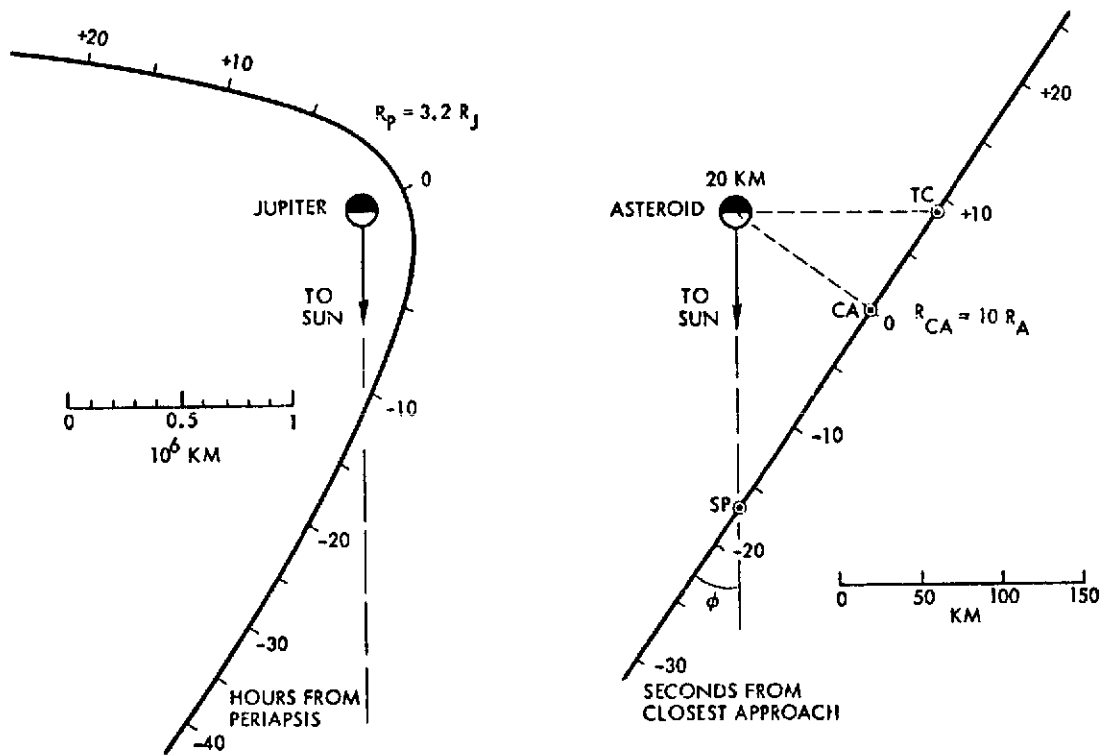


Figure 4-1. Asteroid Flyby Compared to Jupiter Flyby

- The shortness of the asteroid encounter permits only a few close-up images to be taken. A point scan image system as in Pioneer F and G is unsuitable, and a line-scan system is proposed instead. This implies high-data acquisition rates, and necessitates high-data capacity buffer storage and high-telemetry rates (32 Kbps).
- The close approach distance required for asteroid mass determination permits imaging at high-surface resolution, even with a modest optical system.
- Because of negligible asteroid gravity the flyby trajectory remains nearly undeflected. This limits the range of aspect angles for imaging, photometry, and polarimetry compared to the Jupiter flyby.
- Choice of flyby on the sunlit side of the asteroid precludes observation of asteroid wake effects.
- Small asteroid size and uncertainty of exact closest approach point generally prevent prediction of the best aim angle for the optical sensors. The system must operate autonomously since

communication time delay precludes ground control during the brief encounter. By contrast, the extended encounter time of Jupiter permits observation mode changes by ground command if necessary.

In the asteroid flyby example shown in Figure 4-1 the approach is from the sunlit side with the orientation of the approach velocity vector (approach angle  $\phi$  relative to the sun line) similar to the Jupiter flyby. The approach angle varies over a wide range, about 45 to 135 degrees, depending on whether the encounter occurs early or late in the mission, i. e., prior to, at, or after aphelion passage. The viewing angle sequence changes accordingly from one asteroid encounter to the next. The close-up observation sequence is keyed to three points marked on the trajectory in Figure 4-1:

SP = passage of subsolar point: full view of the illuminated disk

CA = closest approach: maximum surface resolution, and maximum line-of-sight rate

TC = passage of the terminator.

Images obtained from points between CA and TC show the surface features in highest contrast and are preferable to images taken near SP, provided the terminator passage occurs in reasonable proximity of the asteroid.

With a change of approach angle  $\phi$  the relative positions and sequence of SP, CA, and TC vary; SP and CA coincide if  $\phi = 90$  and TC moves to infinity; the sequence is reversed if  $\phi > 90$ .

In addition to the geometry illustrated by Figure 4-1 the change in ~~three-dimensional~~ viewing conditions is of interest that occurs with trajectories shifted above or below the plane of the drawing, such that the spacecraft does not pass over the subsolar point. This encounter condition permits a close-up view of the terminator region even if the approach angle  $\phi$  is near 90 degrees, but a full view of the illuminated disk is not possible.

#### 4. 1. 2 Trajectory Characteristics Affecting Encounter Conditions

Encounter conditions that occur at the different asteroids are governed by the characteristics of the spacecraft heliocentric trajectory. Since most asteroids have orbits with low eccentricity and low inclination we make the simplifying assumption that they move in circular, coplanar orbits in the ecliptic plane.

Figure 4-2 shows loci of relative velocity vectors of the spacecraft with respect to any asteroids or meteoroids encountered during the trip (see the insert sketch for explanation). The vertical axis of the plot is oriented toward the sun. The velocity loci are shown for spacecraft trajectories to 3, 4, and 5 AU. Solar distance is indicated by dashed parametric lines across these loci. The velocity vector initially oriented to the left at earth departure (indicated by P for perihelion) rotates in a clockwise direction as the mission progresses. At aphelion (A) the vector points to the right, along the horizontal axis; this means that at aphelion the spacecraft, being overtaken by a faster moving asteroid, appears to approach it from the front. The locus of the return trip from A to P (not shown here) is symmetrical to the outbound locus from P to A.

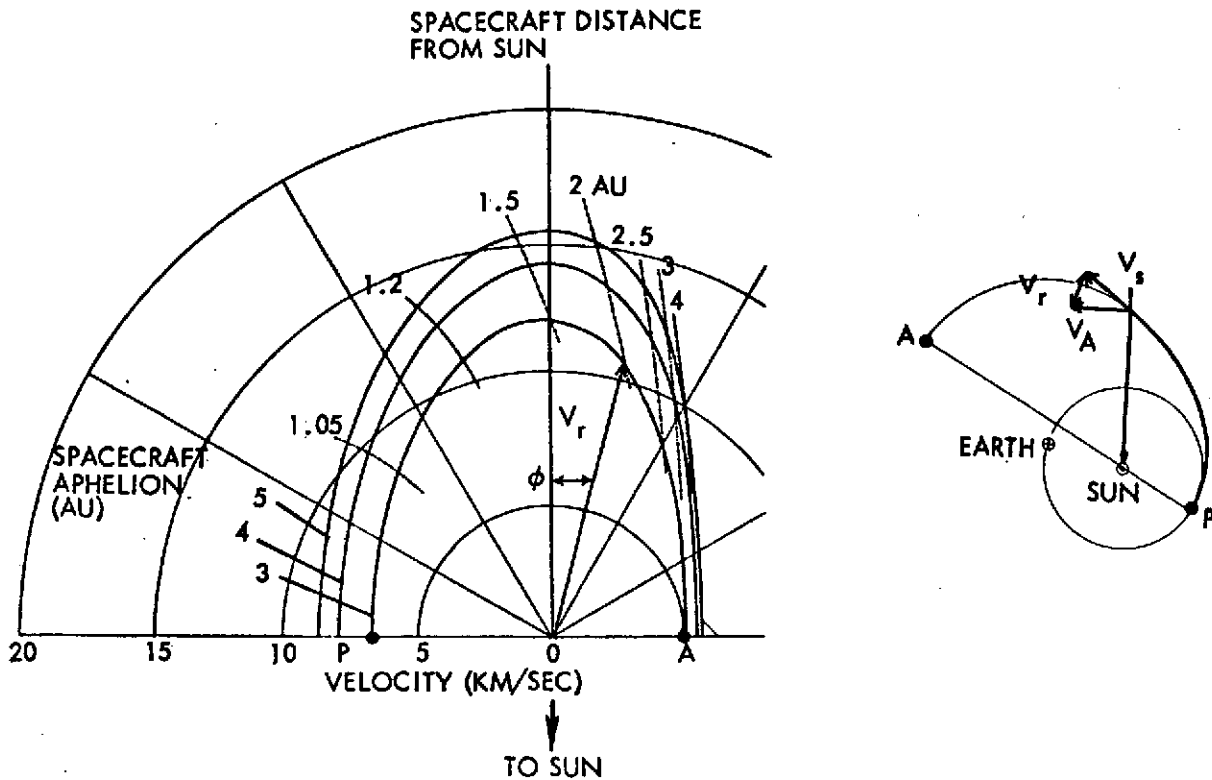


Figure 4-2. Relative Velocity Diagram

For a mission to 3 AU the relative velocity is initially 7 km/sec (at P), increases to a maximum of 14 km/sec at 1.7 AU (before entry into the asteroid belt), and then decreases again to 5 km/sec at A. Velocities in the asteroid belt are bracketed by the 2 AU mark to the right of the vertical axis (and the corresponding point on the inbound locus not shown here).

The change in approach velocity orientations (angle  $\phi$  in Figures 4-1 and 4-2) explains the different viewing conditions for encounters before and after aphelion. The approach angle  $\phi$  is equal to the phase angle of the asteroid as viewed from large distances prior to encounter (provided out-of-plane effects can be ignored). After the encounter the view angle approaches  $180-\phi$ .

The results derived by the above simplified approach are adequate for preliminary discussion of encounter conditions. To determine actual relative velocities in a given mission, the eccentricity and orbit inclination of the target asteroids, and the noncoplanar characteristics of the spacecraft trajectory must be taken into account. Actual encounter velocities can therefore differ by as much as 1 to 2 km/sec in magnitude and by 10 to 15 degrees in orientation from the results derived by the simplified model.

#### 4.2 TRAJECTORY OF 1978 SAMPLE MISSION

Figure 4-3 shows the trajectory of the 1978 mission to asteroids 1184, 420, and 1 which was selected from the mission candidates listed in Table 3-1 as a representative sample.\* The diagram shows the three-dimensional trajectory, projected into the ecliptic plane (X, Y-coordinates), and the out-of-plane component Z plotted versus Y. Portions of the intercepted asteroid orbits are also shown. Time is indicated along the trajectory in 20-day intervals.

The launch date of the nominal mission is 26 May 1978, although a delay to mid-June would be preferable for performance optimization.

---

\* Details of the trajectory were provided by D. R. Brooks of NASA, Langley Research Center, for purposes of this study.

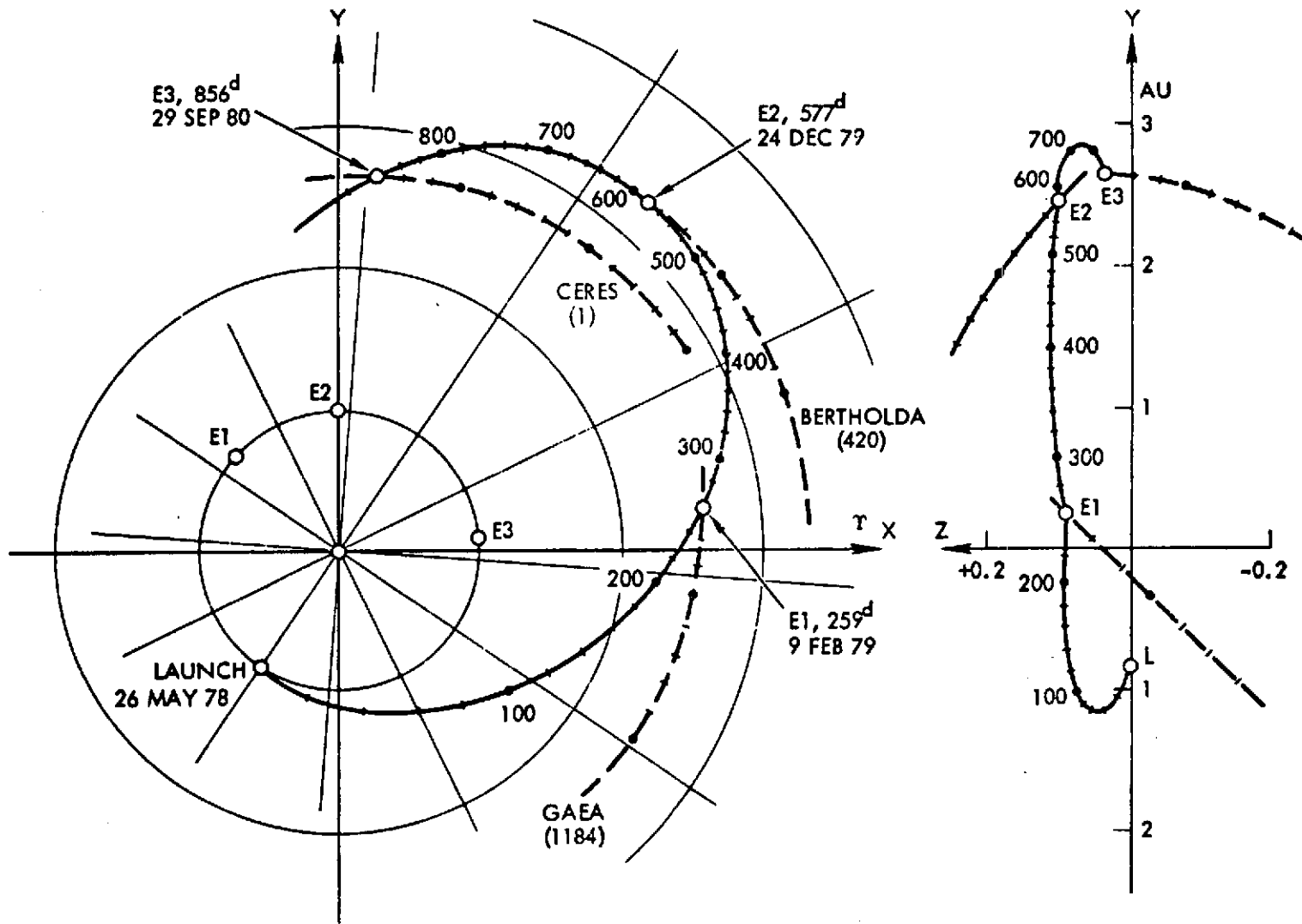


Figure 4-3. Sample Multi-Asteroid Trajectory

as discussed in Section 3.4. In the nominal case the spacecraft would encounter the asteroids Gaea (No. 1184) 259 days after launch, Bertholda (No. 420) 318 days later, near the aphelion of the trajectory, and Ceres (No. 1) 279 days later. The mission ends at 2.6 AU after a total flight time of 856 days, 283 days after aphelion passage (3.3 AU). As shown in the plot, the maximum northerly excursion from the ecliptic plane is about 0.1 AU.

As previously discussed (see Figure 3-5), this mission is in the intermediate range of energy requirements of the candidate missions considered in terms of  $\Delta V$  and  $V_{\infty}$ . The choice of Ceres as the last asteroid to be encountered eliminates the problem of late acquisition for terminal navigation and guidance that one would normally have to face in this part of the trajectory with fainter asteroids (see Section 4.3).

#### 4.3 ASTEROID ACQUISITION PROBLEM

As discussed in Section 4.1 the relative spacecraft velocity with respect to the asteroid varies in magnitude and orientation depending on where the encounter occurs along the trajectory. This variation is of major concern in mission design since it governs the viewing conditions that exist before, at, and after, asteroid encounters. Viewing conditions before the encounter strongly influence the range at which the spacecraft's optical navigation sensor can first acquire the asteroid and hence, the time that is available for terminal guidance corrections.

Pre-encounter asteroid viewing conditions are illustrated in Figure 4-4 (left diagram) for three cases: the encounter occurs (1) prior to aphelion, (2) at aphelion, and (3) after aphelion passage by the spacecraft. For simplicity the events are shown in a two-dimensional geometry. It is evident that the phase angle  $\phi$  at post-aphelion encounter ( $T_3$ ) is unfavorable for early acquisition by the onboard navigation sensor. The conditions worsen with increasing distance from the aphelion passage.

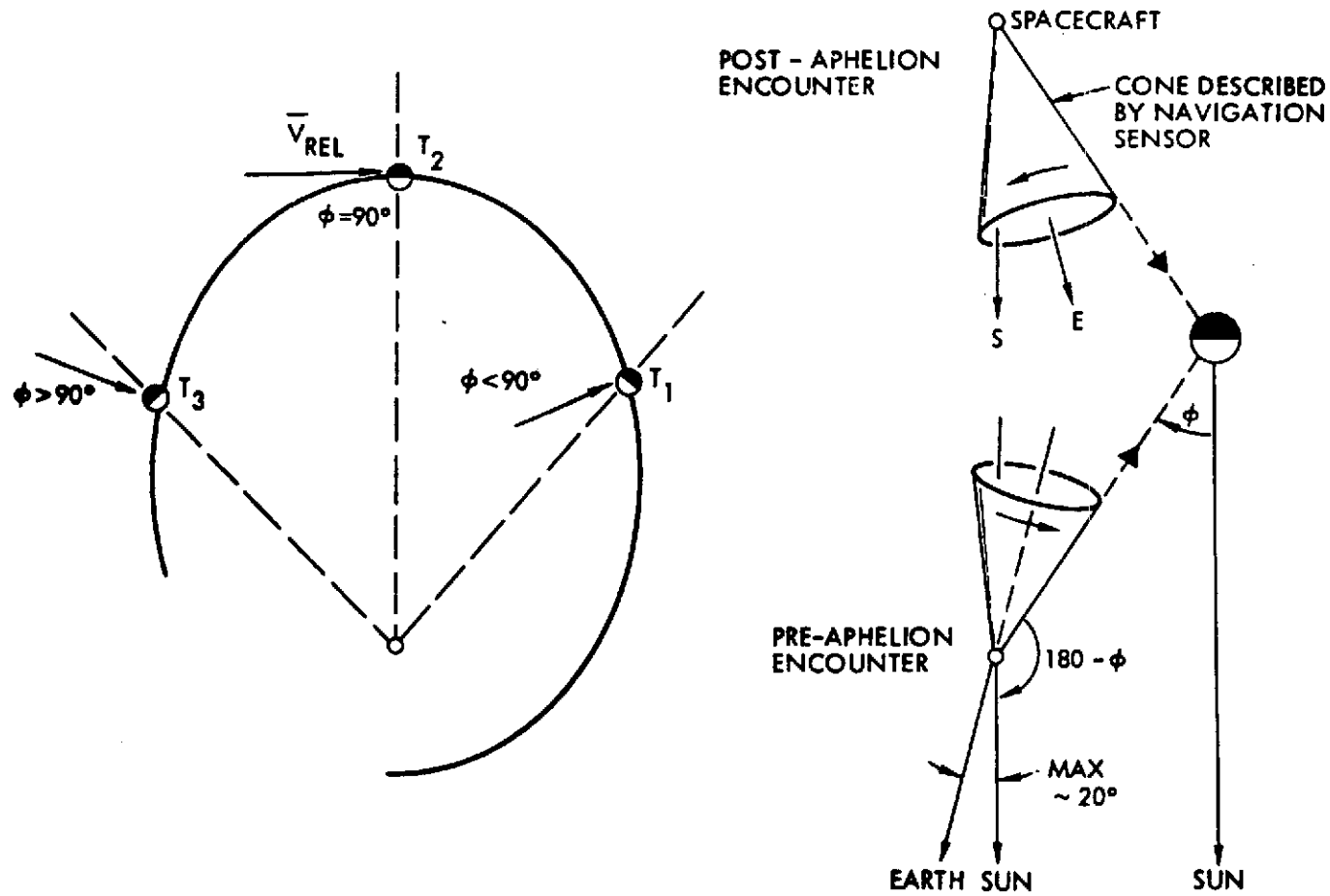


Figure 4-4. Asteroid Viewing Conditions in Encounters Before and After Perihelion

The diagram at the right illustrates the orientation of the spacecraft to-asteroid line of sight relative to the sun and earth vectors for pre-aphelion and post-aphelion encounters. On the spinning, earth-oriented Pioneer spacecraft the optical axis of the navigation sensor describes a cone around the earth vector, as shown. In the case of post-aphelion encounters early asteroid acquisition is made problematic not only because of the unfavorable phase angle of asteroid illumination but also because small cone angles of the sensor optical axis are impractical since the sensor must be placed behind the nine-foot high-gain antenna dish to protect it from direct sun illumination.

In an analysis of the asteroid acquisition range the absolute magnitude of the asteroid, and its distance from the sun at the time of encounter must be taken into account in addition to the influence of the phase angle. The photographic magnitude  $M$  of the target as seen by an observer at distance  $r$  is expressed by

$$M = M_A + 5 \log_{10} (r r_s) + 2.5 \log_{10} f(\phi) \quad 4-1$$

where

$M_A$  = absolute magnitude of the asteroid

$r_s$  = solar distance

$f(\phi)$  = phase function

Distances  $r$  and  $r_s$  are expressed in AU.

Figure 4-5 shows several phase functions  $f(\phi)$  that have been considered in this analysis: the idealized Lambert phase function, the phase function of a diffuse reflecting sphere and the lunar phase function (i. e., the integrated phase function of the lunar disk). A linear function (Reference 3-2)

$$2.5 \log_{10} f(\phi) = 0.023 \phi \quad 4-2$$

is also shown (dashed line) which is based on an average of asteroid observations made from earth. The lunar phase function is in good

agreement with asteroid measurements in the range of observations ( $\phi < 50^\circ$ ) that are feasible from earth. In the absence of a better definition it appears appropriate to use the lunar phase function for purposes of this study. We note that the lunar phase function itself is not well established for large phase angles. The line shown in Figure 4-5 is conservative.

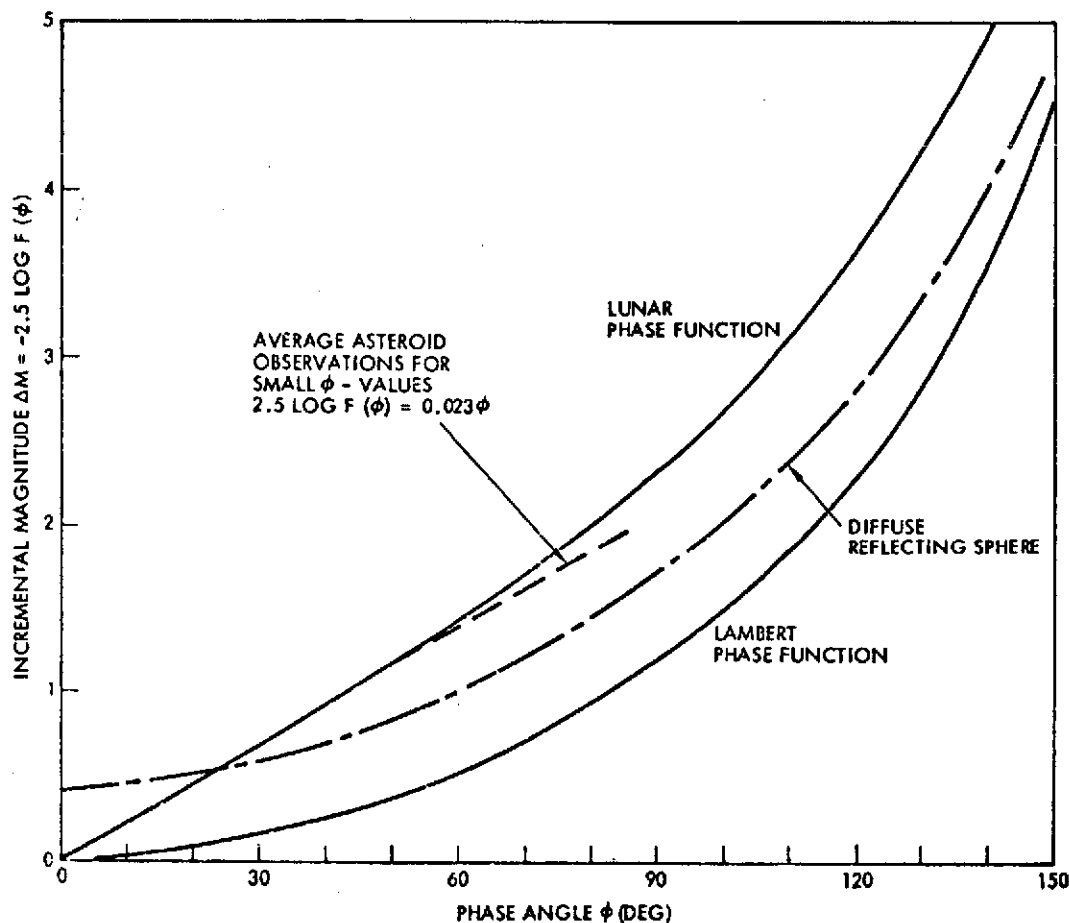


Figure 4-5. Comparison of Several Phase Functions

From the Equation 4-1 the acquisition range  $r_A$  can be determined as the antilog of the expression

$$\log_{10} r_A = \frac{1}{5} (M_V - M_A) - \log_{10} r_s - \frac{1}{2} \log_{10} F_{\text{Lunar}}(\phi_e) \quad 4-3$$

where  $\phi_e$  is the phase angle of the asteroid as seen by the spacecraft prior to encounter. Figure 4-6 gives the variation of  $\phi_e$  with mission characteristics and encounter position (derived from the velocity diagram of Figure 4-1). Using these data, and assuming a sensor detection

threshold  $M_V = 5$ , the asteroid acquisition range  $r_A$  varies with encounter conditions as shown in Figure 4-7.  $r_A$  is plotted as function of solar distance  $r_s$  with asteroid magnitude  $M_A$  as parameter. Four curves are shown for each value of  $M_A$  representing trajectories to 2.5, 3.0, 3.5, and 4.0 AU. The outbound leg of each trajectory is shown by a solid line, the inbound leg by a dashed line. The strong effect of phase angle variation with encounter position is evident in the difference of acquisition range for the outbound and inbound legs of a given trajectory. For example, with  $M_A = 12$ , an encounter position at 3 AU and an aphelion of 3.5 AU, the acquisition ranges are  $2 \times 10^6$  km and  $0.24 \times 10^6$  km, respectively.

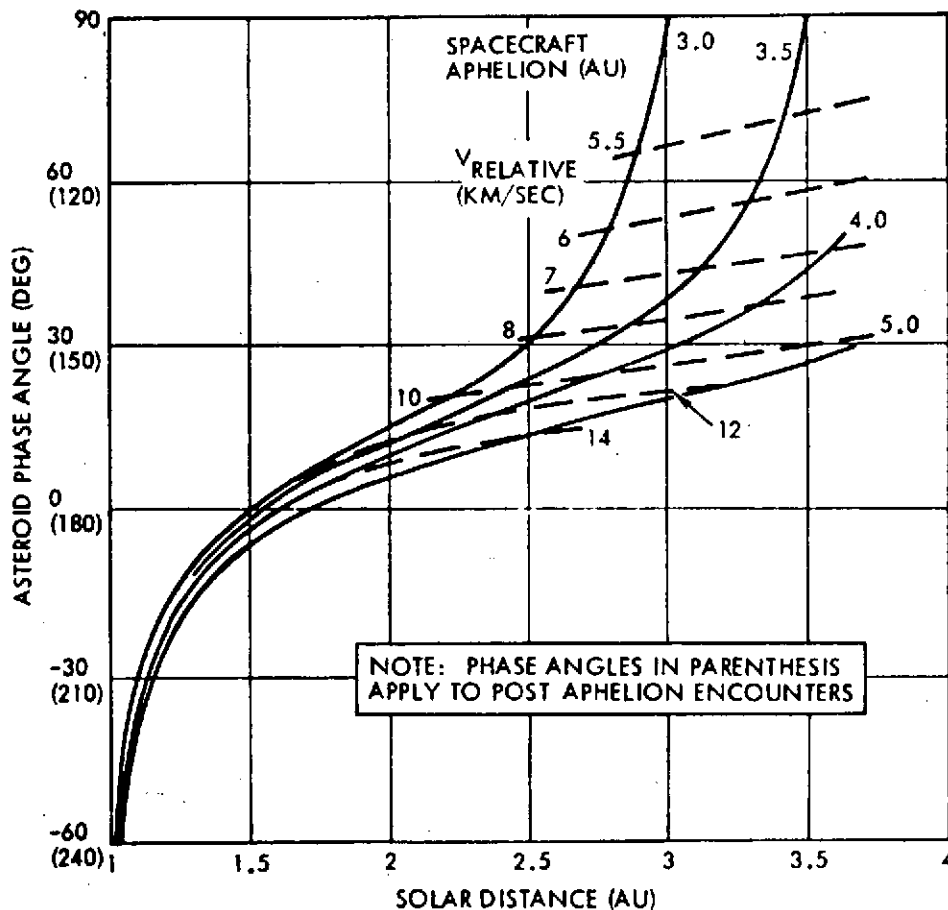


Figure 4-6. Phase Angle Variation Vs Solar Distance and Aphelion Distance

Although a sensor detection threshold of 5th magnitude is assumed here, the graph can also be applied to other detection thresholds  $M_V$  by changing the inscribed parameter  $M_A$  in accordance with  $M_V$  such that the difference  $M_V - M_A$  remains invariant. Note that these curves were derived under the simplifying assumption of inplane encounters and circular asteroid orbits. Actual geometric conditions must be taken into account when analyzing specific missions.

Referring back to Figure 4-6, the relative velocities at the different encounter positions are indicated by dashed parametric lines in addition to

the phase angles. The velocities range from about 5 km/sec for encounters near aphelion to values above 12 km/sec for encounters far from aphelion. A high relative velocity not only shortens the duration of the closest approach phase, but also reduces the time available for terminal guidance maneuvers after asteroid acquisition by the navigation sensor. It is evident from this graph that in an encounter long after aphelion passage, one must contend with adverse viewing conditions as well as a more critical time margin.

In summary, we conclude the following strategy for selecting encounter sequences from a target acquisition standpoint:

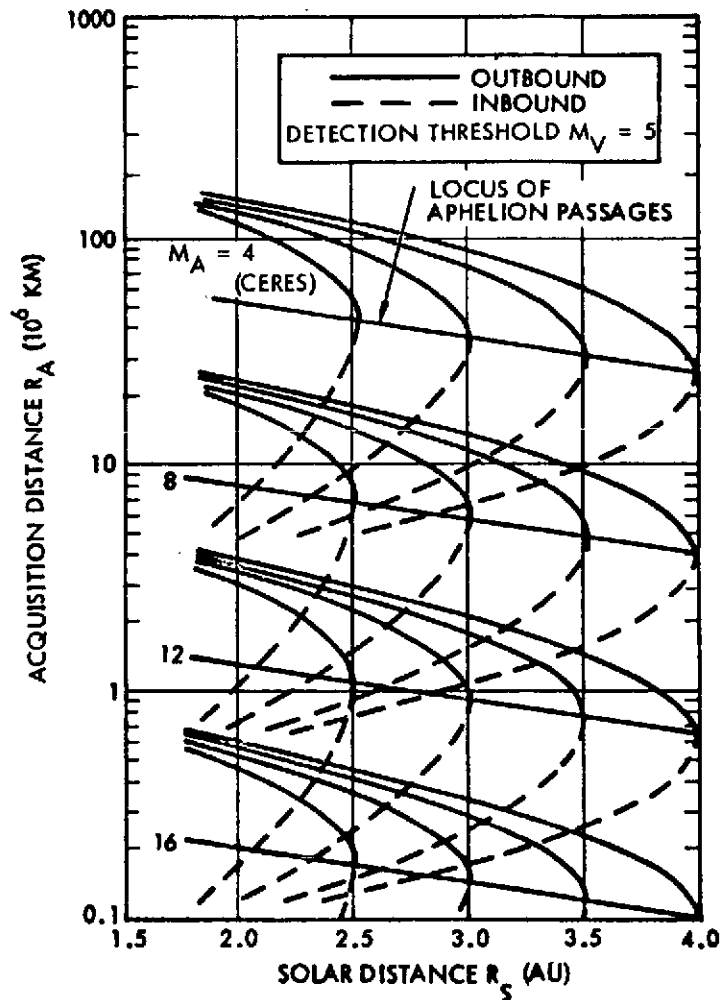


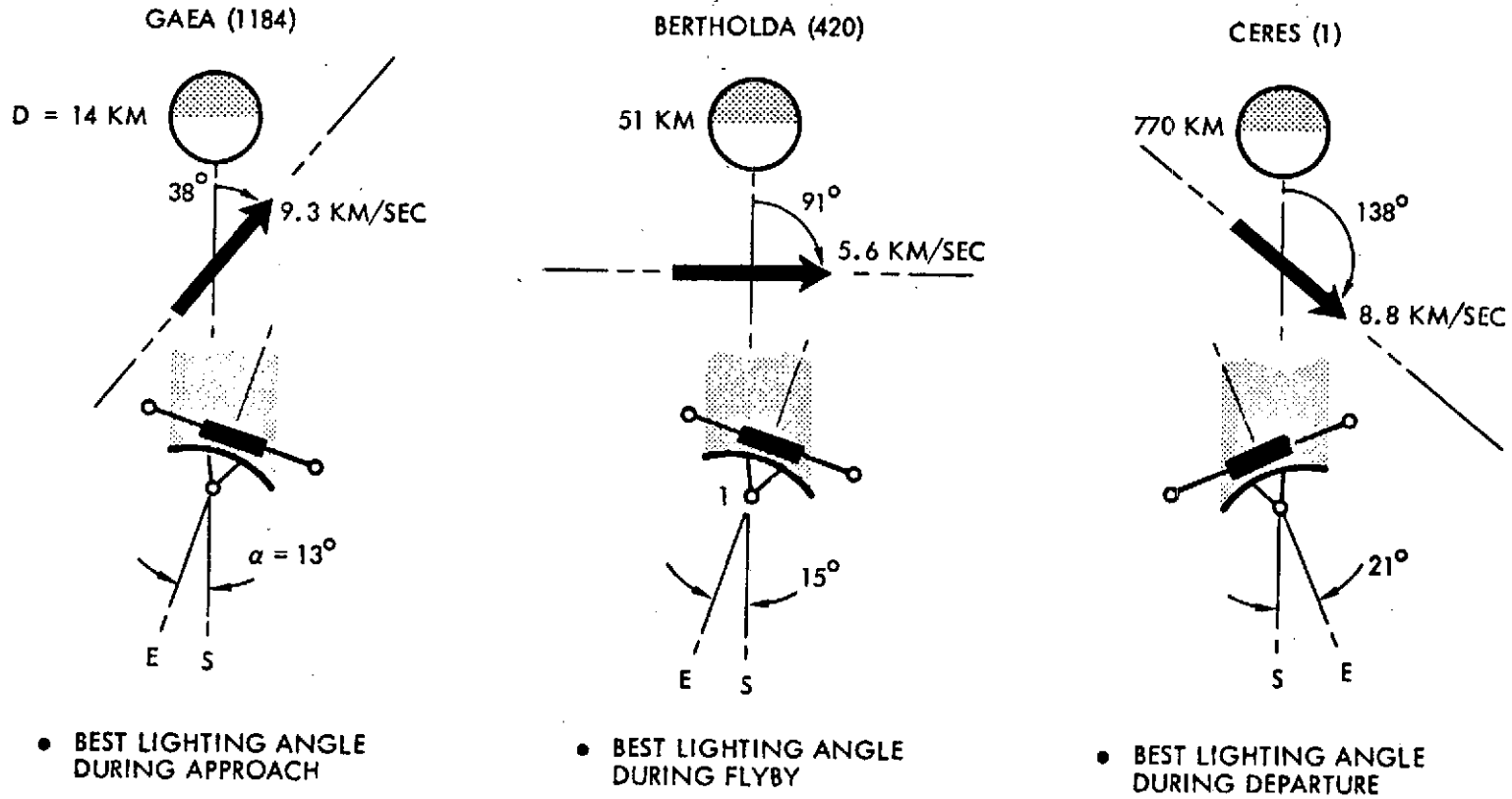
Figure 4-7. Variation of Acquisition Distance with Asteroid Position and Brightness

- Faint asteroids are best encountered early in the mission when the lighting angle is most favorable, i. e. , before aphelion.
- The lighting angle is less favorable at aphelion but at least the relative velocity is low. Reasonably faint asteroids can still be acquired early enough in this position.
- Bright asteroids can be acquired sufficiently early even if the encounter occurs a long time after aphelion.
- Generally, the target encounters must be spaced as far apart as possible to minimize the retargeting maneuvers. If this causes the third encounter to occur long after aphelion, a mission with a large target in third place is preferred. Faint targets in third place are generally not acceptable.

#### 4.4 ENCOUNTER CONDITIONS OF THREE ASTEROIDS IN SAMPLE MISSION

Encounter conditions at the three asteroids (1184, 420, and 1) of the sample mission differ appreciably in accordance with time of occurrence, i. e. , prior to aphelion (2.6 AU), near aphelion passage (3.3 AU) and after aphelion (2.7 AU).

These differences are illustrated in Figure 4-8. In the first case the lighting angle (38 degrees) is favorable for an early target acquisition. In the second case the angle is about 90 degrees. Early acquisition is possible, aided by the greater size of asteroid 420. In the third case the lighting angle (138 degrees) would preclude terminal navigation for targets much fainter than Ceres. In this case the acquisition range is estimated as  $7.5 \times 10^6$  km giving a time margin of nearly ten days for terminal navigation and guidance. No pronounced sun interference with optical sensor operation is anticipated in any of the encounters as can be deduced from the spacecraft orientations illustrated in the chart.



NOTE: PROJECTION INTO ECLIPTIC; GEOMETRY NOT TO SCALE

Figure 4-8. Encounter Conditions of Three Asteroids in Sample Mission

## 4.5 SCIENTIFIC INSTRUMENT POINTING PROGRAM DURING FLYBY

### 4.5.1 Time Variation of Viewing Conditions

The rapid time variation of viewing conditions (approach distances and line-of-sight angles) during flyby is illustrated in Figure 4-9 for several offset distances, assuming a flyby velocity of 6 km/sec. The abscissa axis shows distance along the trajectory and time elapsed. Time markers along the curves indicate the number of spacecraft revolutions, at 12 seconds per revolution.

The optical payload instruments, i. e., the imaging system, photopolarimeter, and IR radiometer, must be controlled to follow the asteroid line-of-sight motion. This is done in accordance with a program of pointing angle commands which is stored onboard the spacecraft, based on ground computed data that are transmitted to the spacecraft prior to the encounter. Updating of the stored program is required during the encounter, to compensate for uncertainties in the predicted encounter conditions.

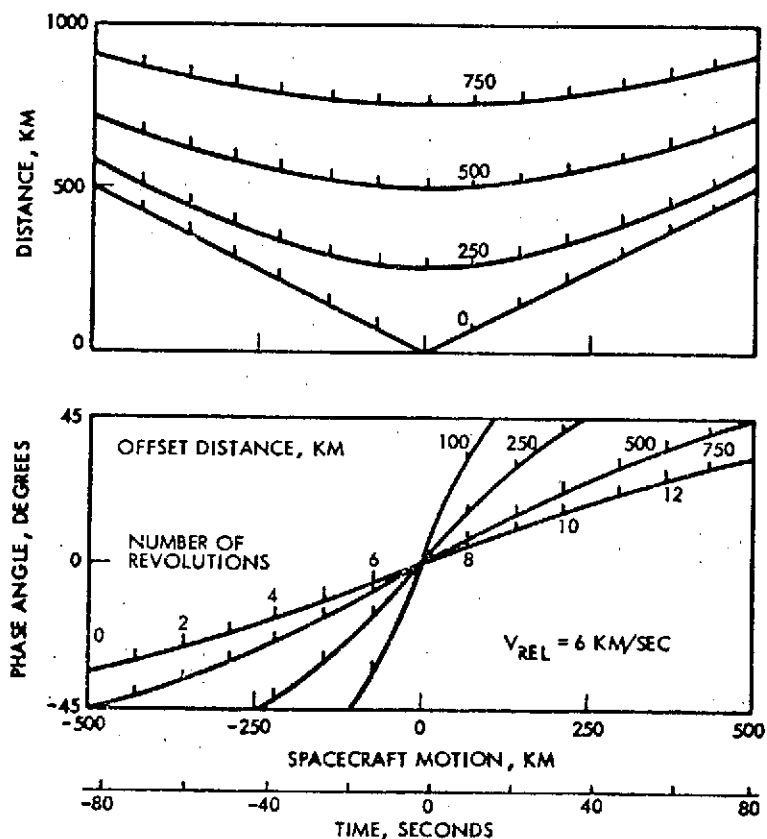


Figure 4-9. Time Variation of Encounter Viewing Conditions

Observation of the asteroid from a spinning spacecraft such as Pioneer, with a variation of line-of-sight angles, as shown in the diagram, requires that the optical instruments be gimbal-mounted and reoriented repeatedly so that they can view the asteroid during successive conical scan cycles. A one-axis gimbal drive is sufficient for this purpose. Details of the three-dimensional sensor pointing geometry will be discussed in the following subsections.

Referring again to Figure 4-9, it is apparent that the line-of-sight rotation can be as large as 40 degrees per revolution of the spacecraft, i. e., between successive asteroid scans. This peak rotation rate occurs only for small offset distances and only during the closest approach, typically over a period of 30 to 40 seconds.

Methods for meeting or circumventing these high-reorientation rate requirements have been investigated. One approach is to increase the offset distance to several hundred kilometers, thereby reducing the peak line-of-sight rate. Another approach is to permit a small offset distance but to limit optical observations to distances where the line-of-sight rate is reasonably small.

Both approaches are not satisfactory since they infringe either on the mass determination objective of the mission (first approach), restrict the surface resolution obtainable by the image system, or restrict the aspect angles observable by the photo-polarimeter (second approach). The preferred approach is to use a gimbal drive actuator capable of sufficiently high slewing rates, and to accept a slightly reduced pointing accuracy (about 0.5 degree). This meets all scientific objectives at the cost of an acceptably small increment in system weight and power drain.

#### 4.5.2 Line-Scan Imaging Geometry

Pointing requirements of the line-scan image system in three-dimensions are explained by the two spherical projections shown in Figure 4-10. The diagram at the left describes the flyby geometry in terms of the ground track that is projected on a sphere. The encounter is assumed to occur prior to aphelion passage as reflected by the relative orientation of the sun and velocity vectors.

122

4-17

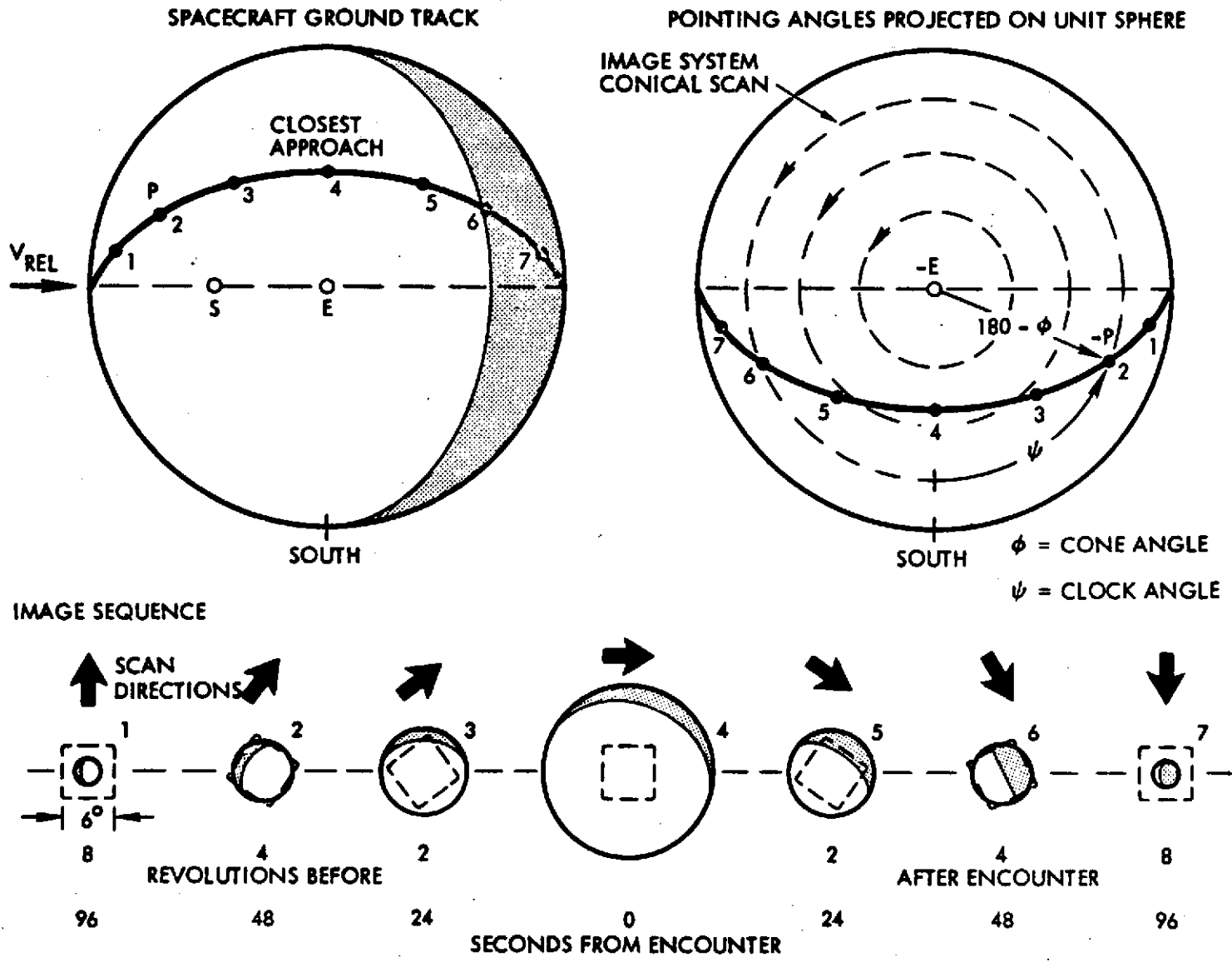


Figure 4-10. Imaging Geometry Near Encounter

In this example, the asteroid diameter is assumed to be 40 km, the closest approach distance is 100 km and the approach velocity 10 km/sec. The flyby trajectory has a northerly offset from the symmetry plane through the sub-sun (S) and sub-earth (E) points such that at closest approach the sub-spacecraft point (point 4 in the diagram) is at 45 degrees latitude north of E.

The diagram at the right shows the corresponding track of pointing vectors from the spacecraft, projected on a unit sphere, such that the spacecraft is at the center and the line of sight pointing to the rear. Point P at left corresponds to -P on the rear hemisphere at right.

Successive conical scans of the image system around the spin axis are depicted by concentric circles around -E (negative earth vector), with cone angles  $\phi$  being represented by the radii, and clock angles  $\psi$  by central angles measured from the reference axis (south). As the spacecraft approaches encounter the cone angle changes from 90 degrees to 135 degrees in the example shown. Overflight of the sub-earth point would preclude imaging at the point of closest approach since the "scan circle" would shrink to a point (-E) in this position.

A sequence of views of the asteroid is illustrated at the bottom of the diagram. The relative motion of the scan line varies during the encounter as shown by the arrows. This explains the reorientation of the image frame in the sequence of asteroid views. The apparent change in orientation of the dark segment of the disk is due to the northerly offset of the flyby trajectory.

As shown by this image sequence, the six-degree field of view of the camera is larger than the asteroid image until the spacecraft is within 480 km, or 48 seconds, of closest approach. Thus, a 96-second time interval is available during which the image system can obtain close-ups equal to, or smaller than, the asteroid disk. At one image per revolution, and for a spin rate of 5 rpm, nine such close-ups can be obtained.

### 4.5.3 Image System Pointing and Updating

The possibility of missing all or part of the asteroid at the time of image system exposure due to an incorrect pointing angle program stored prior to encounter presents a major problem. These pointing errors, unless corrected, can potentially cause the loss of significant scientific information (TV images as well as photometric, polarimetric, and IR radiometer data).

Figure 4-11 explains the nature of the contributing elements of the pointing error  $\Delta\phi$  assuming a two-dimensional pointing geometry. The downrange offset  $\Delta X$  and crossrange offset  $\Delta Y$  contribute error angles  $\Delta\phi_X$  and  $\Delta\phi_Y$ . The effect of  $\Delta X$  will eventually dominate that of  $\Delta Y$  as shown by the equation

$$\frac{\Delta\phi}{\phi} = \left[ \left( \frac{\Delta X}{X} \right)^2 + \left( \frac{\Delta Y}{Y_0} \right)^2 \right]^{1/2} \quad 4-4$$

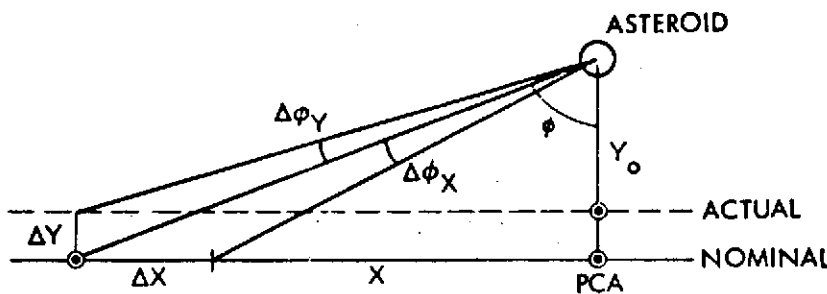


Figure 4-11. Pointing Error Geometry  
(In Two Dimensions)

since the denominator in  $\Delta X/X$  goes to zero while the denominator in  $\Delta Y/Y_0$  remains fixed. Figure 4-12 shows the variation of typical error angle components as  $X$  goes to zero. We note

that the contribution of  $\Delta Y/Y_0$  rapidly diminishes once  $\Delta X/X$  has started to dominate. This is also illustrated in Figure 4-13 (A and B): for example, the  $\Delta Y$  contribution to  $\Delta\phi/\phi$  is 2 percent, if the relative  $\Delta X$  error has increased to five times the value of the relative  $\Delta Y$  error; and only 0.5 percent, if the  $\Delta X$  error is ten times the value of the  $\Delta Y$  error.

These facts facilitate error correction by permitting that the  $\Delta X$  effect be removed first as a systematic error source. This is achieved by adjustment of the clock time that controls the stored  $\phi$  and  $\psi$  pointing programs.

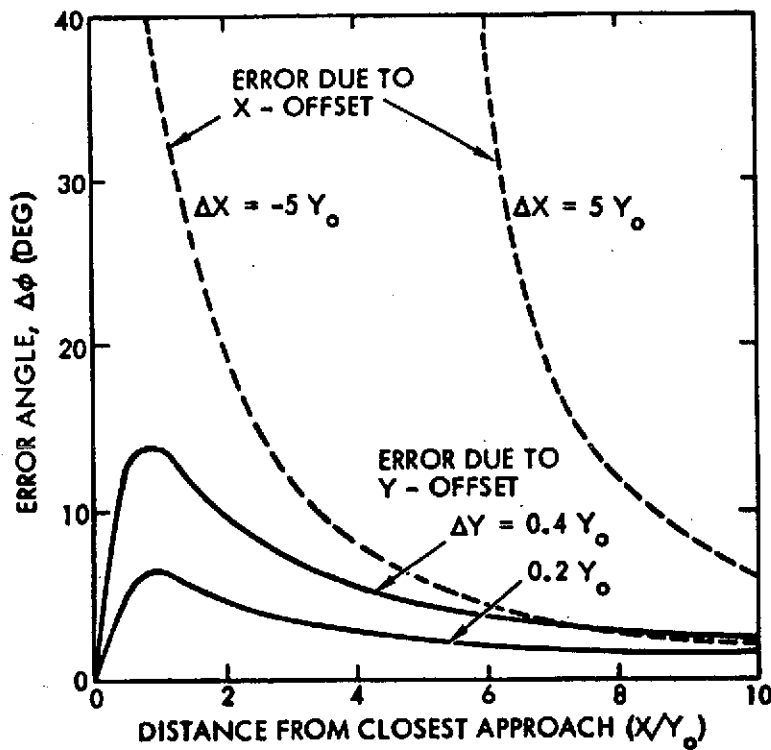


Figure 4-12. Error Angles due to  $\Delta X$  and  $\Delta Y$

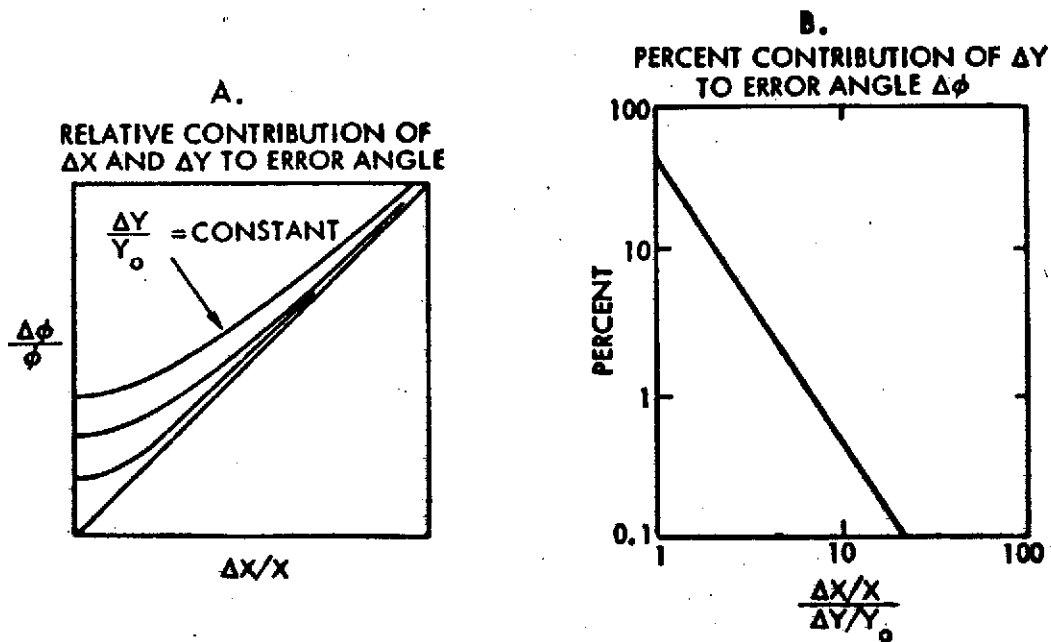


Figure 4-13. Contributions of  $\Delta X$  and  $\Delta Y$  to Pointing Angle Error  $\Delta \phi$

A relatively simple pointing angle updating and correction technique has been devised that uses information available from the image system and by appropriate processing, eliminates the loss of image data almost completely. This feedback technique, that does not require onboard computation, is illustrated by the functional block diagram shown in Figure 4-14.

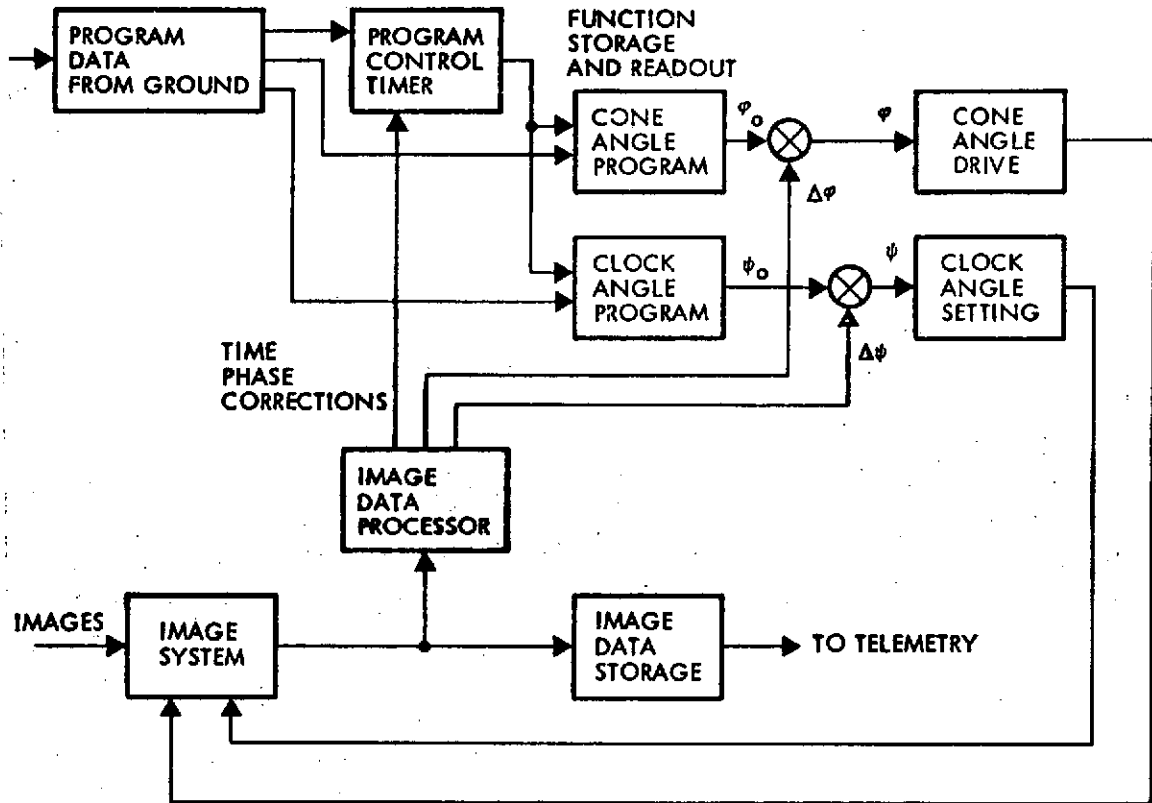


Figure 4-14. Image System Pointing Program and Updating Functional Diagram

The pointing errors include components due to inaccurate prediction of the time and distance of closest approach. As previously discussed, the timing error is more severe and its effects can be sensed first. Re-setting of the program control time minimizes this error source. The remaining errors in cone ( $\phi$ ) and clock ( $\psi$ ) angle can then be corrected by feedback terms  $\Delta\phi$  and  $\Delta\psi$  detected by the Image Data Processor. The processing circuits will be discussed in Section 7. For simplicity, a zero-order (sample-and-hold) correction scheme was adopted that reduces residual errors adequately as shown in Figures 4-15, 4-16, and 4-17.

ASSUMED: CLOSEST APPROACH (NOMINAL) 100 KM; 45 DEG SLANT ANGLE  
 OFFSET ERROR -20 KM  
 SPACECRAFT REL VELOCITY 6 KM/SEC

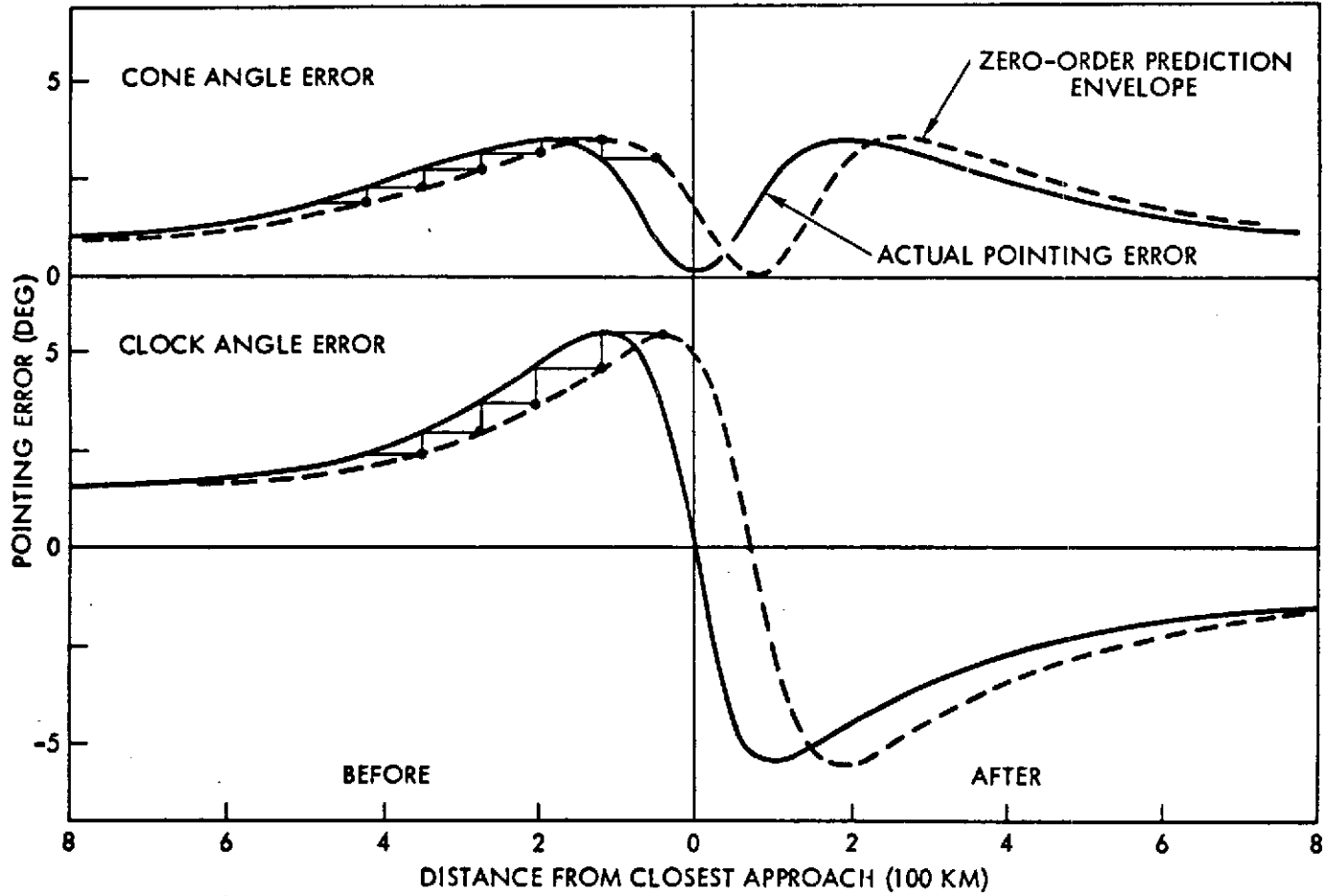


Figure 4-15. Imaging System Pointing Errors Due to Crossrange Offset  $\Delta Y$

Cone and clock angle pointing errors are shown in Figure 4-15 as functions of distance from the point of closest approach, before and after the encounter. (Assumptions on encounter geometry are stated at the top of the chart.) The effect of downrange offset is assumed to have been corrected beforehand by clock time resetting. A zero-order, sample and hold correction scheme is used to update the pointing angles as illustrated by staircase functions and their envelopes (dashed curves). The envelopes are shifted from the actual error curves by a distance corresponding to the time interval between image system exposures, i. e., 12 seconds on the average for a 5 rpm spin rate. For a relative velocity of 6 km/sec the differential distance is 72 km. The residual pointing error is largest at the time of rapid change closest to encounter. This is typical for the simple zero-order correction technique. The residual errors could be reduced very significantly by adopting a first-order rather than zero-order prediction technique using a slightly more complicated error processing program.

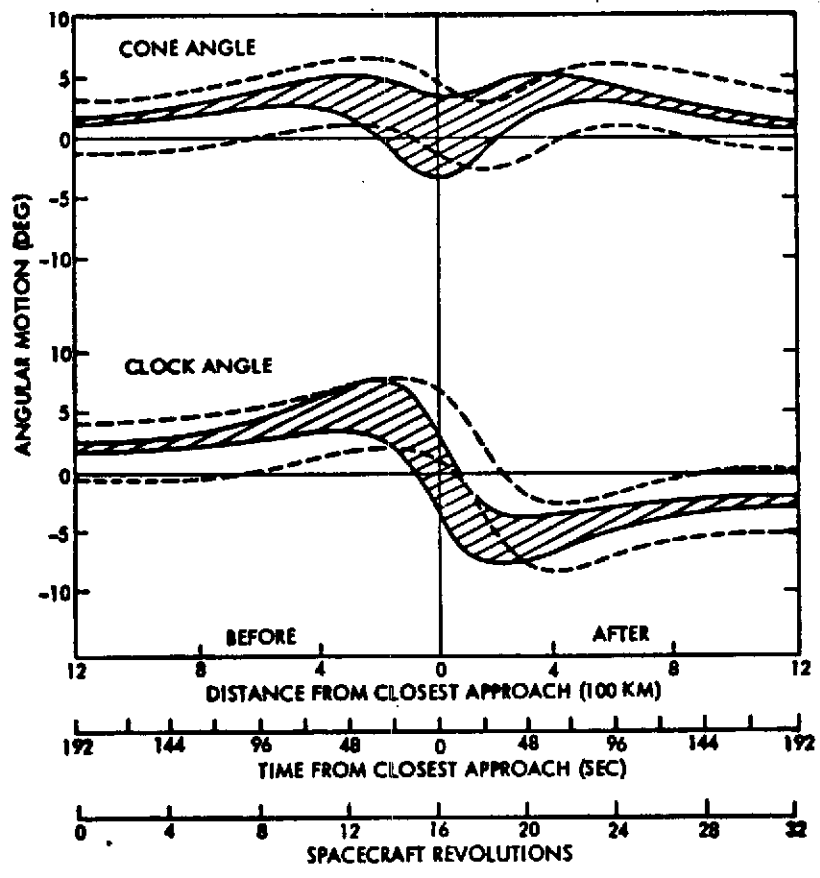
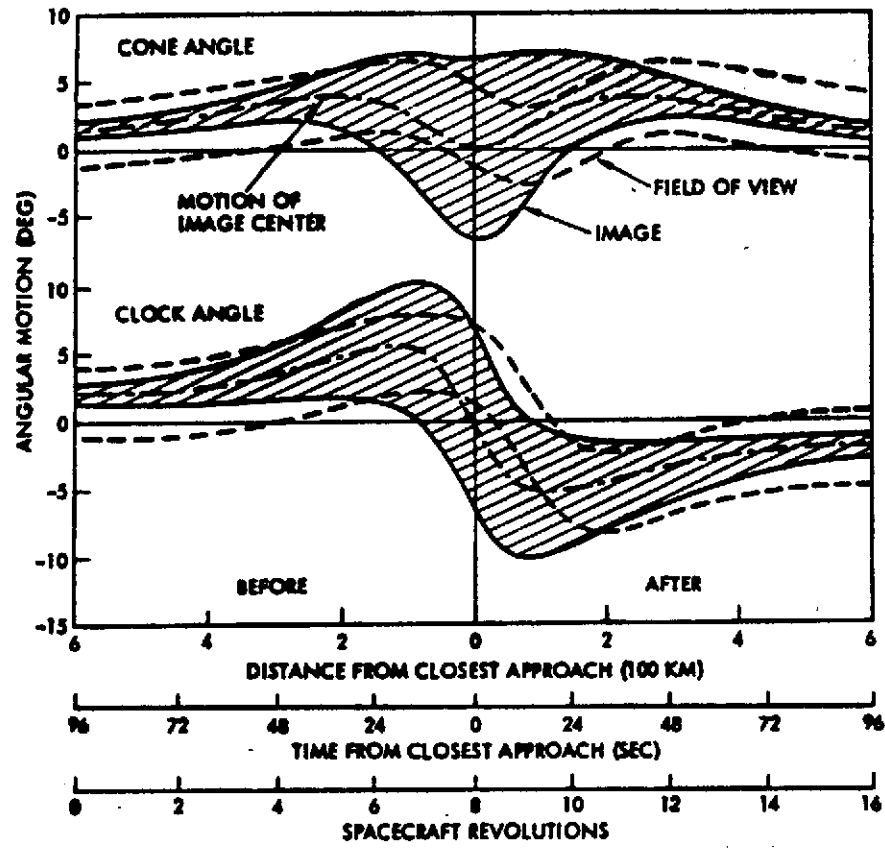
The effectiveness of the proposed pointing correction technique is illustrated in Figure 4-16 (A and B) by comparison of the field-of-view pointing adjustments (dotted lines) with the image motion and size variation (shaded region with solid outline) during the encounter. The examples considered are for nominal closest approach distances of 100 and 200 km with  $\Delta Y$  offsets of 20 and 40 km, respectively. The field-of-view is assumed to be 6 degrees. Uncorrected pointing angles are given by the null axes of the cone and clock angle variations. In general, the residual pointing errors are largest near the point of closest approach. However, since the asteroid (20 km diameter) subtends an angle of about 12 degrees at closest approach in the first example (Figure 4-16A) and 6 degrees in the second example (Figure 4-16B), a TV camera field-of-view of 6 degrees is large enough to compensate for most of the residual pointing errors. The examples also illustrate the substantial loss of image coverage that would occur if the pointing program were left uncorrected, particularly with small subtended angles.

The severe loss of image coverage that can occur in the absence of an onboard updating program is illustrated in Figure 4-17 for field-of-view angles of 6 and 3 degrees. Image coverage is defined here as the

ASSUMPTIONS: ASTEROID DIAMETER 20 KM  
 FIELD OF VIEW 6 DEGREE  
 SPACECRAFT RELATIVE VELOCITY 6 KM/SEC

A. EXAMPLE 1: CLOSEST APPROACH (NOMINAL) 100 KM  
 OFFSET ERROR -20 KM

B. EXAMPLE 2: CLOSEST APPROACH (NOMINAL) 200 KM  
 OFFSET ERROR -40 KM



4-24

Figure 4-16. Camera Pointing Vs Asteroid Image Motion Near Encounter (Zero-Order Pointing Correction)

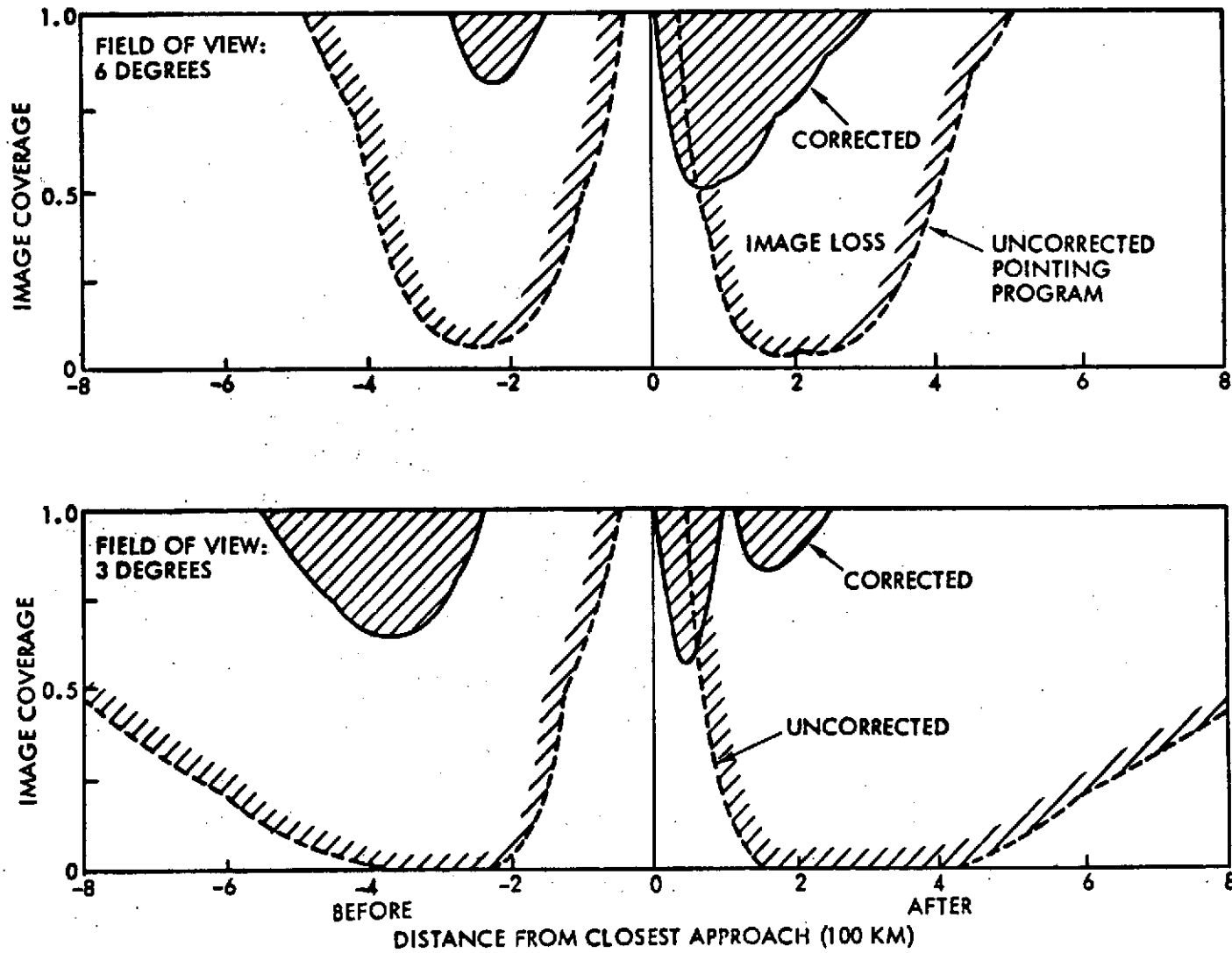


Figure 4-17. Image Loss with Corrected and Uncorrected Pointing Angles (Geometry as in Example 1)

product of the portion of cone angle and clock angle coverage of the asteroid image in percent. The image loss is defined as the complementary quantity (100 percent minus percent coverage). It is seen that the performance of the uncorrected pointing system is seriously degraded for 6 degrees field of view and unacceptable for 3 degrees field of view, since images that would be obtainable near closest approach, but are lost due to inaccurate pointing, constitute the most valuable scientific yield of the mission. Other optical sensors with small fields of view that are pointed in the same direction would also be deprived of close-up observation capability in this case.

By contrast, the proposed correction technique, although relatively simple in implementation, achieves nearly complete image coverage throughout the encounter. The apparent anomaly of a smaller image loss for a 3-degree rather than 6-degree camera field of view is due to the definition of the index of coverage used in this evaluation.

The alternative to improved pointing angles would be acceptance of larger fields of view at a loss of resolution. More study of this problem area is required. We conclude that for the desired field of view of the various optical sensors carried by the spacecraft a pointing correction such as a zero-order or a more sophisticated (possibly first order) prediction technique is essential for meeting the mission objectives. This conclusion also applies to flyby of planetary satellites, e. g., in future Jupiter and Saturn missions.

#### 4.6 SUMMARY OF MISSION EVENT SEQUENCE

The operational sequence differs from that of the nominal Pioneer F and G Jupiter missions primarily in the events leading to the target encounter, and in the encounter operations themselves. The launch phase and initial midcourse corrections remain essentially unchanged, except for the use of the orbital rather than direct ascent mode that would be required in some of the mission candidates, as discussed in Section 3. Our discussion therefore focuses on the encounter event sequence.

Table 4-1 gives a summary of the main events prior to and during asteroid encounter. The first two columns indicate whether the operation involves the ground station, the spacecraft, or both. The last column gives representative times. Actually, the timing of most of the events shown will be influenced by the condition of a specific target encounter, namely approach velocity, target acquisition range, target size, illumination angle, etc.

Table 4-1. Typical Sequence of Main Events Leading to Asteroid Encounter

GROUND	SPACECRAFT	EVENT	TIME
		<u>RETARGETING</u>	
•	•	EXECUTE RETARGETING MANEUVER $R_1$ AS COMMANDED	$E_{N-1} + 1$ DAY
•		TRACK AND DETERMINE NEW SPACECRAFT TRAJECTORY	TO + 6 DAYS
		COMPUTE REQUIRED CORRECTION	+ 6 DAYS
	•	EXECUTE TRIM MANEUVER $R_2$ AS COMMANDED	+ 7 DAYS
	•	RESUME CRUISE MODE	+ 7 DAYS
		<u>TARGET ACQUISITION AND TERMINAL GUIDANCE</u>	
	•	SET STAR MAPPER CONE ANGLE FOR ACQUISITION	$E_N - 6$ DAYS
•		IDENTIFY REFERENCE STARS	- 5 DAYS
•		DETERMINE PRECISE SPIN AXIS ORIENTATION	- 5 DAYS
•	•	ACQUIRE TARGET ASTEROID	- 2 DAYS
•		VERIFY TARGET ASTEROID IDENTITY	2 DAYS
•	•	PERFORM REPEATED NAVIGATION FIXES	FROM 45-40 HOURS
•		COMPUTE TERMINAL GUIDANCE MANEUVER	-40 HOURS
•	•	EXECUTE TERMINAL MANEUVER $T_1$	-36 HOURS
•	•	REPEAT ABOVE SEQUENCE	-30 TO 8 HOURS
•	•	EXECUTE FINAL TRIM MANEUVER $T_2$	8 TO -6 HOURS
		<u>ENCOUNTER SEQUENCE</u>	
•	•	TEST AND RECALIBRATE ENCOUNTER SCIENCE INSTRUMENTS	$E_N - 3$ DAYS
•	•	VERIFY SPACECRAFT ENCOUNTER MODE FUNCTIONS	-2 DAYS
	•	START ASTEROID OBSERVATIONS	-10 HOURS
	•	COMMAND PAYLOAD POINTING SEQUENCE	$E_N - 4$ HOURS
	•	START CLOSE-UP OBSERVATION SEQUENCE	-30 MINUTES
	•	END ASTEROID OBSERVATIONS	+10 HOURS
•	•	START NEXT RETARGETING SEQUENCE	+ 1 DAY

$E_{N-1}$  AND  $E_N$  DESIGNATE ENCOUNTER TIMES AT  $N-1^{ST}$  AND  $N^{TH}$  ASTEROID, RESPECTIVELY

Retargeting, required after each asteroid encounter to prepare for the next, should take place as early as possible. Ground and spacecraft operations involved in the retargeting maneuvers are essentially the same as in Pioneer F and G midcourse corrections. A reorientation of the spacecraft is generally called for, so as to permit using the main axial thruster in providing the velocity increment in the desired direction. However, in some cases (which would have to be selected for this reason unless they occur fortuitously) reorientation is not necessary if the

required velocity increment  $\Delta V$  points essentially radially toward earth. This would be the case (1) if the next asteroid will have to be intercepted at a location inside the current spacecraft trajectory, and (2) if out-of-plane components of the earth vector and the trajectory change are properly matched. At most, two reorientations will be required during a mission, one for each retargeting maneuver; they occur under conditions where timing of the subsequent telemetry reacquisition is not critical.

Figure 4-18 shows the schedule of principal events near the encounter. A logarithmic scale is used to cover the range from 10 million km when encounter preparations must be started, through the closest approach point, at 100 km from the asteroid, to the start of retargeting operations for the next encounter.

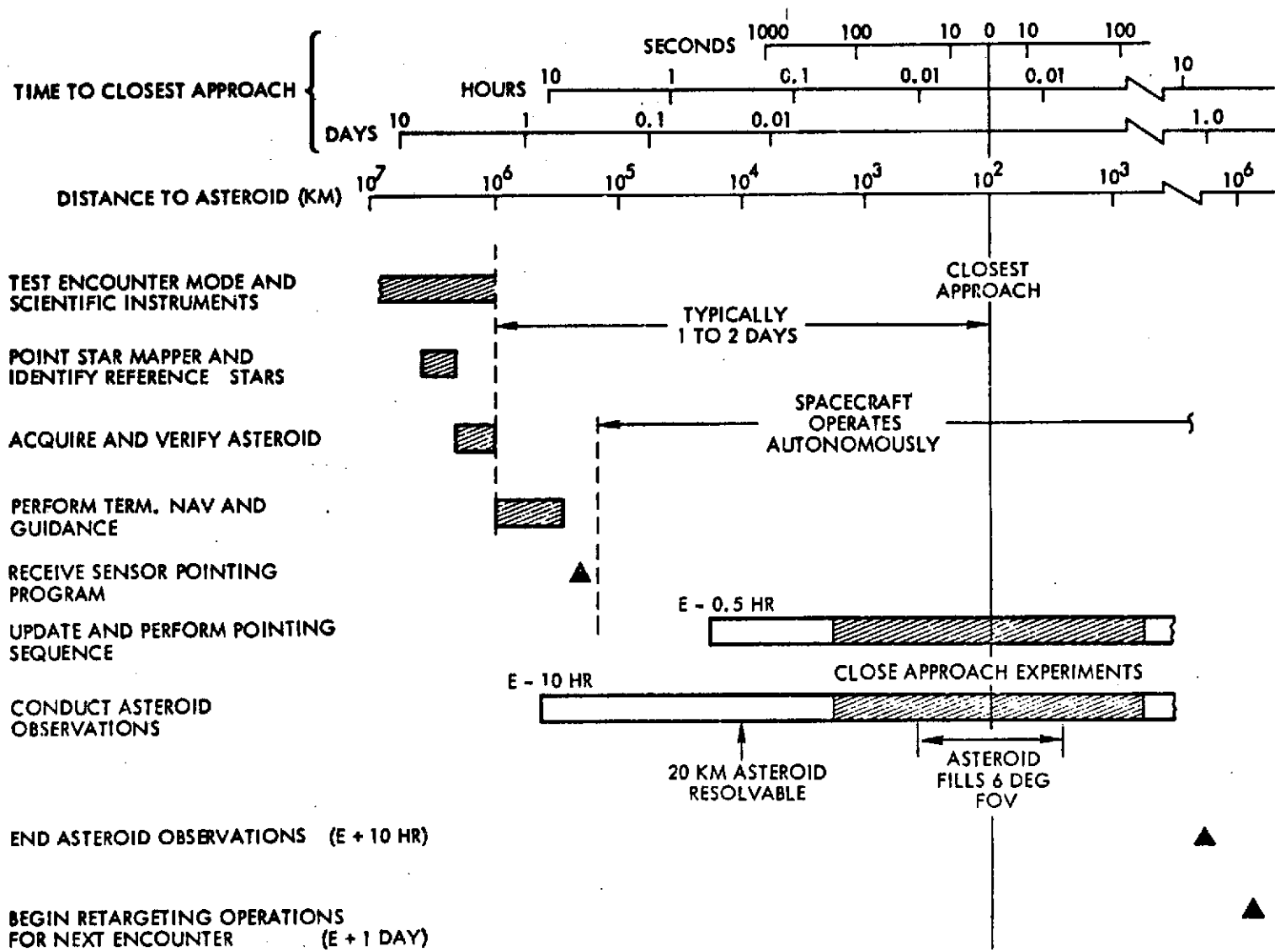
Because of the rapid succession of events in the immediate vicinity of the asteroid and their timing uncertainty, the spacecraft must use its own autonomous command program for about 1 to 2 hours, updated as required, rather than rely on ground commands during that period. Regarding pre-encounter preparation (e. g., terminal maneuvers) that must be performed at least 12 hours before the flyby event, ground commands are necessary because of the required computations that greatly exceed onboard capabilities. The 40 to 60 minute delay in spacecraft-to-earth communications imposes appreciable constraints on the timing of these functions.

Thus, in planning the detailed schedule of events for the multi-asteroid mission, careful attention must be given to this timing problem, the allocation of command functions to ground control and autonomous spacecraft control, and the requirement for onboard data processing.

## 4.7 COMBINED ASTEROID/COMET FLYBY MISSIONS

### 4.7.1 Trajectories

Numerous possibilities exist for missions which include a comet flyby and two or more asteroid flybys (Reference 1-6). Indeed several of these missions require total spacecraft  $\Delta V$  capabilities comparable to those considered for the multi-asteroid mission, i. e., 800 to 900 m/sec. The launch energy is under  $C_3 = 60 \text{ km}^2/\text{sec}^2$ , compatible with the Atlas/Centaur/TE-364-4 injection capability for a 1000-pound spacecraft.



4-29

Figure 4-18. Main Event Sequence Near Encounter  
 (Closest Approach Distance 100 km; Time Scale for  $V_{rel} = 6$  km/sec)

NASA's Small Bodies Mission Advisory Panel has recommended this mission class as part of the proposed asteroid/comet research effort for this decade. (Reference 1-4.)

Two such missions are shown in Figure 4-19. At left is the trajectory of a mission to comet Forbes, launched in August 1977 with flyby of asteroids 49 and 192. The comet is encountered last: 989 days after launch. The retargeting  $\Delta V$  requirements of this mission are on the high side (1056 m/sec), but combination of Forbes with different asteroid targets reduces  $\Delta V$  to the 270 to 930 m/sec range.

At the right is the trajectory of a mission to comet Whipple. Asteroid 939 is encountered 160 days after launch, and Whipple 140 days later. The  $\Delta V$  expenditure thus far is 200 m/sec. With an additional expenditure of 400 m/sec one of several asteroids can be encountered within a year after passing the comet.

Preliminary study of the mission characteristics, terminal navigation and guidance requirements, and the comet flyby geometry shows that basically the modified multi-asteroid Pioneer spacecraft is compatible with this expanded mission type. Problems that require additional study include the augmentation of the payload complement for comet observation and the increase in weight, power, and data rate required for the extra payload instruments. It would be possible to perform two missions with partly different payload complements, emphasizing asteroid observation, in one case, and comet observation in the other.

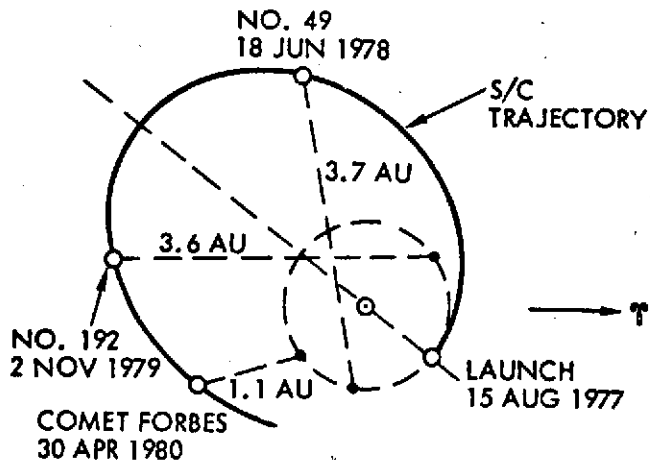
#### 4.7.2 Typical Comet Encounter Geometry

The relative motion of a comet encounter is fundamentally different from asteroid encounters because of the high eccentricity of the comet's orbit and the preference for performing the flyby as close to 1 AU as possible, on returning from the asteroid belt. Reasons for this preference are summarized as follows:

- a) Encounter late in mission, close to 1 AU, has these advantages:
  - Comet is active and bright
  - Simultaneous earth observation if facilitated

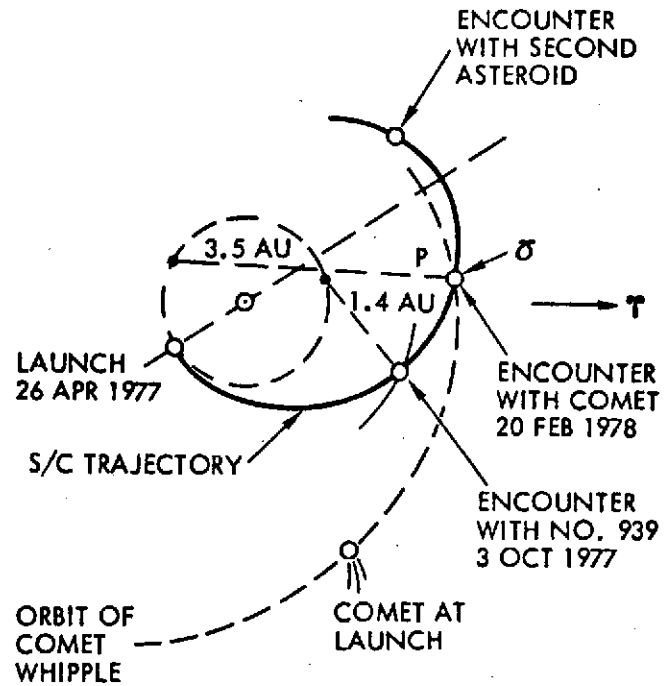
EXAMPLE 1\*

49 - 192 - FORBES  
LAUNCH IN AUGUST 1977



EXAMPLE 2

939 - WHIPPLE - 2ND ASTEROID  
LAUNCH IN APRIL 1977



\*Data from Brooks, Reference 3-2.

Figure 4-19. Combined Asteroid/Comet Flyby Missions

- Updated comet ephemeris simplifies terminal guidance
  - Acceptable hazard of comet dust impingement (last target in sequence)
- b) Encounter geometry permits coma/tail flythrough with possible close approach to nucleus, extended encounter time
  - c) Acquisition range about 10 times greater than for asteroid encounter
  - d) Repeated terminal maneuvers permit accurate close approach.

The most significant aspect of the encounter geometry (shown in Figure 4-20) is the nearly radial, outward pointing relative velocity which permits penetration of both coma and tail. If we assume a tail crossing angle of 10 degrees, a coma diameter of typically  $50 \times 10^3$  km and a tail width of  $10^3$  to  $10^4$  km, the exposure to the cometary environment typically lasts one to two hours even at the high-relative velocity of 15 km/sec. The nucleus may also be observable.

Since the apparent magnitude of the coma varies with the 4th power of solar distance the spacecraft navigation sensor can acquire the comet early in the approach phase and terminal guidance maneuvers are facilitated. For example, the 5th magnitude sensor adopted for the multi-asteroid flyby mission can acquire a 12th magnitude comet at a range of  $15 \times 10^6$  km, if the solar distance is 1.5 AU, this range being about ten times larger than for an asteroid of the same magnitude.

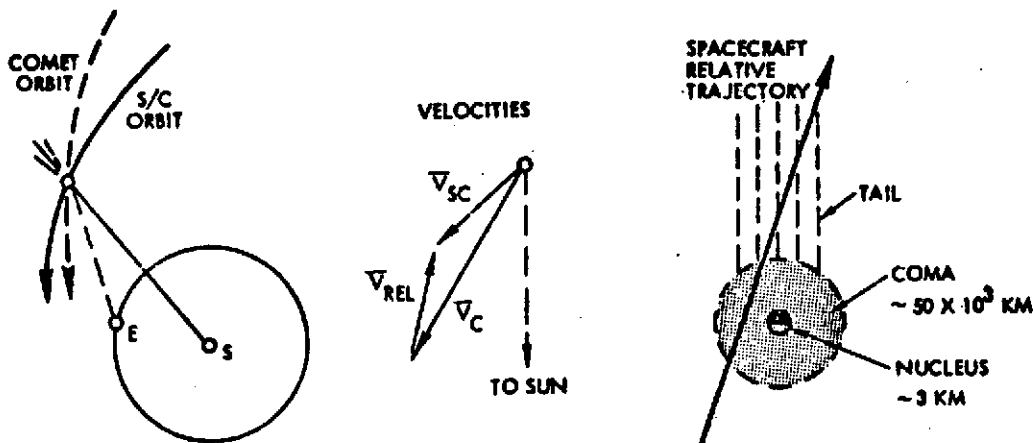


Figure 4-20. Typical Comet Encounter Geometry

## 5. TERMINAL NAVIGATION AND GUIDANCE

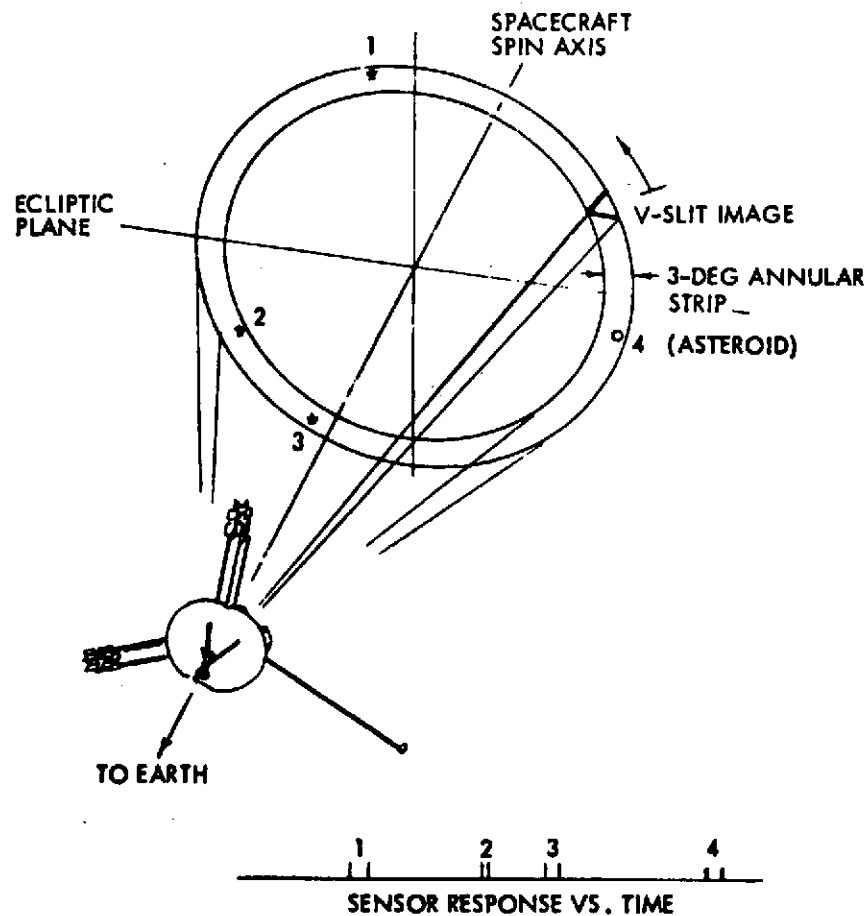
### 5.1 TERMINAL NAVIGATION CONCEPT

Accurate terminal navigation is essential for achieving the very small offset distance at asteroid flyby that is dictated by scientific objectives. An onboard target sensor is required for this purpose since the exact location of the asteroid is not sufficiently well known in advance to permit accurate command guidance by the conventional method, based entirely on radio-tracking of the spacecraft from earth. The a priori uncertainty of the miss distance is dominated by the asteroid ephemeris error that can amount to thousands of kilometers even with the most refined asteroid orbit determination methods.

The feasibility of precise terminal navigation with the aid of an onboard optical sensor has been demonstrated for a three-axis controlled spacecraft by the Mariner 9 and earlier Mariner flights (References 5-1 and 5-2).

The terminal navigation concept proposed for the asteroid flyby mission uses a scanning star sensor that is compatible with the spinning Pioneer spacecraft. This is illustrated in Figure 5-1. The star scanner detects the asteroid and determines its location relative to selected reference stars. As the sensor field of view scans an annular region of the celestial sphere, images of the stars and the asteroid pass the slits of a V-shaped reticle located at the focal plane, and are detected by a photomultiplier. A sequence of pulse pairs is thus generated, as illustrated at the bottom of Figure 5-1. The timing of these pulses indicates the position of the asteroid relative to the reference stars. The mean time and the pulse separation of each pair give the clock and cone angles of the object, respectively. The sensor is gimballed so that the angle of the optical axis to the spacecraft spin axis can be adjusted to include the target in the 3-degree annulus. Interpretation of the pulse sequence permits:

- Identification of the reference stars
- Verification of the asteroid after it is detected by the sensor



TYPICAL INSTRUMENT CONFIGURATION

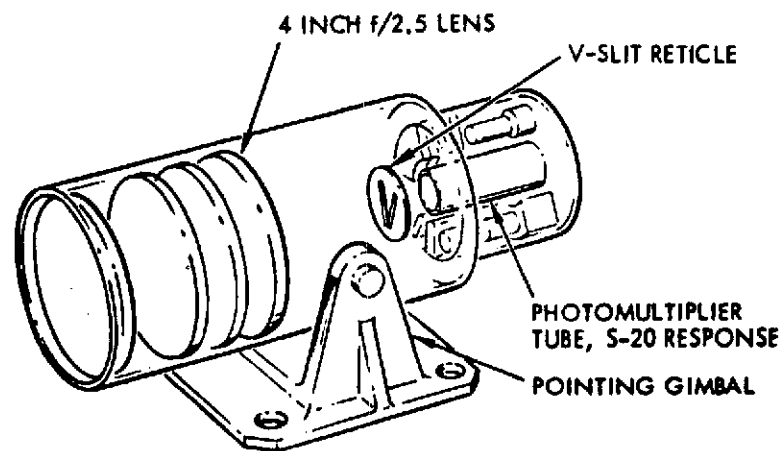


Figure 5-1. Terminal Navigation Sensor and Operational Concept

- Determination of the target's clock and cone angles
- Compensation for uncertainty in spin axis orientation and gimbal angle.

This terminal navigation sensor has been previously proposed and analyzed for advanced Pioneer applications where precision planetary guidance is essential (References 5-3, 5-4, and 5-5). Several versions of the instrument have been developed and tested (References 5-6 and 5-7). If requirements on detection sensitivity and angular precision of the instrument are held to a reasonable level problems of a major new technology development can be avoided.

The block diagram shown in Figure 5-2 defines the functions of terminal navigation and guidance that are assigned to the spacecraft and the ground facility. To minimize the complexity of onboard operations the signals generated by the star scanner are telemetered to the ground for processing and interpretation. The spacecraft only acquires the data and executes guidance maneuvers as commanded from the ground. The ground facility automatically

- Screens the incoming star sensor signals and identifies the reference stars
- Detects and verifies the asteroid by its time-varying brightness and parallax
- Performs orbit determination and updates the position and velocity of the spacecraft relative to the asteroid, using the optical sensor data in combination with radio tracking data and earth-based telescope asteroid observations
- Determines desired trajectory corrections, and
- Transmits maneuver commands to the spacecraft.

The last three steps in this procedure are repeated several times to acquire additional navigational fixes, update the relative spacecraft position, and perform additional maneuvers as required. In this manner gross trajectory errors can be corrected as early as possible to conserve propellant. Residual errors are corrected subsequently as navigational data of higher accuracy are obtained closer to the target. Thus, even

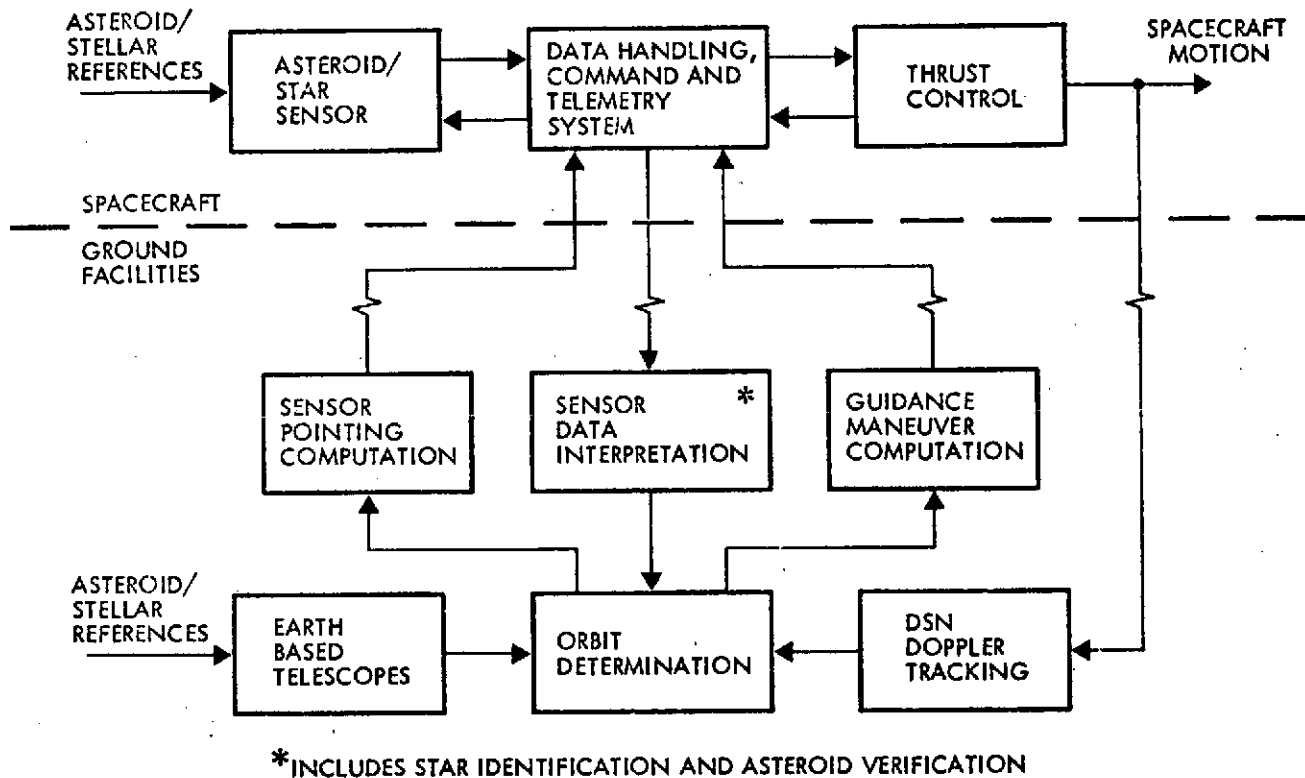


Figure 5-2. Navigation and Guidance Functional Block Diagram

with modest angular resolution a high terminal accuracy can be achieved. Theoretically, a trajectory error of the order of 10 km can be detected at a range of  $10^5$  km by a sensor of 0.1 mrad resolution, and corrected by a trim maneuver of only 1 m/sec. In practice the results are not quite so favorable since the time for repeated navigation fixes, orbit determination, and command signal transmission become more significant close to the asteroid encounter. Typically, the communication delay is 40 to 60 minutes. This means that guidance iterations must be discontinued about 3 to 6 hours before encounter when the spacecraft is still at a range of 75 to 150 thousand km from the target.

Time losses during this critical pre-encounter phase must be minimized, in general, so as to complete the required maneuvers as early as possible and to minimize the  $\Delta V$  expenditure. The navigation and guidance operations can be expedited and time losses minimized as follows:

- 1) The star scanner is commanded to point in the desired direction well in advance of the predicted asteroid acquisition time. This permits identification of reference stars in the annular region scanned by the sensor, ahead of time, and speeds up the subsequent determination of the asteroid's relative position.
- 2) Ground-based data interpretation, orbit determination and guidance command computations are fully automated to minimize the turnaround time between acquisition of navigational fixes and guidance maneuver execution.
- 3) The guidance maneuvers are executed without a spacecraft reorientation.
- 4) Thrust times are shortened by providing sufficiently large thrust levels for axial and radial thrusters. E. g., a 50 m/sec maneuver can be performed in less than one hour by a pair of 1 lbf radial thrusters on a 1000-pound spacecraft, assuming a 25 percent duty cycle (90-degree firing arc).
- 5) Nutation effects caused by perturbing torques due to thruster misalignment are minimized. Thus, the time required for residual wobble to damp out after each maneuver can be reduced to less than 1/2 hour and a significant time lapse before the next navigational fix can be avoided.

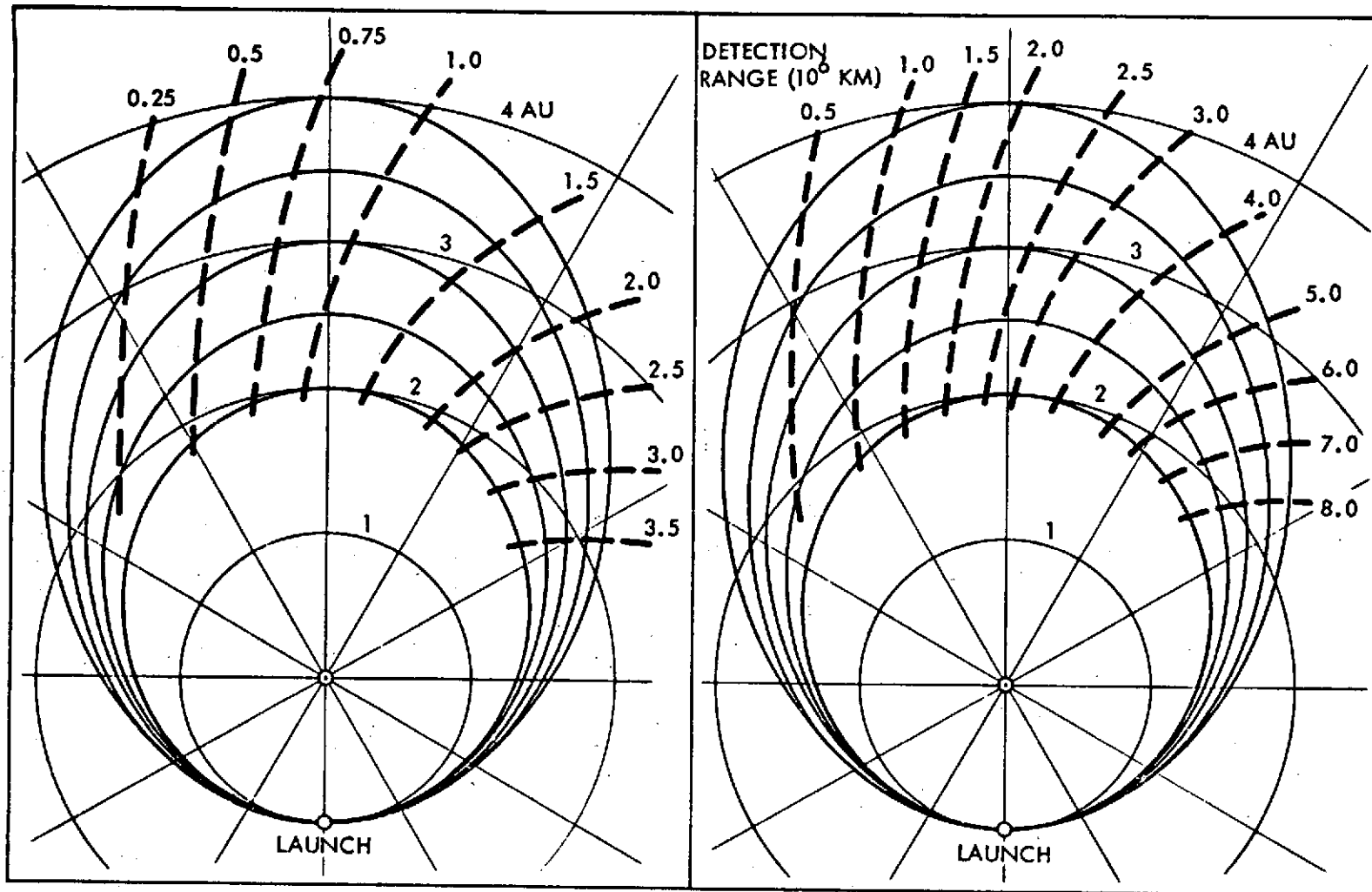
The design and operating characteristics of the terminal navigation sensor determine the accuracy, propellant requirements, and success probability of terminal approach guidance for each encounter. Early target acquisition achievable by a sensor with high detection sensitivity reduces  $\Delta V$  requirements, but increases the weight, complexity, and cost of the system and the effort of data handling, telemetry, processing, and interpretation on the ground. The sensor characteristics also impose constraints on mission selection by determining limits on target size (or brightness) and intercept locations, as previously discussed, i. e., with a less sophisticated sensor the number of available mission options is reduced. These tradeoffs have been investigated and will be discussed in the following subsections.

## 5.2 ASTEROID ACQUISITION RANGE AND LIMITS OF INTERCEPT LOCATIONS

Figure 5-3 shows plots of typical acquisition ranges for asteroids of 12th magnitude if the detection threshold of the navigation sensor is  $M_V = 5$  (left diagram) and  $M_V = 7$  (right diagram). Contours of constant acquisition range, in millions of km, are plotted across spacecraft trajectories through the asteroid belt. Because of unfavorable viewing angles in the second half of the trajectory, i. e., after the aphelion passage, the detection range can become critically short, as previously explained in Section 4 (see Figures 4-6 and 4-7). Note that the time to encounter for a detection range of 0.75 million km in the vicinity of aphelion is about two days because of the small closing velocity of 5 to 6 km/sec. Later in the mission, with the closing velocity increasing to 8 or 10 km/sec, the same detection range only leaves about one day to encounter.

In addition to the  $M_A$  and  $M_V$  examples listed in Figure 5-3, the plots also apply to other combinations of asteroid magnitude and sensor threshold. As was discussed in Section 4.3, the parameter that governs the detection range is the magnitude difference,  $M_A - M_V$ . The more severe case at left is for a magnitude difference of seven. The illustration at the right is for a magnitude difference of five. Since the apparent asteroid magnitude changes by -1 if the range is reduced by 37 percent, and by +1 if the asteroid is 58 percent further away, additional acquisition range contours can be derived readily from those shown.

These detection range contours define limits of intercept locations where  $\Delta V$  requirements for terminal guidance maneuvers can become excessively large. For example, at 1 million km range the correction of a 5000 km trajectory error requires a velocity increment of 50 m/sec if the relative velocity is 10 km/sec. In the left plot the 0.75 million km contour, in the right plot the 1 million km contour, roughly define the boundary of reasonable  $\Delta V$  requirements.



ASTEROID MAGNITUDE  $M_A = 12$

SENSOR THRESHOLD  $M_V = 5$

$$M_A - M_V = 7$$

$M_A = 12$

$M_V = 7$

$$M_A - M_V = 5$$

Figure 5-3. Typical Asteroid Detection Ranges

### 5.3 TERMINAL ACQUISITION AND MANEUVER REQUIREMENTS

Figure 5-4 provides a convenient graphical aid for preliminary assessment of terminal navigation and guidance requirements under given encounter conditions. The diagonals in the diagram are lines of constant ratios of offset distance to range. The maneuver required to correct a given offset error  $\Delta X$  at the range  $R$  is

$$\Delta V = \frac{\Delta X}{R} V_{rel}$$

where  $V_{rel}$  is the relative velocity. The parameter values at the top of the diagonal lines indicate the  $\Delta V$  required for this correction. An upper limit shows conditions where the  $\Delta V$  requirements becomes unreasonably large.

In addition to  $\Delta V$  the diagonals also define the error angle  $\Delta\theta$  subtended at the spacecraft by the offset error  $\Delta X$  since

$$\Delta\theta = \frac{\Delta X}{R}$$

The parameter values inscribed at the bottom of the diagonal lines give the offset error angle that can be detected by a navigation sensor of specified resolution. A lower limit of 0.1 milliradians is indicated in the diagram.

Use of the chart is illustrated for the case of a two-stage terminal maneuver. At a range of  $2.5 \times 10^6$  km a maneuver of 20 m/sec would be required to correct an initial offset distance of 5000 km if the relative velocity is 10 km/sec. A residual offset of 250 km due to the 0.1 millirad error detection threshold is corrected by a second maneuver, requiring 5 m/sec at the range of  $5 \times 10^5$  km, with a residual error of 50 km. These  $\Delta V$  requirements change proportionally with relative velocity, and can be conveniently rescaled from the 10 km/sec reference value if the velocity is different. When used in this manner the chart permits the construction of optimal guidance maneuver iterations given an initial offset and acquisition range and the desired terminal accuracy. Optimal maneuver iterations have been investigated by Pfeiffer and Curkendall (Reference 5-8) using a similar approach.

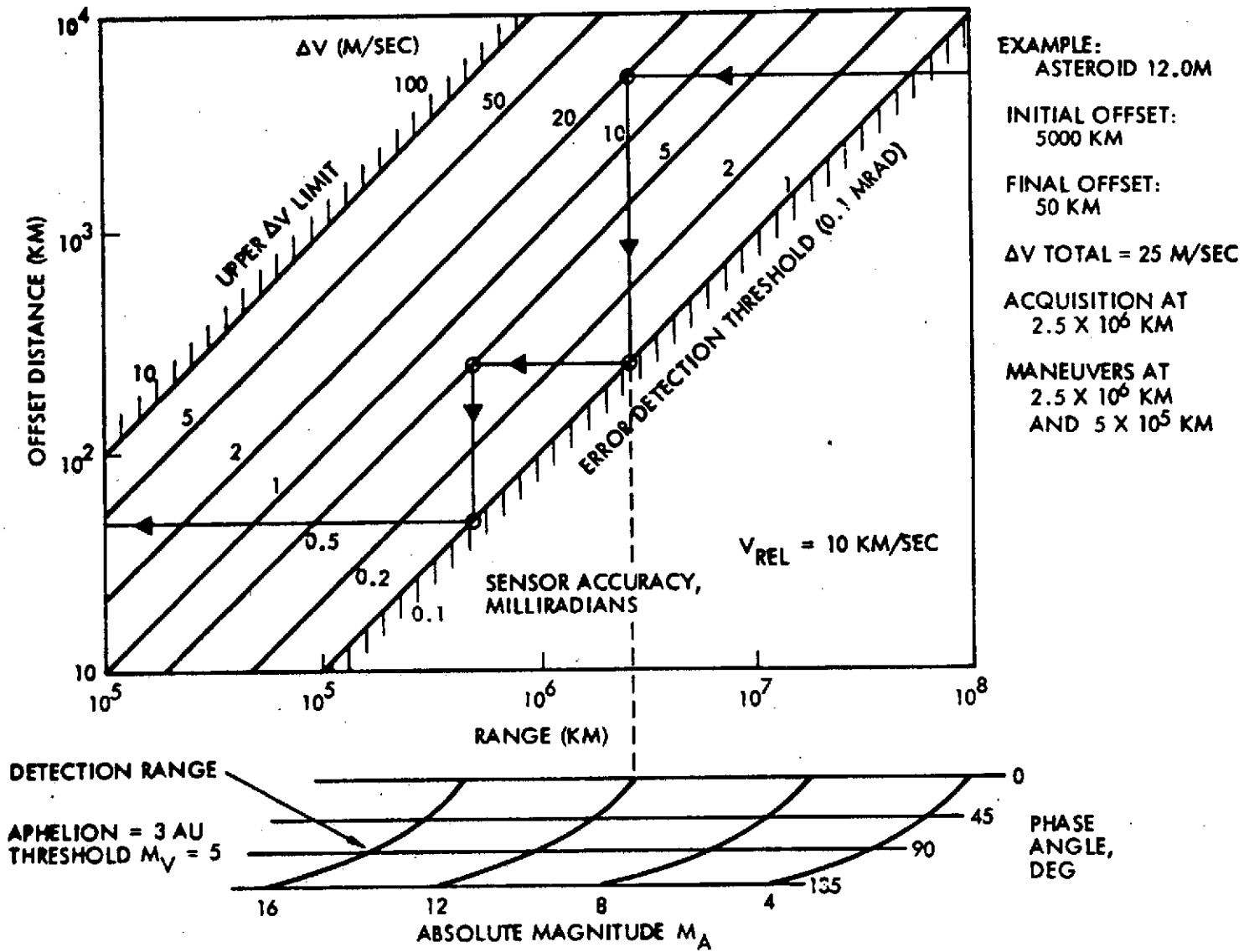


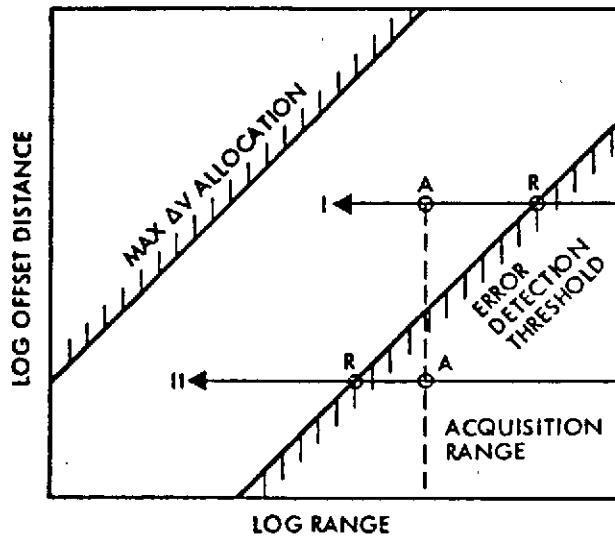
Figure 5-4. Terminal Acquisition and Guidance Maneuver Diagram

The chart at the bottom of Figure 5-4 gives the detection range as function of phase angle and asteroid magnitude, based on the results developed in Section 4 (Figure 4-7). In the example illustrated the 2.5 million km detection range corresponds to an asteroid of 12th magnitude at zero phase, or 8th magnitude at nearly 135 degree phase. An aphelion of 3 AU and a sensor detection threshold of 5th magnitude is assumed. This diagram can also be rescaled conveniently if desired, by using data from Figure 4-7.

Inherent in the use of this graphical technique is the simplifying assumption that maneuvers are performed immediately at the time of asteroid acquisition and without execution errors. A delay of two hours would correspond to a distance of 72 thousand km downrange, and result in a small increase of  $\Delta V$  requirements if the acquisition range is greater than 1 million km. The graphical results can be easily corrected to account for time delays. The accuracy of this graphical analysis is acceptable for preliminary guidance studies as was found by comparison of results with those from actual guidance computations.

The effect of acquisition range limits and resolution accuracy of a given navigation sensor can be examined conveniently by the same diagram as illustrated schematically in Figure 5-5 for two typical cases. The upper horizontal line (Case I) shows the situation where terminal maneuver initiation is delayed because of the acquisition range limit (A). The lower line (Case II) shows the situation where the delay is due the resolution limit (R) of the sensor. The acquisition range limit tends to increase the  $\Delta V$  requirement, particularly if the initial offset error is large. The error resolution limit mainly affects the terminal accuracy.

Figure 5-6 shows the influence of the detection threshold  $M_V$  on  $\Delta V$  and propellant weight  $W_{PR}$  requirements for terminal guidance maneuvers. The initial target offset is 5000 and 10,000 km and the desired terminal accuracy 50 km. The case that was illustrated in Figure 5-4 may serve as an example. (The encounter conditions are the same as those listed in Figure 5-4, and the maneuvers are performed in two or three stages.) The assumed asteroid magnitude is  $M_A = 12$ .



CASE I ACQUISITION RANGE LIMITED  
CASE II ERROR DETECTION LIMITED  
A = ACQUISITION  
R = ERROR RESOLUTION

Figure 5-5. Criteria for Selecting Terminal Sensor Sensitivity and Accuracy

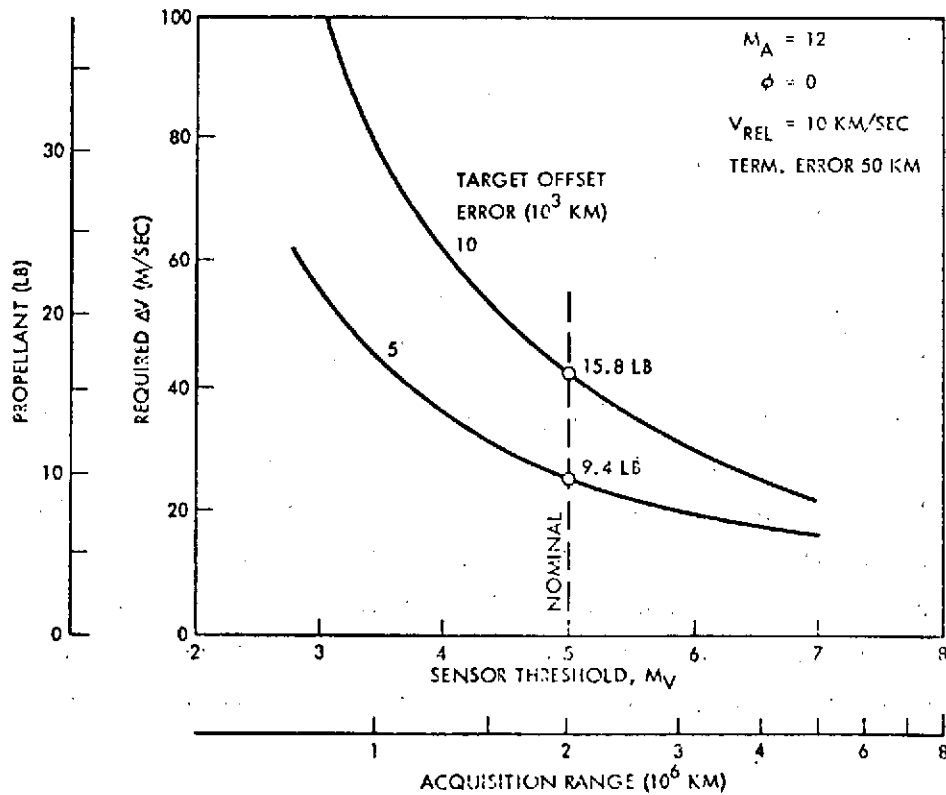


Figure 5-6. Maneuver Requirements Vs. Sensor Detection Threshold and Acquisition Range

The maneuver requirements decrease sharply with increasing threshold sensitivity and, hence, increased detection range. However, most of this reduction is achieved by changing  $M_V$  from 3 to 5. Further reductions in  $\Delta V$  and  $W_{PR}$  beyond  $M_V = 5$  are relatively small. For example, the propellant savings achieved by changing the sensitivity threshold from 5 to 6 are only 2.2 and 4.1 pounds for the cases of 5000 and 10,000 km initial offset, respectively, corresponding to  $\Delta V$ -changes of 6 and 11 m/sec. This shows that a navigation sensor of moderate sensitivity ( $M_V = 5$ ) is adequate under average encounter conditions while an increase in sensitivity would not save enough propellant to warrant the increased sensor complexity and cost. In fact the propellant weight saved is partly offset by a weight increase of the sensor and associated equipment. We note that the above results were obtained for a sensor resolution of 0.1 mrad. A higher resolution does not change the  $\Delta V$  requirement noticeably.

#### 5.4 ASTEROID POSITION UNCERTAINTY

In a recent article on asteroid ephemeris accuracy (Reference 5-9) Marsden states the fact that the position uncertainty of many numbered asteroids exceeds  $10^5$  km; however, only 35 percent of the nearly 700 asteroids surveyed in 1968-69 by the Crimean Observatory (USSR) have residuals of more than 3 arc min ( $2.3 \times 10^5$  km) in right ascension; 45 percent have less than 1.7 arc min ( $1.3 \times 10^5$  km). Marsden also suggests that by properly selecting a small number of asteroids as targets for future missions and refining their ephemeris, the uncertainty can probably be reduced to a few arc seconds (i. e., 1500 to 4500 km).

A concurrent study\* by P. Herget of the Cincinnati Observatory's Minor Planet Center has determined the best currently obtainable ephemerides for selected asteroids including those of the 1978 sample mission, Ceres (No. 1), Bertholda (No. 420), and Gaea (No. 1184).  $1\sigma$  position uncertainties of ten asteroids in heliocentric coordinates  $x$ ,  $y$ ,  $z$ , and the corresponding RSS-values  $\sigma_r$  are quoted here from Reference 1-6 (see Table 5-1). Herget has indicated that the worst of these values

---

\*Sponsored by NASA, Langley Research Center.

could be reduced by a factor of 2 or 3 by more extensive analysis of existing observations, but that reductions by more than a factor of 5 are not feasible even with an intensive observational campaign started two or three years prior to an actual mission.

Interpreting these results in terms of required terminal navigation and guidance capabilities we conclude that an a priori miss uncertainty of  $5 \times 10^3$  km ( $3\sigma$ ) for reasonably selected target asteroids is probably a conservative estimate. The examples presented in Section 5.3 and those to follow in Section 5.5 show that a  $\Delta V$ -capability of 50 m/sec allocated for terminal guidance in each of the encounters should be adequate to meet mission requirements allowing that in a three-target mission some asteroids may require significantly less than that amount.

Table 5-1.  $1\sigma$  Ephemeris Uncertainties of Ten Selected Asteroids

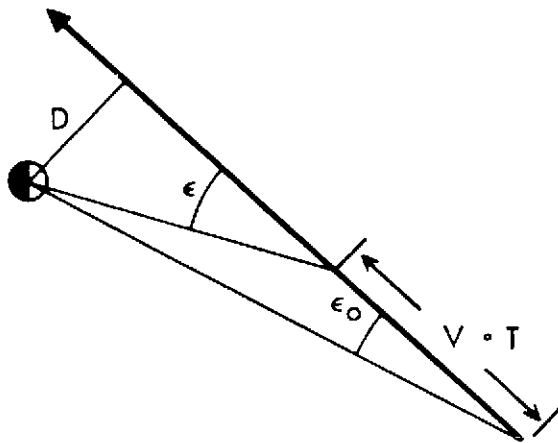
ASTEROID	JULIAN DATE 244XXXX.5	$1\sigma$ UNCERTAINTIES				
		$\sigma_X$	$\sigma_Y$	$\sigma_Z$	$\sigma_R$	
1 CERES	4502	320	57	100	340	} USED IN SAMPLE MULTI-ASTEROID MISSION
1184 GAEA	3903	956	2606	1968	3400	
420 BERTHOLDA	4222	1000	972	778	1598	
49 PALES	3680	1305	469	600	1511	} USED IN ASTEROID/COMET MISSION OPTIONS
300 GERALDINA	3938	1678	1692	1416	2772	
609 FULVIA	4115	2852	5574	3880	7366	
192 NAUSIKAA	4178	513	1248	1078	1727	
303 JOSEPHINA	4107	2498	4660	3565	6377	
327 COLUMBIA	4199	789	1990	1619	2684	
592 BATHSEBA	4126	1492	3080	1736	3837	

FROM REFERENCE 1-6, BASED ON A CURRENT STUDY BY P. HERGET, CINCINNATI OBSERVATORY MINOR PLANET CENTER.

## 5.5 ILLUSTRATIVE TERMINAL GUIDANCE EXAMPLES

Examples of alternate implementations of terminal navigation and guidance are given in this section to illustrate differences in maneuver requirements and terminal accuracy.

Figure 5-7 describes the principle of acquiring navigational fixes by repeated triangulation. The equation given in the diagram defines the offset distance  $D$  in terms of the observation angles  $\epsilon$  and  $\epsilon_0$  and the



$$D = V \cdot T \frac{\sin \epsilon \sin \epsilon_0}{\sin (\epsilon - \epsilon_0)}$$

Figure 5-7. Navigation by Simple Two-Point Triangulation

determine the offset distance D.

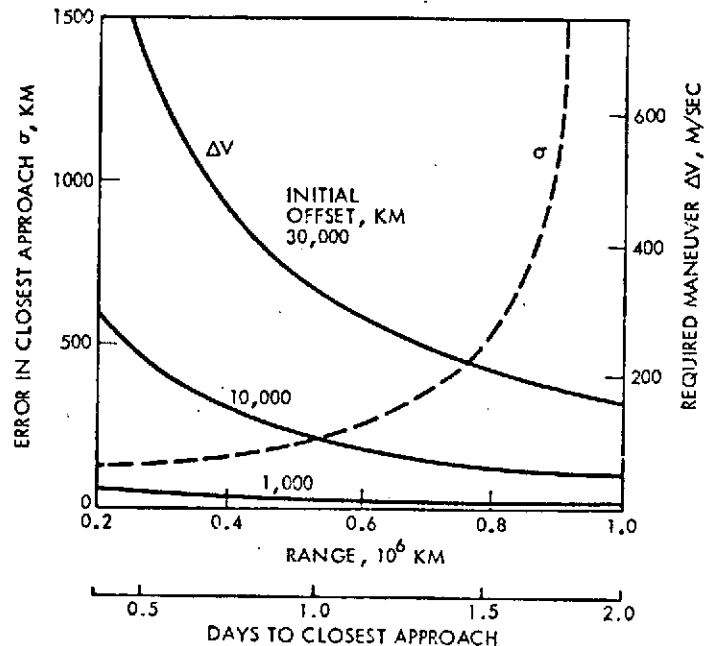
Figure 5-8 shows the terminal navigation accuracy obtainable by a simple two-point navigational fix, and the  $\Delta V$  requirements for correcting the target offset by a single maneuver that is performed at the completion of the navigation fix, i. e. , at a time interval T after initial target acquisition. The results are plotted as functions of the distance and time from the point of closest approach at the time of maneuver execution. Velocity requirements are too high for practical purposes since the maneuver must be delayed too long in order to reduce the miss uncertainty. The  $\Delta V$  requirement is proportional to the offset distance to be corrected and can be as large as several hundred m/sec under the conditions assumed in this example.

Two obvious improvements are indicated:

- 1) Use of least squares optimization to reduce the navigational error for a given sensor accuracy
- 2) Use of repeated terminal maneuvers to permit early correction of a large fraction of the initial offset error when the maneuver is still reasonably inexpensive, followed by trim maneuvers as accuracy of navigational fixes improves.

distance  $V \cdot T$  traveled between observations where V is the velocity and T the time interval. The method is simple but requires an appreciable time interval between observations to obtain a sufficiently large angular difference  $\epsilon - \epsilon_0$  for an accurate determination of D in the presence of sensor errors  $\delta\epsilon$ .

The accuracy of navigation fixes can be improved and the required time interval reduced for a given sensor error if a least squares computing technique is used to



ASSUMPTIONS	
APPROACH TO CERES AT $V = 6$ KM/SEC	VELOCITY ERROR 3 M/SEC
ACQUISITION AT $10^6$ KM	SENSOR ACCURACY 0.1 MILLIRAD
SOLAR DISTANCE 2.8 KM	SINGLE NAVIGATION FIX (2 OBSERVATIONS)

Figure 5-8. Upper Limit of Navigation Error and Maneuver  $\Delta V$

With these improvements in navigation and guidance technique much more satisfactory results are obtained as illustrated by the results given in Table 5-2, for an initial target offset of 10,000 km. For a sensor error of 0.1 mrad the terminal miss is between 30 and 50 km ( $1\sigma$ ) and the total  $\Delta V$  requirement for two or three iterated maneuvers is about 50 or 100 m/sec depending on whether initial acquisition occurs at 1 million or one-half a million km. If the sensor error is increased to 0.5 mrad the terminal miss becomes 134 and 237 km, respectively, while the  $\Delta V$  requirements are essentially the same as in the case of the 0.1 mrad sensor error. The assumed encounter conditions and guidance characteristics are listed at the bottom of the table. The tabulated results also provide a verification of the guidance requirements that can be derived by graphical analysis using the terminal maneuver diagram, Figure 5-4.

Table 5-3 gives maneuver allocations and  $1\sigma$  terminal errors for the three encounters of the 1978 sample mission, using a 5th magnitude sensor

Table 5-2. Examples of Terminal Maneuver Requirements and Accuracy

CONDITIONS ASSUMED		NO. OF MANEUVERS	MANEUVER TIMING (HR)	MANEUVER ΔV (CUMULATIVE)		TERMINAL MISS STANDARD DEVIATION (KM)
R (10 <sup>6</sup> KM)	σ <sub>SENSOR</sub> (MILLIRAD)			MEAN (M/SEC)	STANDARD DEVIATION (M/SEC)	
1.0	0.1	3	46.0 43.0 26.6	48.9	1.3	30.5
1.0	0.5	3	46.0 43.0 23.8	51.8	1.3	134
0.5	0.1	2	22.8 20.4	97.4	5.4	49.4
0.5	0.5	2	22.88 20.1	99.5	5.4	237

ASSUMPTIONS: INITIAL UNCERTAINTY: 10,000 KM  
 RELATIVE VELOCITY: 6 KM/SEC  
 TIME BETWEEN MEASUREMENTS: 10<sup>3</sup> SEC  
 FINAL MANEUVER TO OCCUR NO LATER THAN 10 HOURS BEFORE ENCOUNTER  
 EXECUTION ERRORS (1σ), PROPORTIONAL: 0.01  
 BIAS ERROR: 0.1 M/SEC

Table 5-3. Terminal Maneuver Allocations in Sample Mission

SENSOR DETECTION THRESHOLD: M<sub>V</sub> = 5, SENSOR RESOLUTION (1σ): ε = 0.1 MILLIRAD

TARGET ASTEROID	3σ- POSITION UNCERTAINTY (10 <sup>3</sup> KM)	ACQUISITION RANGE (10 <sup>6</sup> KM)	IDEALIZED TERMINAL MANEUVERS			ΣΔV <sub>i</sub> (M/SEC)	ΣΔV' <sub>i</sub> (M/SEC)	TERMINAL ERROR (1σ) (KM)
			1	2	3			
NO. 1184 GAEA	10.3	2.2	46.0	4.6	2.4	53.0*	69.0*	20
NO. 420 BERTHOLDA	4.8	3.0	8.4	2.8	2.8	14.0	18.2	12
NO. 1 CERES	0.7	7.5	5.6	3.0	1.7	10.3	13.4	19
ΔV' <sub>TOTAL 1</sub> = 100.6 M/SEC ΔV' <sub>TOTAL 2</sub> = 125.2 M/SEC ADJUSTED FOR 3σ ERROR IN NAVIGATION SENSOR								

NOTE: \*IDEAL ΔV<sub>i</sub>: MANEUVERS PERFORMED INSTANTLY, WITHOUT EXECUTION ERROR  
 ACTUAL MANEUVERS (ΔV'<sub>i</sub>) ASSUMED 30 PERCENT LARGER THAN IDEAL ΔV<sub>i</sub>

detection threshold and 0.1 mrad resolution. In each case three iterated maneuvers are carried out to minimize total  $\Delta V$  requirements. Acquisition ranges are 2.2 million km for the smallest asteroid (1184), 3 million km for the intermediate (420), and 7.5 million km for the largest asteroid (1). Maneuver allocations range from 69 m/sec for the worst case to 13.4 m/sec for the least demanding case. The total allocation for the mission is increased to 125.2 m/sec to account for (1) the non-ideal execution of maneuvers, and (2) the effect of  $3\sigma$  sensor resolution errors. Note that these results were obtained by the graphical analysis technique, with a precision of the order of five percent.

## 5.6 TERMINAL NAVIGATION SENSOR DESIGN CHARACTERISTICS AND ERROR SOURCES

### 5.6.1 Design Characteristics

Figure 5-9 illustrates the star scanner principle of operation. At the top is a functional block diagram of the detection process. The lower half shows the operation of the V-slit reticle and waveforms generated by the photomultiplier detector and by the bandpass filter that processes the photomultiplier output. The pulse pair which is generated by detection of the asteroid or star image as it passes through the reticle slits provides the desired clock and cone angle information as indicated on the waveforms. The filtered output pulses are shaped to give a more precise detection of the time at which the image crosses the two slits than the original pulses generated by the photomultiplier independent of pulse amplitude.

To minimize the effect of sky background on the detection process the dimensions of the reticle slits must be made as small as possible. The slit length is dictated by the desired field of view which must be sufficiently large to acquire at least three reference stars in scanning the celestial sphere. With a 3-degree field of view the annular region being scanned at a half cone angle of 22.5 degrees is 429 degrees<sup>2</sup>. The average number of stars of 5th magnitude or brighter varies from 0.01 near the galactic pole to 0.1 at the galactic equator. Thus, at least four stars are available near the pole and 11 near the galactic equator. There is enough margin for acquiring enough reference stars at smaller half cone angles even in the case where part of the scan cycle is close to the galactic pole.

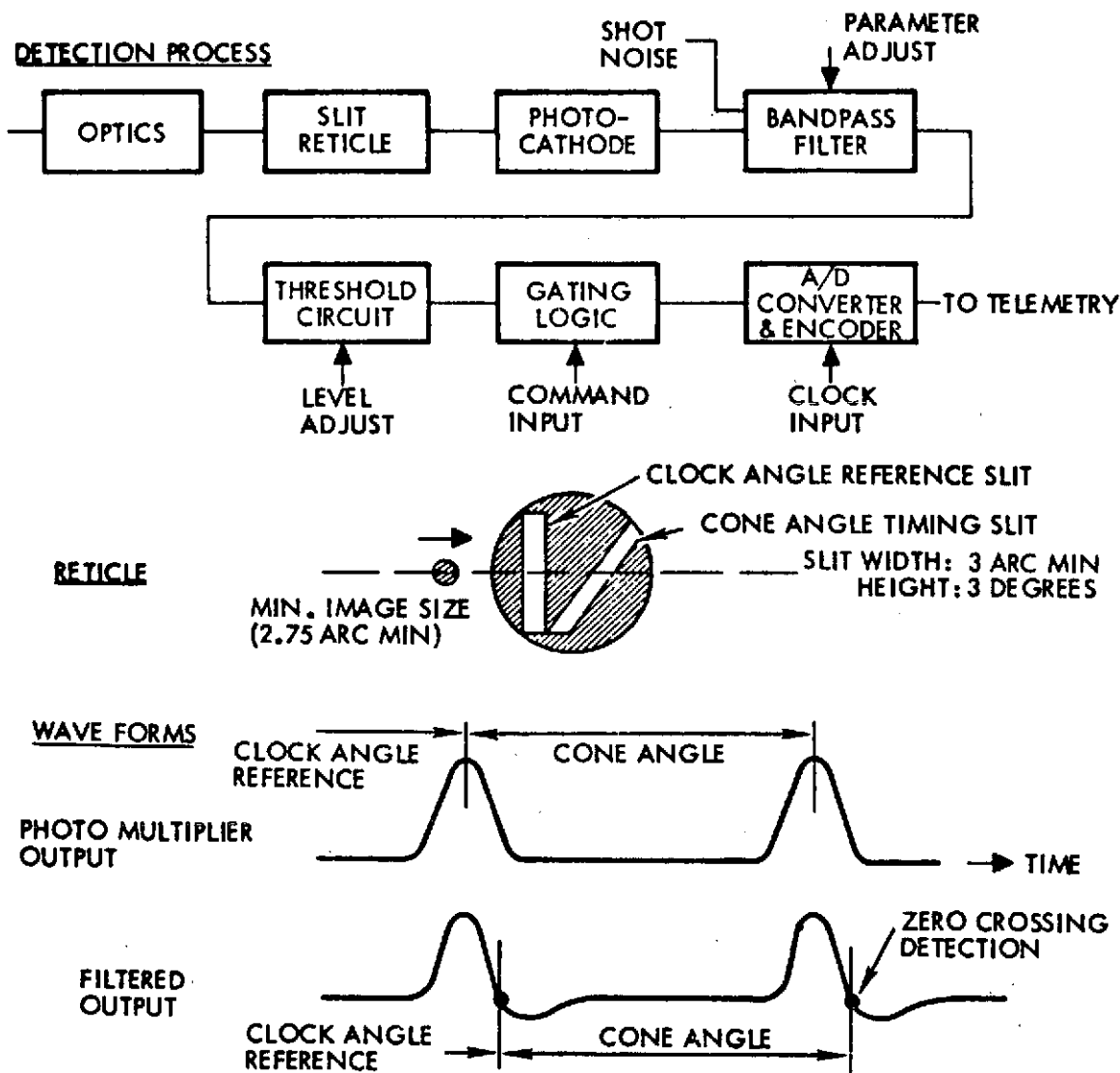


Figure 5-9. Star Mapper Principle of Operation

The slit width selected in the proposed design is 3 arc min. This reduces the sky background effect without decreasing the passage time of the asteroid and star images below the limit of adequate signal strength. The optical characteristics and detector circuits selected in the proposed star sensor design give a signal-to-noise ratio of at least 10:1 for a slit width of 3 arc min and a minimum image crossing time of 1.73 m/sec at the 5 rpm spin rate.

Table 5-4 summarizes the sensor design characteristics. A 4-inch diameter lens of super-Farron quality with 3.48 inches focal length has been selected. The wide aperture is required to assure

detection of 5th magnitude objects while the short focal length is dictated by the dimensions of the photocathode and the desired width of the annular region (3 degrees) to be scanned on the celestial sphere. The geometry of the V-slit reticle requires a 4.2-degree field of view to accommodate a reticle of 3-degree slit height.

A short overall dimension of the instrument is desired for convenient mounting on the side of the spacecraft equipment bay with gimballed reorientation capability covering cone angles from 60 to 165 degrees (as measured from the earth line-of-sight). Although the optics of the instrument would not be exposed to direct sunlight under most encounter conditions, being shaded by the antenna dish, a light shade of 12-inch maximum length is needed to protect the instrument against reflected light from nearby appendages, namely the RTG support structure and magnetometer boom.

Table 5-4. Sensor Characteristics

OPTICAL SYSTEM	OPERATION
<p><u>LENS DIAMETER:</u> 4 INCHES (~10 CM)  <u>FOCAL LENGTH:</u> 3.48 INCHES (8.8 CM)  <u>LENS TYPE:</u> SIMILAR TO SUPER-FARRON  <u>COLLECTING AREA:</u> 81 CM<sup>2</sup>  <u>TRANSMITTANCE:</u> 75% BETWEEN 3000 AND 8500 Å  <u>BLUR SPOT DIAMETER:</u> 2.76 ARC MIN AT 2° OFF AXIS  <u>FIELD OF VIEW:</u> 4.2 CIRCULAR  <u>RETICLE:</u> TWO SLITS - 3 ARC MIN WIDTH  3 DEGREE HEIGHT</p>	<p><u>GIMBAL RANGE:</u> 70° TO 165° CONE ANGLE  (FROM EARTH VECTOR)  <u>ZONE COVERAGE PER SPIN CYCLE:</u>  AT 22.5 DEGREE HALF-CONE ANGLE: 429 DEG<sup>2</sup>,  4 TO 11 STARS  AT 90 DEGREE HALF-CONE ANGLE: 1700 DEG<sup>2</sup>,  16 TO 44 STARS  <u>TELEMETRY:</u> 95 BITS PER SOURCE 380-760 BITS PER  SPIN CYCLE  (AVERAGE ~30 TO 60 BPS AT 5 RPM)  <u>OPERATION MODES:</u> a) NAVIGATION SENSOR  b) STELLAR REFERENCE  ASSEMBLY (ADJUSTABLE  THRESHOLD)</p>
<p>.....  <u>DETECTOR CIRCUIT</u></p>	<p>.....</p>
<p><u>PHOTOMULTIPLIER:</u> EMR 541E-01-14  S-20 SPECTRAL RESPONSE  <u>CURRENT GAIN:</u> 10<sup>6</sup> (2.67 EACH OF 14 DYNODES)  <u>SENSITIVITY THRESHOLD:</u> 5TH MAGNITUDE STARS  <u>SIGNAL-TO-NOISE RATIO:</u> &gt;10 FOR 5TH  MAGNITUDE STARS</p>	<p><u>RSS ERRORS:</u> CONE ANGLE 30-40 ARC SEC  CLOCK ANGLE 20-30 ARC SEC  .....  <u>ESTIMATED POWER AND SIZE</u>  <u>POWER:</u> 4 TO 5 WATTS  <u>WEIGHT:</u> 10 LBS (INCLUDES GIMBAL SYSTEM)  <u>VOLUME:</u> 6 X 6 X 14 INCHES (15 X 15 X 36 CM)</p>

### 5.6.2 Error Sources

An error analysis of the star sensor cone and clock angle measurements under typical encounter conditions has been performed and is summarized below. Since angle measurements are performed in terms of pulse time detection, any timing errors in the detection process are directly convertible into angular errors.

Error sources external to the sensor proper also contribute to the total error of navigational observations, unless compensated, including residual wobble of the spacecraft spin axis, uncertainty of the exact spin axis orientation with respect to the spacecraft center line, and inaccuracy of gimbal orientation. The last two error sources are detectable by interpretation of the star map generated during a spin cycle and can be compensated with the accuracy that is inherent in the angular resolution of the star sensor itself.

Results of the analysis are given in Table 5-5 to show the different effect that some of the error sources have on clock and cone angle measurements. The table also shows the changes in cone and clock angle errors due to variation of the sensor pointing angle with respect to the spin axis. Typical errors are listed for half-cone angles of 90 and 22.5 degrees.

Random jitter is seen to be a principal error source. This error source contributes the essential differences in the RSS values given at the bottom of the table. This is explained as follows. Small random variations occur in the time of zero crossing of the clock and cone angle pulses (Figure 5-9) as the result of superimposed shot noise. These variations affect the angle measurement as random jitter. The susceptibility of the measurement to this error source depends on pulse shape. For a pulse with a steep slope, or short rise and fall time, the time of zero crossing shows smaller variations due to jitter than for a pulse with longer rise and fall times. Comparing the cases of large and small cone angles of the sensor optical axis we find that the scan rate decreases with the cone angle, and the rise time increases. Hence, the increased error levels shown of Column 2 and 4 compared to Columns 1 and 3, respectively.

Table 5-5. Star Mapper Error Sources ( $1\sigma$ )

ERROR-SOURCE HALF-CONE ANGLE	CLOCK ANGLE ERROR (ARC SEC)		CONE ANGLE ERROR (ARC SEC)	
	90°	22.5°	90°	22.5°
1 RANDOM JITTER	11	18	19	31
2 SKY BACKGROUND	7	7	8	8
3 ELECTRONIC FILTER VARIATION	3	3	4	4
4 THRESHOLD CIRCUIT VARIATION	5	5	4	4
5 RETICLE GEOMETRY	3	3	3	3
6 THERMAL STABILITY	3	3	3	3
7 ALIGNMENT/CALIBRATION ERRORS	10	10	10	10
8 CLOCK STABILITY	1	1	1	1
9 OFFSET DUE TO FINITE IMAGE SIZE	15	15	15	15
RSS	23	27	28	37

Comparing the clock and cone angle detection process (Figure 5-9) we note that clock angles are detected when the star image crosses the radial slit, and cone angles when the image crosses the slanted slit of the reticle. Since the rise time of signal pulses increases with the slant angle, the cone angle measurements are more susceptible to random jitter than the clock angle measurements.

The RSS error values in Table 5-5 reflect the variations due to random jitter effect. In the most favorable case the RSS error is only 23 arc seconds but it increases to 37 arc seconds in the worst case shown. A change in half-cone angle to less than 22.5 degrees would further increase the total errors to values greater than 27 and 37 seconds in clock and cone angle, respectively. However, as can be seen from the analysis of encounter conditions (e. g., Figures 4-6 and 4-8) operation in that region of cone angles is generally not required.

Other significant error sources listed in the table are alignment/calibration errors (10 arc seconds) and offset due to finite image size (15 arc seconds). The effect of finite image size occurs only for measurements at relatively close range and can be corrected by accounting for the known image size of the target through a variable bias term introduced into the navigational computer program as required.

In summary, these results show that the sensor can meet the desired accuracy of navigational observation (0.1 mrad) under favorable operating conditions. Under extreme conditions, e. g., a small half-cone angle, the accuracy is degraded to 0.2 mrad which would reflect in terminal guidance errors of 20 to 30 km ( $1\sigma$ ) in cases where the iterated terminal guidance process must be discontinued as early as 100 to 150 km from the encounter because of high approach velocities. Under favorable conditions the sensor can achieve terminal accuracies of the order of 10 km according to the results presented earlier in this section.

Improvement of overall sensor accuracy to meet a 0.1 mrad error specification under all operating conditions would require considerable refinement in optical design and signal detection and processing techniques. This appears unwarranted by the results obtained in this study.

### 5.6.3 Operational Requirements

Principal operating modes of the star sensor and functional requirements and constraints that govern its application in various mission phases are briefly described in the following paragraphs.

- 1) Preparations for the asteroid acquisition and terminal navigation sequence are started at least two days in advance of the projected acquisition time. The sensor is pointed at the desired cone angle, and star data are transmitted to earth for identification and selection of reference stars. The exact aim point of the spin axis and the exact cone angle of the sensor's optical axis can be determined at this time.
- 2) Since a high-telemetry bit rate is available details of star and asteroid signals can be transmitted to the ground to expedite early asteroid detection and discriminate against

false alarms. Actually the probability of false alarms is extremely small under normal conditions ( $10^{-8}$ ) and is not of much concern in this application.

- 3) Under typical encounter conditions and for distances greater than 1 million km, the asteroid line-of-sight rotates at a rate of 0.3 to 0.6 degree per day. The position uncertainty of the asteroid reflects in a  $1\sigma$  error circle of less than 1 degree diameter.

Since the field of view is 3 degrees, resetting of the sensor cone angle is generally unnecessary during the initial acquisition and navigation phase. However, as target range decreases, a few reorientations of the sensor will be required; e. g., at  $10^5$  km range, the rotation rate is 5 to 10 degrees per day.

- 4) During navigational observations any residual spacecraft wobble must be held to less than 0.1 millirad. Precession maneuvers, to keep the high-gain antenna pointed at earth, are ruled out during that time. Such maneuvers can be performed before or after the navigation phase. At least one-half hour must be allowed after each guidance maneuver iteration before resuming navigational fixes, in order to let residual nutations subside below the 0.1 mrad level.
- 5) The instrument serves the dual function of navigation sensor and star reference assembly. During normal cruise operation the gimbal angle of the sensor is set to a selected reference star, e. g., Canopus, and adjusted periodically to follow the star's apparent motion. The same signal processing as in the navigation mode can be used to generate the roll reference signal, except the second star pulse is ignored. The threshold setting is raised to discriminate against stars fainter than the selected reference star.
- 6) The sensor cannot continue its nominal roll reference function during the time prior to asteroid encounter when navigational observations are required. However, an alternate roll reference can be selected from the reference stars used in the navigational mode. This requires a modification of onboard sequencing and data handling procedure.

## REFERENCES

- 5-1. T. C. Duxbury, G. H. Born, and N. Jerath, "Viewing Phobos and Deimos for Navigating Mariner 9," presented at AIAA/AAS Astrodynamics Conference, Palo Alto, California, September 11-12, 1972. AIAA Paper No. 72-927.
- 5-2. C. H. Acton Jr., "Processing On-Board Optical Data for Planetary Approach Navigation," presented at AIAA 10th Aerospace Sciences Meeting, San Diego, California, January 17-19, 1972, AIAA Paper No. 72-53.
- 5-3. Final Report: "Pioneer Outer Planets Missions," 16707-6001-R0-01, TRW Systems Group, Redondo Beach, California, July 13, 1970.
- 5-4. R. A. Park, K. R. Jenkin, and D. M. Layton, "Terminal Guidance Sensing from a Spinning Spacecraft," presented at the American Astronautical Society 17th Annual Meeting - The Outer Solar System, Seattle, Washington, June 28-30, 1971, Paper No. AAS-71-121.
- 5-5. Final Report: "Study to Adapt Solar Electric Propulsion to the Pioneer F and G Spacecraft," 22125-6001-R0-00, TRW Systems Group, Redondo Beach, California, October 15, 1972.
- 5-6. T. M. Walsh and Robert L. Kenimer, "Analysis of a Star-Field Mapping Technique for Use in Determining the Attitude of a Spin-Stabilized Spacecraft," NASA Technical Note, NASA TN D-4637, Washington, D. C., July 1968.
- 5-7. D. L. Mackison, R. L. Gutshall, and F. Volpe, "Star Scanner Attitude Determination for the OSO-7 Spacecraft," presented at the AIAA/AAS Astrodynamics Conference, Palo Alto, California, September 11-12, 1972, AIAA Paper No. 72-922.
- 5-8. D. W. Curkendall and C. G. Pfeiffer, "A Discussion of Guidance Policies for Multiple-Impulse Correction of the Trajectory of a Spacecraft," presented at the AIAA Guidance and Control Conference, Cambridge, Massachusetts, August 12-14, 1963, AIAA Paper No. 63-334.
- 5-9. B. G. Marsden, "Precision of Ephemerides for Space Missions," presented at 12th Colloquium of the International Astronomical Union, "Physical Studies of the Minor Planets," Tucson, Arizona, March 8-10, 1971.

## 6. SPACECRAFT DESIGN

### 6.1 CONSTRAINTS AND SELECTION CRITERIA

As specified by the study guidelines, the mission is to be implemented by adapting the Pioneer F and G spacecraft configuration to the operational requirements of multiple asteroid flyby. Modifications are to be held to a minimum. Considering the aspects of the mission that require spacecraft capabilities not included in the Pioneer F and G Jupiter flyby, the required principal design adaptations can be outlined grossly as follows:

- Addition of propulsion capability to meet retargeting and terminal guidance requirements
- Addition of a terminal navigation sensor
- Change in payload instruments to meet the scientific objectives of asteroid flyby.

Changes in the Pioneer F and G configuration aimed at providing these principal adaptations lead to additional design modifications ("secondary adaptations") which become necessary to assure system integrity, to support the principal design changes and add-on capabilities, and to facilitate the operation of the modified system as a whole. For example, the provision of extra propellant capacity, by enlarging the centrally located 16-inch tank to 26 inches, necessitates relocation of equipment and requires enlargement of the equipment bay as a secondary adaptation. Another example is the support of higher telemetry rate requirements which are introduced by the addition of a line-scan image system to the scientific payload. This leads to an augmentation of the communication system by a dual S-/X-band telemetry link as a secondary adaptation requirement.

However, the logic of design modifications illustrated by these examples must not be allowed to spread into an overall redesign that would be out of scope with the initial intention of holding such changes to a minimum. Thus, the ground rule was adopted to limit spacecraft modifications to those changes that are essential to accomplishing the mission but to exclude others that would improve mission capabilities, scientific data yield, etc. at considerable extra cost or added complexity.

At the outset of the study it became apparent that many of the required modifications already existed in the conceptual design of the Pioneer Jupiter Orbiter Spacecraft, Configuration 1 (Reference 1-8). These include:

- A propulsion capability for maneuvers up to 900 m/sec provided by 300 pounds of hydrazine propellant
- A two-stage blowdown propulsion/feed system with external ullage tanks
- An enlarged equipment bay necessitated by the increase in tankage; and
- A dual X-/S-band communication system.

These features can be adopted essentially without change from the Jupiter orbiter design study, thus saving new design and analysis effort.

An important programmatic consideration in the evolution of the Pioneer spacecraft family is to provide maximum spacecraft design commonality for different missions in the late 1970's; Jupiter orbiter, Saturn orbiter, and multiple asteroid or asteroid/comet flyby missions. This objective is served by adopting as many design features of the Jupiter orbiter configuration as possible, consistent with asteroid mission requirements.

In keeping with the study guidelines, the extent and cost of modifications from the baseline Pioneer F and G design was held within reasonable limits by applying the following criteria to the selection of new design features, new subsystem elements and new operating modes:

- The basic configuration dimensions and system layout is to remain unchanged
- The configuration is to be compatible with the Atlas/Centaur/TE-364-4 booster and a 10-foot (Intelsat) shroud
- Dynamic balance and spin stability characteristics are to remain essentially unchanged by maintaining the same mass distribution, e. g. , with the center of mass confined to the plane of the deployed RTG's and the magnetometer boom

- Launch, deployment, and cruise modes and orientations of the spacecraft are to remain essentially unchanged, including the stowage and deployment concept
- Structural changes are to be held to a minimum, with dynamic load paths essentially unchanged
- The thermal design is to remain essentially unchanged, the thermal environment of the new mission being actually less severe
- Although power distribution and power budget details are subject to change, the total power requirements are to be met by the present SNAP-19 RTG's
- The attitude control concept and implementation is to remain unchanged, i. e., pointing accuracy requirements during any mission phase are to be limited to present Pioneer F and G capabilities
- Basic properties of electrical integration, including control of EMI, magnetic cleanliness, etc., are to remain essentially unchanged
- Test requirements are to remain essentially unchanged
- System reliability requirements are to be no more severe than in the Jupiter flyby mission, in view of comparable mission durations
- Provisions for science payload accommodation are to be comparable to those of Pioneer F and G with at least the same payload weight capacity and power allocation. Instrument mounting, deployment, and articulation may be modified considering the difference in scientific mission objectives and target observation requirements.

## 6.2 SCOPE OF THE DESIGN STUDY

A major part of the study effort was concentrated on mission analysis and definition of system requirements. Consequently the effort devoted to spacecraft and subsystem design had to be limited in scope. It included primarily the following tasks:

- Definition of the spacecraft design concept
- Identification of required changes from the baseline Pioneer F and G configuration

- Conceptual design of modified or added sub-system elements
- Definition of payload instrument accommodation
- Preliminary weight allocations and power budget.

Principal modifications of the baseline Pioneer system that are necessary in order to meet asteroid mission requirements will be described in greater detail than design features that remain basically unchanged. The comprehensive descriptions of Pioneer F and G operational characteristics to be found in Reference 1-8 and other Pioneer program documents provide background and detail that is omitted in this report.\*

System modifications were studied in sufficient detail to establish their feasibility within the constraints of the present state of technology. In some instances, a reasonable growth of technology, or adaptation of available new technology to routine spacecraft design was assumed to provide improved design options and mission characteristics. With the earliest mission date probably not before the end of this decade, further advances in the technology of optical navigation sensors and line-scan image systems can be reasonably projected.

In the absence of detailed subsystem design characteristics, and with only a tentative selection of payload instruments possible at this time, the weight and power allocations derived in this study are preliminary, based on best estimates rather than detailed analysis. These estimates were in part substantiated by extrapolation from Pioneer F and G design characteristics and use of Jupiter Orbiter design data wherever applicable.

## 6.3 SPACECRAFT CONFIGURATION

### 6.3.1 Configuration Layout

The proposed configuration of the Pioneer asteroid spacecraft is illustrated in Figure 6-1. The side view drawing shows the spacecraft in a stowed configuration, inside the dynamic envelope of the 10-foot Intelsat shroud. The plan view, looking aft, shows the spacecraft with stowed and deployed appendages.

---

\*Applicable design data and functional descriptions from TRW's Jupiter Orbiter Study (Reference 1-8) are quoted or adapted in this report as warranted by the context.

ORIGINAL PAGE IS  
OF POOR QUALITY

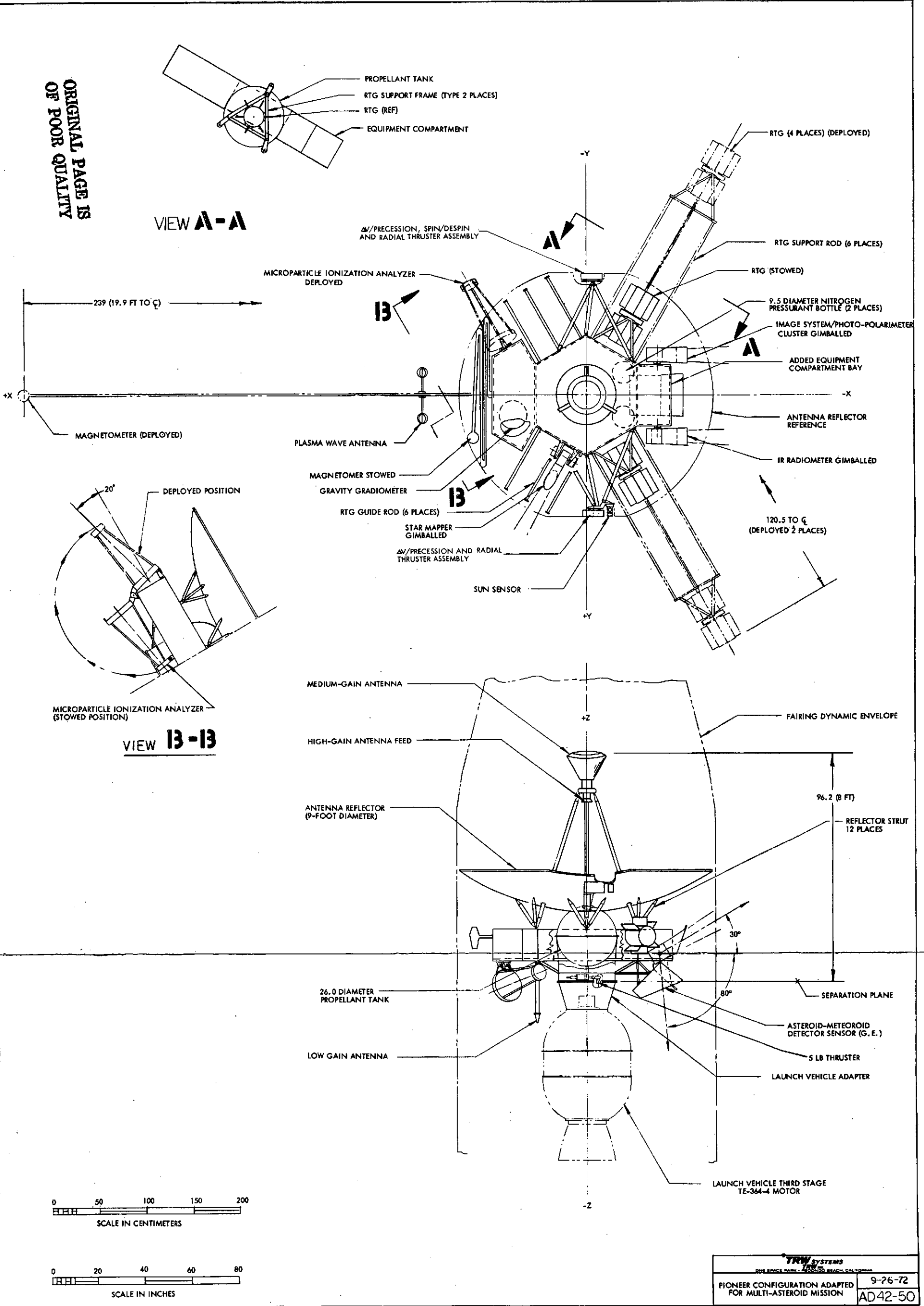


Figure 6-1. Spacecraft Configuration

Although the modified spacecraft retains the general geometrical and structural layout of Pioneer F and G some differences are evident. This is best illustrated by a perspective view of Pioneer F and G, shown in Figure 6-2, in which the principal changes in design and payload composition adopted for the asteroid spacecraft are indicated. For example, outlines of the enlarged propellant tank and the extended equipment compartment are shown in the drawing by dashed lines. These design features were adopted from the Pioneer Jupiter Orbiter since essentially the same increase in propulsive capability is required.

The modified equipment bay of the asteroid Pioneer is shown in Figure 6-3. The increased propellant tank and the addition of two pressurant gas tanks necessitates rearrangement or relocation of components which in the baseline Pioneer configuration are located close to the center of the bay. The original arrangement of components in the Pioneer F and G equipment compartment is shown in Figure 6-4 for comparison.

To house some of the displaced equipment and to accommodate new payload instruments a square-shaped box, 26 x 15 x 14 inches in size, is attached to the hexagonal center body on the side opposite the science compartment of the original design. The add-on compartment provides convenient mounting space for the gimballed optical sensor assembly, giving the sensors an unobstructed view over a large cone angle range (see Figures 6-1 and 6-3).

### 6.3.2 Design Modifications

Several alternative approaches for distributing the increased propellant and pressurant gas volume within the confines of the existing central equipment compartment were investigated in the Jupiter Orbiter study. The adopted configuration, using one large central propellant tank and two external ullage tanks, is preferred because:

- 1) It accommodates the largest propellant mass in the available volume
- 2) It minimizes tankage weight
- 3) It facilitates the use of a simple but efficient two-stage blowdown technique for propellant pressurization.

ORIGINAL PAGE IS  
OF POOR QUALITY

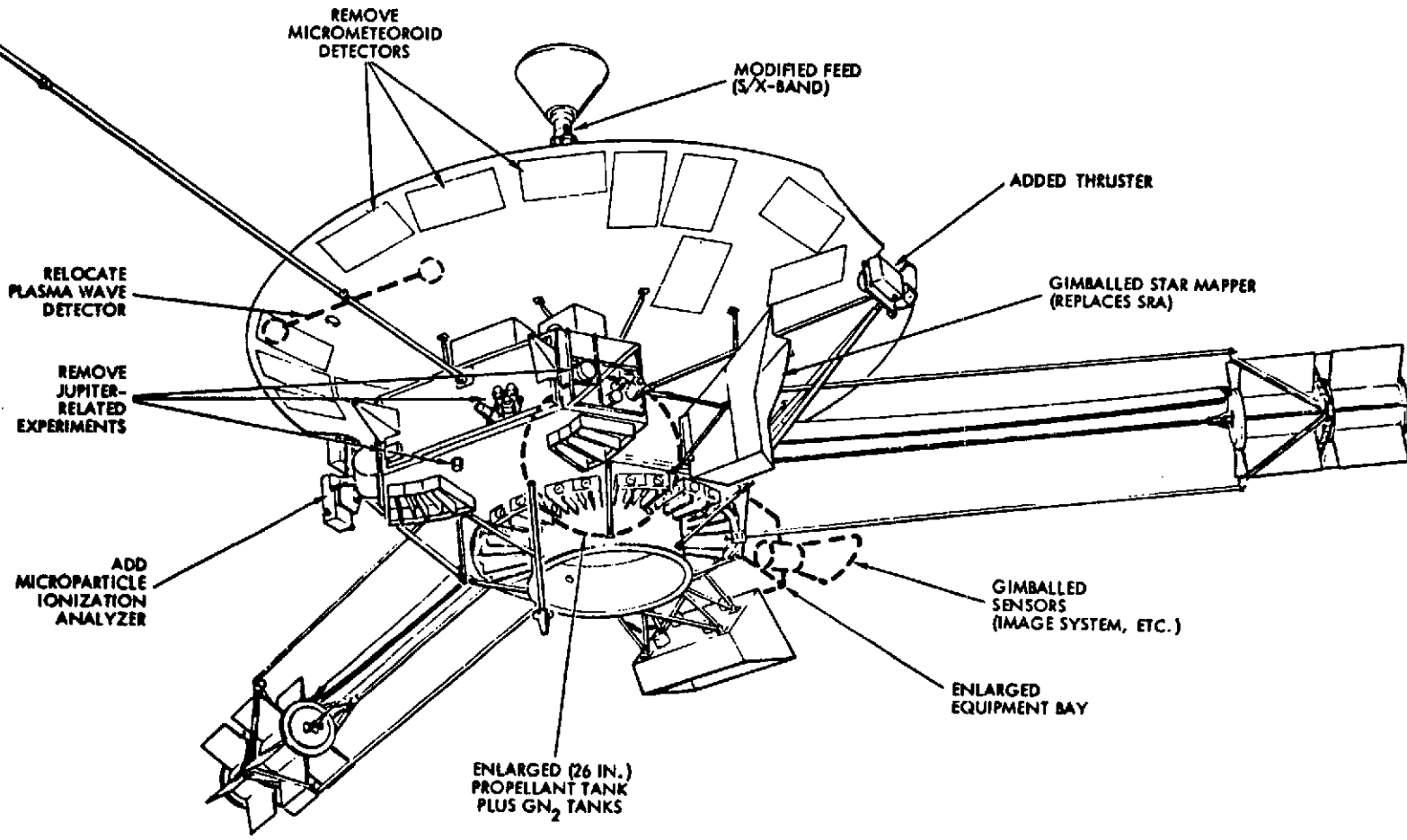
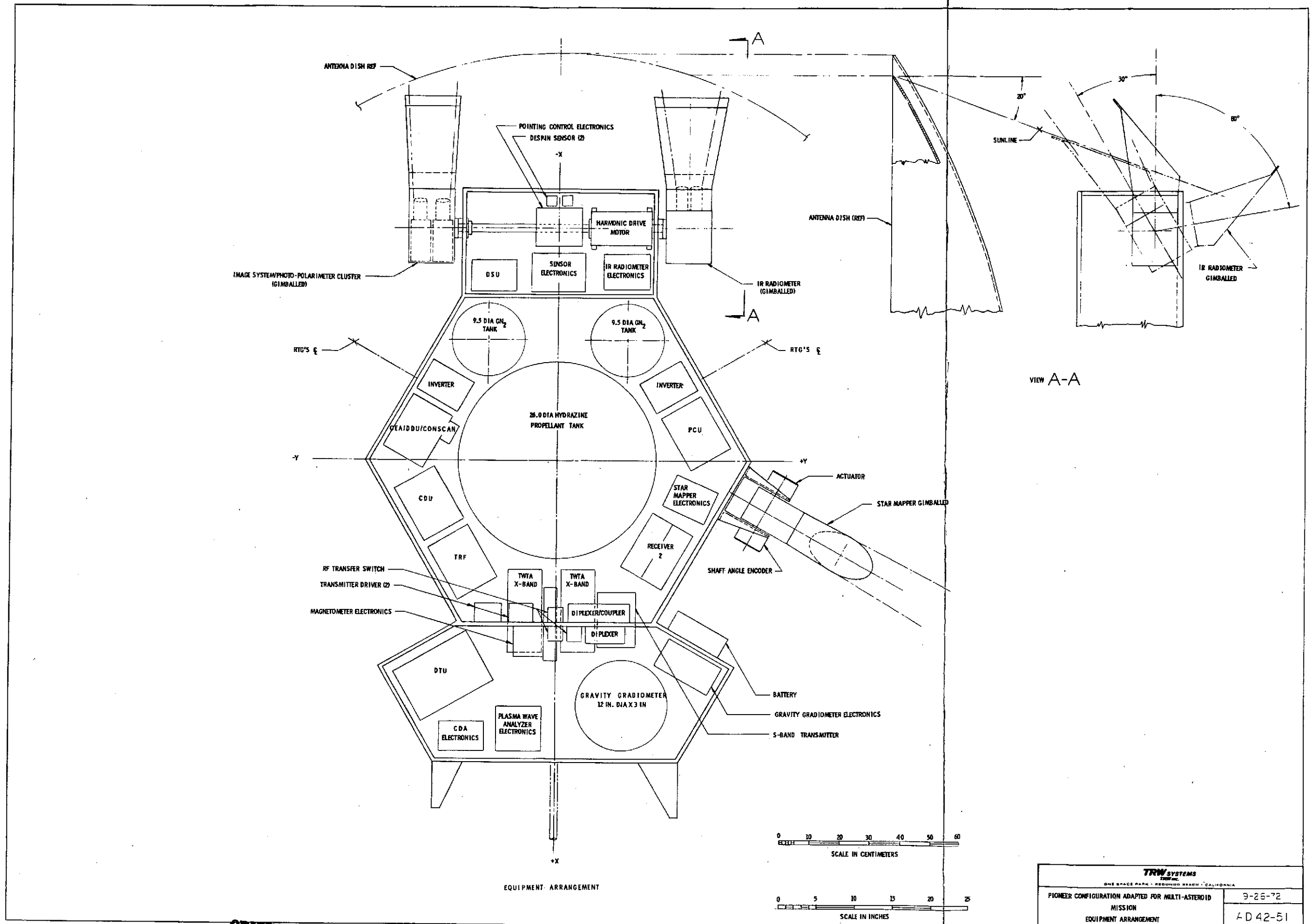


Figure 6-2. Pioneer Modifications for Asteroid Mission



ORIGINAL PAGE IS  
OF POOR QUALITY

Figure 6-3. Equipment Bay Layout

FOLDOUT FRAME /

FOLDOUT FRAME 2

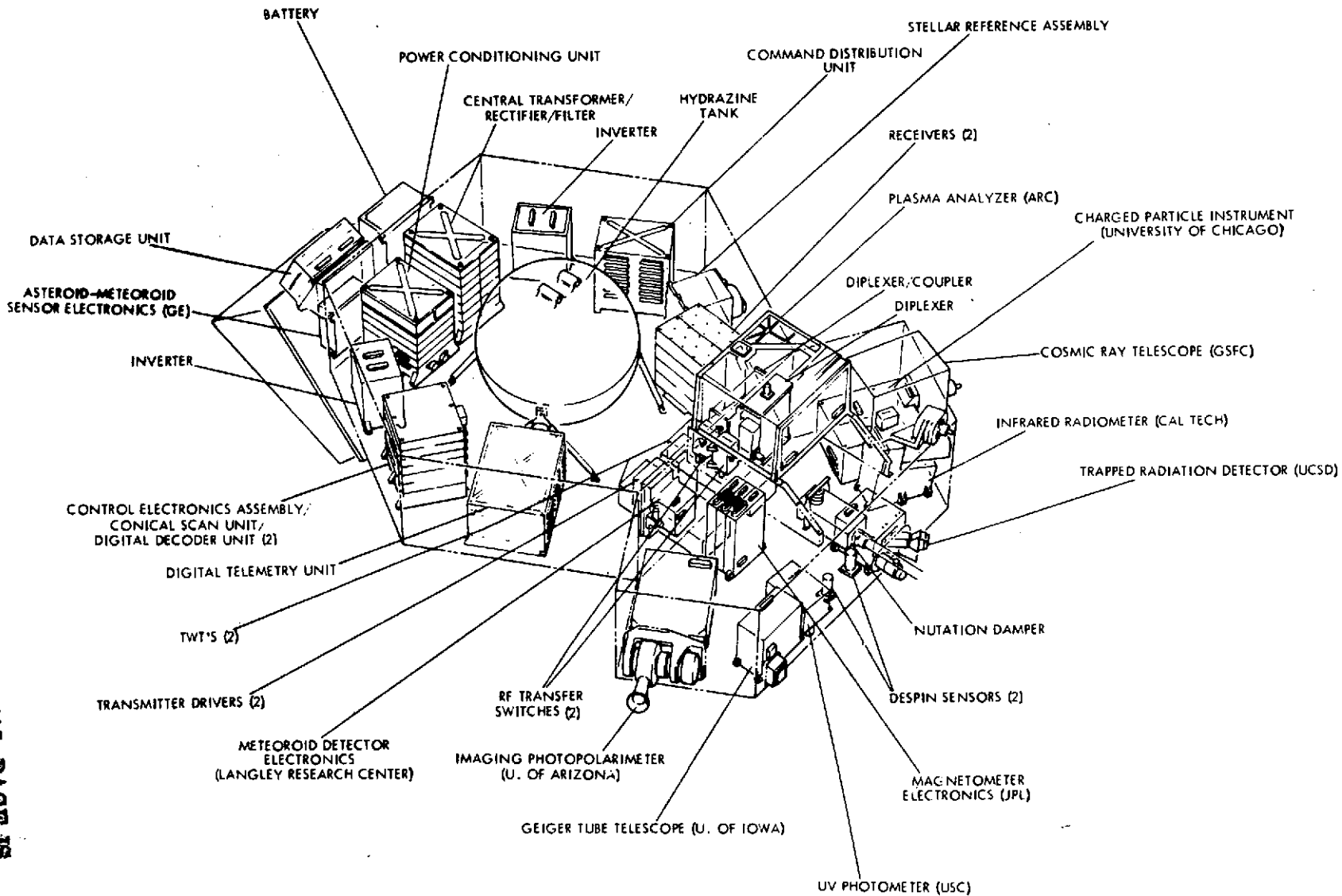


Figure 6-4. Pioneer F and G Equipment Compartment

Actually the tank size adopted for this configuration is about as large (26-inch diameter) as it can be made without requiring significant structural modifications, e. g. , providing a greater separation of the spacecraft upper structure from the equipment bay. This approach would introduce considerable changes in mass properties and require costly structural redesign.

The selected design approach requires less severe "secondary" configuration changes. However, even in this case some structural modifications are necessary to accommodate a 26-inch propellant tank at the center of the equipment bay, in addition to providing the extra equipment mounting space mentioned before:

- The spacing between the guide rods of each RTG deployment arm must be increased to provide the necessary clearance for the larger tank.
- A circular cutout must be provided in the center of the equipment mounting platform so the bottom of the tank can protrude by several inches.
- Similar cutouts must be provided in the top enclosure of the equipment bay and in the center of the 9-foot antenna dish.
- The support structure for the propellant tank must be modified and supports for the new pressurant gas tanks must be added.

The Jupiter Orbiter study has shown that these modifications do not introduce any fundamental design difficulties. The enlargement of the equipment compartment requires only a modular change of the existing spacecraft center body without affecting the remaining structure. The small change in mass distribution caused by this addition does not affect the mass balance significantly.

The protrusion of the propellant tank through a cutout in the antenna dish has only a minimum effect on antenna performance which can be neutralized by covering the tank top with RF-absorbent material.

Protective covers against micrometeoroid impact damage are required for the protruding top and bottom segments of the propellant tank. This requires the addition of a circular honeycomb panel at the bottom

which closes the open adapter ring. The addition of a similar meteoroid shield on top can provide the desired RF-absorbent cover to neutralize distortions of the antenna beam pattern.

A preliminary study of the micrometeoroid impact hazard during the asteroid belt cruise was performed to determine whether additional shielding is required. The results, summarized in Appendix C indicate that the probability of damaging meteoroid impact in this mission is actually somewhat smaller than during the comparatively much shorter asteroid belt crossing of the Jupiter Pioneer missions. Actually, the particle impact count observed by the present Pioneer 10 mission on its way through the asteroid belt reveals a much lower flux than had been anticipated on the basis of published models of meteoroid spatial density in the asteroid belt. Consequently, no requirement for additional protection of the asteroid Pioneer against micrometeoroid damage is foreseen.

### 6.3.3 Configuration Detail

The arrangement of deployable structures (RTG support arms and magnetometer boom) and the deployment procedure are the same as for Pioneer F and G and the Jupiter Orbiter. The deployed magnetometer boom augments the mass balance of the spacecraft, and, in combination with the wobble damper mounted at its root, provides the principal mechanism for suppression of nutation effects due to perturbing torques.

The spin axis orientation and desired precession maneuvers are controlled in the same manner as in Pioneer F and G, by two axial thruster clusters mounted on opposite sides of the spacecraft, near the rim of the high-gain antenna dish. One of the two thruster assemblies includes a pair of spin/despin thrusters which are oriented circumferentially and control the spin rate during the initial deployment sequence and during the rest of the mission. (Unlike the Jupiter Orbiter the spacecraft does not require a spin rate increase during main thrust phases, since the axial thruster has a much smaller thrust level.)

Trajectory control is exercised by a pair of axial thrusters as in Pioneer F and G and by radial thrusters that have been added in this configuration to the thruster assemblies on both sides. The radial

thrusters operate in a pulsed thrust mode over a 60 to 90-degree arc of the spin cycle. They are mounted at a cant angle of 12 degrees relative to the positive and negative Y-axes such that the line-of-action passes through the nominal c. g. location to minimize precession effects.

The main impulse for retargeting maneuvers is provided by an axial 5-lbf hydrazine thruster located inside the adapter ring near the bottom of the propellant tank. As shown in the design drawing (Figure 6-1) the thruster is offset from the spacecraft center line such that the line-of-action passes through the nominal c. g.

The gimballed optical sensor used to perform terminal navigation and to generate roll reference pulses is mounted on the side of the equipment platform, replacing the stellar reference assembly of Pioneer F and G, as shown in Figures 6-1 and 6-3. The gimbal rotation covers a cone angle range of 50 to 165 degrees.

Although normally shaded by the antenna dish from direct exposure to the sun, the sensor is equipped with a light shade for protection against reflected light. The light shade also protects the sensor against direct sunlight under the rare conditions where the sun-spacecraft-earth angle exceeds 30 degrees. The small (4.2-degree) circular field-of-view of the instrument simplifies the design of the light shade and reduces its size compared to that of the stellar reference assembly used in Pioneer F and G.

#### 6.3.4 Accommodation of Science Payload Instruments

Additional modifications of the baseline Pioneer configuration are required for accommodation of the payload instruments including instrument placement, orientation, protection, and deployment.

The payload proposed for the asteroid mission (see Section 2) includes these instruments

- Image system
- Photopolarimeter\*
- IR radiometer\*
- Asteroid/meteoroid detector\*

---

\*Also carried by Pioneer F and G.

- Magnetometer (Also carried by Pioneer F and G.)
- Microparticle ionization analyzer
- Plasma wave detector
- Gravity gradiometer

Instrument dimensions are not firmly defined at this time, and the arrangement shown in Figures 6-1 and 6-3 is to be regarded as tentative.

As shown in Figure 6-3 the three optical instruments (line-scan imaging system, photopolarimeter, and IR radiometer) that must be re-oriented repeatedly during the asteroid encounter are mounted on a common drive shaft and rotated by a single actuator. The sensors are arranged on opposite sides of the add-on equipment compartment, in a location normally shaded by the antenna dish. An unobstructed view over a cone angle range from 60 to 170 degrees is available, as illustrated by View A-A. The design of the light shades that protect the sensor assemblies against direct and reflected sunlight is illustrated in the figure.

The asteroid/meteoroid detector (Sisyphus) is retained in the same position and on the same support structure as in Pioneer F and G, with the centerline pointing at 135-degree cone angle. This location is compatible with the proposed enlargement of the equipment platform and with gimbal rotation of the optical sensors.

The microparticle ionization analyzer is 32-inches long and has a baseplate of 14 inches diameter. Because of its dimensions and orientation requirement this instrument is stowed under the equipment platform during launch, (see Figure 6-1, View B-B). A fixed-orientation is suggested for simplicity. However, several reorientations of the instrument during the mission around the deployment hinge would enhance the scientific data return because of the changing flux direction of micrometeorites relative to the spacecraft.

The magnetometer boom is of the same length as in the Pioneer F and G spacecraft. A greater boom length may be preferred to reduce magnetic cleanliness requirements of the spacecraft center body and the electromechanical drive assemblies used by the navigation sensor and the optical payload sensors. A longer boom would also improve the mass

balance by compensating for the extension of the payload platform on the side opposite the boom.

The plasma wave antenna shown in the plan view of Figure 6-1 can be conveniently deployed along with the magnetometer boom from its folded and stowed position.

The gravity gradiometer is housed in a 12 x 3-inch cylindrical can mounted inside the payload bay in a location no longer occupied by payload equipment in the modified design (see Figures 6-3 and 6-4). Its spin axis should ideally be aligned with the spacecraft spin axis to minimize cross coupling or bias effects. Misalignments due to uncertainty of the actual Pioneer spin axis orientation can be detected and compensated by measurements in flight. Similarly, any bias due to centrifugal effects at the mounting location of the instruments can be calibrated in flight. This bias is only an indirect influence on gradiometer measurements as a result of non-zero transverse bearing loads.

#### 6.3.5 Functional Block Diagram

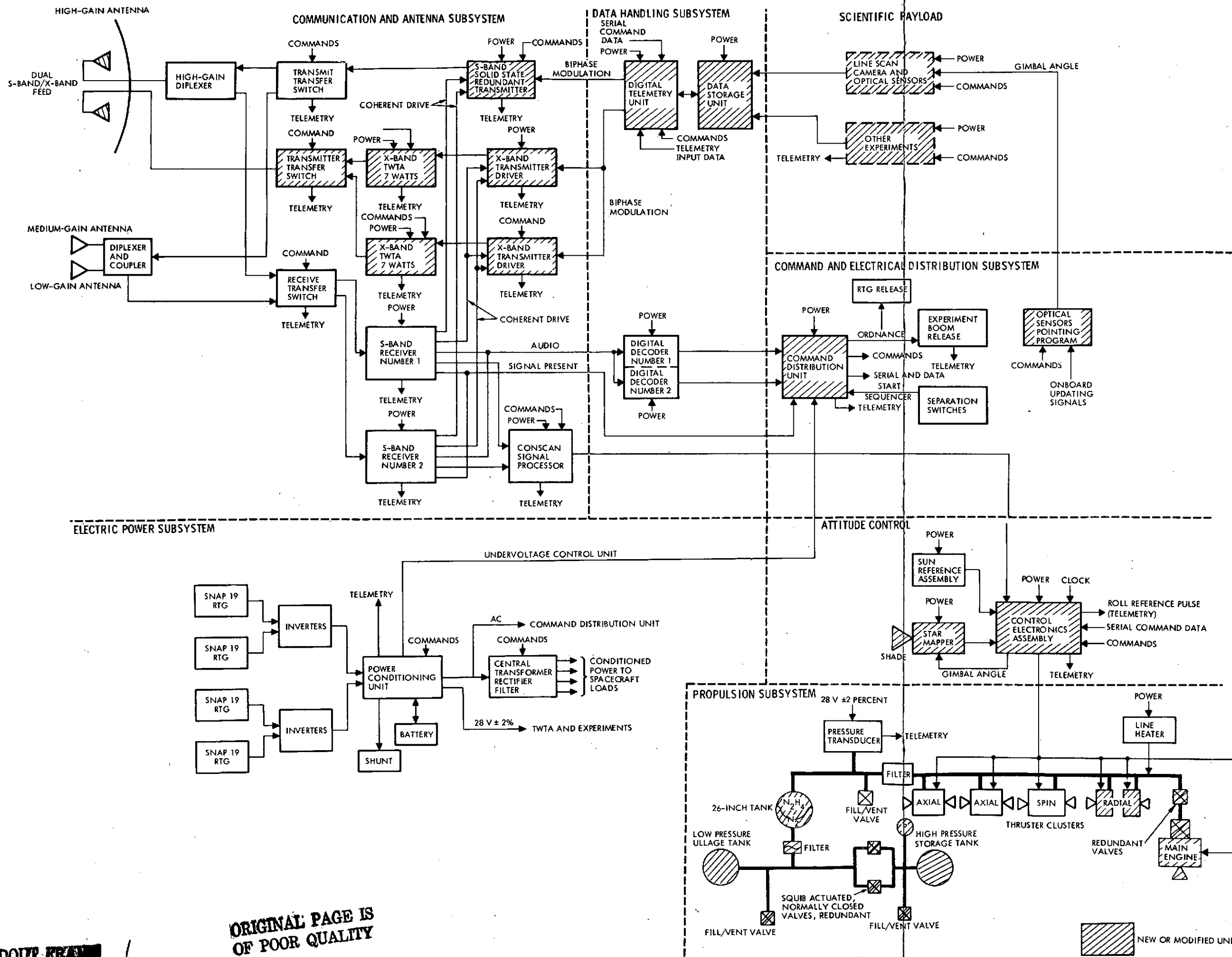
The functional block diagram shown in Figure 6-5 is very similar to that of Pioneer F and G, with the basic electrical design concept essentially unchanged. Required modifications and additions are indicated by cross-hatching.

Principal modifications in individual subsystems and interfaces are summarized as follows.

The major change in communications and data handling is the adoption of dual-mode S-/X-band telemetry to provide the large downlink data rates necessitated by the improved line-scan image system. This design modification was already adopted for the Jupiter Orbiter.

The digital telemetry unit is changed accordingly, and a high-data capacity solid-state data storage system is substituted for the 50 kbit core memory of the baseline design. This data storage system is used as a buffer for image system data that are acquired at a duty cycle of 1:60 and read out continuously by the telemetry system.

With a different complement of payload instruments and changed observation modes the command sequences and command distribution



OLDOUT FRAME 1

ORIGINAL PAGE IS OF POOR QUALITY

OLDOUT FRAME 2

Figure 6-5. Functional Block Diagram

functions must be modified. Onboard data processing is used to update the stored optical sensor pointing program. The addition of an onboard computer can thus be avoided.

The attitude control system uses the same control modes and control sequence logic as the baseline system. However, the replacement of the baseline star reference assembly by a gimballed star mapper requires modifications in the control electronics assembly. This sensor must be controlled to provide clock angle reference pulses during the cruise mode as well as terminal navigation fixes during the pre-encounter mode. Attitude changes for major guidance maneuvers are controlled in the same manner as in Pioneer F and G and the Jupiter Orbiter.

The block diagram of the propulsion system shows the modifications required for the increased maneuver capability and additional thrust modes of the asteroid spacecraft.

Modifications of subsystem interfaces occur in many areas of the system as a result of the changes described above. The modifications involve primarily the flow of command signals and telemetry input data. The changes also affect power distribution and control, although the power subsystem configuration is left essentially unchanged. New interface functions are also introduced by the articulated sensor packages not carried by the baseline spacecraft or the Jupiter Orbiter.

## 6.4 MASS PROPERTIES

### 6.4.1 Weight Summary

A weight breakdown for the asteroid spacecraft was obtained by using weight elements of Pioneer F and G and of the Jupiter Orbiter as a basis and estimating incremental weight changes due to addition of components or due to increase in size, structural support requirements, etc. A more direct weight estimate of every component could not be determined within the framework of this study.

Table 6-1 gives the preliminary weight breakdown ( $W_2$ ) of the asteroid spacecraft compared to Pioneer F and G (weight elements  $W_0$ ), and the Jupiter Orbiter (weight elements  $W_1$ ). The table also lists the weight increments  $\Delta W_1$  and  $\Delta W_2$  by which the weight estimates  $W_1$  and  $W_2$

Table 6-1. Electric Power Requirements (Watts) (Steady Loads)

SUBSYSTEMS	PIONEER F&G W <sub>0</sub>	JUPITER ORBITER CONFIGURATION 1		MAF SPACECRAFT		REMARKS
		$\Delta W_1$	W <sub>1</sub>	$\Delta W_2$	W <sub>2</sub>	
ELECTRICAL POWER	39		39		39	
COMMUNICATIONS	23	(+2)	25	+5	30	X-BAND ADDED
ANTENNAS	46	(+5)	51		51	WAVE GUIDES AND SWITCH
DATA HANDLING	12		12	+5	17	ADDED DSU
ELECTRICAL DISTRIBUTION	36	(+4)	40		40	INCREASE CABLING AND CDU
ATTITUDE CONTROL	13	(+2)	15	+3	18	ADDED NOZZLES
GIMBALS PLUS ACTUATORS				+15	15	
PROPULSION (DRY)	23	(+35)	58	+6	64	LARGER TANK PLUS THRUSTER
THERMAL CONTROL	16	(+2)	18	+3	21	INSULATION FOR ADDITIONAL COMPARTMENT EXTERNAL PAYLOAD
STRUCTURE						
RTG SUPPORT	22		22		22	
PRIMARY	43	(+7)	50	+5	55	LARGER COMPARTMENT PLUS REINFORCED SUPPORT
SECONDARY AND METEOR- OID PROTECTION	39	(+2)	41	+3	44	TANK METEOROID PROTECTION
BALANCE WEIGHT PROVISIONS	9	(+5)	14		14	HEAVIER SPACECRAFT
RTG'S	<u>120</u>		<u>120</u>		<u>120</u>	
SUBTOTAL	441	(+64)	505	+45	550	
SCIENTIFIC INSTRUMENTS	66	(+4)	70	+5	75	ADDED INSTRUMENTS
SPACECRAFT (DRY)	<u>507</u>	(+68)	<u>575</u>	+50	<u>625</u>	
UNUSABLE PROPULSION AND PRESSURANT	<u>2</u>		<u>9</u>		<u>9</u>	
SPACECRAFT	509		584		634	
USABLE PROPELLANT	<u>59</u>		<u>295</u>		<u>340</u>	
SPACECRAFT (WET)	568		879		974	
ADAPTER	<u>30</u>		<u>40</u>		<u>40</u>	
GROSS SYSTEM	598		919		1014	

differ from the corresponding values in preceding columns. Principal causes of each weight increment are listed in the last column of the table.

Specific weight assumptions require additional explanation.

- 1) Larger size subsystems are reflected by weight increments  $\Delta W_2$  for communications (larger transmitter power), propulsion dry weight (larger tank but smaller main thruster), and for additional structural support and thermal control.
- 2) Addition of components is reflected by weight increments  $\Delta W_2$  in data handling (addition of interface equipment and accommodation of high data rates in DTU), attitude control (radial thrusters, gimbal drives) and secondary structure.
- 3) No weight increments  $\Delta W_2$  are shown for subsystems that are unchanged from Pioneer F and G or the Jupiter Orbiter such as power subsystem and RTG's, antenna, and electrical distribution.

As a result the total increase  $\Sigma \Delta W_2$  in dry weight excluding science payload, is conservatively estimated as 45 pounds. This adds to the increase  $\Sigma \Delta W_1 = 64$  pounds already accounted for in the various modifications that were adopted for the Jupiter Orbiter. Thus, the dry weight (excluding payload) of the asteroid spacecraft is estimated to be increased by 109 pounds, or 25 percent, from the corresponding value (441 pounds) of Pioneer F and G. A total of 75 pounds is allocated to science payload.

The gross system weight of the asteroid spacecraft amounts to 1014 pounds, including a 40-pound weight allowance for the spacecraft adapter. The corresponding launch hyperbolic excess velocity is 7.6 km/sec ( $C_3 = 58 \text{ km}^2/\text{sec}^2$ ).

Note that in comparing these weight characteristics with performance data presented in Section 3 (see Figures 3-3 and 3-7) allowance should be made for the weight difference of the spacecraft adapter (40 pounds) which was not included in the preliminary performance calculations.

It should also be noted that the gross weight and payload characteristics listed in Table 6-1 represent conditions for a "nominal" mission requirement. The specific  $\Delta V$  and  $V_\infty$  requirements of a selected mission

may not require all of the nominal propellant load (340 pounds) or all of the injected weight capability of the launch vehicle at a specified value of  $V_{\infty}$ .

The performance data in Section 3 were calculated assuming a highly conservative  $I_{sp}$  value of 215 seconds. With a more realistic  $I_{sp}$  value of 225 seconds a net payload weight margin of about 40 pounds above the values in Figures 3-3 and 3-7 can actually be realized for a specified  $\Delta V$  requirement and a given propellant load.

#### 6. 4. 2 Estimated Mass Properties

The spacecraft moments of inertia  $I_x$ ,  $I_y$ ,  $I_z$ , and c. m. locations of the Pioneer asteroid spacecraft are very nearly equal to those of the Pioneer Jupiter Orbiter since the only significant mass distribution difference between the two vehicles involves masses that are located at or very close to the respective spacecraft centers.

The validity of this statement is substantiated by comparing moments of inertia of the Pioneer F and G and the Jupiter Orbiter, which differ more significantly in configuration than the Jupiter Orbiter and the asteroid spacecraft. Table 6-2 shows that the moments of inertia of the heavier Orbiter spacecraft are only from 3 to 10 percent larger than those of Pioneer F and G. The last column in the table shows how strongly the contribution of the deployed masses (RTG's and magnetometer boom) dominates the moments of inertia, thus masking the lesser effects of mass distribution changes near the center.

The approximate mass properties of the asteroid spacecraft (based on the Jupiter Orbiter data) are listed in Table 6-3 for several stages of spacecraft deployment, and for start and end of mission life.

Table 6-4 lists the limits that have been established for mass property parameters such as moment-of-inertia ratios and c. g. locations in order to satisfy pointing accuracy and dynamic stability requirements. All of these limits are satisfied by the spacecraft mass properties given in Table 6-3.

ORIGINAL PAGE IS  
OF POOR QUALITY

Table 6-2. Moments of Inertia for Pioneer F and G and Jupiter Orbiter (slug-ft<sup>2</sup>)

	1	2	3	4
	PIONEER F/G	JUPITER ORBITER	DEPLOYED APPENDAGES ONLY	% CONTRIBUTION ON 2
$I_x$	284	294	260	88
$I_y$	180	202	170	84
$I_z$	434	461	320	70

Table 6-3. Jupiter Orbiter - Mass Properties Estimate

	WEIGHT (LBS)	$\bar{X}$ (IN.)	$\bar{Z}$ (IN.)	MOMENT OF INERTIA (SLUG-FEET <sup>2</sup> )			$\frac{I_z}{I_x}$	$\frac{I_z}{I_y}$	$\frac{2I_z}{I_x + I_y}$	$K = (K_x K_y)^{1/2}$
				$I_x$	$I_y$	$I_z$				
AT IGNITION OF TE 364-4 MOTOR	3188	0	-20.4	592	592	196	0.33	0.33	0.33	
AT TE 364-4 BURNOUT	1071	0	9.3	186	188	120	0.64	0.64	0.64	
SPACECRAFT STOWED	879	0	18.6	73	74	112	1.53	1.51	1.52	
AT START OF LIFE	879	-4.2	18.6	294	202	461	1.57	2.28	1.86	0.85
AT END OF LIFE	584	-6.3	18.6	294	200	460	1.56	2.30	1.86	0.86

\* LONGITUDINAL CENTER OF GRAVITY FROM SEPARATION

Table 6-4. Mass Properties Requirements

<ul style="list-style-type: none"> <li>● SPACECRAFT PLUS THIRD STAGE             <ul style="list-style-type: none"> <li>● LIMIT THIRD STAGE INJECTION ERRORS:                 <ul style="list-style-type: none"> <li>- SPACECRAFT C.G. OFFSET <math>\leq 0.050</math> INCH</li> <li>- SPACECRAFT SPIN PRINCIPAL AXIS <math>\parallel</math> TO Z <math>\leq 0.003</math> RADIAN</li> <li>- SPACECRAFT PLUS THIRD STAGE <math>I_z/I_x, I_x/I_y \leq 0.90</math></li> </ul> </li> </ul> </li> <li>● STOWED SPACECRAFT             <ul style="list-style-type: none"> <li>● ATTITUDE STABILITY:                 <math display="block">\frac{I_z}{I_x}, \frac{I_z}{I_y} \geq 1.1</math> </li> </ul> </li> <li>● DEPLOYED SPACECRAFT             <ul style="list-style-type: none"> <li>● ATTITUDE STABILITY:                 <math display="block">\frac{I_z}{I_x}, \frac{I_z}{I_y} \geq 1.1</math> </li> <li>● LIMIT CRUISE MODE POINTING ERROR: SPIN PRINCIPAL AXIS <math>\parallel</math> TO Z <math>\leq 0.15</math> DEGREE</li> <li>● LIMIT POINTING ERROR DURING <math>\Delta V</math>: C.G. X-Y LOCATION KNOWN TO:                 <ul style="list-style-type: none"> <li>- <math>\leq 1.6</math> INCH FOR CONFIGURATION 1 AND</li> <li>- <math>\leq 0.10</math> INCH FOR CONFIGURATION 2</li> </ul> </li> <li>● LIMIT NUTATION DURING PRECESSION: <math>K = K_0 \pm 0.05</math> <math display="block">K = \left( \frac{I_z - I_x}{I_y} \cdot \frac{I_z - I_y}{I_x} \right)^{1/2}</math> </li> </ul> </li> </ul>
---

## 6.5 DYNAMICS

The dynamic characteristics of the selected asteroid spacecraft configuration are the same as those of the Jupiter Orbiter since the mass properties are practically identical, as discussed in the preceding section. In all cases where perturbing effects on the asteroid spacecraft are equal the results of the Jupiter Orbiter dynamic analysis remain valid and are summarized in this section. However, in some cases the perturbing torques acting on the spacecraft, and hence the dynamic responses, are an order of magnitude smaller because of the reduced axial thrust level (5 lbf compared to 50 lbf). These cases will be treated separately.

### 6.5.1 Attitude Stability and Pointing

The Pioneer F and G scheme of spin stabilization is used to maintain inertial orientation of the spacecraft's Z axis.

Spin is initially provided by a Centaur-mounted spin table which spins up the spacecraft and third stage to approximately 60 rpm. During the first three minutes after Centaur separation, including 45 seconds of TE-364-4 thrusting and a two minute and 15 second wait period for residual thrusting to decay, the spacecraft is spinning about an axis of minimum moment of inertia. In this configuration, energy dissipation due to propellant sloshing causes nutation to increase. Starting with a nutation angle of 2.5 degrees induced by third stage thrusting this will increase the angle by less than 0.5 degree.

After third stage separation, the spacecraft spins about an axis of maximum moment of inertia, and the propellant motion causes nutation to decay. During the approximately three-minute period after spacecraft/third stage separation, before the RTG's are deployed, the nutation angle will be reduced to 2.5 degrees.

The spacecraft continues to spin about the axis of maximum moment of inertia after the appendages are deployed. Since the deployed appendages are quite flexible, the simple stability criterion that requires the spin axis moment of inertia to be maximum is no longer sufficient to ensure attitude stability. However, with mass properties and appendage dimensions that are almost equal to the Pioneer F and G values, it can be concluded that the spacecraft is stable by similarity.

Alignment of the spin axis with respect to the theoretical centerline is achieved by pre-launch balancing of the stowed, empty spacecraft and properly locating and aligning the consumables and deployables. The approach for maintaining dynamic balance is the same as that used on Pioneer F and G and in the Jupiter Orbiter. It has the following features:

- All deployables and consumables are located at the same Z-level as the spacecraft c. g.
- Combined RTG and magnetometer deployment moves the spacecraft c. g. perpendicular to the Z axis in the -X direction.

The spin axis misalignment is given by

$$\epsilon_{\text{spin axis}} = 57.3 I_{xz} / (I_z - I_x)$$

With  $I_z - I_x = 166 \text{ slug-ft}^2$  and a product of inertia uncertainty  $I_{xz} = 0.33 \text{ slug-ft}^2$  (RSS estimate) as derived for the Jupiter Orbiter the estimated spin axis misalignment is 0.12 degree. This is within the tolerance of 0.15 degree allowable for Pioneer F and G.

#### 6.5.2 Third Stage Injection Errors

Accuracy of third stage injection is dependent upon mass properties of the combined third stage/spacecraft vehicle, thrust vector misalignment with respect to the vehicle c. g., and spin rate. It is assumed here that the spin rate is 60 rpm and that the mass properties requirements given in Section 6.4 are satisfied.

For a conservatively estimated body-fixed, transverse torque of 14,900 pounds x 0.10 inch = 1490 inch-pound (assumed constant throughout the entire thrusting duration) the injection errors will not exceed the following values (see Jupiter Orbiter study):

- Angular dispersion of  $\Delta V$  vector = 0.48 degree
- Reduction in magnitude of  $\Delta V$  vector = negligible
- Nutation angle (from thrust misalignment only) = 2.5 degrees.

Correction of the velocity vector misalignment is well within the capability of the spacecraft.

Assuming that the 2.5-degree nutation angle is not reduced by propellant motion, the spacecraft nutation angle present after third stage separation and despin will increase to 3.2 degrees. Appendage deployment can easily be accomplished with this nutation angle. (Pioneer F and G can deploy appendages with an initial nutation angle of 10 to 15 degrees.)

#### 6.5.3 Nutation Damping

Since the nutation damper design, the magnetometer boom, and the spacecraft mass properties have remained essentially unchanged, approximately the same nutation damping characteristics as for Pioneer F and G will be achieved; i. e., a damping time constant of 10 minutes or less at a 5 rpm spin rate.

#### 6.5.4 $\Delta V$ Maneuvers

Pointing and spin rate errors will occur during maneuvers performed with the 5-pound main axial thruster or with the auxiliary axial and radial

$\Delta V$  thrusters. The errors are caused by body-fixed torques resulting from thrust vector-to-c. g. misalignments.

The main axial thruster produces a misalignment torque equal to (thrust) x (one-half of nominal X-axis travel of c. g.) or 5 pounds x 1.1 inch = 5.5 inch-pound.

The canted radial thruster produces a torque equal to (thrust) x (Z-axis offset of c. g.) x (cos  $\delta$ ) where  $\delta = 12$  degrees is the thruster cant angle relative to the Y-axis. This misalignment torque is 1.5 pounds x 1 inch = 1.5 inch-pound.

The auxiliary axial  $\Delta V$  thrusters produce an unbalance torque resulting from force unbalance and Y axis offset of the c. g. The estimated torque is 1.5 inch-pound.

Maximum pointing errors occur when the propellant tanks are nearly empty. At that time, the inertia ratios  $I_z/I_x$  and  $I_z/I_y$  are minimum, and the thrust vector-to-c. g. offset is maximum.

A bound on the oscillating pointing error occurring during the  $\Delta V$  maneuver is given by

$$\alpha \leq 57.3 \frac{2T}{(I_z - I_x) S^2}$$

where

$\alpha$  is the pointing error (degree)

T is the transverse torque (ft-pound)

$I_z, I_x$  are spacecraft moments of inertia with tanks empty (slug-ft<sup>2</sup>)

S is the spin rate (radians/second).

After the thrust is terminated, the wobble portion of  $\alpha$  will decay exponentially with a time constant of less than ten minutes leaving a residual pointing error  $\beta$ , which is bounded by the expression

$$\beta \leq 57.3 \frac{2T}{I_z S^2}$$

Evaluating these equations using the torques indicated above and moments of inertia given in Section 6.4, the following representative values of  $\alpha$  and  $\beta$  are obtained (see Table 6-5).

Table 6-5. Maximum Pointing Errors (Degrees)

ERROR DUE TO	MAXIMUM POINTING ERROR DURING MANEUVER ( $\alpha$ )	RESIDUAL AFTER NUATION DECAY ( $\beta$ )
MAIN AXIAL THRUSTER (5 LB) MISALIGNMENT TORQUE	1.0	0.5
RADIAL THRUSTER (1.5 LB) MISALIGNMENT TORQUE	0.3	0.15
AUXILIARY AXIAL (0.75 LB) UNBALANCE TORQUE	0.3	0.15
RSS	1.1	0.55

Considering the low level of these pointing errors compared to those experienced by the Jupiter Orbiter at low-spin rate, a spinup maneuver prior to a main thrust phase which was proposed for that configuration to control pointing errors is not required in the case of the asteroid spacecraft.

Analysis of spin rate changes due to thrust misalignment torques shows that for the small thrust level used in this spacecraft these changes do not exceed 0.02 rpm and therefore present no problem.

#### 6.5.5 Optical Sensor Pointing

The question of optical sensor pointing accuracy arises in two areas:

- 1) Accuracy of navigational fixes by the star mapper
- 2) Perturbations of spacecraft attitude due to rapid rotation of the optical science sensor package during the critical phase of an asteroid encounter.

The first problem involves holding the observational errors due to residual wobble to a level of less than 0.1 mrad. This can be met by allowing the spacecraft to settle into a steady state with negligible wobble errors after each attitude perturbation. Residual pointing errors present no problem since they have no influence on the accuracy of the navigational observation.

The second problem involves the precession and nutation effects resulting from angular momentum exchange during rapid rotation of the sensor package. Mass distribution changes can be ignored because of the small mass of the sensor package and its location close to the c. g. of the spacecraft.

The requirement for control of pointing errors and residual nutations during the close approach phase is not stringent, and errors of several milliradians can be accepted without causing degradation in asteroid imaging. The worst case momentum exchange effect occurring under maximum sensor slewing rates of 5 deg/sec is actually less than 0.25 mrad.

Optical sensor pointing errors due to spacecraft dynamics have been evaluated and will be discussed in Section 7.2. In all cases considered, these errors can be reduced to levels compatible with pointing accuracy requirements of the mission.

## 6.6 POWER REQUIREMENTS

Table 6-6 lists estimated power requirements of the asteroid Pioneer spacecraft at various mission phases. These requirements can be met by the present SNAP-19 RTG power sources as will be discussed in Section 7. The total power requirement varies from 78.2 W as a minimum, with only cruise science instruments (16.6 W) operating, to 126 W during the pre-encounter/encounter phase when the entire payload complement (30.3 W) is turned on. These estimates represent only the steady loads. During the first two years of operation, the four SNAP-19 RTGs provide a satisfactory power margin (130 watts two years after launch). After this time, with available power becoming marginal some of the less essential experiments may be turned off, unless enough battery power is available to augment the power supply during the short period of an encounter.

Estimated pulse loads (adapted from Pioneer F and G) are given below to indicate typical requirements. None of the pulse loads need overlap since they are all commanded separately. The peak pulse is due to changing transmitters or receivers between antennas. The auxiliary thruster will be used intermittently throughout the mission, while the

Table 6-6. Estimated Power Requirements by Mission Phase

EQUIPMENT	LAUNCH	CRUISE-DORMANT	CRUISE-XMIT	CRUISE-RECEIVE	PRE-ENCOUNTER ENCOUNTER
DIGITAL TELEMETRY UNIT	3.8	3.8	3.8	3.8	3.8
DIGITAL DECODING UNITS	1.0	1.0	1.0	2.0	1.0
DATA STORAGE UNIT	5.0	5.0	5.0	5.0	5.0
RECEIVERS (2)	3.4	3.4	3.4	3.4	3.4
TRANSMITTER DRIVER	1.0	1.0	1.0	1.0	1.0
CONSCAN	1.2	1.2	1.2	1.2	1.2
SUN SENSOR	0.5	0.5	0.5	0.5	0.5
CONTROL ELECTRONICS ASSEMBLY	2.7	2.7	2.7	2.7	2.7
OPTICS POINTING ELECTRONICS	0.5	0.5	0.5	0.5	0.5
STAR SENSOR	1.0	1.0	1.0	1.0	1.0
COMMAND DISTRIBUTION UNIT	3.6	3.6	3.6	4.6	3.6
SUB-TOTAL (CTRF OUTPUT)	23.8	23.8	23.8	25.7	23.8
CTRF LOSSES (63% EFF)	<u>13.9</u>	<u>13.9</u>	<u>13.9</u>	<u>15.1</u>	<u>13.9</u>
CTRF INPUT	37.7	37.7	37.7	40.8	37.7
PROPULSION TRANSDUCERS	0.2	0.2	0.2	0.2	0.2
PROPULSION HEATERS	2.0	2.0	2.0	2.0	2.0
S-BAND TRANSMITTER	4.0	4.0	4.0		4.0
X-BAND TRANSMITTER (7 W R-F, 28% EFF)	25.0		25.0		25.0
GIMBAL DRIVE	2.0	2.0	2.0	2.0	2.0
COMMAND DISTRIBUTION UNIT	0.2	0.2	0.2	0.2	0.2
PCU LOSSES	3.0	3.0	3.0	3.0	3.0
EXPERIMENTS		16.6	16.6	16.6	30.3
SUB-TOTAL	74.1	65.9	90.7	64.8	104.4
CABLE LOSSES (2% OF LOAD)	<u>1.5</u>	<u>1.4</u>	<u>1.8</u>	<u>1.3</u>	<u>2.1</u>
	75.6	67.1	92.5	66.1	106.5
RTG INVERTER LOSSES (88% EFF)	<u>10.4</u>	<u>9.1</u>	<u>12.9</u>	<u>9.1</u>	<u>14.7</u>
	86.0	76.2	105.4	75.2	121.2
RTG CABLE LOSSES (4%)	<u>3.4</u>	<u>3.0</u>	<u>4.2</u>	<u>3.0</u>	<u>4.8</u>
VEHICLE TOTAL POWER	89.4	79.2	109.6	78.2	126.0

ORIGINAL PAGE IS  
OF POOR QUALITY

6-30

<u>Function</u>	<u>Watts</u>
Experiment	5 - 8
Transfer switch (commanded switching between antennas)	14 (50 millisecc)
Thruster pair (every firing)	11.2
Main thruster	10
Battery heater	1.6

main thruster (which requires about ten watts) is operated only twice during the mission. This thruster will never be fired simultaneously with the auxiliary thruster pairs, thus the two peaks can be kept separated. If the combined steady and pulsed power requirements should exceed the available power as augmented by the battery, equipment or experiments will have to be temporarily shut down.

## 7. SUBSYSTEMS

This section discusses the subsystems of the multi-asteroid mission spacecraft and describes the principal modifications from existing Pioneer F and G hardware and from design concepts developed for the Pioneer Jupiter Orbiter (Configuration 1). Emphasis in this discussion will be on subsystems with major modifications that are dictated by the asteroid mission objectives and operating modes. Subsystems with modifications of more routine type will be described in less detail.

The principal concern in the subsystem study, as in the overall spacecraft design, has been to limit the extent and cost of modifications while insuring that the basic mission objectives can be met. As the results presented in the preceding sections have shown, this economical approach in system adaptation is reflected by some constraints on mission performance, and on selection of mission parameters, none of which are so severe as to compromise the scientific value of the mission.

### 7.1 PROPULSION SUBSYSTEM

#### 7.1.1 General Approach

The propulsion subsystem is designed to perform attitude control, midcourse trajectory corrections, retargeting, and terminal maneuvers. As discussed in Section 3, the total maneuver requirements range from 850 to 950 m/sec depending on the particular asteroid mission profile selected. The basic objective of the study was to identify a minimum risk approach that meets the mission requirements while utilizing as much of the existing Pioneer F and G propulsion system hardware as practical.

Pioneer F and G uses a simple blowdown hydrazine propulsion system. Trajectory and orientation control is exercised by axial and circumferential thrusters mounted in two clusters on opposite sides of the spacecraft near the rim of the high-gain antenna. The axial thrusters are operated in the continuous thrust mode to provide fore and aft  $\Delta V$  corrections, and in the pulsed mode to precess the spacecraft spin axis. The circumferential thrusters are used to change or adjust the spacecraft spin rate.

This control thruster configuration can be adopted without change as part of the asteroid spacecraft propulsion system. A modification of the overall system is required to provide the required larger propulsion capability. For this purpose the modified propulsion system design of the Jupiter Orbiter spacecraft can be adopted which has nearly the same total maneuver  $\Delta V$  capability as that required for the asteroid spacecraft. This system must be augmented by the addition of a pair of radial thrusters that can be integrated with the thruster assemblies of the Pioneer F and G configuration.

Radial thrust, exercised in a pulsed thrust mode in combination with axial thrust, permits maneuvers in any direction without requiring a re-orientation of the spacecraft. This is an essential propulsion mode required for the asteroid spacecraft in contrast to the baseline Pioneer and the Jupiter Orbiter, because of the frequent small maneuvers that must be performed in this mission.

#### 7. 1. 2 Propulsion Requirements and Constraints

The propulsion subsystem is required to provide impulse for attitude control and  $\Delta V$  maneuvers, similar to the Pioneer F and G subsystem. For the asteroid mission however, the subsystem must provide additional impulse for retargeting and terminal guidance maneuvers. This added requirement dictates a significant increase in the propellant load relative to Pioneer F and G, and has a significant impact on the propulsion subsystem design.

Compared to the Jupiter Orbiter mission which has a similar total  $\Delta V$  requirement, the thrust requirements for the asteroid spacecraft differ primarily in two respects:

- 1) Thrust time for the major trajectory changes ( $\Delta V \cong 600$  m/sec for retargeting) is not a critical factor and does not have to be limited for thrust effectiveness reasons as in the orbit insertion maneuver. Hence, a much smaller thrust level than the 50 lbf main thrust selected in the Jupiter Orbiter is sufficient for this mission.

- 2) A large number of maneuvers, rather than only a midcourse correction and a major maneuver at destination, is required in the asteroid mission, including two retargeting maneuvers, six or more terminal guidance maneuvers, and several trim maneuvers. This requires that an unconstrained thrust orientation capability be provided without spacecraft reorientation, e. g., by a thrust mode combining axial thrust and pulsed radial thrust.

Design constraints of the Pioneer configuration make the addition of a thruster canted 12 degrees from the radial direction (78 degrees cone angle) more convenient than a thruster in purely radial orientation. Such a thruster can be added to the existing Pioneer control thruster assembly.

The requirement for the addition of a pulsed off-axis (radial) thrust capability to avoid frequent spacecraft reorientation, and hence, interruption of communications coverage via the high-gain antenna, is based on the following considerations:

- The large number of  $\Delta V$  maneuvers ( $\geq 12$ ) required during the mission, as explained above.
- Complications and possible risk to mission success caused by repeated loss of telemetry. Even the command link capability via the omniantenna could be lost if the earth-line were to coincide with a null of the antenna pattern in the reoriented spacecraft attitude.
- Critical timing of terminal maneuvers which makes a time loss due to reorientation maneuvers unacceptable.
- Complications involved in reacquisition of reference stars and target asteroids by the navigation sensor.

An exception to this reorientation constraint is permissible only in the case of the major retargeting maneuvers. Since these maneuvers involve about two-thirds of the total  $\Delta V$  capability of the spacecraft, the loss in thrust effectiveness due to pulsed radial thrust operation, in combination with axial thrust, can be excessive and is generally not acceptable. Losses in thrust effectiveness are caused by the vector combination of axial and radial thrust components, by the finite length of

the thrust arc, (which results in a cosine-loss), and by the reduction of effective  $I_{sp}$  in pulsed operation. This will be further discussed below.

Precession and nutation effects that build up during a  $\Delta V$  maneuver as a result of thrust misalignment or unbalance must be controlled to avoid loss of earth lock. Even with S-band instead of X-band coverage during the maneuver, permitting orientation changes of up to about  $\pm 2$  degrees, the precession and nutation effects limit the permissible misalignment torques.

Residual nutations after each terminal guidance maneuver should be minimized to limit wobble decay time so as to permit early resumption of navigational fixes in iterated terminal guidance.

To permit accurate fixes the residual wobble angle must not exceed 0.1 mrad. This requires that a nutation damping time of about 5 time constants ( $\sim 1$  hour) be allowed during which the wobble amplitude decays from an initial value of 1 deg. to 0.1 mrad.

Trim pulses can be used to compensate for known thrust misalignment effects and thus to minimize wobble. This requires that calibration measurements be made from time to time during the mission to update the correction program.

### 7.1.3 Alternative Approaches and Tradeoffs

#### 7.1.3.1 Off-Axial Thrusting

Alternative approaches for achieving the required off-axial thrust capability include these options:

- Use the spin/despin thrusters in pulsed operation, e. g. , alternate thrusters operating during opposite portions of the spin cycle, to provide a thrust component perpendicular to the spin axis.
- Add a pair of radial thrusters at 90-degree cone angle in a location separate from the present thruster cluster.
- Add a pair of canted radial thrusters to the present thruster assembly using a cone angle dictated by the location of this assembly in the Pioneer configuration.

The concept of using the spin/despin thrusters was discarded because of the unacceptably large precession side-effect produced by repeatedly thrusting in the same inertial direction with a thrust offset along the Z-axis. To compensate this effect an unacceptably large additional thrust impulse by the precession thrusters would be required. Considering the moment arms of the Pioneer configuration, this would amount to about one-half the impulse expended to achieve the desired  $\Delta V$  maneuver, i. e., imposing a 50-percent maneuver penalty.

The second approach which requires the addition of purely radially oriented thrusters was also discarded because of unfavorable installation aspects. If these thrusters are mounted on the spacecraft center body in the plane containing the nominal c. g. there is a potential interference with spacecraft and payload functions due to exhaust plume impingement. In any case, a location separate from the existing control thruster assemblies would necessitate additional propellant lines and cabling. This can be avoided by integrating the radial thruster with the present assembly and accepting a cant angle offset.

Addition of one canted radial thruster to each of the existing thruster assemblies is desirable to provide redundancy and to double the radial  $\Delta V$  impulse obtainable per spin cycle. The thrust level of the pulsed radial thruster should preferably be larger than that of the axial thruster to provide effectively the same thrust capability in the two directions. The proposed thruster has a nominal thrust level of 1.5 lbf. Thus, for a +45-degree thrust arc of each thruster, the total effective radial thrust impulse per revolution is equal to that of the pair of 0.75 lbf axial thrusters in the present configuration.

#### 7. 1. 3. 2 Losses in Off-Axial Thrust Operation

Losses in propellant utilization that result from combined axial and radial thrusting are due to

- a) Vectorial addition of thrust components
- b) Reduced  $I_{sp}$  of pulsed thrust operation
- c) Effect of thrusting over a finite arc rather than impulsively (cosine loss)

The vector combination loss varies with the desired thrust orientation. It is zero for purely axial or purely radial thrust operation (or in the case of a cant angle, for operation purely at this cant angle). Maximum losses occur about halfway between the purely axial and purely radial (or canted radial) orientations.

The combined  $I_{sp}$  loss and cosine-loss can be minimized by an appropriate choice of pulse duration, so as to avoid significant  $I_{sp}$  losses that would occur for very short pulses and significant cosine losses for longer pulses. This is illustrated in Figure 7-1. A 2-second pulse, corresponding to a total thrust arc of 60 degrees, is nearly optimum with  $I_{sp}$  losses and cosine losses about 4 percent each. The combined loss increases to about 12 percent for a pulse length of 3 seconds, i. e., a total thrust arc of 90 degrees, due to the increase in cosine loss with length of the thrust arc.

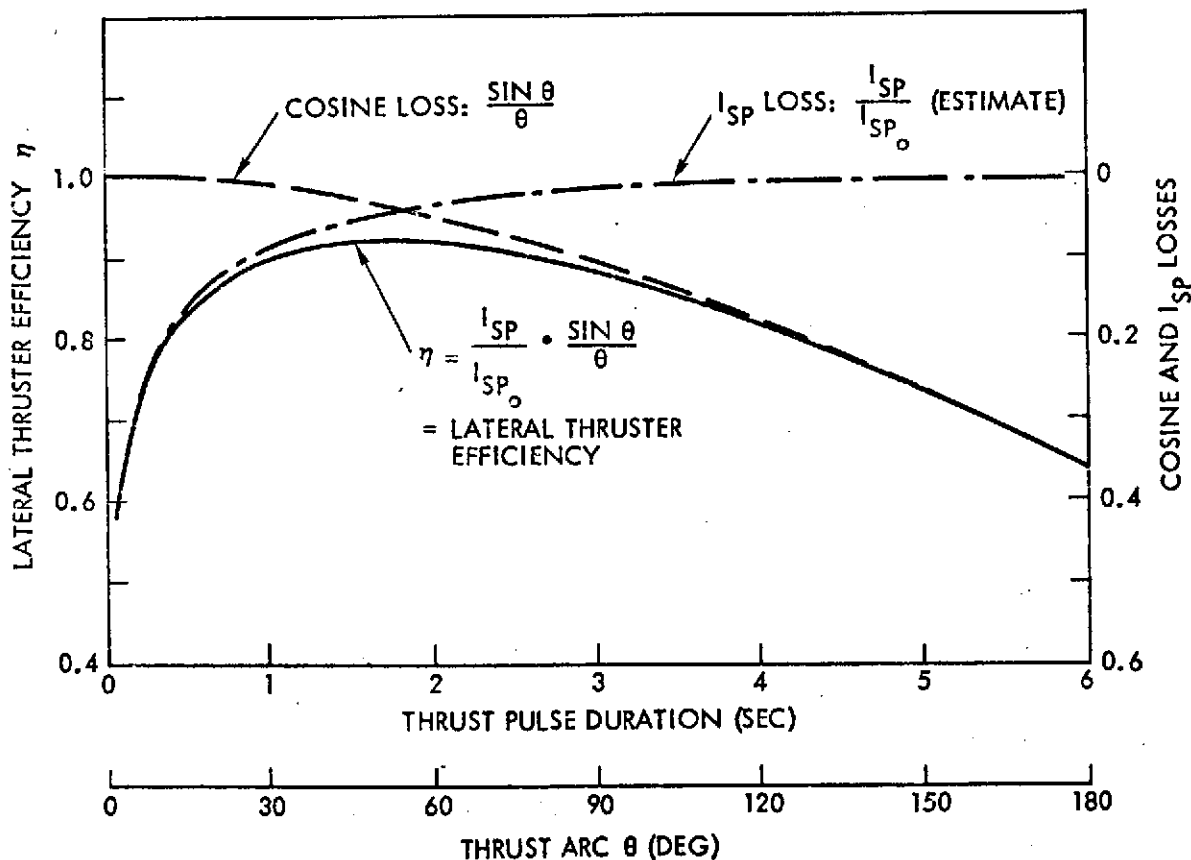


Figure 7-1. Lateral Thruster Efficiency

The combined effect of these losses has been analyzed in a concurrent TRW study, and some of the results are presented here.\* Figure 7-2 shows the variation of thrust effectiveness under varying thrust orientations in the spacecraft Z-Y plane. Thrust effectiveness is expressed in terms of the effective  $\Delta V$  increment obtainable per unit propellant expenditure, normalized to the  $\Delta V$  resulting from a purely axial thrust. A reference circle of radius 1 is used to show the variation of thrust effectiveness with thrust cone angle compared to the ideal case of no losses.

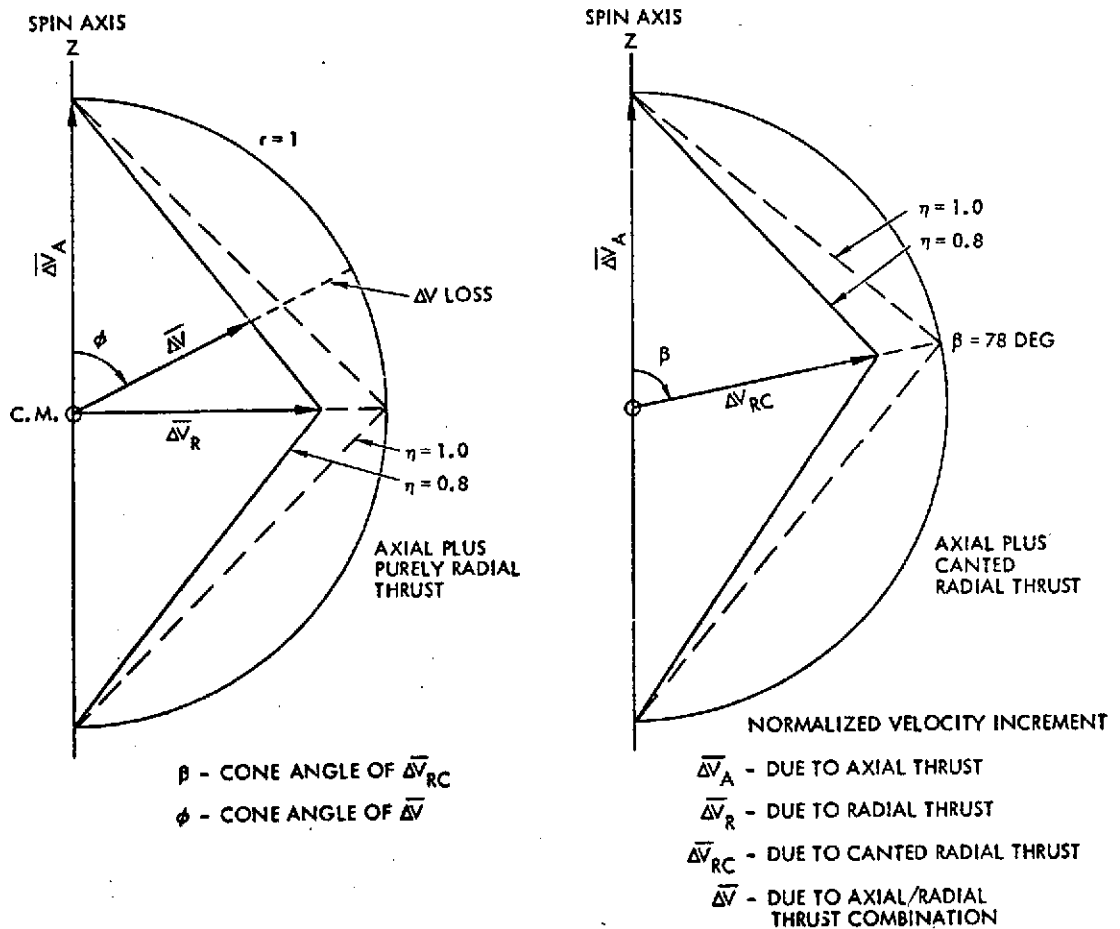


Figure 7-2. Velocity Increments Due to Combined Axial and Radial Thrust

The two diagrams shown in Figure 7-2 illustrate the cases of a purely radial (left) and a canted radial pulsed thruster (right). The apex of the triangles depicting the thrust effectiveness variation with cone

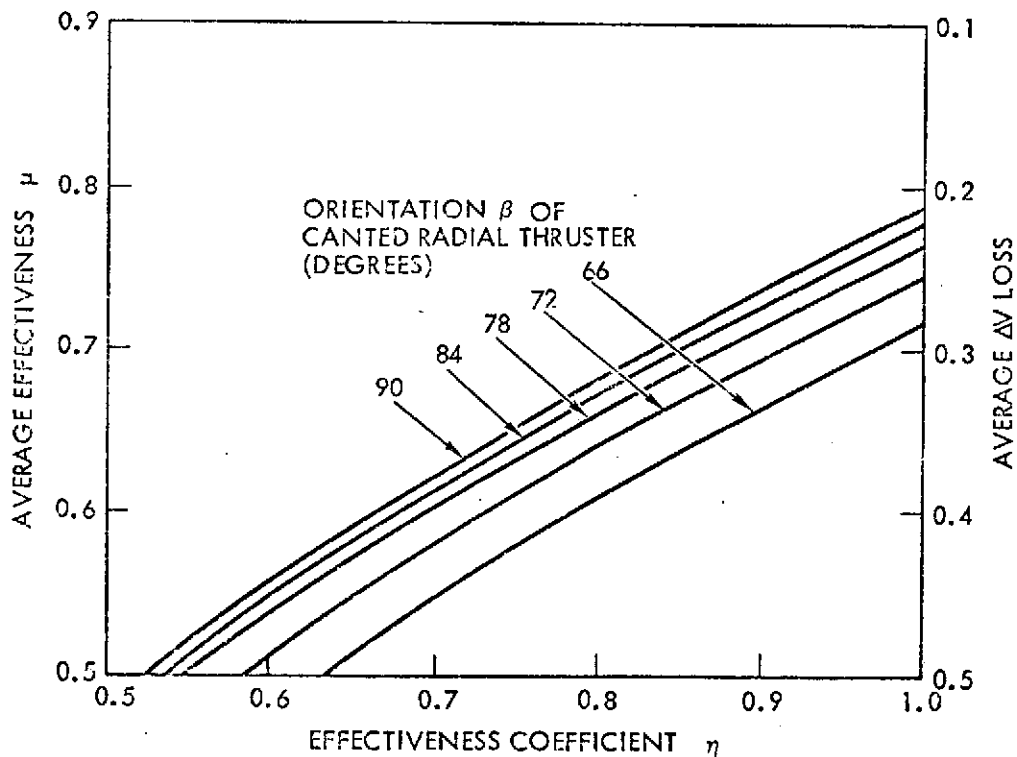
\*From an unpublished report by W. J. Dixon, TRW Systems.

angle would be at unity radius in the absence of pulse losses, as indicated by dashed lines.

The triangles in Figure 7-2 also indicate the losses under out-of-plane thrust conditions. One can visualize this by letting the triangle rotate with the spacecraft around the Z-axis. This shows that the variation of thrust effectiveness with cone angle does not vary with clock angle.

If arbitrary maneuvers are considered where thrust orientations are assumed to be equally likely in all directions, an average thrust effectiveness coefficient  $\mu$  can be defined which takes the relatively higher percentage of thrust requirements in radial directions compared to those in axial directions into account. This implies averaging over all orientations on a sphere rather than over the cone angle only.

Figure 7-3 shows the average thrust effectiveness  $\mu$  as function of thrust efficiency  $\eta$ . This parameter includes only the pulsed thrust losses ( $I_{sp}$  and cosine losses), e. g.,  $\eta = 0.92$  for a two-second thrust arc.



( $\eta$  INCLUDES  $I_{sp}$  AND COSINE LOSSES ONLY)

Figure 7-3. Average Thrust Effectiveness for Combined Axial and Radial Thrust with Arbitrary Maneuver Orientations in Three Dimensions

The curves in Figure 7-3 are shown for various orientation angles  $\beta$  of the canted radial thruster. We note that the cant angle offset of 12 degrees ( $\beta = 78$  degrees) has only a small influence on the average value  $\mu$  compared to the case of zero cant angle (see also Figure 7-2).

We conclude from this discussion that combined  $\Delta V$  losses of 25 to 30 percent are typical under the conditions assumed here. Since this penalty only affects the small maneuvers for which a total  $\Delta V$  of 150 m/sec has been allocated, an allowance of 56 m/sec of extra  $\Delta V$  capability is adequate, or about 21 pounds of extra propellant. This allowance has been included in the  $\Delta V$ -budget shown in Section 3.7 (Table 3-3).

We also note that in some instances off-axial thrust can be permitted for major maneuvers if radial components are sufficiently small. Thus, 10 pounds of extra propellant expenditure would permit off-axis orientations of 6 or 8 degrees, and 20 pounds, 12 or 20 degrees in a 300 m/sec maneuver, depending on whether the axial component is oriented fore or aft. This amount of extra propellant may actually be affordable in exchange for avoiding spacecraft reorientation, depending of course on the total maneuver requirements of a selected mission. A low- $\Delta V$  mission could afford this more readily.

#### 7.1.3.3 Thrust Level Considerations

The thrust level of the Pioneer F and G axial control thrusters is nominally 0.75 pound. This thrust level was adopted in the present design primarily to restrict the minimum impulse in small precession maneuvers to a low level. If the thruster is used for axial  $\Delta V$ -corrections, the low-thrust level requires an extended thrust time.

Figure 7-4 shows the magnitude of the  $\Delta V$  increment obtainable as function of thrust acceleration level for various thrust durations. For example, a 1-lbf axial thruster requires between 40 minutes and 1 hour to achieve a velocity increment of 30 m/sec, depending on the amount of propellant left, for a gross spacecraft mass of 1000 pounds. This thrust duration is sufficiently short in mission phases where time is not critical. During terminal maneuvers the  $\Delta V$ -increments become successively smaller as time-to-encounter decreases, such that thrust durations reduce to a few minutes for each residual velocity correction of 5 m/sec.

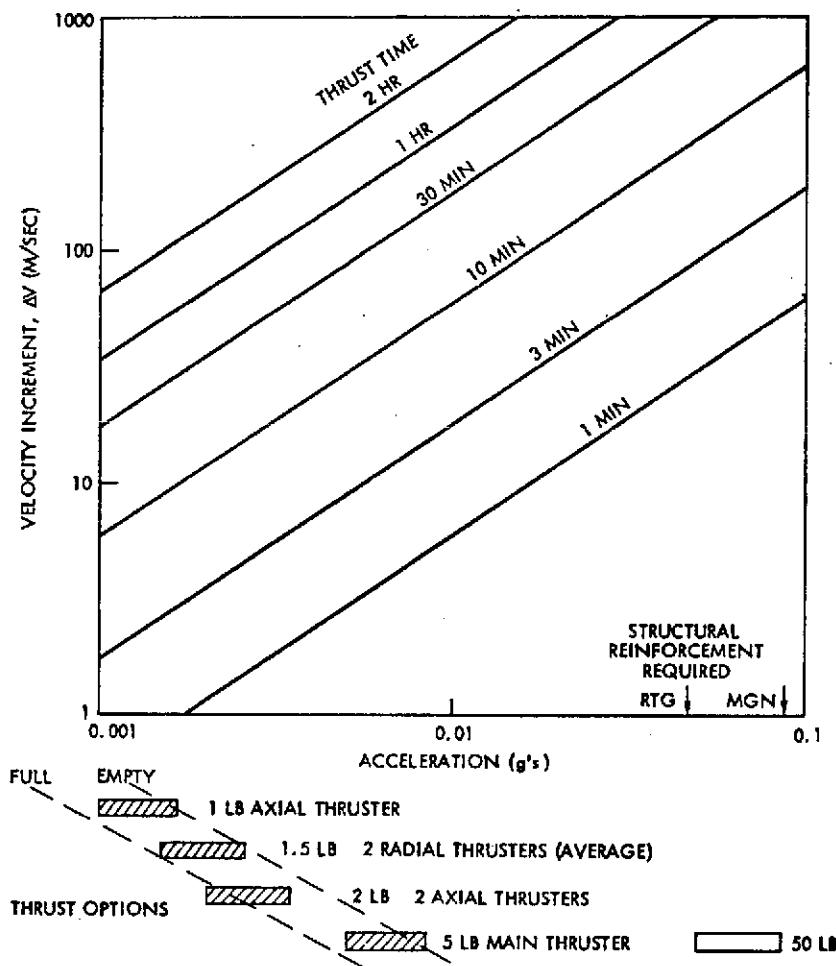


**Figure 7-4. Velocity Increment Vs Acceleration**

The main axial thruster to be used for the large retargeting maneuvers has a thrust level which was tentatively selected as 5 lbf. Two considerations apply in the selection of this value: (1) extended thrust times up to several hours are not serious because the maneuver is performed at a non-critical phase of the mission. Thus, the large 50 lbf thrust level selected for the Jupiter Orbiter deboost maneuver is not required here, and the structural load on deployed appendages can be reduced to a level where no reinforcement is required. The threshold of required reinforcements is 0.04  $g$  for the RTG arms and 0.09  $g$  for the magnetometer boom. (2) Excessively long thrust times during which the spacecraft must remain in off-earth orientation can be avoided with the selected 5-pound thrust level: Figure 7-4 shows that a 300 m/sec maneuver requires only between one and two hours.

Reduction of thrust level also means a reduction of misalignment torques that would cause nutation to build up during continuous thrust operation. The maximum nutation angle during main thrust firing is 1.7 degrees corresponding to a disturbance torque of 0.5 ft-lb. For the large 50 lbf thrust level required in the Jupiter orbit insertion maneuver the nutations would become unacceptably large, and a spin-up to 10 to 15 rpm is required before thrust application. The smaller 5 lbf thruster eliminates this complication.

During the main retargeting maneuvers the spacecraft is oriented off the earthline unless mission characteristics are exceptionally favorable, making reorientation unnecessary (see Section 3). Small nutation angles are desirable even in this mode, though not dictated by pointing requirements of the high-gain antenna. A large nutation angle would complicate the open-loop reacquisition maneuver that must be performed after completion of the thrust phase.

#### 7.1.3.3 Propellant Tank Size

Increase in propellant tank size to 26-inches diameter gives a total usable propellant capacity of 340 pounds compared to 300 pounds for the 25-inch tank selected for the Jupiter Orbiter spacecraft. The extra one-inch size introduces a small design complication, identified in the Jupiter Orbiter design study: the load transfer to the 25-inch adapter ring upper flange requires a slightly tapered instead of a cylindrical support structure which must also be reinforced to support the heavier tank. On the other hand, the more than 12 percent increase in propellant capacity achievable by the small (four percent) increase in diameter provides a margin of 100 m/sec in total  $\Delta V$  capability. In the discussion of performance characteristics (Figure 3-3) it was shown that with a payload-weight/propellant-weight exchange ratio of about 2:1 the 40 pounds of extra propellant make a difference in payload capacity of about 80 pounds, which encompasses the entire payload weight to be carried.

An upper limit to the tank size increase is dictated in part by the tank mounting requirement which is governed by the spacecraft c. m. location and the control of products of inertia, as discussed in Section 6. Under this constraint the selected tank size requires a 20-inch circular

cutout in the center of the high-gain antenna dish, unless the structure is changed to move the antenna dish upward. (This option was ruled out as an unacceptably costly structural change.) With the dimensions of the existing configuration a further increase of the tank diameter by one inch would increase the cutout by 2.5 inches, a 27-percent increase in area compared to the 20-inch cutout of the proposed design. Even without analysis of the impact of such a modification on antenna characteristics, it is apparent that a 26-inch tank size is about the largest that can be accommodated without demanding significant additional structural modifications.

#### 7.1.3.4 Use of External Ullage Tanks

A detailed comparison of design options for distribution of propellant volume and pressurant gas volume was performed in the Jupiter Orbiter study. As a result the configuration using two external pressurant tanks rather than internal ullage was found to be preferable from a standpoint of propellant capacity, weight savings and effective pressurization of the hydrazine. This configuration was adopted for the asteroid spacecraft.

The two external pressurant tanks permit the use of the simple but efficient two-stage blowdown pressurization technique which raises the average pressure of the unregulated system and thus achieves a significantly higher average  $I_{sp}$  value. Table 7-1 (from the Jupiter Orbiter study) compares the characteristics of a single-stage blowdown, two-stage blowdown and a pressure-regulation system.

Table 7-1. Pressurization System Characteristics

	Single-Stage Blowdown	Two-Stage Blowdown	Pressure Regulation
Impulse	91 percent	95 percent	100 percent
Complexity	Least	Nominal	Most
Cost	Least	Nominal	Most
Weight	Least	Nominal	Most
Hardware status	Available	Available	Available

#### 7.1.4 Propulsion Subsystem Description

Adaptation of the blowdown pressurization, monopropellant hydrazine system of the current Pioneer F and G to the asteroid spacecraft requirements was found to be the simplest most economical approach. The propulsion subsystem schematic is presented in Figure 7-5. The recommended modifications include a larger, 26-inch diameter propellant storage tank, external pressurant tanks for two-stage blowdown (propellant tank repressurization), a main axial and two canted radial thrusters. The system retains the current Pioneer F and G feed system components and attitude control thrusters. Hydrazine technology is well advanced and monopropellant systems are inherently simple. Therefore, they offer low cost, and relatively short program schedules. These, in addition to the adequate performance, make a hydrazine subsystem best suited for this application.

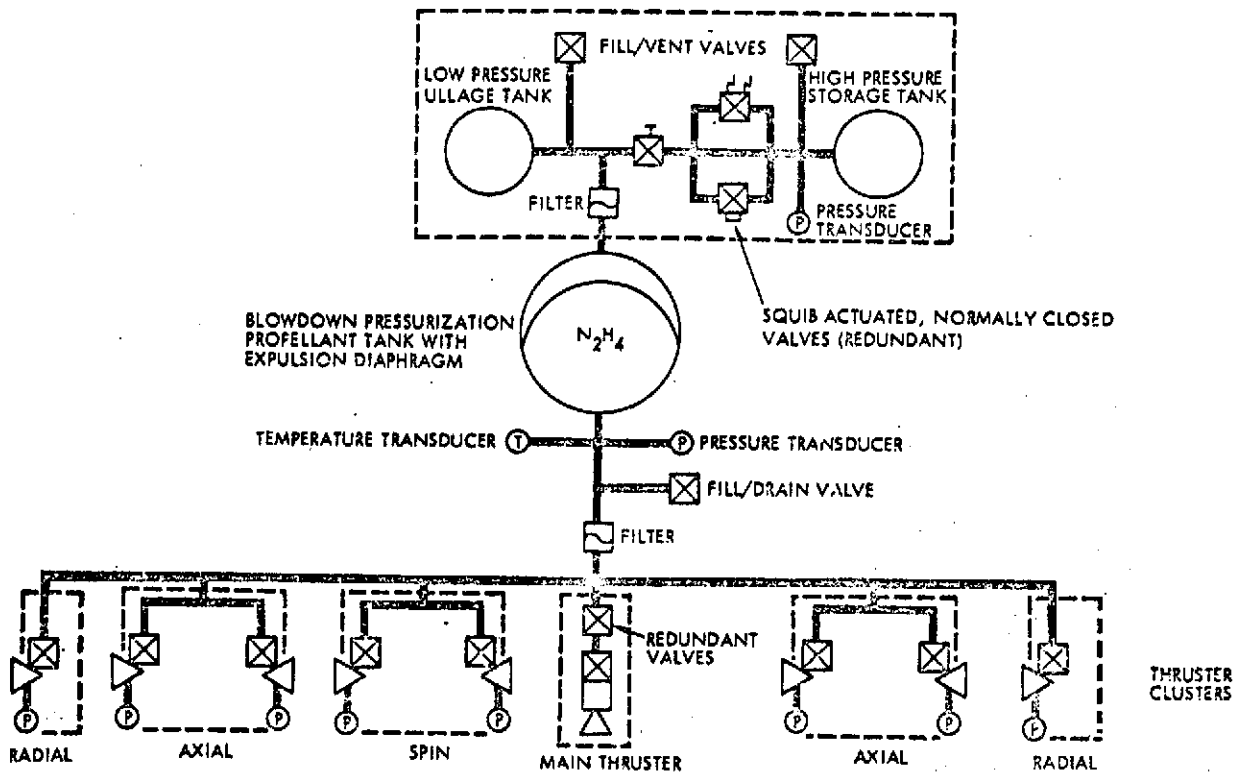


Figure 7-5. Hydrazine Propulsion System

The 340-pound propellant load is stored in a single tank located on the spacecraft spin axis. This tank is of the same design as the Pioneer F and G tank, except larger in diameter, and incorporates an EPT-10 expulsion diaphragm. Pressurant for two-stage blowdown operation is stored in two external tanks of 9.5-inch diameter. This size tank is available from TRW's Intelsat III spacecraft program. One tank is pressurized to 550 psia; the other is pressurized to approximately 2000 psia and isolated from the 550 psia system. As propellant is used, the ullage volume increases and the pressure drops accordingly. After approximately 50 pounds of hydrazine is expelled, the ullage volume and low-pressure system pressures are at a point where the high-pressure tank isolation valves can be actuated open onboard or by ground command. (See Figure 7-6.) This repressurizes the propellants to approximately 550 psia. The low pressure at the end of life is 150 psia. Figure 7-7 shows the corresponding variation of  $I_{sp}$  and illustrates the performance advantage of maintaining an increased average pressure.

Spacecraft attitude control and midcourse trim maneuvers are accomplished in a manner identical to Pioneer F and G with low-thrust thruster clusters. These units will have essentially the same mounting, interfaces, and plumbing as the current Pioneer F and G subsystems.

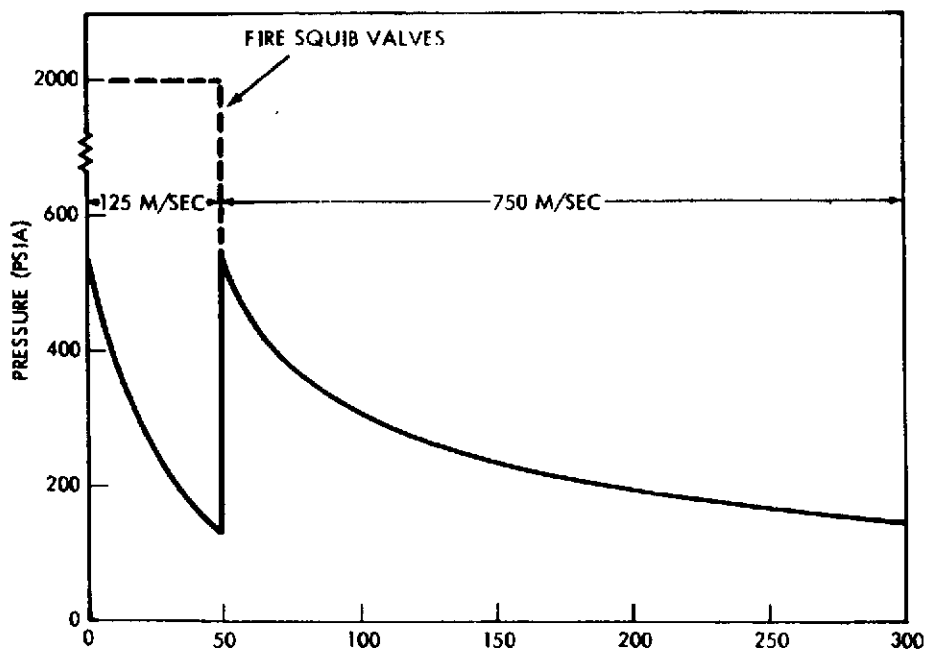


Figure 7-6. Propulsion Subsystem Pressures Vs Propellant Expended (Two-Stage Blowdown)

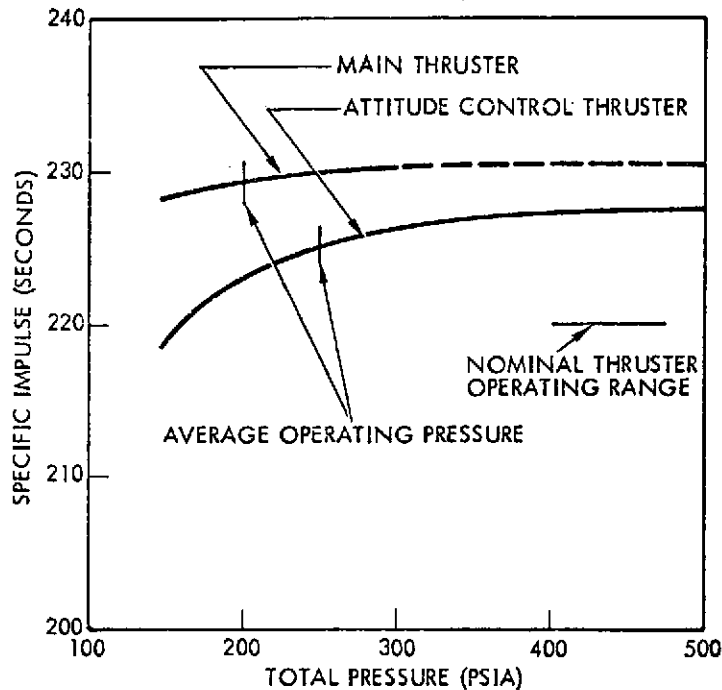


Figure 7-7. Hydrazine Subsystem Performance,  
 $I_{sp} = 226$  sec (nominal)

The main axial impulse for retargeting maneuvers is provided by a 5 lbf hydrazine thruster. Parallel redundant multiple cycle isolation valves are recommended to insure leak tightness over the three-year mission and maximize mission flexibility. The isolation valves will normally be commanded open first, then the thruster valve. The maneuver can be terminated by commanding either the isolation or the thruster valve closed first. This valving approach allows the mission to be successfully completed in the event a main thrust hydrazine valve fails in the open position.

Pioneer F and G fill and drain valves, pressure transducers, temperature sensors, and radioisotope heaters are also used on the recommended subsystem. A modified version of the existing pressure transducer will be used to monitor the high-pressure system pressures. Squib valves proved on a TRW military satellite are recommended for high-pressure tank isolation.

Thermal control for a large portion of the propulsion subsystem will be similar to the current Pioneer F and G, i. e., both electrical and

isotope heaters are recommended. Power requirements for the recommended hydrazine subsystem are dependent on system operations. Approximately one watt for pressure/temperature sensors is required during inactive modes. Approximately 6-11 watts will be required during attitude control maneuvering depending on the number of thruster firings, and 10 watts during main thruster firing.

## 7.2 ATTITUDE CONTROL SUBSYSTEM

### 7.2.1 Summary

The present Pioneer F and G attitude control subsystem is made up of a conical scan processor, sun sensor assembly (SSA), stellar reference assembly (SRA), despin sensor assembly (DSA), and control electronics assembly (CEA).

The attitude control subsystem (in conjunction with the propulsion subsystem) provides spin control, spin axis pointing control, and velocity control. In addition, it references scientific experiments, and provides telemetry of attitude control functions.

The spacecraft communications subsystem, using an offset antenna feed, generates an RF signal, amplitude modulated in a sine wave whose magnitude is a function of the angular distance from the spacecraft spin axis to the earth-line. This sine wave is processed, and a nulling mechanization using the precession control thrusters, aligns the spin axis to the earth.

The SSA and SRA provide sun and star pulses, respectively, for establishing a reference about the roll axis. The SSA pulses are used during open-loop precession and as a redundant roll reference backup for indexing scientific experiments. The SRA provides the primary roll reference for indexing experiments and serves as a secondary reference for open- and closed-loop precession maneuvers. The DSA, used only during the despin operation, signals when the reduced spin speed is compatible with successful RTG deployment. The CEA processes sensor inputs, input commands, and commands the velocity, precession and spin control thrusters, in addition to controlling power to all units within the CEA and providing processed sensor pulses and telemetry outputs.

Spin speed is reduced from the stowed condition level to an intermediate speed to permit RTG and magnetometer deployment. Post-deployment spin speed is maintained near 4.8 rpm in response to ground commands. Precession maneuvering and velocity control is performed using the precession velocity control thrusters controlled either in real-time (closed-loop) or by programmed commands.

The ACS for the asteroid spacecraft is virtually identical to that of Pioneer F and G (see Figure 6-4). Minor changes and additions are necessitated by the large  $\Delta V$  requirement. The large velocity corrections are performed by a 5-pound engine in lieu of the precession/velocity thrusters, requiring a minor modification in the command structure. Additional reorientation maneuvers for engine burn are accommodated without change.

The stellar reference assembly of the baseline Pioneer is replaced by the gimballed star sensor which is used for navigational observations, and to provide roll reference pulses from a selected reference star at times when the sun reference pulse is not suitable, i. e. , when the earth and sunline are too close to coincidence. The ACS also controls the gimbal angles of the star sensor and the optical science sensor assembly.

### 7.2.2 Recommended Design

The attitude control subsystem design is based upon the Pioneer F and G design. Modifications and additions reflect the increased operational demands of the asteroid missions. All fundamental characteristics of the Pioneer F and G ACS are retained, with augmentation only as required.

Spin Period Sector Generator/Roll Reference. The spin period sector generator (SPSG) of Pioneer F and G is driven by a roll reference pulse generated by either the sun sensor assembly or the star sensor. It divides each spacecraft spin revolution into 512, 64 and 8 sectors for use in experiment data indexing and conscan signal processing, for example. It also issues a "filtered" roll pulse, approximately in synchronism with the input roll pulse. The SPSG can be operated in the non-spin averaging mode, spin-averaging mode, or ACS mode. In the non-spin averaging mode, the period between successive roll pulses is used as the period over the next spin revolution. In the spin-averaging mode, the SPSG

measures the period over 64 revolutions instead of one revolution, thereby reducing measurement quantization errors.

Gimballed Star Sensor. The star sensor is operated in two modes:

- 1) Navigational observation mode
- 2) Stellar reference mode.

The instrument, described in Section 5, is gimballed to point in the cone angle direction required for acquisition of the asteroid prior to encounter (Mode 1) or for generating roll reference pulses from a bright reference star such as Canopus (Mode 2). During operation in Mode 1, a roll reference pulse can be obtained from one of the stars used as navigational references. This requires some additional gating logic and signal processing. The threshold of the instrument is reset in Mode 2 to eliminate all but the brightest reference star signals after this reference has been verified by the ground station. The pulse pair generated by the V-slit reticle poses no problem in the roll reference mode if the second pulse (cone angle detection pulse) is rejected by the instrument's gating logic.

The design of the light shade is simple for this instrument owing to the much smaller (4.2 degree) circular field of view compared to the  $38 \times 0.5$  degree field of view of the stellar reference assembly which is being replaced. Thus, any stray light from nearby appendages (magnetometer boom and RTG deployment structure) can be effectively shielded out.

The gimbal drive is actuated by a precision stepper motor. A digital shaft encoder is used to provide accurate cone angle data. Actually the accuracy of the gimbal drive is not critical to Mode 1 or 2 operation, since in both cases the instrument is held at a fixed gimbal angle while reference signals are obtained. Star maps generated by the sensor and telemetered to the ground can be used to determine the actual cone angle setting within the accuracy limits of optical detection and readout, i. e., 0.1 to 0.2 mrad.

Gimballed Optical Sensor Assembly. The attitude control system operates the common gimbal drive actuator for the three-optical science

sensors (image system, photopolarimeter and IR radiometer). A stepper motor actuator with precision shaft angle pickoff is used for this purpose. Actually, precision of pointing control is not essential to this unit since on close approach to the asteroid, pointing program errors of up to 0.5 degree may occur. Of greater importance is fast rotation capability during the most critical one to two minutes of the encounter. Angular rates of up to 5 degrees per second must be provided under extreme conditions. Details of the gimbal drive mechanism require further study.

Updated Sensor Pointing Program. As explained in Section 4, a stored payload pointing program is used as reference which is augmented during asteroid flyby by a feedback pointing correction, based on angular errors detected by the image system processor circuitry.

Figure 7-8 shows the principle of cone and clock angle error detection. The diagram on the left shows the image frame being swept by the spin motion along a circle of fixed cone angle. Cone and clock angle errors,  $\Delta\phi$  and  $\Delta\psi$ , due to an inaccurate pointing program stored onboard the spacecraft, can be detected by determining the offset of the asteroid image centroid relative to the frame. The enlarged view of the image frame on the right illustrates the process: a count of electronic scan cycles give the  $\Delta\phi$ -coordinate, and a count of spacecraft clock pulses during the electronic scan, starting at the time of the peak intensity, gives the  $\Delta\psi$ -coordinate. The electronic circuit used to implement this image center detection process is shown in Figure 7-9.

This figure shows a conceptual block diagram of the image sensor processing electronics required for onboard updating of the cone and clock angle pointing program.

The sensor output data in analog form are compared to the output of a digital-to-analog converter representing the content of an accumulator. The accumulator is reset to zero at frame start. The count of clock pulses in the accumulator is proportional to the peak intensity of the image pulses generated during the time scan and electronic scan. The lower half of the circuit determines which of the successive electronic scans generates the peak signal, and where in this scan the peak occurs. These two counts are transferred to storage registers and provide the basic clock and cone angle coordinates of the image center relative to the image frame.

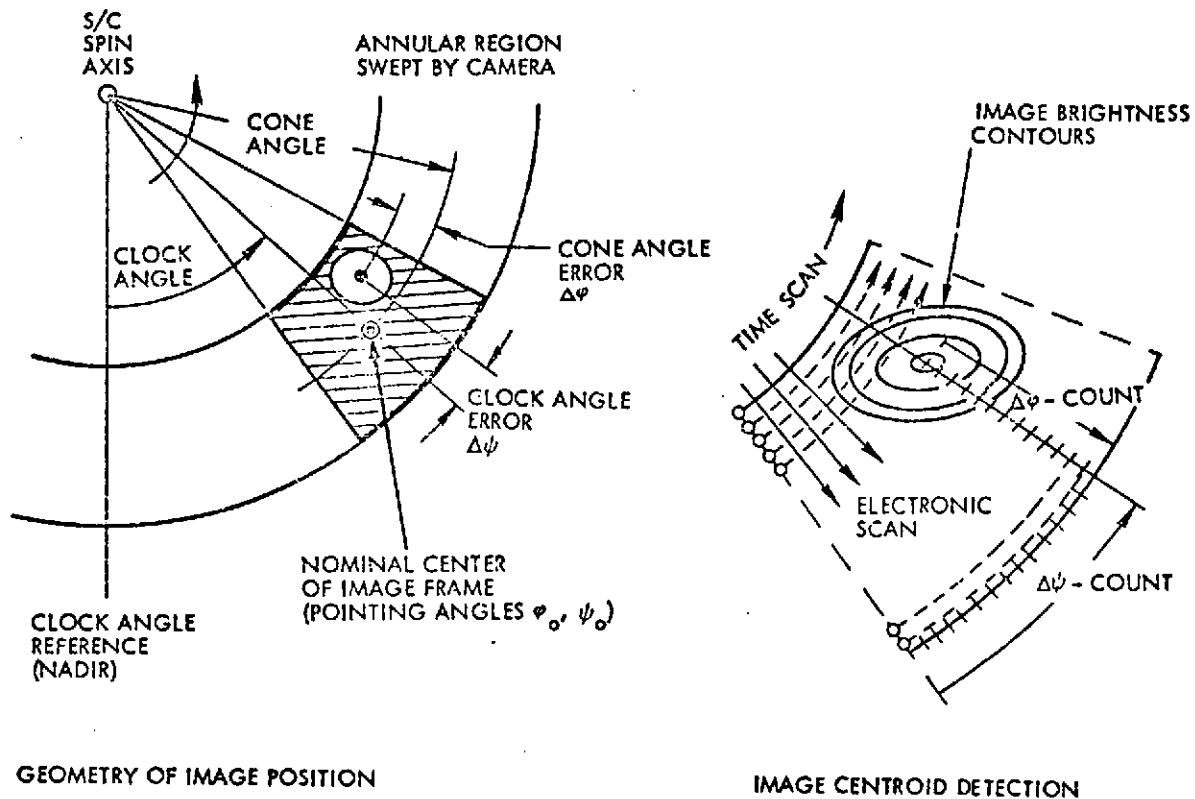


Figure 7-8. Detection of Clock and Cone Angle Errors by Image Data Processing

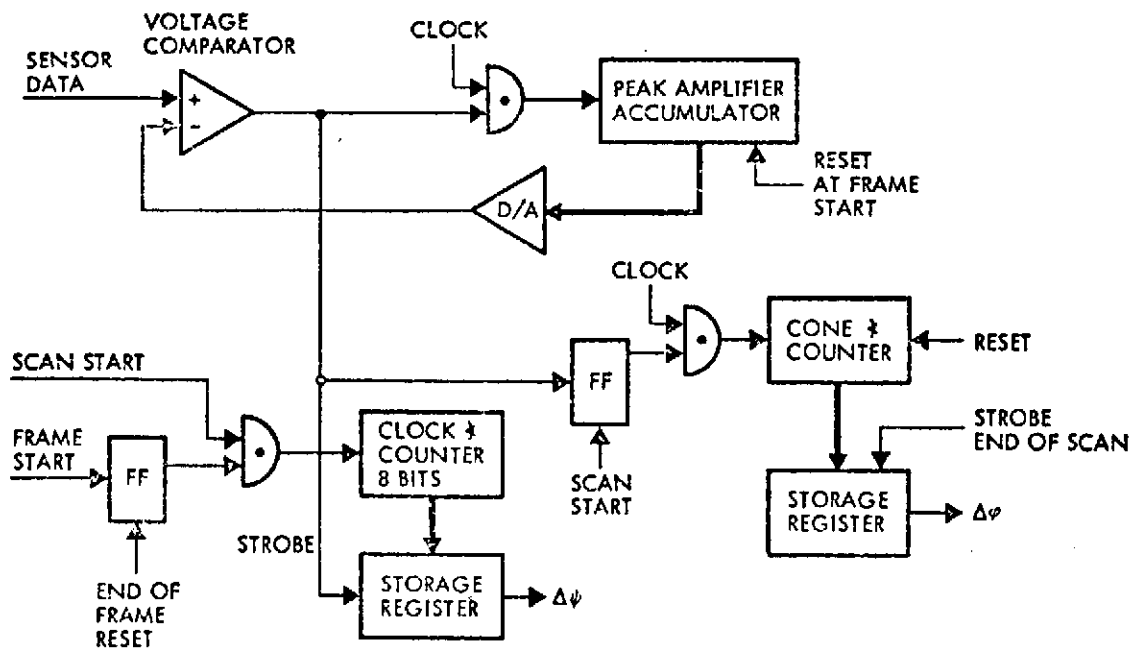


Figure 7-9. Image Data Processing for Cone and Clock Angle Detection

ORIGINAL PAGE IS  
OF POOR QUALITY

### 7.2.3 Wobble and Precession Effects

Table 7-3 summarizes the wobble and precession effects due to disturbance torques acting during continuous or pulsed thrust operation. The effect of momentum exchange due to rapid reorientation of the gimballed optical sensor package at encounter is also included (Item 2).

Table 7-3. Wobble and Precession Effects

1.	RESIDUAL WOBBLE DURING NAVIGATION FIXES (~20 MINUTE DELAY TIME AFTER MANEUVERS)	<0.1 MRAD
2.	EXCURSIONS DUE TO GIMBALLED SENSOR ROTATION AT ENCOUNTER (ASSUMED 150 DEGREE ROTATION IN 2 MINUTES)	<0.25 MRAD
3.	MAXIMUM NUTATION DURING CONTINUOUS FIRING OF MAIN (5 LBF) THRUSTER. (DISTURBANCE TORQUE 0.5 FT-LB)	1.7 DEGREES
	MAXIMUM NUTATION AFTER CUTOFF, INITIALLY	1.1 DEGREE
4.	NUTATION ANGLES DUE TO PULSED RADIAL THRUST (DISTURBANCE TORQUE 0.1 FT-LB)	0.3 DEGREE
	NOTE: DISTURBANCE TORQUE CAN BE COMPENSATED BY AXIAL TRIM PULSE (INFLIGHT CALIBRATION) REDUCING IT BY 1 TO 2 ORDERS OF MAGNITUDE)	
5.	PRECESSION DUE TO UNCORRECTED RADIAL THRUST DISTURBANCE TORQUE (0.1 FT-LB)	~1.6 MRAD PER CYCLE
	IF COMPENSATED TO 5 PERCENT	~1 DEG/HOUR

In order to reduce interference by nutation and precession effects with precision pointing requirements, e. g., during the terminal navigation phase, and to keep the narrow one-degree antenna beam pointed at earth during extended pulsed thrust operation, the misalignment of the radial thrusters can be compensated by small trim pulses of the axial ACS/ $\Delta V$  thrusters. The magnitude of the required trim pulses can be determined in flight and updated as c. g. shifts develop.

The results summarized in the chart show that nutation and precession effects can be controlled adequately during all mission phases.

### 7.3 DATA HANDLING SUBSYSTEM

In developing the data handling subsystem design for the multiple asteroid flyby mission, the basic approach was to utilize existing hardware to the maximum possible extent. The data handling subsystem (DHS) includes equipment which perform the telemetry, command, and temporary high-speed data storage functions. Telemetry functions include sampling, A/D conversion, and formatting telemetry into a serial data stream suitable for modulating the telemetry transmitter. Command functions include demodulation and authentication of uplink commands and, in some cases, distribution of commands. The data storage functions include temporary storage of high-speed imaging and telemetry data for immediate downlink transmission during encounter modes.

#### 7.3.1 Data Handling Design Concept

The flight-proven Pioneer F and G data handling equipment is used as a baseline, modified to handle high-rate imaging and telemetry data. In addition to the Pioneer F and G equipment is a P-MOS semiconductor memory, of a design similar to that being considered for Pioneer Venus, and a video imaging system which has been built and tested for another project. The video imaging and storage interface is the same technology as the memory.

The DHS configuration is presented in Figure 7-10 showing the command data and telemetry interfaces. The data handling subsystem comprises the modified Pioneer F and G digital telemetry unit (DTU), the Pioneer F and G digital decoding units (DDU), the Pioneer F and G command decoding unit (CDU), the lightweight, low-power data storage units (DSU), and the video imaging compatibility equipment (VICE).

Telemetry. Figure 7-11 presents the existing flight-proven Pioneer F and G DTU configuration. Critical functions are redundant to provide high-probability of mission success. Spacecraft timing is provided by a crystal oscillator stable to  $10^{-5}$  per 24 hours. Eight selectable bit rates and 23 format combinations accommodate variable telemetry requirements of mission cruise and encounter modes. The DTU data multiplexer provides 258 housekeeping channels and 32 serial digital mainframe channels.

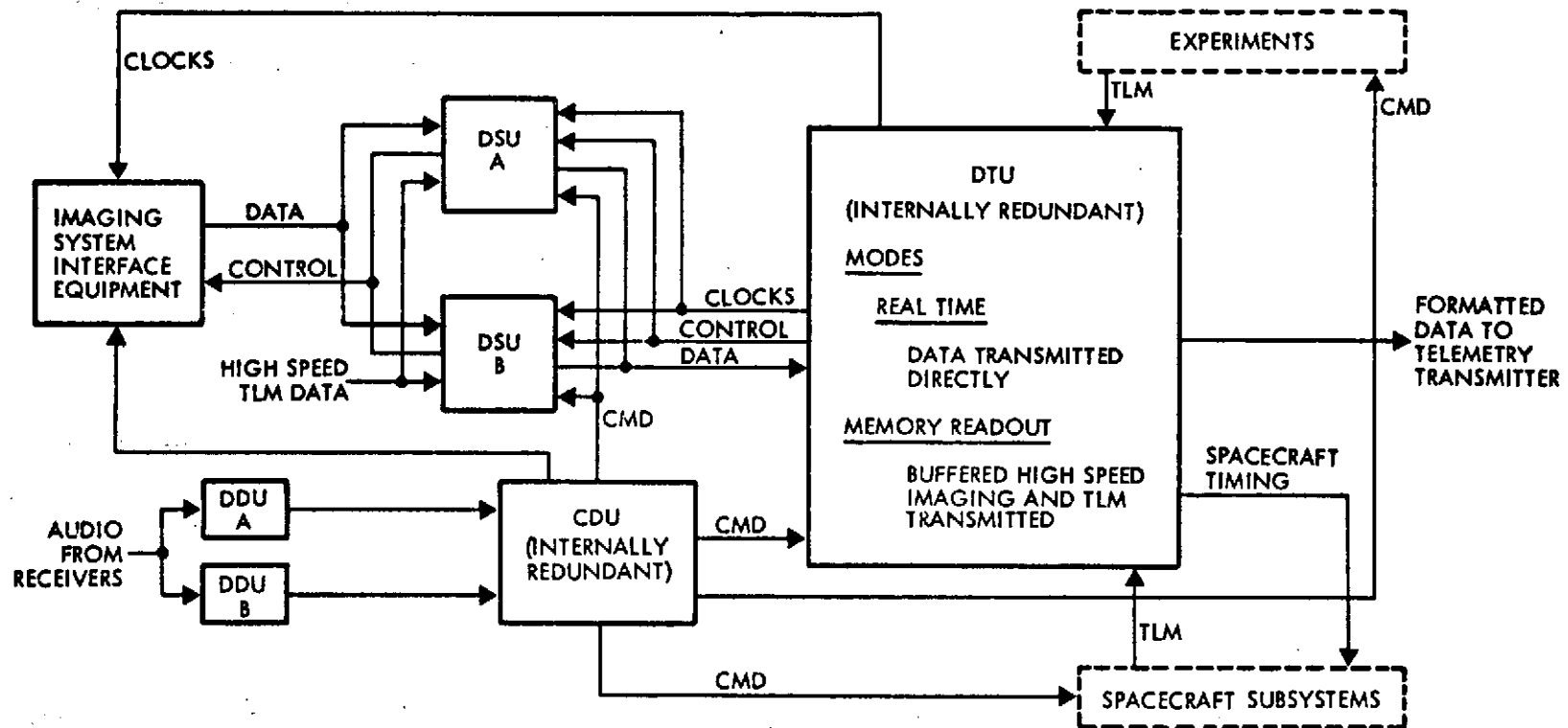
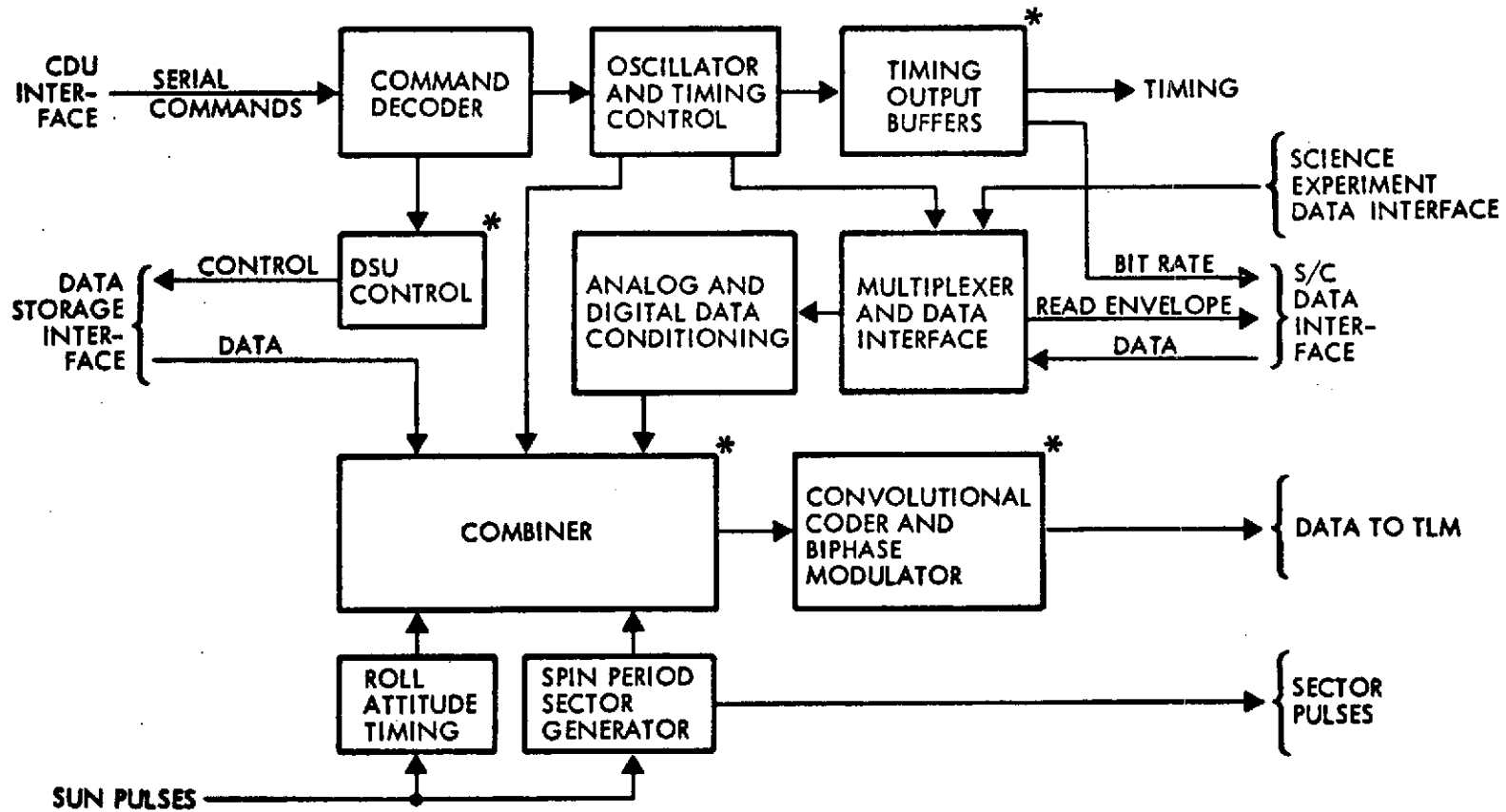


Figure 7-10. Data Handling Subsystem



\* MODIFIED FOR HIGH BIT RATE DATA TRANSMITTAL DURING ENCOUNTER.

Figure 7-11. Digital Telemetry Unit

For the cruise mode, formatted data is telemetered in real time in one of 23 formats at one of 7 bit rates between 1 bps and to 2048 bps. Telemetry data is interleaved with fixed-word format data, encoded by a 32-bit constraint convolutional coder and biphase modulated at 32.8 kHz for downlink transmission.

During the encounter portion of the mission the normal real-time data collection is interrupted and the high-bit rate data from the DSU video imaging and high-rate telemetry data is fed directly into the output coding and modulating logic of the DTU. The data bit-rate of this process is 32.8 kbps and the subcarrier frequency is 131 kHz. Such a capability can be incorporated into the Pioneer DTU by a redesign of the DSU interface logic: a small modification of the combiner is required to inhibit its function during high-speed operations; the convolutional coder and biphase modulator are modified to operate at slow and fast; and the timing output buffers must provide a high-rate clock signal to drive the DSU and the VICE.

The spin period sector generator divides the period between sun pulses into 512 sectors and provides outputs of 512, 8, and 1 pulses per revolution to the science instruments and attitude control subsystem.

The roll attitude timing logic determines the time between sun or star reference pulses and start of the telemetry mainframe to be used for data correlation and for real-time ACS backup modes. The extended frame counter identifies up to 8192 mainframes to correlate spacecraft data sampling to ground station time.

Command Demodulation. In the flight-proven Pioneer DDU the 1 bps command is authenticated by using a 4-bit parity Hamming code to reduce the probability of executing a false command to less than  $1.1 \times 10^{-9}$  with a signal-to-noise ratio of 17.3 dB at the decoder input. The DDU provides a serial command output to the CDU which includes three bits for routing serial commands to the subsystems.

Figure 7-12 illustrates the basic DDU circuit blocks, the fail-safe cross-strapped receiver interface and the interface with the CDU. Power switching is used in the digital section to conserve power when not processing a command. Power is applied to the analog portions of both redundant decoders at all times to prevent lockout modes.

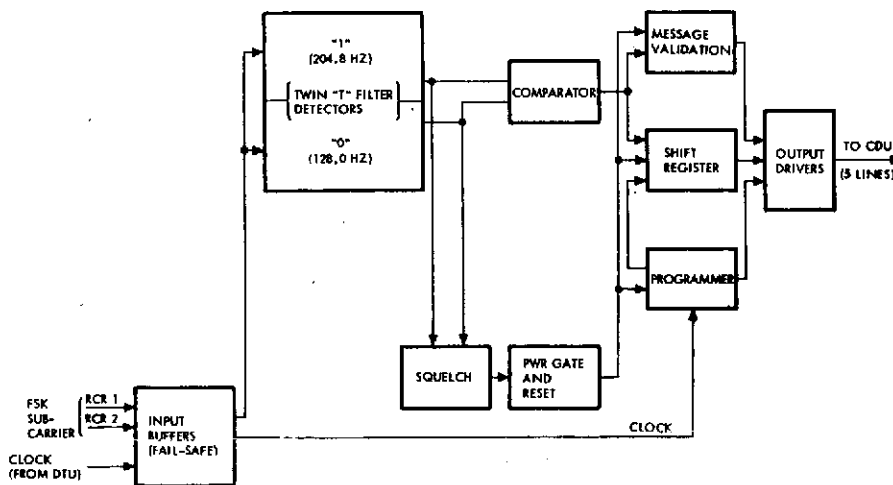


Figure 7-12. Pioneer Digital Decoder Unit

Command Processing and Distribution. The CDU consists of sub-assembly "slices" containing printed circuit boards, which facilitate modification of specific functions to meet new requirements or additions for growth.

The CDU redundant command processors (Figure 7-13) decode discrete commands from the digital decoder units (DDU) in the data handling subsystem, process them to produce user-compatible outputs, and then distribute the outputs. Both processors are contained in a single slice and the outputs are contained in a single slice and the outputs are cross-strapped for added reliability.

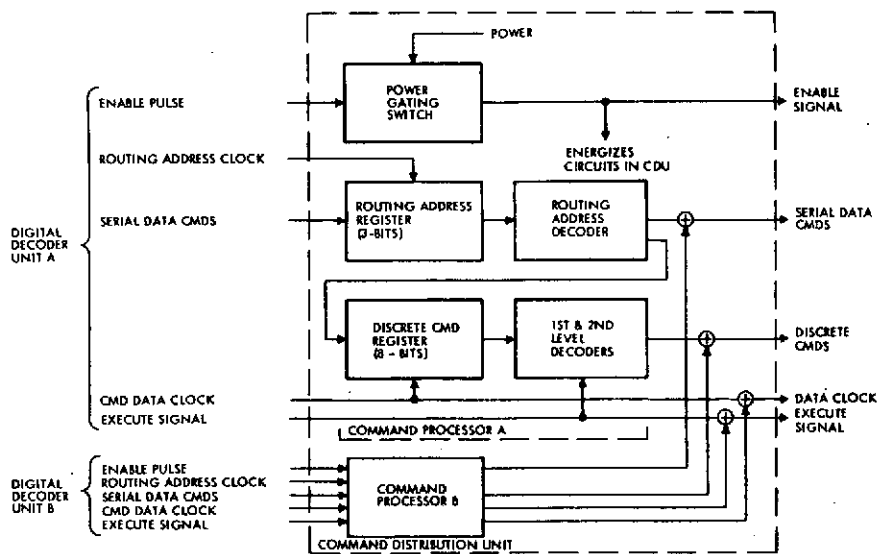


Figure 7-13. Command Processing

ORIGINAL PAGE IS  
OF POOR QUALITY

Video Imaging Compatibility Equipment. Figure 7-14A shows the interface equipment necessary between the video imaging system and the storage unit. This equipment includes five parallel 256 bit dynamic P-MOS registers which are loaded at a 4.1 Mbps rate and unloaded at a 500 kbps into the DSU. The clocks for these registers are supplied by the modified Pioneer DTU.

Data Storage Unit. The equipment for temporary storage of high-rate imaging and telemetry data during encounter is shown in Figure 7-14B. The design is a new lightweight, low-power dynamic P-MOS memory of the type being considered in the current Pioneer Venus design study. The imaging data is formatted and stored in five parallel registers after each of 195 samples per scan. High-rate telemetry data taken during encounter is stored in a dedicated register. After the last sample of each scan the registers are emptied out consecutively at 32 kbps to the DTU for downlink transmission. The time to load the memory is 0.2 sec and the time to empty it, at 32 kbps, is 9.4 sec.

### 7.3.2 Solid State Imaging

Figure 7-15 shows the block diagram for the solid-state imaging system data flow. (See also Section 2.) There are 195 sensors in a line which generate 195 scan samples during 0.2 sec of each 12 sec spacecraft revolution. Figure 7-16 shows the scan pattern obtained for one image frame (195 by 195 samples) and the associated timing. Each of the 195 sensors is exposed for each of the 195 sample times during the 0.2 sec scan. The total time for each exposure is a little more than 1 millisecond: 10  $\mu$ sec to bias the photojunction, about 1 millisecond of light exposure and about 78  $\mu$ sec to read out the samples through the five parallel multiplexed, A/D converter channels.

Referring again to Figure 7-15, the outputs of the sensors are conditioned by the light sensory amplifiers (LSA), sampled by the five 39-position multiplexers, and digitally encoded to 6 bits by the A/D converter for digital readout. The sampling and conversion time is 2  $\mu$ sec per position of the multiplexer. The sensor array is pre-calibrated with gain adjustments for each of the 195 elements stored in the onboard read-only memory (ROM). When each position of the multiplexer

ORIGINAL PAGE IS  
OF POOR QUALITY

7-28

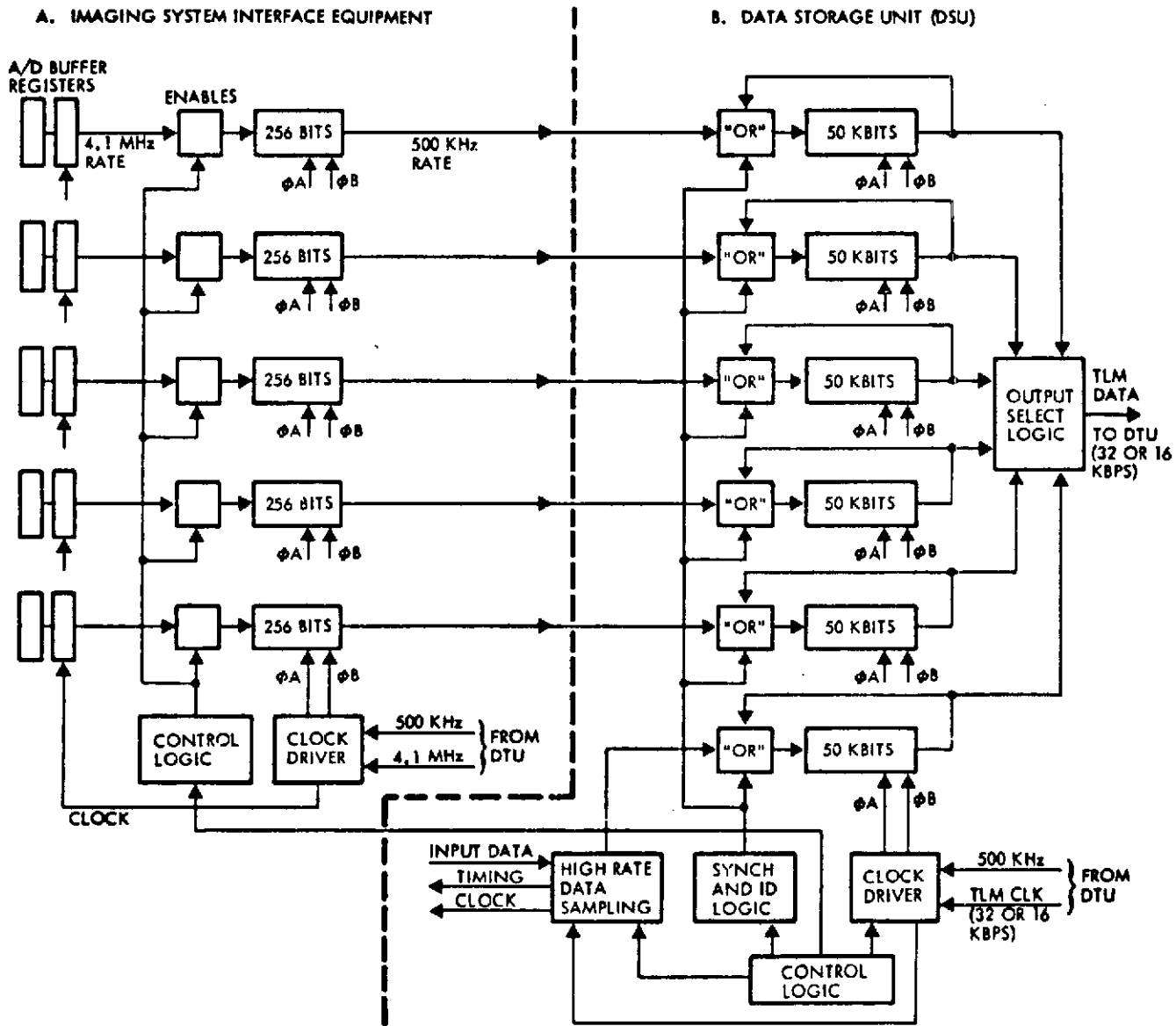


Figure 7-14. Imaging System/Data Storage Unit Interface

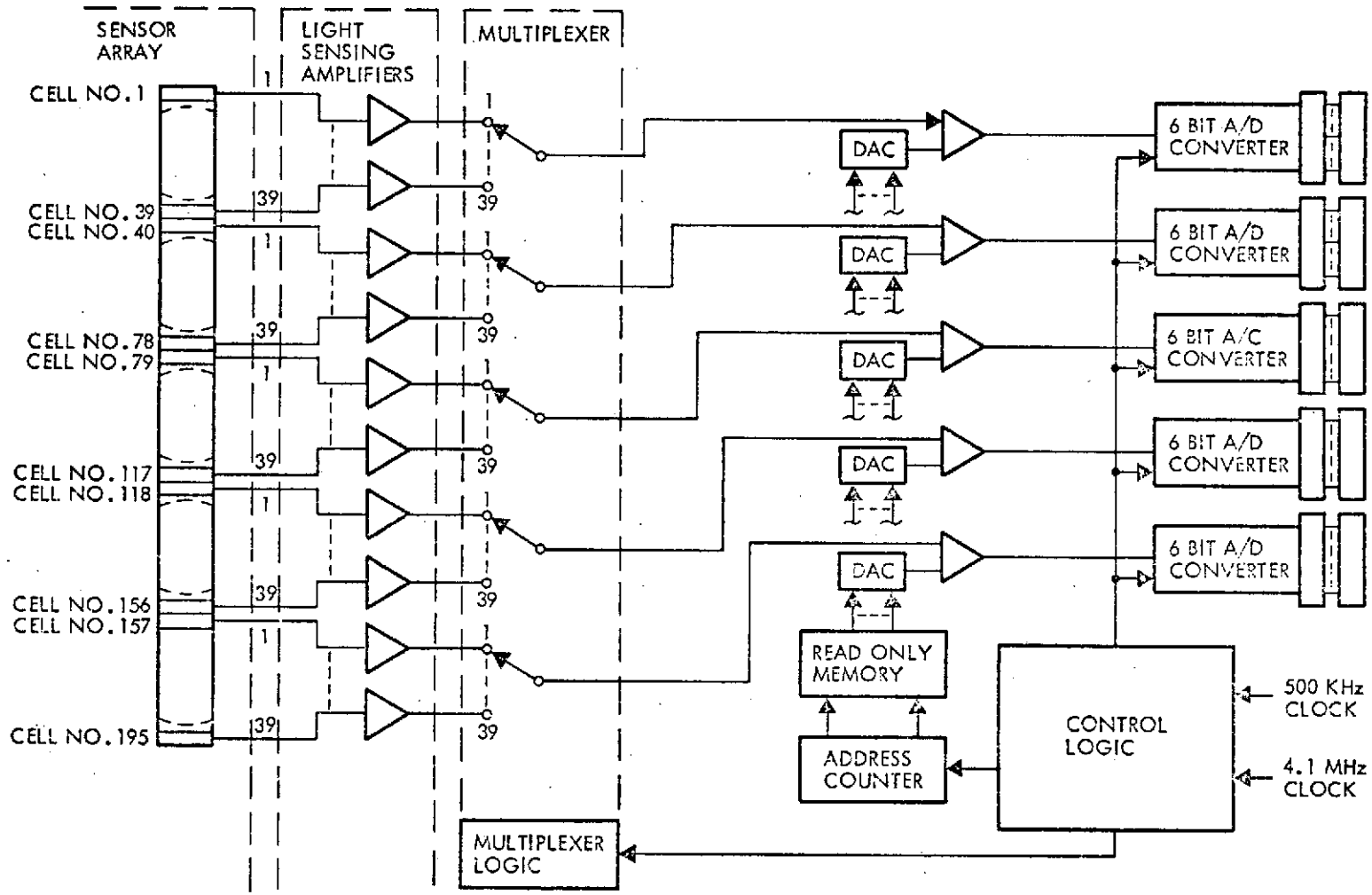
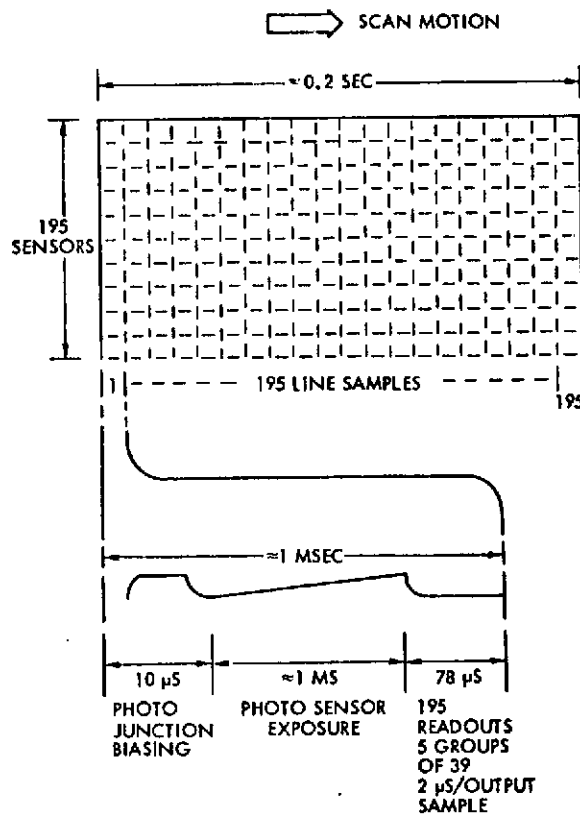


Figure 7-15. Solid-State Imaging Equipment



**Figure 7-16. Solid-State Imaging Timing**

is selected the corresponding gain calibration data is fed into the scaling amplifier to normalize the data for each subsequent sample.

The clock-rate for the A/D converter is 4.1 MHz for conversion and shifting processes. The output from the A/D converter is fed to the video imaging compatibility equipment at 4.1 MHz for intermediate storage before telemetering at 32.8 kbps.

### 7.3.3 Cruise and Encounter Modes

During the cruise mode the DHS uses low data rates (16 to 2048 bps) to conserve power and the DSU, VICE and SSI equipment are turned off. The telemetry system operates on S-band.

For the encounter mode the DSU, VICE and SSI are commanded on, the 32.8 kbps rate is selected and the high-rate imaging data can be telemetered along with other high rate data using X-band.

#### 7.3.4 Required Modifications

The basic requirements for data handling can be met by modifying or adapting the present Pioneer F and G equipment. This approach minimizes costs and schedule problems. The proposed design adaptation of the DTU from Pioneer F and G involves the following modifications and additions:

- Maximum bit rate increased from 2048 bps to 32,768 bps
- Science and engineering subcommutators expanded
- High-speed memory interfacing electronics added.

To increase the bit rate to 32,768 bps, the following modifications must be made to the existing Pioneer DTU design:

- Replace the analog to digital (A/D) converter with a faster circuit, potentially available from another program
- Redesign the programmer logic
- Speed up the main-frame and subcommutator multiplexers.

The present A/D converter cannot operate at a higher bit rate so a different converter design would have to be incorporated onto the analog subframe board, necessitating a redesign of that board.

The programmer logic and timing must be modified to increase the bit rate (2048 to 32,768 bps). This change requires a redesign of the two redundant programmer boards.

To increase the multiplexer speed the multiplexer interface circuits, the multiplexer driver circuits, and the multiplexer logic and timing must be redesigned. These changes require redesign of the digital subframe board, the analog subframe board, and the two redundant main frame multiplexer boards, and in addition affect the redesign of the programmer boards.

The proposed science subcommutator exceeds the capacity of the Pioneer F and G science subcommutator. The required expansion of the science subcommutator is achieved by providing more input gates, more

gate drivers and additional control logic. Such a change requires redesign of the A/D subcommutator boards, an additional subcommutator board and an additional signal connector.

In summary, the redesign of the baseline Pioneer DTU, presently configured on nine circuit boards, affects every board. Two additional circuit boards are to be added for the expanded science subcommutator and the data storage interfacing electronics.

The chassis would be enlarged to enclose eleven boards and contain three additional connectors. The footprint would be the same as in Pioneer F and G, viz, 83 square inches with the following increases in size, weight, and power:

	<u>Pioneer F and G</u>	<u>Asteroid Spacecraft Configuration</u>
Size	454 cubic inches	560 cubic inches
Weight	7.8 pounds	9.6 pounds
Power	4.7 watts	7.5 watts

To test the redesigned DTU, the DTU test set also must be redesigned, as follows:

- Maximum bit rate increased to 32,768 bps
- Subcommutator interface expanded
- Subassembly test set modified; eleven new cards, new holding fixture and cabling.

#### 7.4 COMMUNICATIONS

A functional block diagram of the proposed communication subsystem is shown in Figure 7-17 with changes from the Pioneer F and G configuration identified. The configuration is similar to that of Pioneer F and G with the following exceptions:

- An enhanced downlink capability, comprised of redundant X-band drivers and TWTA's (seven watts), has been added. The matching network (attenuator) used between the driver and TWTA to adjust driver output power for optimum TWTA performance is not required.
- An X-band transfer switch, utilizing waveguide ports, has been added to permit selection, by ground command, of either X-band TWTA/driver pair.

ORIGINAL PAGE IS  
OF POOR QUALITY

7-33

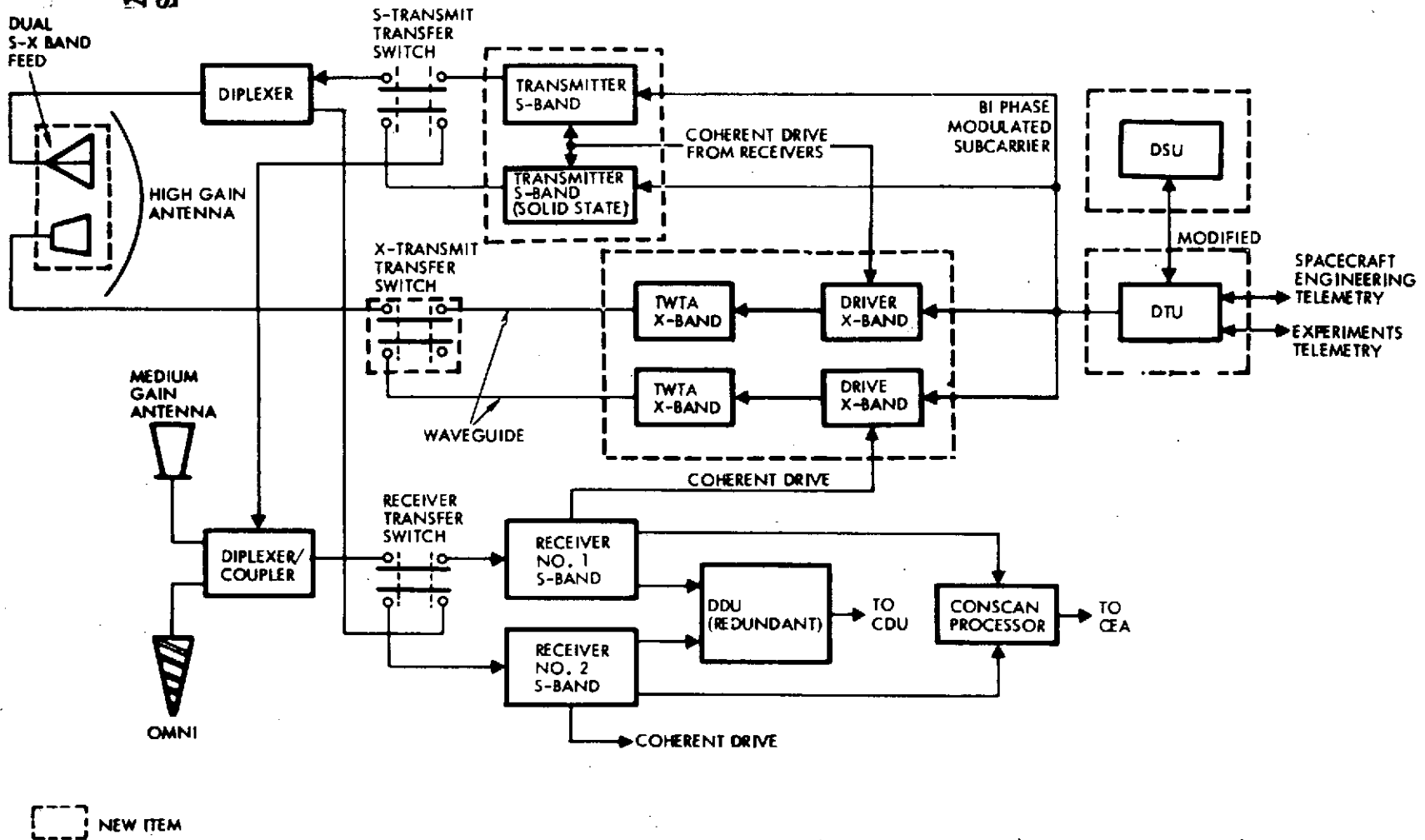


Figure 7-17. Communication Subsystem Functional Block Diagram

- A waveguide transmission line interconnects both TWTA's with the transfer switch and the high-gain antenna.
- The downlink redundant S-band driver/TWTA (eight watt) arrangement has been replaced by redundant solid-state transmitters (one watt).
- The high-gain antenna S-band feed is replaced with a dual S- and X-band feed and the high-gain antenna feed movement mechanism, employed on Pioneer F and G is deleted.
- A 20-inch hole at the vertex of the reflector permits protrusion of the enlarged propellant tank.

The modifications proposed for the asteroid spacecraft application are practically identical to those adopted in the Jupiter Orbiter design concept. In both cases the principal objectives is the same, namely to enhance telemetry channel capacity within the power constraints imposed by the existing RTG's, in order to accommodate higher data rates from the science payload.

Table 7-4 summarizes the essential differences between elements of the Pioneer F and G communication subsystem and those proposed for the asteroid spacecraft.

#### 7.4.1 Communication Subsystem Requirements

##### 7.4.1.1 Telemetry Performance

The primary requirement imposed on the telemetry link is to achieve the highest possible bit rate consistent with minimizing the modifications to the spacecraft and constrained by the available electrical power. The spacecraft transmitter is a major consumer of electrical power; 27.8 watts is required by the Pioneer F and G TWTA. The power requirements for the majority of the remaining units are comparable to Pioneer F and G.

The increased data rate requirements, dictated primarily by an increased imaging capability envisioned for the missions to be performed, justify seeking an increased downlink telemetry bit rate capability. The use of X-band frequency is a straightforward solution which can provide

the necessary gain. Increasing the diameter of the high-gain antenna for achieving the required gain is not feasible with the 10-foot diameter shroud of the Atlas/Centaur booster. No consideration has been given to a deployable antenna which would provide further gain improvement because of the substantial complexity and cost impacts.

Theoretically, increasing the link frequency from S- to X-band (8.4 GHz) provides a potential 11.3 dB advantage. Practical limitations, e. g., increased antenna pointing losses and atmospheric attenuation, restrict this link enhancement to approximately 8 dB, which is adequate. However, the X-band approach can be used only with the DSIF 210-foot subnet.

**Table 7-4. Communication Subsystem Modification Summary**

Unit	Pioneer F and G	Asteroid Spacecraft
High-gain antenna	Nine-foot paraboloid; focal point feed	20-inch hole at vertex for propellant tank protrusion
High-gain antenna feed	Cavity-backed, crossed dipole	Dual S- and X-band
Feed movement mechanism	Thermal actuator	Deleted
Medium-gain antenna	Corrugated horn	Unchanged
Omni antenna	Log conical spiral	Unchanged
S-band transfer switch	Procured from Teledyne Microwave	Unchanged
X-band transfer switch	Not applicable	New item
Diplexer	Procured from Wavecom	Unchanged
Diplexer/coupler	Procured from Wavecom	Unchanged
X-band transmitter	Not applicable	New item, seven watt RF output
X-band driver	Not applicable	New item
S-band transmitter	Eight watt TWTA; procured from Watkins/Johnson	One watt solid state device
S-band driver	50 mw power output	Deleted
Matching network	Coaxial attenuator	Deleted
Receiver	Phase lock loop; 20 Hz threshold loop bandwidth	Add coherent drive to X-band drivers
Digital decoder unit	PCM/FSK format	Unchanged
Conscan processor	Digital maximum likelihood estimator	Unchanged
RF transmission lines	Coaxial (semi-rigid and flex)	Coaxial and waveguide

#### 7. 4. 1. 2 Dual Frequency Transmission

DSIF tracking station coverage of the spacecraft for the critical period encompassing injection and several hours thereafter is essential for the following operations:

- Initiate sequencer backup commands in case of despin, appendage deployment, or initial orientation maneuver anomaly
- Turn on experiments for near-earth calibration
- Assess spacecraft health and take corrective action, as required
- Obtain thruster pair calibration during initial orientation maneuver.

DSIF-51 (Johannesburg) is the only station providing reasonable visibility of the spacecraft for a representative range of ascent trajectories for this mission. This station is configured with an 85-foot antenna, and hence, has only an S-band receive/transmit capability. Only the 210-foot subnet is provided with an X-band receive capability. Therefore, it is imperative that S-band transmission, capable of fulfilling the aforementioned requirements, be provided in addition to X-band.

The design goal is to design the respective S- and X-band downlinks to obtain a minimum carrier loop signal-to-noise ratio of 20 dB, measured in the ground receiver loop bandwidth.

#### 7. 4. 1. 3 Receiver Requirements

The receiver requirements are basically the same as for Pioneer F and G, therefore, no requirement for modification of the receiver is foreseen.

#### 7. 4. 1. 4 Ground Station Requirements

The DSN multiple mission telemetry (MMTS) is specified as being capable of accommodating 2, 048 bps, maximum. The maximum data rate of 32, 768 bps proposed exceeds the DSN MMTS capability to demodulate and decode convolutionally coded telemetry data. Consideration must be given to installing mission-dependent special-purpose decoding equipment to implement this function.

Wideband data lines (WBDL), capable of transmitting data rates from 10 to 150 kbps are planned to be operational by 1974 at all 210-foot subnet stations, if funding is approved.

7. 4. 1. 5 Summary of Problem Areas and Proposed Solutions

Table 7-5 summarizes principal problem areas inherent in the design adaptation and operation of the modified Pioneer F and G communication subsystem, and lists proposed solution approaches. Actually, the modifications required for the asteroid spacecraft are almost identical to those proposed for the Jupiter Orbiter and have been extensively analyzed during that study. Further details may be found in TRW's Final study report on the Jupiter Orbiter (Reference 1-9).

Table 7-5. Communication System Problem Areas

PROBLEM	APPROACH TO RESOLUTION
REQUIRED MAXIMUM BIT RATES (16 - 32 KBPS) EXCEED CAPABILITY OF 32 KHZ SUBCARRIER	PROVIDE SUBCARRIER FREQUENCY $\geq$ FOUR TIMES HIGHEST SYMBOL RATE THROUGH MINOR DTU MODIFICATION. RETAIN 32 KHZ SUBCARRIER FOR SYMBOL RATES $\leq$ 4 KSPS
X-BAND ANTENNA NARROW BEAMWIDTH REQUIRES MORE ACCURATE EARTH POINTING	REDUCE CONSCAN PROCESSOR THRESHOLD FROM 0.3 DEGREE TO 0.2 DEGREE BY MEANS OF EXTERNAL PROGRAMMABLE PLUG
WEATHER - DEPENDENCE OF X-BAND TRANSMISSION (ATMOSPHERIC ATTENUATION)	PLAN ENCOUNTER PERIOD TO PERMIT SIMULTANEOUS COVERAGE FROM MULTIPLE EARTH STATIONS
SEQUENTIAL DECODING OF CONVOLUTIONAL CODED DATA NOT AVAILABLE AT DSS FOR BIT RATES $>$ 4,096 BPS.	AUGMENTATION OF PRESENT CAPABILITY IS ANTICIPATED PRIOR TO TIME PERIOD OF THIS MISSION. ALTERNATIVELY, USE SPECIAL PURPOSE DECODER.
X-BAND HARDWARE DEVELOPMENT: TRANSMITTER DRIVER, TWTA, TRANSFER SWITCH, S-/X-BAND FEED	TECHNOLOGY EXISTS. OFF-THE-SHELF EQUIPMENT EXPECTED TO BE AVAILABLE FROM OTHER PROGRAMS

7. 4. 2 Recommended Communication Subsystem Design

The recommended communication subsystem design is based primarily on achieving higher telemetry rates while retaining as much of the simplicity, reliability, and technology of Pioneer F and G as possible. (See Figure 7-17.) The major departure from Pioneer F and G philosophy is the adoption of X-band frequencies to provide the prime telemetry support. As discussed earlier, this approach was a natural outgrowth of the limited electrical power allocation to the transmitter and the ever-present

demand for higher data rates to meet new requirements of increasingly sophisticated scientific experiments. The principal contributor of high-data rates in this mission is the line-scan image system. Recourse to X-band frequencies, with the inherent increase in communication link gain, offers an attractive practical solution.

The X-band link performance is weather-dependent, whereas S-band is independent. Cloud cover or rain can introduce losses ranging from tenths of dB's to many dB's, depending on the density of cover. However, even under these infrequent adverse conditions, the X-band link will perform at least as well as an equivalent S-band link, the atmospheric losses being offset by the 8 to 11 dB link gain advantage.

To minimize the risk of losing telemetry at the time of an asteroid encounter, due to weather conditions at the ground station, consideration has been given to providing coverage by more than one DSN station at the critical time. Conditions that favor or hinder multiple DSN coverage are discussed in Appendix D.

While design uncertainties and differences in operating conditions exist, implementation of the X-band capability clearly fulfills the present requirements with a minimum spacecraft impact. It also provides flexibility to meet increased, but unforeseen, new requirements. The DSIF 210-foot subnet will be required to acquire telemetry at X-band.

During the launch, ascent, and initial DSIF station acquisition phases of the mission the communication activity, both uplink and downlink, will be similar to that of Pioneer F and G. Checkout of the X-band link will normally follow completion of the initial orientation maneuver, spacecraft health verification, and experiment activation. Execution of a conscan operation will be required more frequently to ensure sufficiently accurate earth pointing with the narrow antenna beamwidth (0.8 degree) at X-band. Simultaneous S- and X-band transmission is possible, and recommended, during this operation to maintain continuous telemetry coverage.

Routine telemetry reception at X-band will be possible, but not essential, during most of the cruise phase of the mission. The one-watt S-band link, via the high-gain antenna, will support bit rates up to

256 bps at maximum communication range. The substantially increased capability of X-band is available, however, as required. Tracking operations by the DSN 85-foot subnet must be performed at S-band to obtain two-way coherent doppler.

Communications coverage during midcourse maneuvers will utilize the S-band link operating through the medium-gain/omni-antenna system in a manner similar to Pioneer F and G.

Tracking and telemetry operations at X-band during the cruise phase are constrained by the necessity for more frequent update of the spacecraft pointing attitude to maintain adequate earth illumination by the narrow beamwidth antenna. Rate of change of the spacecraft-earth line, induced principally by the relative earth-spacecraft trajectory geometry and to a lesser extent by solar pressure, is predictable and may be compensated by appropriate open-loop precession or by consscanning. The S-band downlink provides increased assurance that telemetry communications will be continuously available in the event the spacecraft "drifts" beyond the X-band beamwidth.

During asteroid encounters telemetry operations will be conducted at X-band to obtain the maximum possible bit rates. However, simultaneous S-band transmission is permissible within the electrical power budget allocations.

Telemetry. Representative data rates for the X-band and S-band telemetry links are shown in Figure 7-18 as a function of earth-spacecraft range, with transmitted power plotted parametrically. For all cases, a carrier phase modulation index of 1.15 radians has been used to maximize the data rate over the communication range of interest.

The X-band performance predictions are based on minimal atmospheric losses. X-band performance is, however, weather-dependent and cloud cover or rain could introduce additional losses which would degrade performance. In that event a lower bit rate may be selected or primary data collection responsibilities shifted to a station free of the adverse conditions.

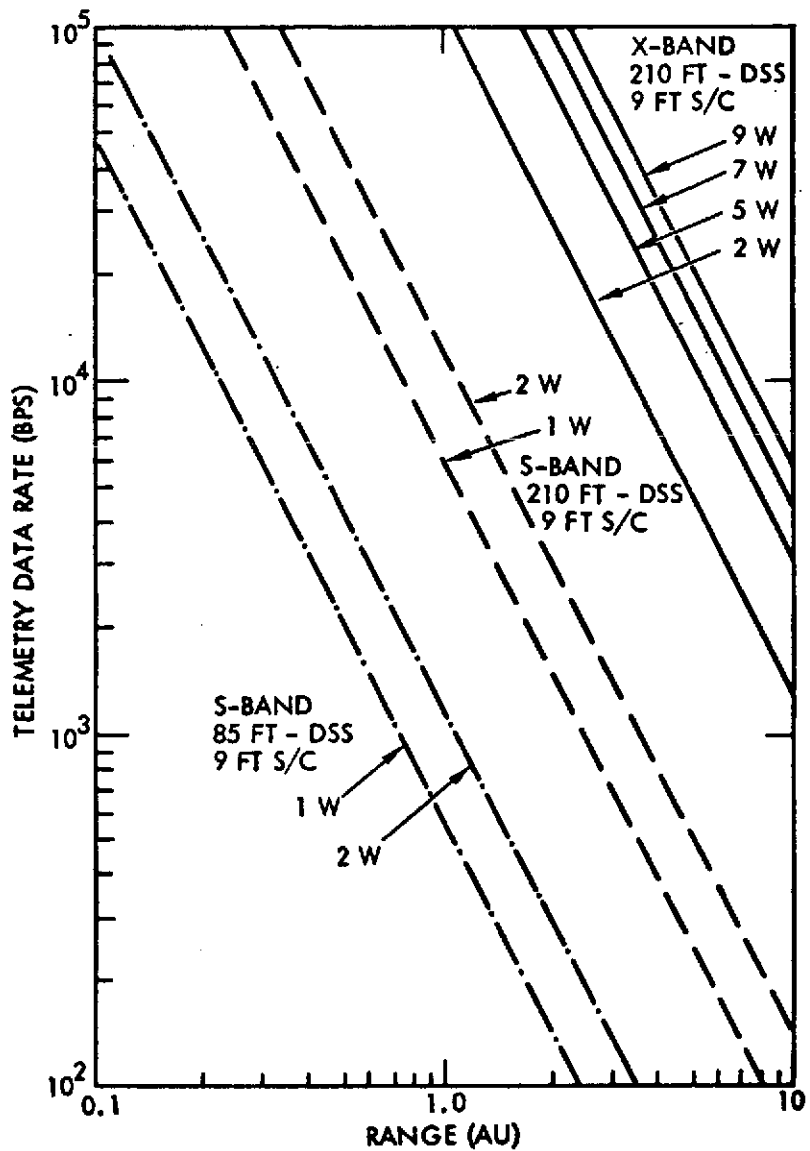


Figure 7-18. Representative Telemetry Data Rates\*

All performance estimates are based on the use of convolutional coding of the telemetry data and sequential decoding by the ground station computer. Although the DSN is currently limited to decoding bit rates less than 4096 bps, it is anticipated that increased capability to accommodate higher bit rates will be fully operational by the mid-1970's to support planned outer planet missions.

\* Note: The bit rate performance estimates were obtained from a computer program developed by NASA/ARC, Spacecraft Data Systems Branch, and provided to TRW Systems.

Communication Range and Data Rate Contours. The performance of the X-band telemetry link was evaluated in terms of typical mission profile characteristics to determine whether the high-data rate requirements occurring during asteroid encounter can be adequately satisfied. Figure 7-19 shows contours of communication ranges of 3, 3.5, and 4 AU mapped across a set of trajectories in the ecliptic plane. The corresponding telemetry bit rate is 32.8 kbps if the transmitter power is 5, 7, and 9 watts, respectively. The spacecraft antenna is the standard Pioneer F and G 9-foot dish.

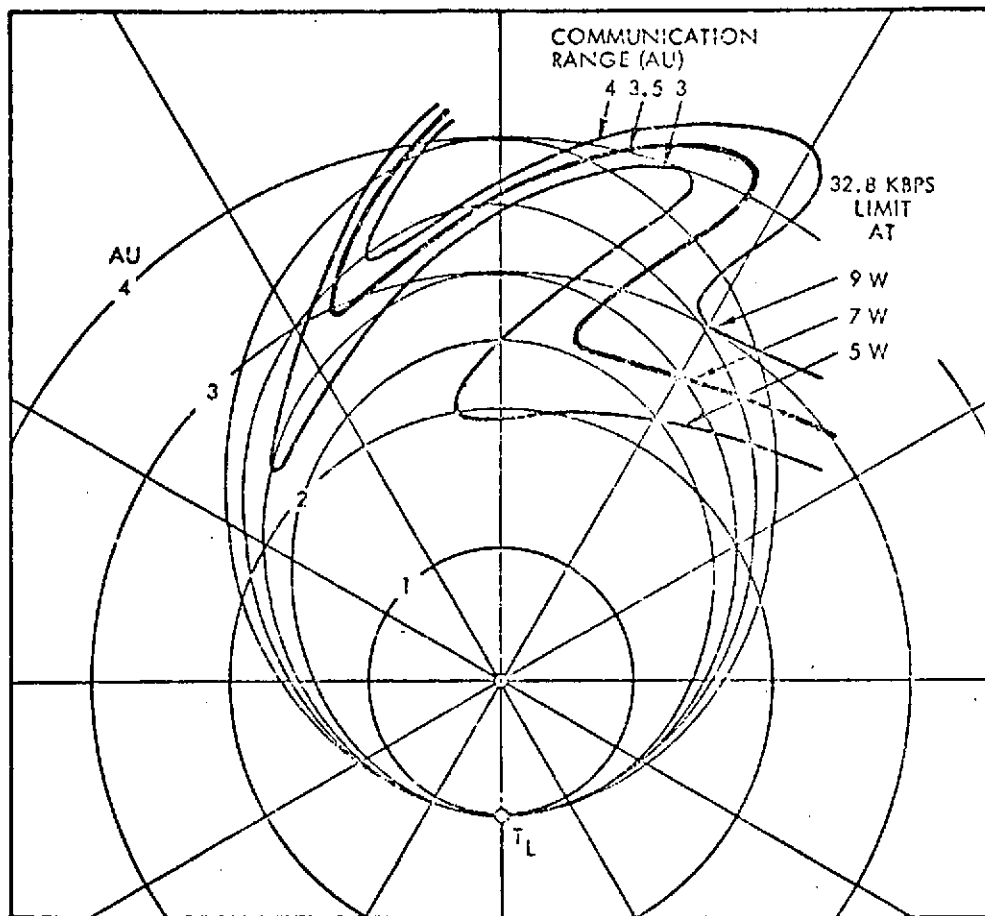


Figure 7-19. Communication Range and Data Rate Contours

Two conspicuous intrusions of the range contours into the area traversed by typical asteroid mission trajectories are noticeable which correspond to times when spacecraft and earth are on opposite sides of the sun (superior conjunction). These areas delineate regions of lower

bit rate capability; for example, at 7-watt transmitter power the bit rate is 32.8 kbps inside and 16.4 kbps outside of the contour line. This influence on mission capabilities is not considered critical. In cases where the data acquisition rate of the image system (~19 kbps) cannot be met by the telemetry link, i. e. , if the data rate is lower than 32.8 kbps, the effect would be that one image frame must be skipped every two or three revolutions of the spacecraft.

Command. No command modifications to the Pioneer F and G are contemplated. The fixed 1 bps command bit rate is adequate for all identified requirements. A 2 db reduction in the uplink telecommunications RF power budget margin with the high-gain antenna is charged to the fixed-feed offset. However, this presents no loss of performance capability.

Earth-Pointing. X-band frequency for downlink transmissions necessitates imposing more stringent earth-pointing requirements on the conscan control system to minimize the pointing error loss. Whereas a pointing error of 0.4 degree at S-band produced only a 0.2 dB pointing loss, a pointing error of only 0.2 deg. at X-band is equivalent to a 1 dB gain loss. The importance of improving the earth-pointing accuracy is evident.

The Pioneer F and G conscan threshold setting is 0.3 degree for the high-gain antenna. Error budget analysis indicates there is a high probability that a conscan maneuver will be terminated at the desired threshold setting. A modest reduction in the threshold setting to approximately 0.2 degree creates no major impact. It is probable that the specification of some error sources such as antenna mechanical alignment uncertainties may have to be tightened. No conscan processor modifications are required; the external programmable plug provides flexibility in selecting the desired threshold.

Candidate X-Band Transmitter Tubes. Several advanced X-band TWTA's have been developed that would be applicable to this mission. A potential candidate is the Watkins-Johnson Model WJ-130 which was developed for an Air Force program. The power output must be increased from 3.3-watts to 7 watts, and the frequency increased from 7750 MHz to 8400 MHz to meet the requirements of the asteroid spacecraft. The

25-watt TWT under development for JPL could be adapted for the 7-watt requirement.

A tube efficiency of 45 percent is a design objective which is dependent on new technology involving two-stage collector development. An overall efficiency of 28 percent for the 7-watt TWTA appears more realistic using proven tube construction techniques, and making allowances for losses when operating into a mismatched load and inclusion of an output power monitoring device. This would require a transmitter input power of 25 watts.

X-Band Driver. The X-band transmitter driver has the same features as the present S-band driver: inclusion of an auxiliary oscillator (TCXO) for noncoherent operation and provision for coherent drive from either S-band receiver.

S-Band Transmitter. The S-band transmitter, a solid-state unit, has the multiple function previously performed by the S-band driver and TWTA. It is capable of operating noncoherently from an internal oscillator or coherently from a drive signal supplied by either receiver.

Combined S-/X-Band Feed. As in the Jupiter Orbiter a dual S-/X-band feed with rigid waveguide horns is proposed for this application. This permits the phase centers of the two feeds to be placed closer together than with separate feeds. The waveguides are fed by orthogonal probes to achieve circular polarization and the antenna has a gain at S-band of about 29.5 dB on boresight with a 5-degree beam at the half-power points. The S-band gain on the spin axis is about 28 dB and the X-band gain is about 41 dB since the X-band feed is not offset. Figure 7-20 illustrates the concept and its installation on the antenna tripod.

The Pioneer F and G medium-gain horn and high-gain feed configuration is depicted in the left portion of the figure. The forward-facing medium-gain horn provides communications over broad spatial angles at intermediate and close ranges. The axis of the medium-gain horn is tilted approximately 9 degrees with respect to the spin axis to produce an amplitude modulation of the uplink RF signal by the conical scanning motion of the offset pattern. The "conscan" signal is used for closed-loop precession of the spin axis toward earth.

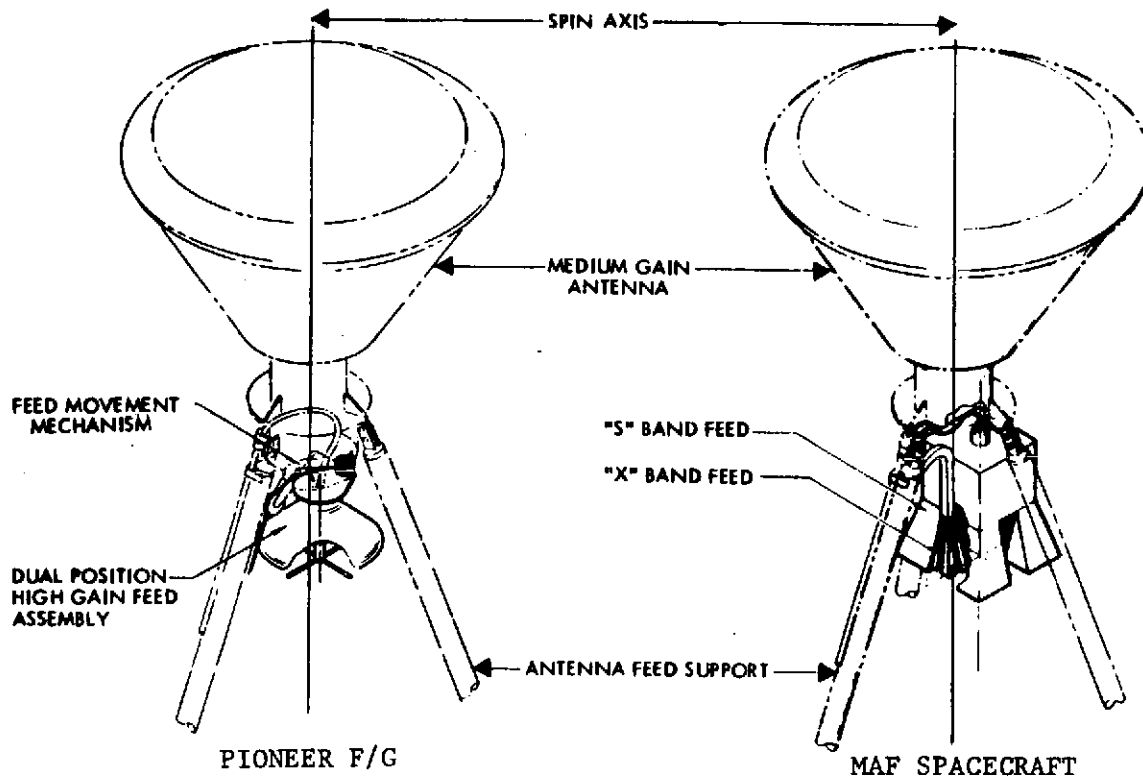


Figure 7-20. Antenna Feed System

The high-gain antenna is used both for fine adjustment of the earth-pointing attitude and for data transmission at the extended mission ranges. A movable feed is used to optimize the performance of both functions.

The right side of the figure shows the proposed combined S- and X-band feed installed on the antenna tripod. The S-band feed horn is permanently displaced from the reflector focal point to squint the beam with a resultant -1 dB crossover. The X-band feed horn is positioned in one of the S-band waveguide ridges and is coincident with the focal plane axis. This approach increases reliability by eliminating the feed movement mechanism without compromising the performance of the primary (X-band) data link.

Paraboloidal Reflector. Protrusion of the enlarged propellant tank through a 20-inch diameter hole at the vertex of the high-gain antenna reflector is not anticipated to cause any adverse effect on the antenna pattern. However, tests must be performed in conjunction with the dual S-/X-band feed development effort to verify this.

Assuming that the propellant tank behaves as a convex RF reflecting surface, the radiation scattering effect may increase the sidelobe level slightly. Negligible gain loss ( $<0.2$  dB) should occur since the blockage associated with this discontinuity in the paraboloidal surface is coincident with that arising from the medium-gain antenna, which is part of the existing configuration.

The principal uncertainty pertains to the effects, if any, of the modified antenna, on the conscan performance parameters. Range tests with a full-scale engineering model antenna, including a simulated propellant tank protrusion, should be performed to resolve this concern. If test results should show that antenna performance is significantly degraded, several approaches would be available to remedy the problem:

- Addition of a reflecting cone positioned over the propellant tank protrusion with the apex pointed at the feed. The objective is to deflect the radiation which would normally impinge on the propellant tank.
- Addition of a zone plane situated over the propellant tank and positioned, relative to the dish surface, to minimize performance losses.
- Application of suitable RF-absorbent material over the exposed propellant tank to minimize the scattering effect.

## 7.5 POWER AND ELECTRICAL DISTRIBUTION

### 7.5.1 Summary

The electric power subsystem is that of the Pioneer F and G spacecraft with only a minor modification. The functional block diagram is shown in Figure 7-21. The prime energy source consists of four RTG's which convert thermal energy directly into electrical energy at a voltage of 4.2 Vdc. Four inverters, which are housed in two inverter assembly (IA) packages, change the prime electrical energy into a more useful form; i. e. , 30.5 Vrms at 2.5 kHz. The utilization of the prime energy is controlled by the power control unit (PCU) with excess power being dissipated in an external shunt radiator. The subsystem also includes a central transformer/rectifier unit (CTRF) which changes the

ORIGINAL PAGE IS  
OF POOR QUALITY

7-46

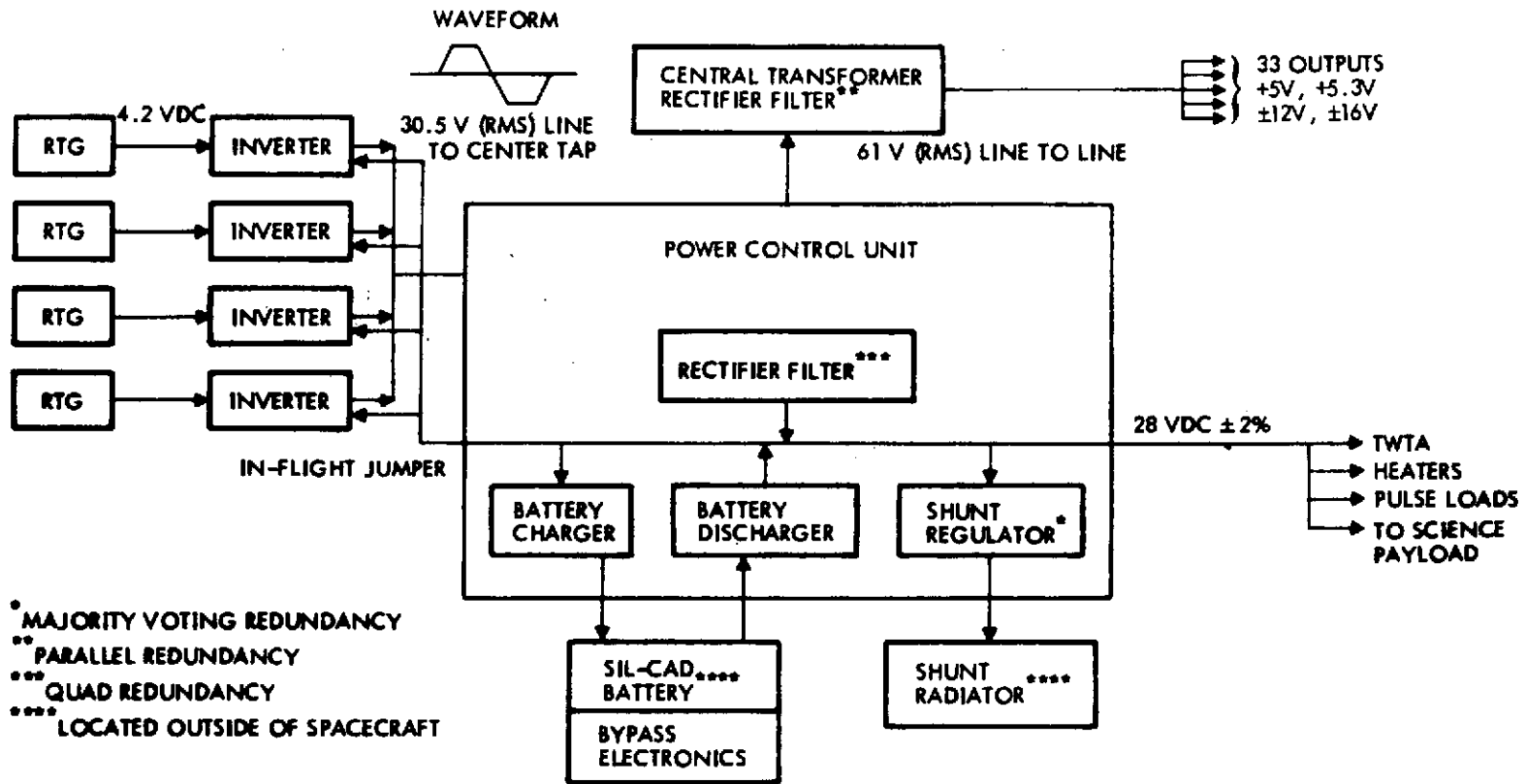


Figure 7-21. Electric Power Subsystem Block Diagram

high voltage AC power to low DC levels required by the loads. The CTRF also provides regulation and fault isolation for the loads. The CTRF would be modified to accommodate the optical pointing electronics and the additional data storage unit.

The power subsystem in its present configuration can meet the power requirements of the asteroid mission if a reasonably tight power budget is adhered to. Thus, it appeared preferable to avoid substitution of more advanced RTG power sources now under development for the present SNAP-19 units thereby minimizing system modifications. If conditions should warrant this, such a substitution could be decided on at a later time.

#### 7.5.2 Electrical Power Requirements

Table 7-6 compares power requirements of the asteroid spacecraft with those of Pioneer F and G and the Jupiter Orbiter, Configuration 1. The entries listed for the asteroid spacecraft summarize the power budget previously discussed in Section 6.

For the asteroid spacecraft two cases are considered: one with all experiments operating simultaneously, the other with some of the experiments that are less essential turned off during flyby, (i. e., the microparticle analyzer, the asteroid/meteoroid detector and the plasma wave detector).

Also listed in the table is the RTG power available at the time of the three asteroid encounters of the sample multi-asteroid mission and the available power margin. This margin is very small at the time of the third encounter if all payload instruments are operating. In the interest of minimizing system modifications, substitution of higher power RTG's (that would also involve a weight increase) for the SNAP-19 RTG units of Pioneer F and G has been ruled out. The small power margin available at the end of the mission (2.34 years) is acceptable, with battery power augmentation of 5 watts available for ten hours during the encounter period, or with the least essential experiments being turned off during the last encounter to meet contingencies, if necessary.

Table 7-6. Electric Power Requirements (Watts)  
(Steady Loads)

ITEM	PIONEER F&G	JUPITER ORBITER	MAF SPACECRAFT	
DATA HANDLING	5.6	6.1	9.8	
COMMUNICATIONS	33.7	19.6	34.7	
ATTITUDE CONTROL	3.7	4.2	4.7	
COMMAND DISTRIBUTION	3.3	3.8	3.8	
PROPULSION HEATERS	2.0	8.0	3.0	
TRANSDUCERS	0.2	0.4	0.2	
GIMBAL ACTUATORS	-	-	2.0	
CTRF LOSSES	10.2	10.9	13.9	
PCU LOSSES INCLUDING POWER SYSTEM	7.8	7.8	3.0	
EXPERIMENTS	<u>24.0</u>	<u>27.0</u>	<u>28.3</u>	(20.9)*
SUBTOTAL	90.5	87.8	102.4	(95.0)
CABLE LOSSES (2% OF LOAD)	0.6	0.6	2.0	(1.9)
RTG INVERTER LOSSES (88% EFFICIENCY)	13.3	13.1	14.2	(11.9)
RTG CABLE LOSSES (4%)	<u>4.2</u>	<u>4.1</u>	<u>5.0</u>	<u>(4.2)</u>
TOTAL	108.6	105.6	123.6	(107.8)
<u>SAMPLE MAF-MISSION</u>				
RTG POWER AVAILABLE AT 1ST ENCOUNTER (0.71 YRS)			144.0	
2ND ENCOUNTER (1.58 YRS)			135.0	
3RD ENCOUNTER (2.34 YRS)			127.0	
POWER MARGIN				
1ST ENCOUNTER			20.4	(36.2)
2ND ENCOUNTER			11.4	(27.2)
3RD ENCOUNTER			3.4	(19.2)

\* LESS POWER REQUIRED IF LESS ESSENTIAL EXPERIMENTS ARE TURNED OFF AT ENCOUNTER.

It should also be noted that the missions are of less than 2.4 years' duration on the average, since asteroids encountered late in the mission can generally not be detected early enough by the navigation sensor in this region of the trajectory (except for large asteroids such as Ceres in the sample mission). In the case of a comet flyby at the end of the mission (about three years) the SNAP-19 power would be inadequate, particularly with additional experiments included in the science payload.

### 7.5.3 Power Availability During the Mission

Figure 7-22 shows the representative power profiles of current-technology RTG power sources over three years of mission life. Included are the SNAP-19 used by Pioneer F and G, a higher powered

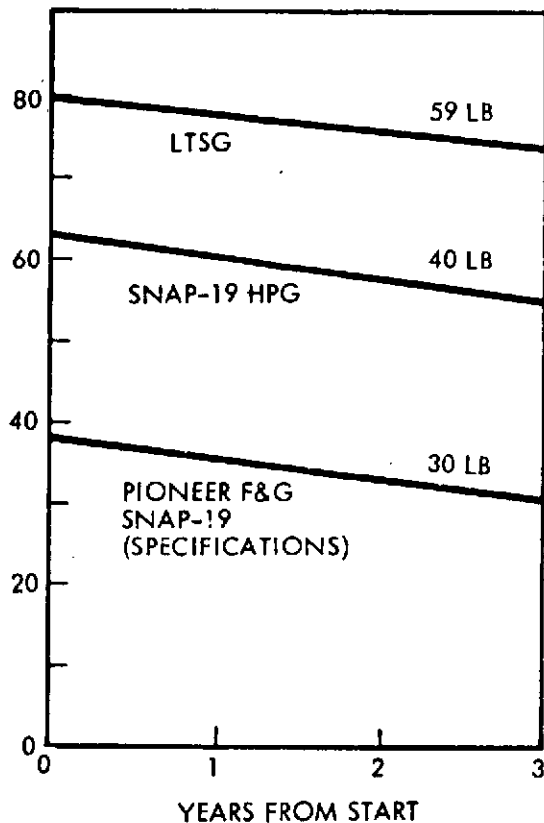


Figure 7-22. Representative Power Profile of Present and Advanced RTG's

shows contours of available power and corresponding flight times on trajectories through the asteroid belt. The power becomes marginal only in an area that generally excludes extended missions because of the limits of feasibility of terminal navigation.

version (HPG) of the SNAP-19 and the developmental low-temperature silicon-germanium (LTSG) generator that has been studied by TRW. The multi-hundred watt (MHW) generator, also currently under development, would supply more than 280 watts after two years in flight, greatly exceeding the requirements of this mission, and is not included in the graph.

The SNAP-19 RTG's of Pioneer F and G that have been adopted for the multi-asteroid spacecraft provide only 125 watts after 2.5 years. A conservative estimate of power requirements with all science payload instruments turned on is in the range of 120 to 125 watts. Figure 7-23

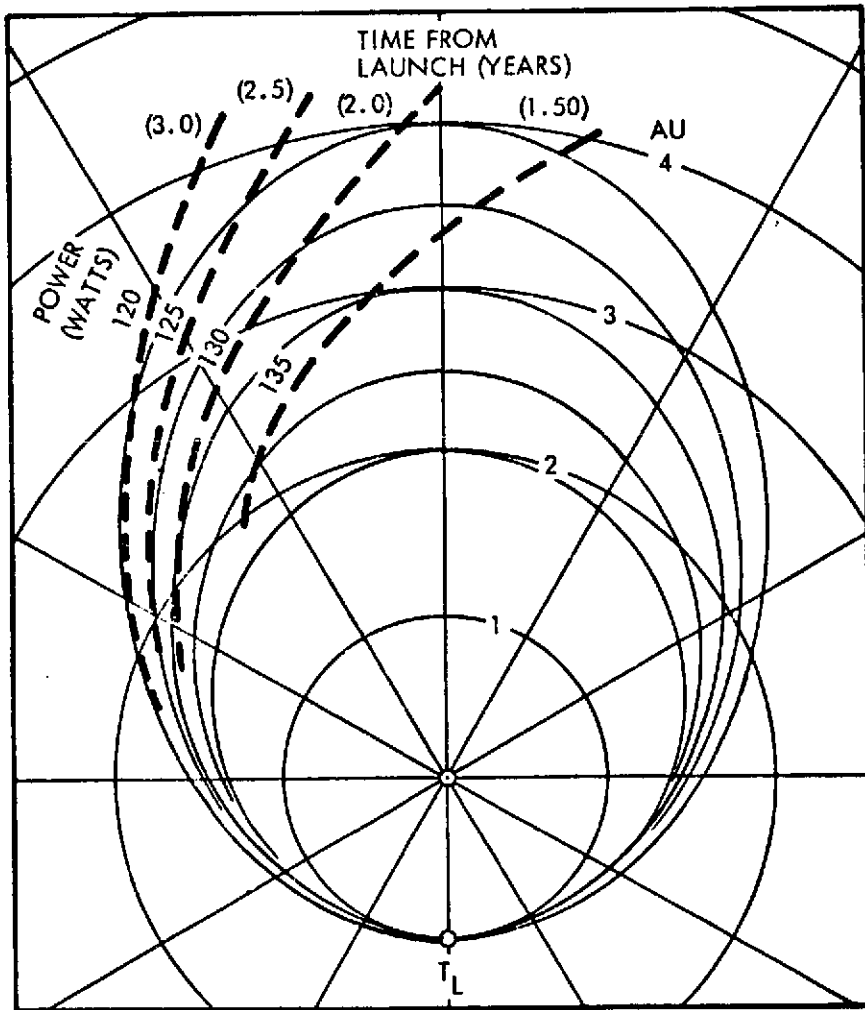


Figure 7-23. Contours of Available Power Across Mission Profiles (Pioneer RTG's)

## 7.6 THERMAL SUBSYSTEM

Thermal control requirements of the asteroid spacecraft are less severe than those of Pioneer F and G, with maximum solar distances reached by the spacecraft being limited to less than 80 percent of Jupiter's. Hence, the thermal subsystem of Pioneer F and G can be adopted with minimum change. The only change, or addition, required involves thermal protection of externally mounted and gimballed sensors, not carried by Pioneer F and G, and thermal control of the enlarged propulsion system.

### 7.6.1 Summary

The basic Pioneer F and G thermal subsystem has the following features:

- The equipment and experiment bays are thoroughly insulated to make the spacecraft as independent as possible of the sun.
- Active control, provided by about three square feet of bimetal actuated louver panels on the base platforms, is used to dissipate the absorbed solar input and internal heat dissipation.
- The sun sensor, thruster clusters, and the magnetometer are heated with twelve watts of radioisotope heater units (RHU's).

The increased propulsion capability required for the asteroid mission is provided by use of a larger hydrazine tank. Heaters are required for the enlarged hydrazine tank and for the added thruster. Other spacecraft subsystems, enroute environment and internal power levels are comparable to those of Pioneer F and G. The thermal control subsystem requires correspondingly little additional change.

### 7.6.2 Recommended Approach

The thermal control subsystem for the asteroid spacecraft is almost identical with the present Pioneer F and G subsystem. It is still an insulated compartment with louvers which radiate excess heat to space and with local heaters for appendages such as thrusters. This system can dissipate 132.4 watts of internally generated heat even when the sun is looking at the side of the spacecraft as it does in the beginning of the mission (1 AU). Or with the sun on the front of the spacecraft (on the antenna) and at 4 AU, the internal temperature at the hydrazine tank can be kept above 40<sup>o</sup>F with less than 80 watts of internally generated heat (assumes that one RTG has failed completely).

The hydrazine tank requires 2-watt thermostatically controlled electric heaters and a 3-watt radioisotope heater unit, and the lines require a total of 3 watts of thermostatically controlled electric heat. Also 2 watts of thermostatically controlled electric heaters and 3 watts of radioisotope heater unit are required for the added main thruster.

Externally mounted optical sensors are individually insulated against excessive heat loss. Since they are in a dormant mode during most of the mission, they will probably require small heaters. Mounted on the outside of the equipment bay and shaded by the antenna dish, no problems due to solar heating are anticipated. The fact that those instruments are attached to the main spacecraft body rather than mounted in an external payload platform simplifies thermal control requirements.

### 7.6.3 Comparison with Pioneer F and G Thermal Conditions

Tables 7-7 and 7-8 list the predicted temperature ranges of Pioneer F and G flight equipment and payload instruments under various exposure conditions ranging from 1 AU to 6 AU, and with solar illumination from the front or side. The first columns specify minimum and maximum acceptance temperatures. These data, although not applying directly to the asteroid mission, provide useful temperature brackets for this spacecraft, even without further analysis. The upper temperatures are typical for the Jupiter as well as the asteroid mission because of the comparable environment at 1 AU. The lower temperatures, applying to 6 AU, can be regarded as conservative low-temperature extremes that will never be reached by the asteroid spacecraft subsystems and payload equipment.

Table 7-7. Pioneer F and G Flight Equipment Temperature Predictions (Degrees F)

EQUIPMENT	ACCEPTANCE TEMPERATURES		SIDE SUN (1 AU)	FRONT SUN (1 AU)	FRONT SUN (6 AU)
	MINIMUM	MAXIMUM			
PCU	20	160	152	124	57
TRF	20	140	130	99	61
INVERTER	20	145	123/134	97/108	66/67
DIPLEXERS	20	100	92/94	63/66	45/46
TWTA (ON)	20	125	108	83	63
CDU	20	105	95	68	46
RECEIVERS	25	100	89/90	62/64	44/45
STELLAR REFERENCE ASSEMBLY	0	65*	91	54	35
DRIVERS	30	100	95/98	68/70	48/50
DTU	20	95	94	69	49
DSU	20	105	87	58	25
CEA, DDU, CONSCAN	20	105	97	72	46
BATTERY	0	60*	71	52	12
PROPULSION TANK	40	110	100	72	46

\* BASED ON FRONT SUN OPERATION

Table 7-8. Pioneer F and G Flight Experiment Temperature Predictions (Degrees F)

EXPERIMENTS	ACCEPTANCE TEMPERATURES		SIDE SUN (1 AU)	FRONT SUN (1 AU)	FRONT SUN (6 AU)
	MINIMUM	MAXIMUM			
MAGNETOMETER	-4	149	104	76	60
METEOROID	-22	122	98	69	52
CHARGED PARTICLES	-20	104	81	47	34
TRAPPED RADIATION	-20	104	99	52	38
UV PHOTOMETER	-40	122	98	62	48
GEIGER TUBE	-20	100	92	57	43
IMAGING PHOTO-METER	-20	120	90	60	47
COSMIC RAY	-20	104	93	58	44
PLASMA	-20	90	100	70	53
ASTEROID/METEOROID	-58	122	124	95	53
IR RADIOMETER	-22	90	83	44	32
EXPERIMENT PLATFORM	0	90	87	68	42

## APPENDIX A

### MICROMETEOROID PHOTO-SENSOR

#### 1. GENERAL DESCRIPTION

The micrometeoroid photo-sensor system (Reference A-1) was conceived by TRW for use in missions passing through the asteroid belt. Particle or asteroid parameters are deduced by photo-detecting sunlight reflected from the object and measuring the temporal and amplitude characteristics of this radiant input as the object traverses the system's 30-degree optical field of view (FOV). The pointing direction of the system is along the spacecraft spin vector. The optical configuration consists of a 152 mm focal length,  $f/0.87$  objective which focuses the light onto the photocathode of a S-11 photomultiplier tube (see Figure A-1). The 80-mm diameter active surface of each tube is masked by a reticle consisting of alternate opaque and transparent rings. Because of the spinning motions, star images will describe circular paths on the reticle, staying within one band and not producing any modulation in the photomultiplier signal. As a detectable object passes through the field of view, the object image traces a path across the photo surface generating an output pulse train which is processed to give field-of-view transit time, apparent object radiance, orbital plane relative to a system reference plane, and range variation of the objects observed as well as the encounter event rate. Appropriately signal conditioned, this data is telemetered to earth for data reduction. Using estimated values of object mean velocity, albedo, size and population density of objects ranging from  $10^{-5}$  grams up can then be determined.

This system operates on a simpler principle than the Sisyphus system because it requires only a single optics and signal processing involves fewer geometrical quantities. The major disadvantage is the inability of the system to measure velocity or range, although it can detect relative angular velocities.

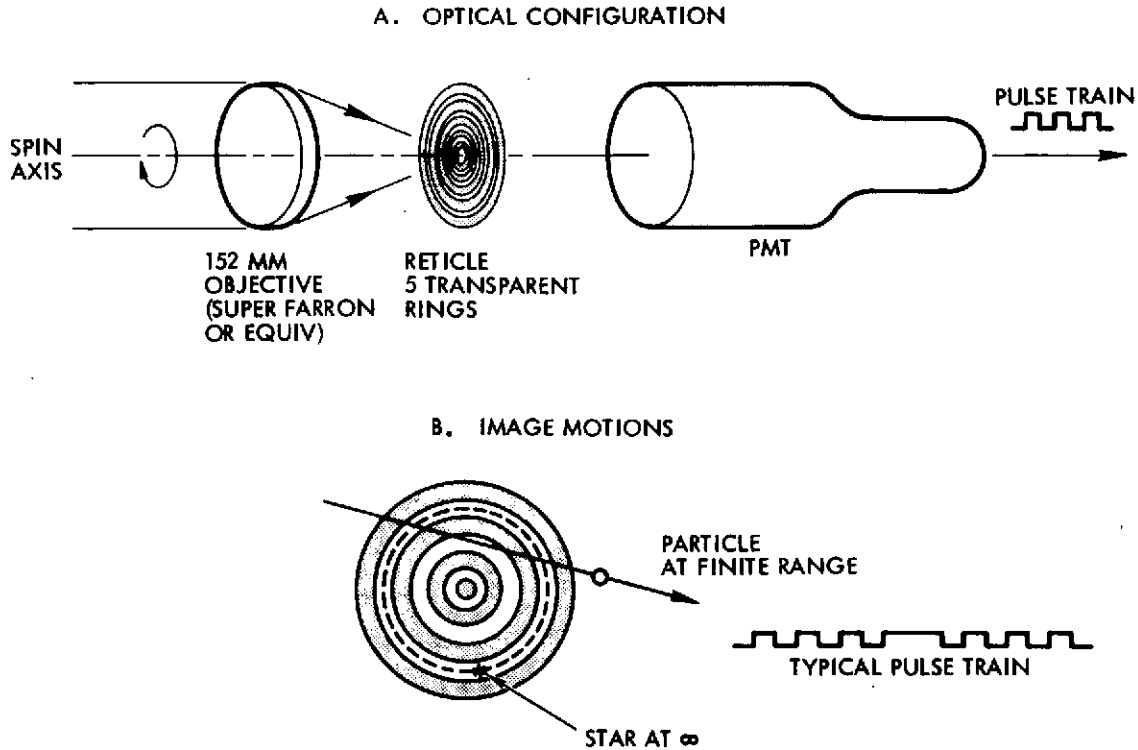


Figure A-1. Meteoroid Photosensor System

## 2. SYSTEM PERFORMANCE

For a spherical object of radius  $r$ , at distance  $R$  from the sensor, the voltage signal-to-noise ratio is given by

Measured	Computed from known or assumed values	Computed from measurements	Unknown
$S/N$	$= \frac{PFD}{4a^2 \theta} \left( \frac{2 t_o n}{N_s P_s \Delta f \pi} \right)^{1/2}$	$\cdot \frac{1}{R^2}$	$\cdot r^2$

where the parameter descriptions and assigned values are listed in Table A-1. To the extent that assumed parameter values are accurate and  $S/N$  and  $R$  can be accurately measured, a determination of  $r$  can then be made.  $R$  is estimated by dividing an assumed cross-range velocity,  $V$ , by the measured angular rate,  $\omega = \theta_c/T$  where  $T$  is the total transit time and  $\theta_c$  is the angular chord length traced by the object across the system field-of-view. For a threshold  $S/N$  of 5, the maximum range  $R_M$  at which an object of radius  $r$  may be detected is given by the relation  $R_M = 6 \times 10^5 r$ . Thus an object of 50-meter size could be detected at a range of 30,000 km.

Table A-1. Micrometeoroid Photosensor System Parameters

Parameter Symbol	Parameter Description	Value
1. D	Lens diameter	178 mm
2. P	Particle albedo	0.05
3. F	Solar flux between 0.4 and 0.6 $\mu$ at 1 AU from sun	$2 \times 10^{17}$ photons/ (cm <sup>2</sup> -sec)
4. t <sub>o</sub>	Optics transmittance	0.7
5. n	Photocathode quantum efficiency	0.1 electrons/ photon
6. a	Approximate asteroid belt distance from the sun	$\sqrt{10}$ AU
7. (S/N) <sub>o</sub>	Threshold post-detection signal-to-noise voltage ratio	5
8. $\theta$	Sensor system field-of-view	30 deg
9. N <sub>s</sub>	Star field density normalized to stellar magnitude of 10 reduced by 2 due to mask blocking factor	50 per sq deg
10. P <sub>s</sub>	Star flux rate due to 10th magnitude star	$10^2$ photons/ (cm <sup>2</sup> -sec)
11. $\Delta f$	Post-detection, pre-threshold filter bandwidth	25 cps
12. K	Ratio of mask angular line width to total field of view	0.1
13. V	Mean cross range velocity of particles at $\sqrt{10}$ AU	10 km/sec

### 3. RATE OF DETECTION OF LARGER METEOROIDS BY THE TV IMAGE SYSTEM

The rate of detection depends on the size and abundance of the meteoroids and asteroids, and on the sensitivity of the optical system. Even with a 6th or 9th magnitude detection threshold there will be few detectable encounters of sizeable target objects.

Figure A-2 shows apparent magnitudes of asteroid bodies at various distances  $d$  as a function of diameter  $D$ . An asteroid of 1 km diameter must be within  $5 \times 10^5$  km to be detected as a 6th magnitude object. A solar distance of 2.5 AU is assumed as basis of this plot.

Figure A-3 shows the ideal detection range of objects from 0th to 9th magnitude as a function of object diameter. The example of a 1 km diameter object requires a detection range of  $5 \times 10^5$  km with a sensitivity threshold of 6th magnitude stars. This graph does not take actual optical characteristics of the image system into account.

Figure A-4 uses the above data and a nominal meteoroid flux model to determine the number of objects that can be detected per day by an ideal detection system with an assumed 20-degree field-of-view. The sensitivity threshold again is the parameter in this graph.\*

An additional set of curves in this diagram gives the time required for the object to cross the 20-degree field of view, which depends on the detection range implied by the diameter of the object and the system's detection threshold a 10 km/sec relative velocity was assumed as typical for the encounter.

The graph shows that a sensitivity threshold of 9th magnitude would yield slightly more than one detection over a 10-day interval for objects of 1 m diameter, and a single detection every 100 days for objects of 100 m diameter. Detection of the more abundant smaller objects runs into a lower size limit given by the minimum time of crossing the field of view for which the detection system is designed. A 1 second lower limit would make the minimum object size approximately 10 cm.

Reference A-1. "Proposal for Electro-Optical Micrometeoroid Detector Feasibility Study," TRW Systems Proposal No. 10782, 11 December 1967.

\* These results, derived for a 20-degree field of view, should be updated to reflect the 50 percent larger field-of-view angle (30 degrees) assumed in the analysis.

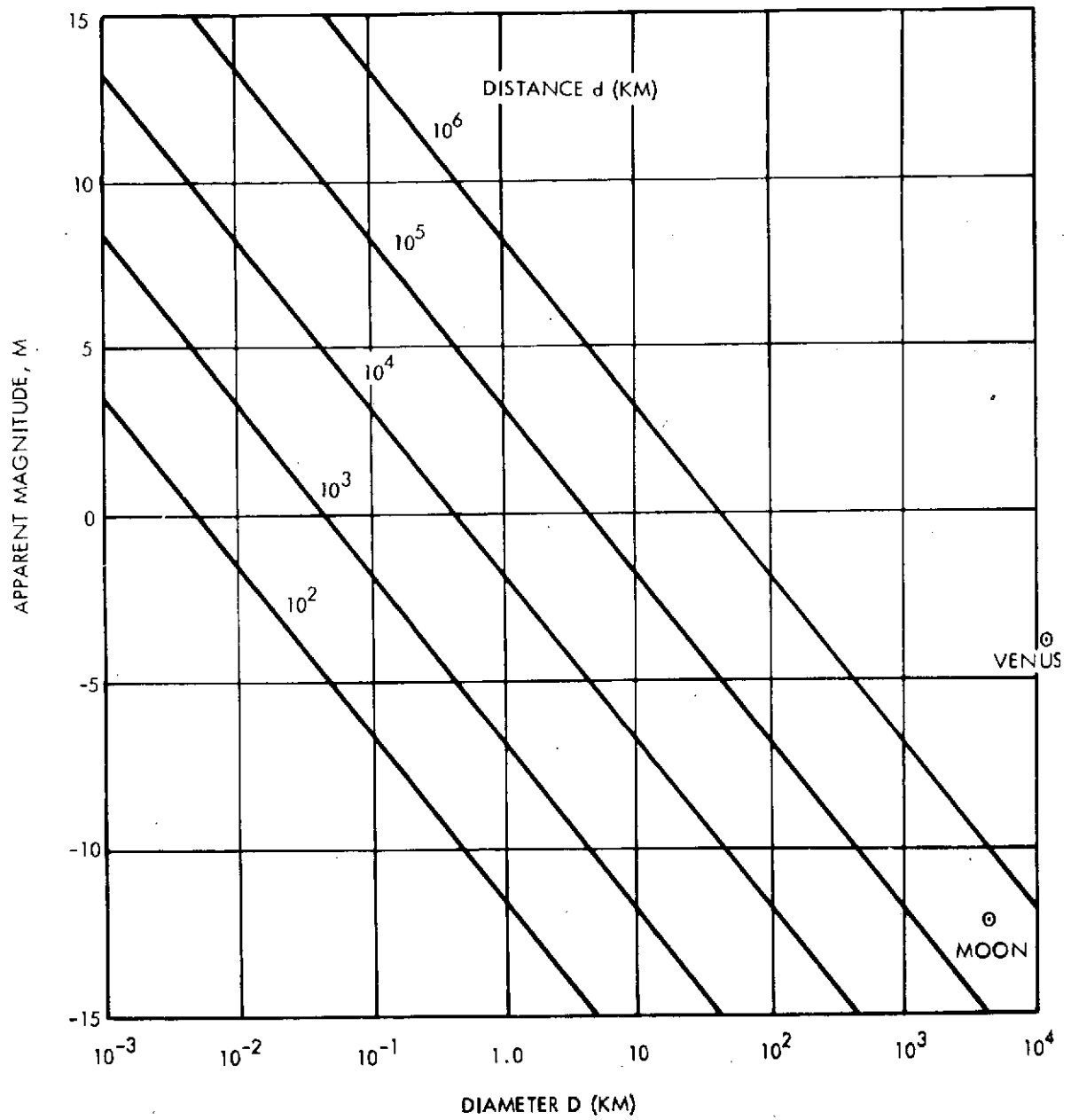


Figure A-2. Apparent Magnitudes of Asteroid Bodies

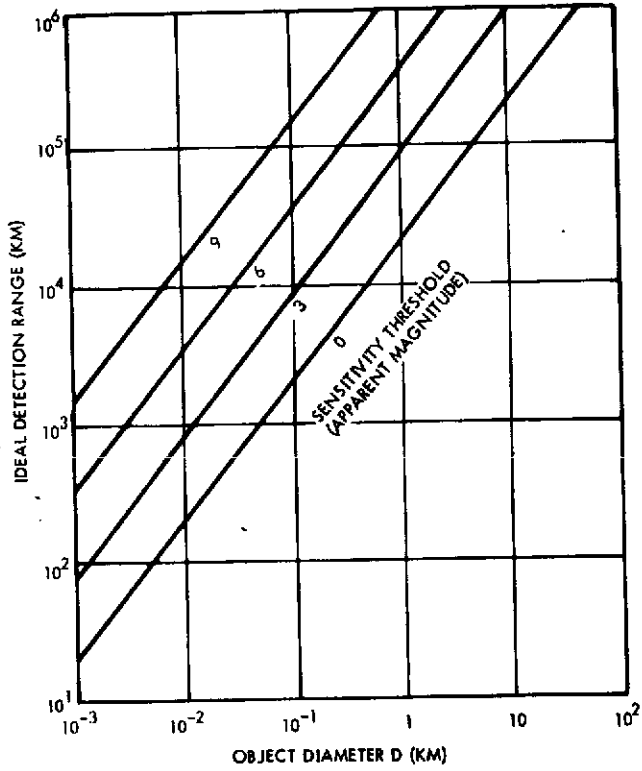


Figure A-3. Ideal Detection Range

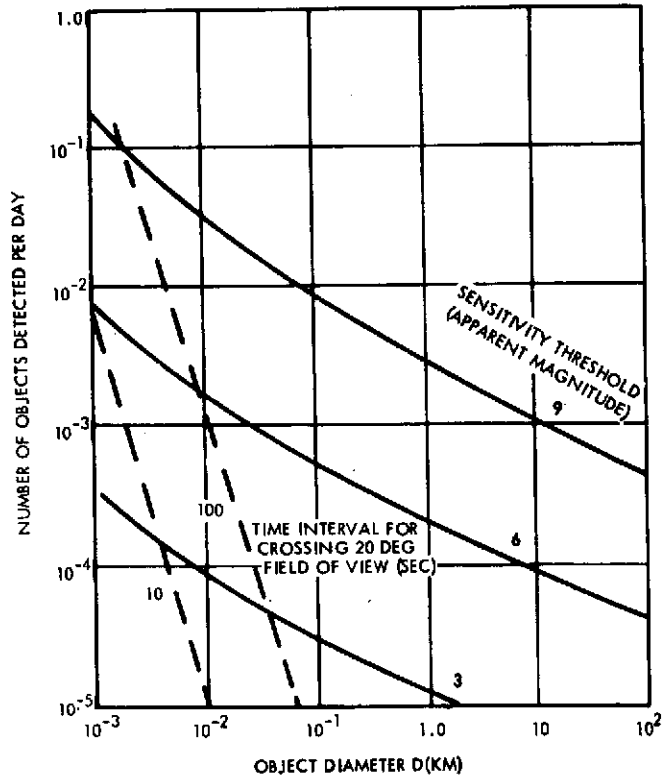


Figure A-4. Number of Objects Detected per Day

## APPENDIX B

### ESTIMATED NUMBER OF ACCESSIBLE ASTEROIDS FOR A MISSION WITH ARBITRARY LAUNCH DATE

An estimate of the number of accessible asteroids for arbitrarily timed missions can be obtained by assuming a uniform random distribution of asteroids in a given volume of the asteroid belt. The key parameter in this estimate is the assumed maneuver capability  $\Delta V$  of the spacecraft which determines asteroid accessibility.

Figure B-1 defines the model underlying this analysis. A tube of radius  $r_T$  with the reference trajectory as centerline is assumed as the volume in space that contains the number  $N_T$  of asteroids accessible by retargeting maneuvers  $\Delta V_T$ . For a three-asteroid mission only the second and third asteroid require retargeting maneuvers from the reference trajectory. An average  $\Delta V_T$  requirement is defined by letting the second and third asteroid be located at the outer wall of the tube and on the centerline, as illustrated in the diagram. The length of the tube is

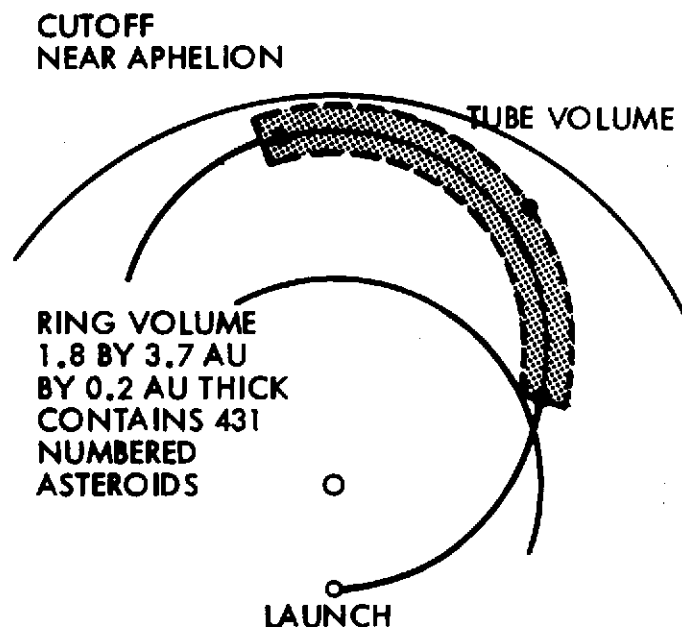


Figure B-1. Assumed Model for Calculation  
of Accessible Asteroids

determined by assumed start and end points of the encounter sequence. The start occurs at entry in the asteroid belt and the encounters are terminated at a central angle 75 degrees from the start. This places the end point not far beyond aphelion passage. This provides a realistic estimate of flyby opportunities since encounters long after aphelion passage are hampered by unfavorable lighting angles and, hence, increasingly difficult terminal navigation requirements.

The following additional assumptions were made in this calculation:

- A ring-shaped volume of the asteroid belt, 1.8 by 3.7 AU and 0.2 AU thick contains 431 numbered asteroids (see Reference 3-1) on the average. Thus, the spatial density is about  $2.5 \times 10^{-23}$  numbered asteroids per  $\text{km}^3$ .
- This number is doubled if unnumbered asteroids are also accepted as targets.
- A typical reference trajectory is assumed to have an aphelion of 3.6 AU and zero inclination to the ecliptic plane.
- The second maneuver requirement is estimated to be of the same magnitude as the first under average conditions (low  $\Delta V_T$  estimate) or up to three times larger than the first under worst-case relative positions of the second and third target asteroids, (upper  $\Delta V_T$  estimate). The upper estimate gives a total  $\Delta V_T$ , twice as large as the first.

The resulting number of asteroids  $N_T$  in the tube volume and upper and lower estimates of maneuver requirements  $\Delta V_T$  are plotted versus tube radius  $r_T$  in Figure B-2. This shows that for a maneuver limit of 500 m/sec the accessible tube radius varies between 4.5 and 9 million km, and the number of accessible asteroids at any launch date ranges from less than one to more than six, depending on the assumed number of asteroids in the ring volume defined above. If a larger maneuver capability of 1000 m/sec were assumed (not compatible with the modified Pioneer propellant capacity) the number of accessible asteroids would increase, varying from 3 to 30, i. e., about five times more asteroids by doubling the maneuver capability.

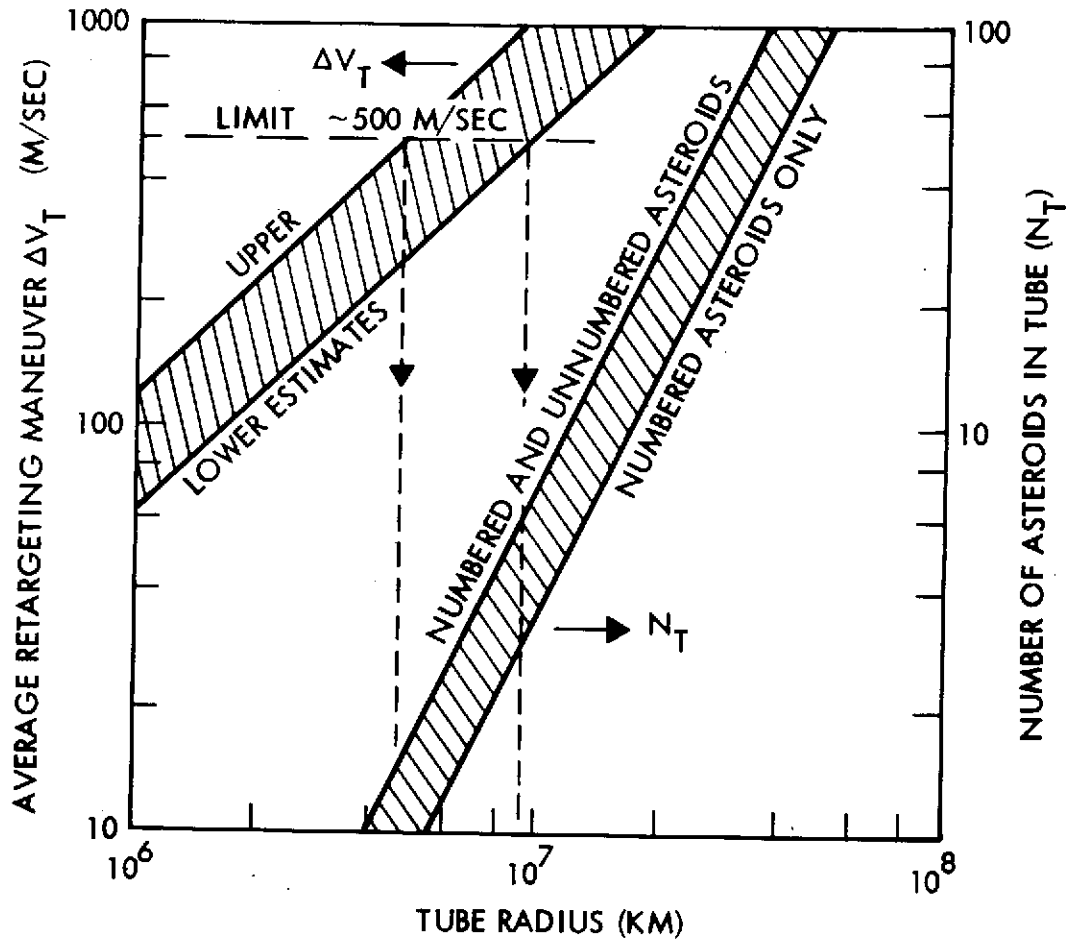


Figure B-2. Number of Asteroids in Tube and Required Retargeting Maneuver.

Figure B-3 shows the probability of finding  $M$  or more asteroids in the tube volume for arbitrary launch dates, if, on the average, the number of asteroids in the tube is  $N_T$ . This calculation, dealing with the probability of occurrence in small sample cases, is based on a Poisson distribution of encounters. The graph on the left gives this probability as a function of the desired number of asteroids in the mission ( $M$ ), the graph at the right as a function of average retargeting maneuver requirements  $\Delta V_T$  and tube radius  $r_T$ . The average number of accessible asteroids  $N_T$  in the tube is the parameter of the curves shown in both graphs. As an example, the probability of finding three or more accessible asteroids for missions with arbitrary launch dates is 0.5 if  $N_T = 3$ . The average total maneuvering requirement for this case is about 650 m/sec.

These results are in general agreement with the many examples of possible mission candidates that are listed in Reference 3-1.

$N_T$  = AVERAGE NUMBER OF ASTEROIDS IN TUBE VOLUME

B-4

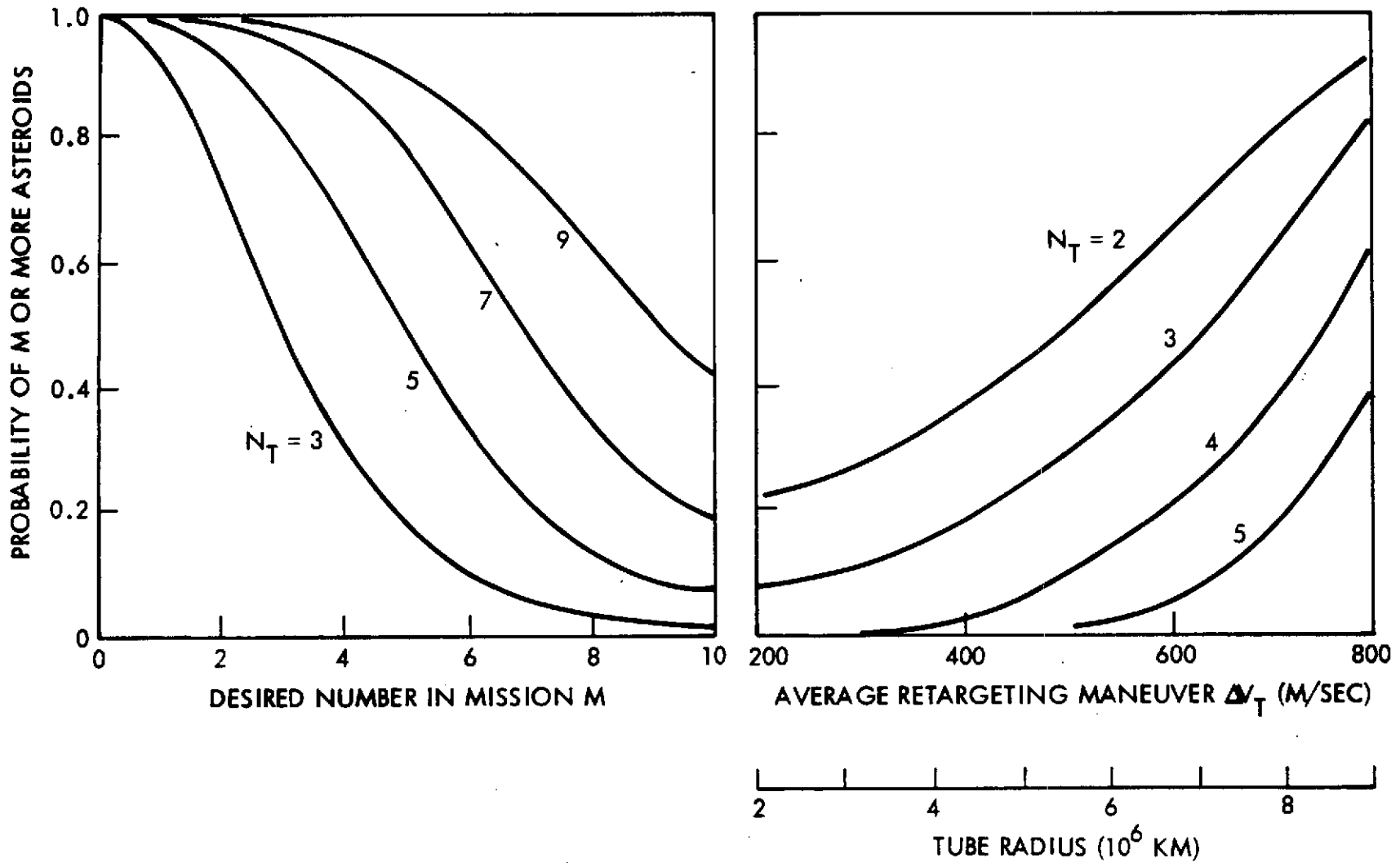


Figure B-3. Probability of Finding Multiple Asteroid Mission Opportunities at Random Launch Dates

## APPENDIX C

### MICROMETEOROID EXPOSURE DURING ASTEROID ENCOUNTER

A preliminary analysis was performed to compare the micro-meteoroid exposure of the asteroid spacecraft to that of Pioneer F and G, and to determine whether additional meteoroid impact protection must be provided. The difference of the two mission profiles from a standpoint of meteoroid impact hazard involves primarily the length of time of exposure and the relative velocity of particles encountered. The flux density  $\phi$  in particles per  $m^2$ /sec increases in proportion with the relative velocity which is about 50 percent larger, on the average, for the rapidly moving Jupiter probe than for the asteroid probe. Another factor is the angle of incidence and the shielding provided by the high-gain antenna during that part of the asteroid mission where meteoroids would tend to impact from the front.

For the mission profile of the asteroid probe the incident angle changes continuously. Initially, after entry into the asteroid belt the particles tend to come from the rear; at the time of aphelion passage they tend to come from the side in a direction opposite to the spacecraft heliocentric velocity; after aphelion passage the incidence is increasingly from the front. This analysis is based on the simplifying assumptions that:

- 1) The majority of the particles encountered are of asteroidal origin and move in circular coplanar orbits with the spacecraft.
- 2) The spacecraft is sun-oriented rather than earth-oriented. Actually, during the asteroid belt cruise the sun-probe-earth angle varies between +20 and -20 degrees and affects the incidence angles accordingly.

The number of particles of mass  $m$  or greater that impact a spacecraft with exposed area  $A$  per unit time is given by:

$$N = A S V_r \cos \phi \text{ (particles per } m^2/\text{sec)}$$

where

- S - number density of particles of mass m or greater  
(particles per m<sup>3</sup>)
- V<sub>r</sub> - relative velocity of particles relative to the spacecraft  
(m/sec)
- A - exposed area (m<sup>2</sup>)
- φ - orientation angle of relative velocity vector  $\bar{V}_r$  with  
respect to the surface normal of A

Thus the number of impacts during a mission that remains in the asteroid belt for a total time T (sec) is given by

$$N_T = AS_o \int_0^T \frac{S}{S_o} V_r \cos \phi \, dt = AS_o \int_0^T F(R) \, dt$$

where S<sub>o</sub> is a reference number density which reflects the maximum particle flux in the center of the asteroid belt, and the density S is a function of solar distance R. The integration must take the range variation of the integrand  $F(R) = \frac{S}{S_o} V_r \cos \phi$  into account. This integrand will be referred to as exposure index.

Figure C-1 shows the variation of the exposure index F(R) (in km/sec) with solar distance for Pioneer 10 and a 4 AU asteroid belt probe. The principal difference between the two curves (dashed lines) is explained by the dissimilarity in the normal velocity component V<sub>r</sub> cos φ of the incident particles (solid lines). In the case of the asteroid probe this component goes to zero at aphelion (R = 4 AU). Shielding by the antenna dish is assumed to exclude damage due to particles striking the front side of the spacecraft. Hence, the exposure index corresponding to the probe's return trajectory is set equal to zero.

The exposure index also reflects the range variation of the relative density S/S<sub>o</sub>, in accordance with a nominal model of particle distribution across the asteroid belt (Reference C-1). The maximum of this distribution occurs at R = 2.8 AU.

Figure C-2 shows the exposure index F(R) replotted as a function of time from entry into the asteroid belt. (The predicted incidence of

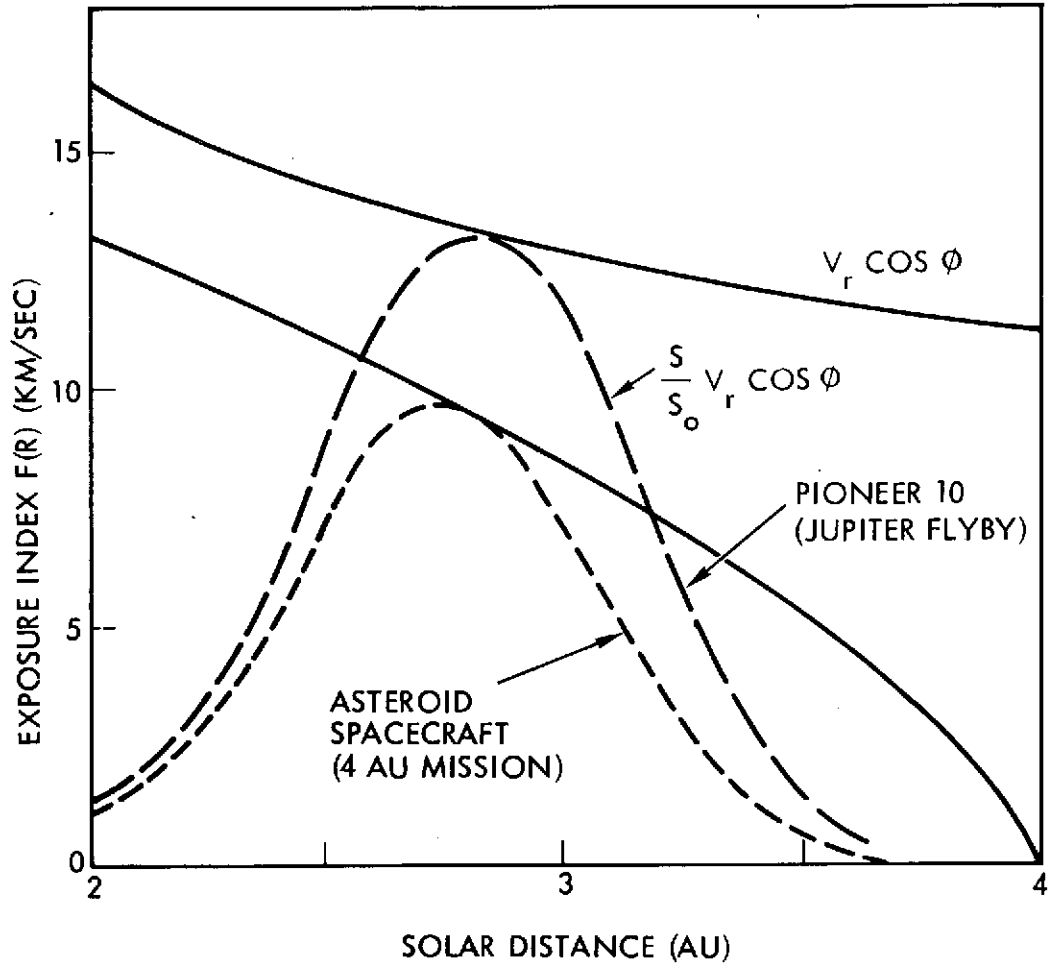


Figure C-1. Exposure Index for Pioneer 10 and Asteroid Spacecraft versus Solar Distance

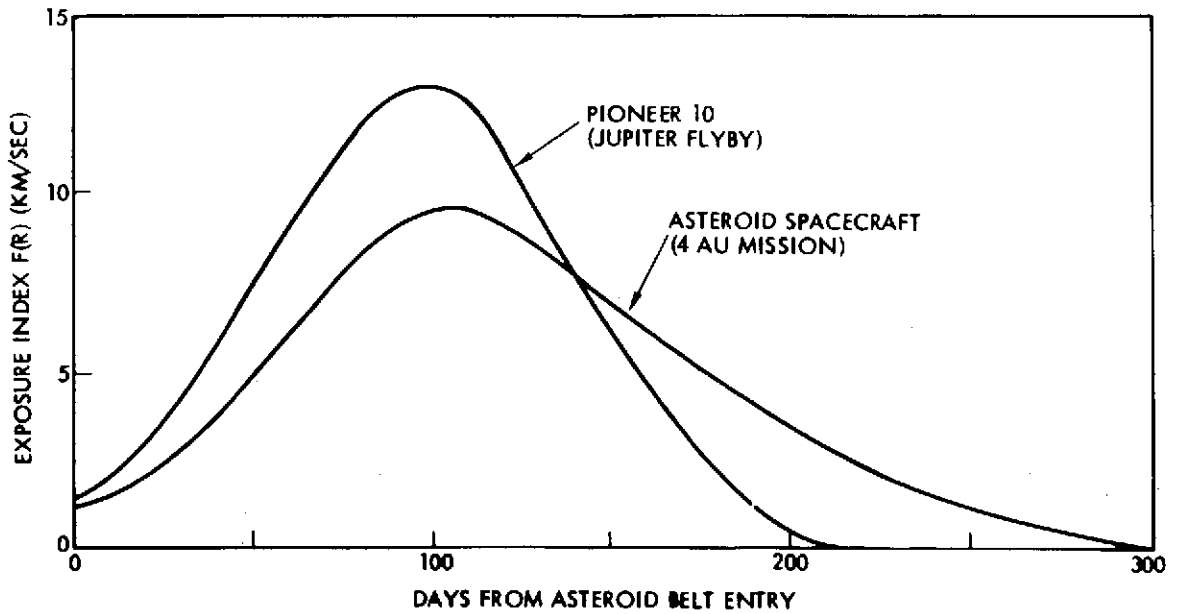


Figure C-2. Exposure Index for Pioneer 10 and Asteroid Spacecraft versus Time

particles before entry into the asteroid belt is small according to the nominal model of the spatial density  $S(R)$  and has been ignored here.)

The area under the two curves in Figure C-2 represents the normalized total number of particles of mass  $m$  or greater that strike the rear of the spacecraft during the two missions. To obtain an actual number this integral must be multiplied by a reference density  $S_0$  and the exposed area  $A$ .

Without calculating the actual number of bits predicted by this model we note that the area under the asteroid probe curve is slightly smaller than that under the Pioneer 10 curve. The integrals are  $1.1 \times 10^{10}$  and  $1.2 \times 10^{10}$  (in units of meters), respectively. This shows that the exposure hazard for the asteroid probe is about comparable to that of the Pioneer 10 and no added protection is required (other than the local shielding of the protruding propellant tank section in front and rear, as discussed in Section 6).

We also note that results obtained for the asteroid mission is conservative assuming a 4 AU aphelion and hence, an exposure time that is about 30 to 50 percent longer than that experienced for a more typical mission to 3-3.5 AU. Secondly, the asteroid density distribution may actually vary less strongly with range than in the nominal model of  $S/S_0$ .

This appears likely on the basis of preliminary data regarding micrometeoroid impacts counted by Pioneer 10 as of this writing. In that case the difference in the time histories of  $V_r \cos \phi$  for the two spacecraft would tend to favor the asteroid probe compared to the Jupiter probe, and would make the integrated particle count of the asteroid probe relatively even smaller.

As a quantitative example we consider impacts by particles of  $10^{-3}$  grams or larger. Published models of the spatial density vary between  $10^{-13}$  and  $10^{-10}$  per  $m^3$  for this value of  $m$ . With an exposed area of about  $1.3 m^2$  and using the above values of the normalized integral  $\int_0^T F dt$ , the number of bits projected for both missions is of the order of  $10^{-3}$  to 1.

## APPENDIX D

### MULTIPLE DSIF STATION COVERAGE (210-FOOT ANTENNAS)

The use of X-band telemetry introduces the problem of weather dependence at the ground station. In contrast to other planetary missions for which X-band telemetry is projected the MAF mission is characterized by extremely brief target encounters. During the critical few minutes of encounter there cannot be any margin for failure of downlink communications. The mission plans should therefore include provisions for multiple DSIF station coverage at each asteroid encounter.

Figure D-1 shows overlap zones of the Goldstone, Madrid and Canberra stations where 210-foot antennas are located. Figure D-2 illustrates in geometrical terms the influence of the launch season on northern versus southern latitude tracking capabilities during the mission. Preliminary analysis of combined coverage by the Goldstone and Madrid stations yields qualitative results on favorable and unfavorable launch seasons which are listed at the bottom of Figure D-2. Combined Goldstone/Canberra coverage is less dependent on the launch season but is available for at most five hours per day. This problem requires further study as mission plans begin to materialize.

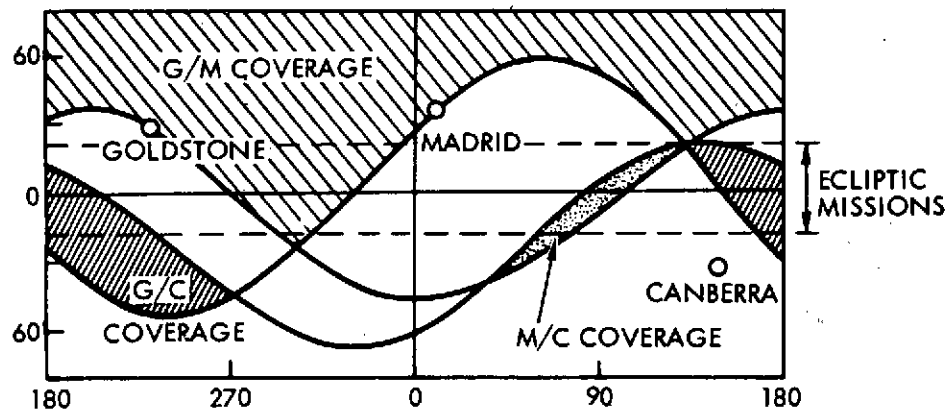
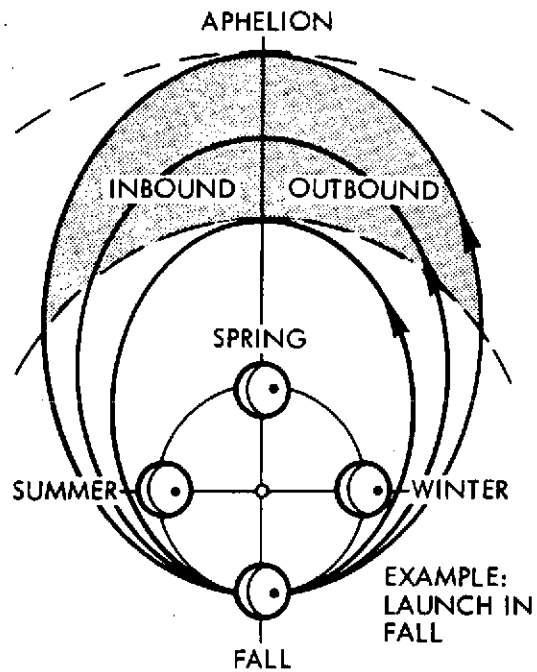


Figure D-1. DSN Coverage for Ecliptic Missions



**GOLDSTONE/MADRID COVERAGE:**

MAXIMUM OVERLAP:  
100 DEG  $\approx$  6.6 HOURS

LAUNCH SEASON	MISSION PHASE		
	OUTBOUND	APHELION	INBOUND
SPRING	GOOD	FAIR	POOR
SUMMER	FAIR	GOOD	FAIR
FALL	POOR	FAIR	GOOD
WINTER	FAIR	POOR	FAIR

**GOLDSTONE/CANBERRA COVERAGE:**

NEARLY UNIFORM REGARDLESS OF LAUNCH SEASON AND ARRIVAL TIME.  
70 TO 75 DEG OVERLAP  $\approx$  4.8 HOURS

Figure D-2. Seasonal Influence on DSN Coverage